

Final Report

for

MICROWAVE RADIOMETER DESIGN AND DEVELOPMENT

Volume II of 2 Volumes
(Appendixes)

15 November 1967


Contract No. NAS 5-9680

168-16707

Goddard Space Flight Center

Contracting Officer: R. L. Krenning
Program Officer: C. Catoe


C. U. Falco
Advanced Microwave
Systems Division


G. Oister
Program Manager

Prepared by

Aerojet-General Corporation
Space Division
9200 East Flair Drive
El Monte, California

for

Goddard Space Flight Center
Greenbelt, Maryland

CONTENTS

		<u>Page</u>
Appendix I	NIMBUS Radiometer Antenna Patterns	I-1
Appendix II	Ferrite Circulator-Switches	II-1
Appendix III	Position of Horizontally-Polarized Grating Lobes	III-1
Appendix IV	Effect of Waveguide Tolerances on Phase Front of Ported-Array Elements	IV-1
Appendix V	Review of Basic RF Preamplifier Gain Require- ments for the NIMBUS Radiometer Receiver. . .	V-1
Appendix VI	Phase-Shifter Coil Requirement	VI-1
Appendix VII	Beam Angle for 94 Percent Crossover	VII-1
Appendix VIII	Phase Shifter and Drive Requirements	VIII-1
Appendix IX	Suppression of a Cross-Polarized Field With a Ground Plane	IX-1
Appendix X	Monte Carlo Analysis	X-1
Appendix XI	Beam Positions for Scanning and Other Miscellaneous Topics	XI-1
Appendix XII	Beam Efficiency of a Scanning Planar Array Antenna	XII-1
Appendix XIII	Continuous One-Piece Waveguide Flange for the NIMBUS Antenna	XIII-1
Appendix XIV	Phase Shifter Drive/Bias Coil; Fundamental Design	XIV-1
Appendix XV	An Electronically-Scanned K-Band Phased Array for Space-Borne Radiometric Applications	XV-1
Appendix XVI	Antenna Pattern Range for Space-General Corporation	XVI-1
Appendix XVII	NIMBUS Breadboard Linearity Measurements	XVII-1
Appendix XVIII	The Measurement of ΔT	XVIII-1
Appendix XIX	Circuit Description of NIMBUS IF Amplifier, Post Detection, and Switch Driver Circuits . .	XIX-1
Appendix XX	Bench Calibration of Meteorological Satellite Radiometer	XX-1
Appendix XXI	Measurement of NIMBUS Antenna Radiometric Efficiency	XXI-1
Appendix XXII	Preliminary NIMBUS Breadboard Test Pro- cedure (Preliminary Testing)	XXII-1
Appendix XXIII	NIMBUS Radiometer Test Set - Telemetry Interface Circuitry	XXIII-1
Appendix XXIV	Evaluation of the Breadboard Microwave Meteorological Radiometer and Scanning Antenna	XXIV-1
Appendix XXV	Frequency Stability of Solid State Source	XXV-1
Appendix XXVI	Test Results of Solid State Source	XXVI-1
Appendix XXVII	NIMBUS Phase Shifter Design	XXVII-1
Appendix XXVIII	A Solid State Local Oscillator Source at 19.35 GHz	XXVIII-1

CONTENTS (Continued)

	<u>Page</u>
Appendix XXIX	Antenna Measurements XXIX-1
Appendix XXX	Cryogenic Bench Test Set XXX-1
Appendix XXXI	Relations for the Exact Calculation of Radiometric Temperatures of Cryogenic-Cooled Sources XXXI-1

Appendix I
NIMBUS RADIOMETER ANTENNA PATTERNS

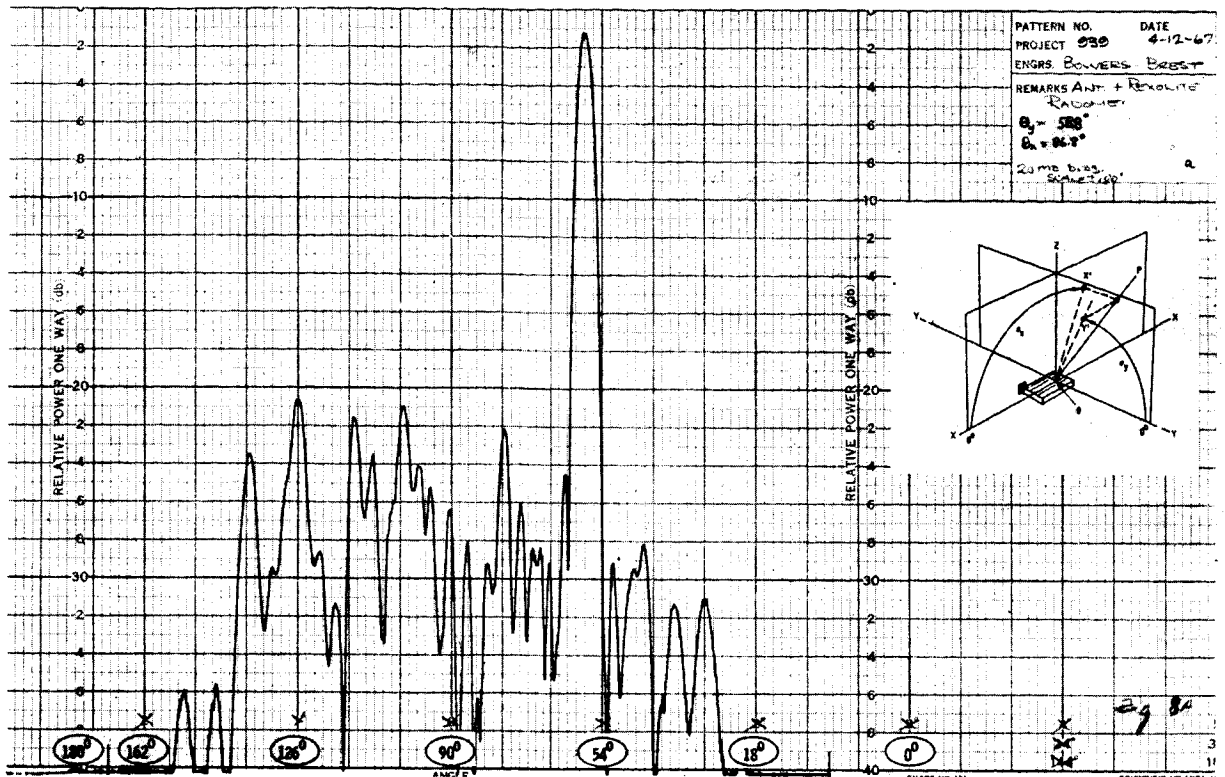
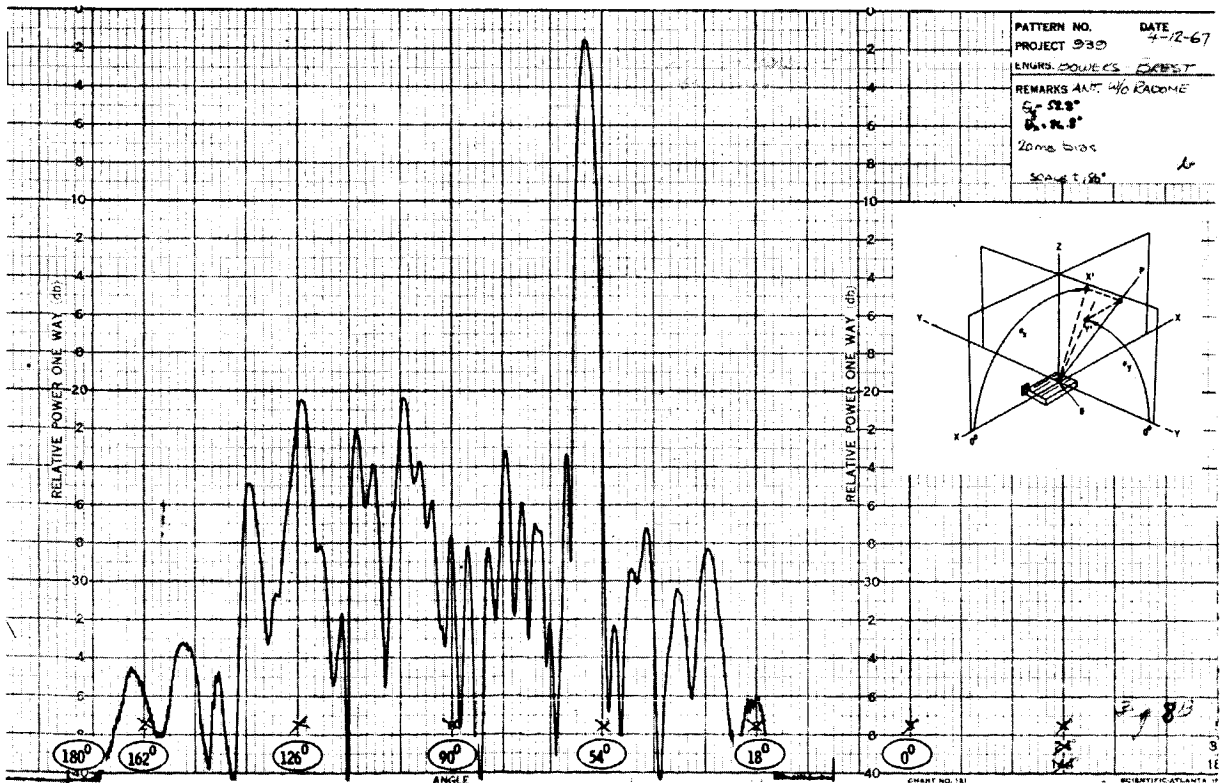


Figure I-1. a. Antenna Pattern, $\theta_y = 58.8^\circ$ with Radome



b. Antenna Pattern, $\theta = 31^\circ$ without Radome

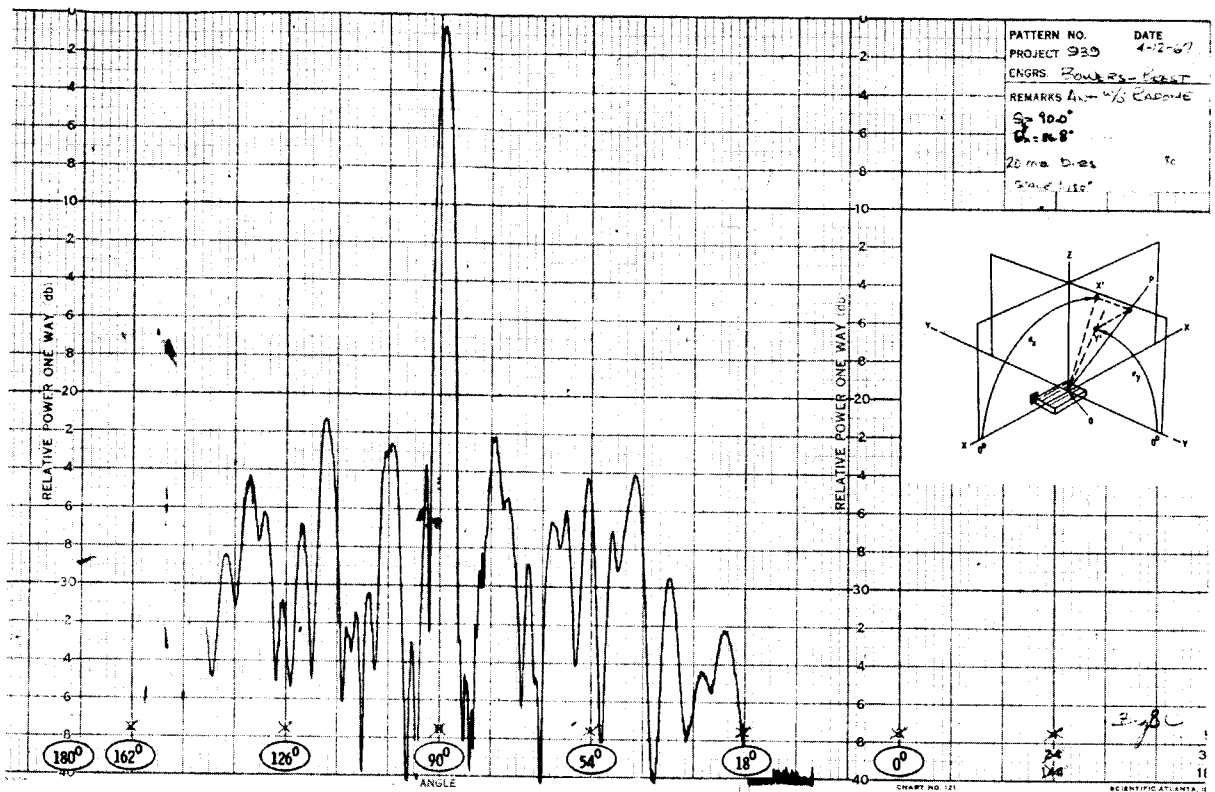
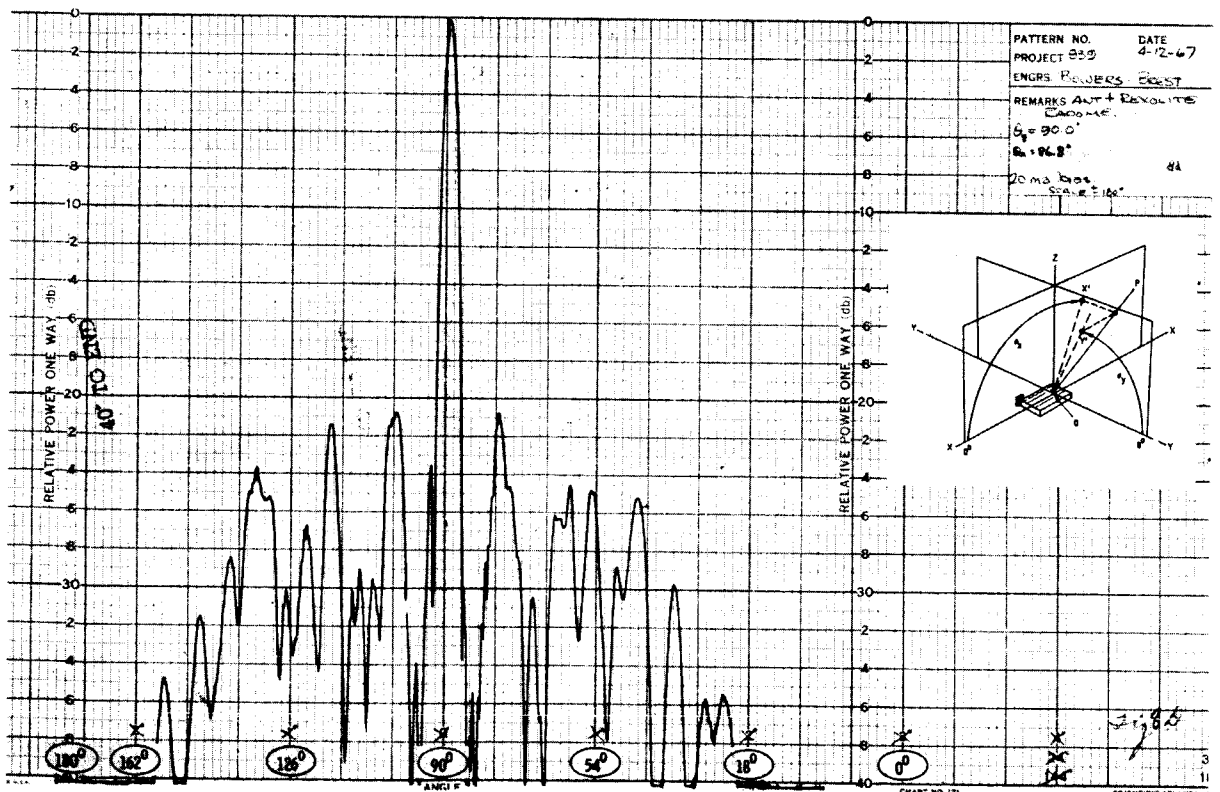


Figure I-2. a. Antenna Pattern, $\theta_y = 90^\circ$ without Radome



b. Antenna Pattern, $\theta_y = 90^\circ$ with Radome

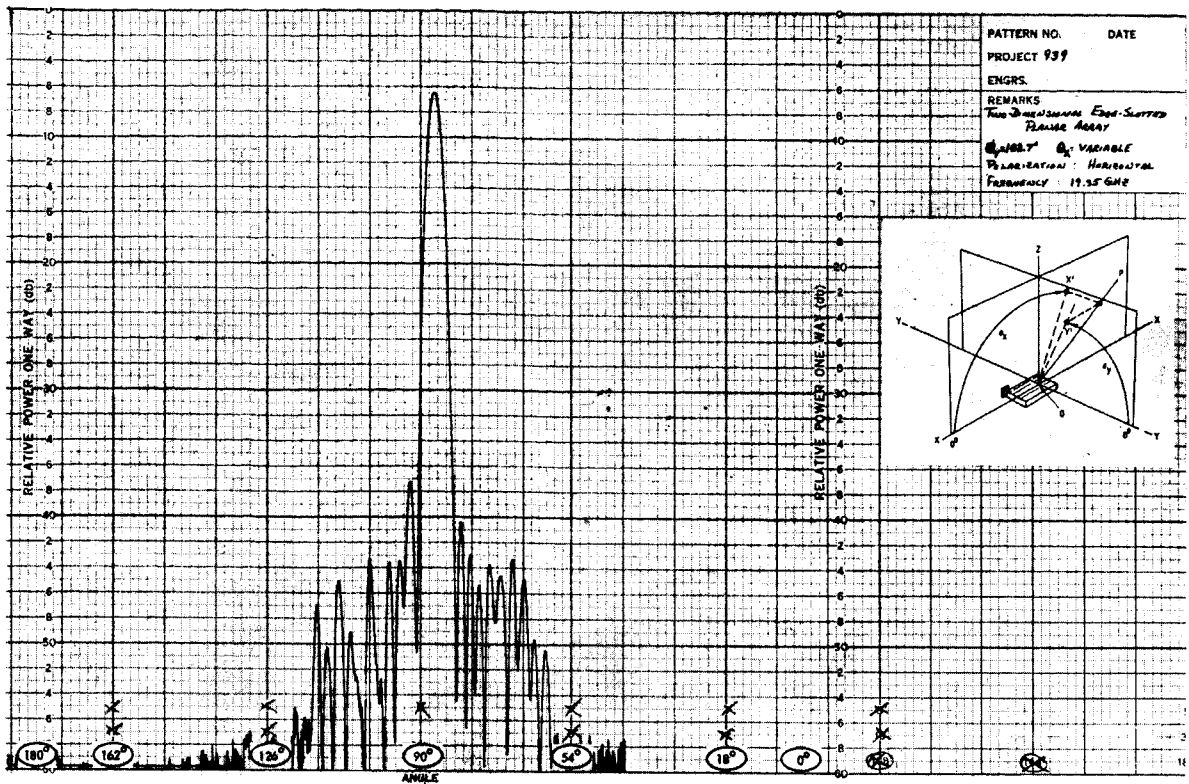
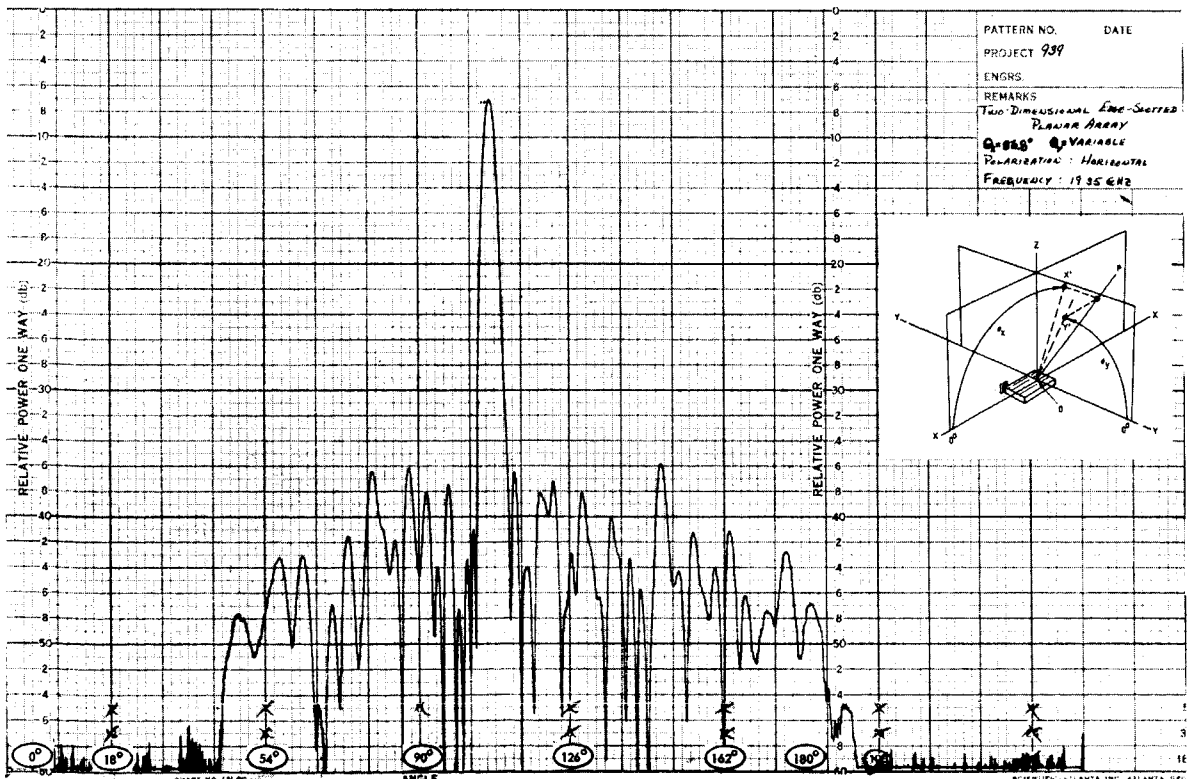


Figure I-3. a. Antenna Pattern, θ_x Variable, $\theta_y = 103.7^\circ$ without Phase Shifters^y



b. Antenna Pattern, θ_x Variable, $\theta_y = 86.8^\circ$ without Phase Shifters^y

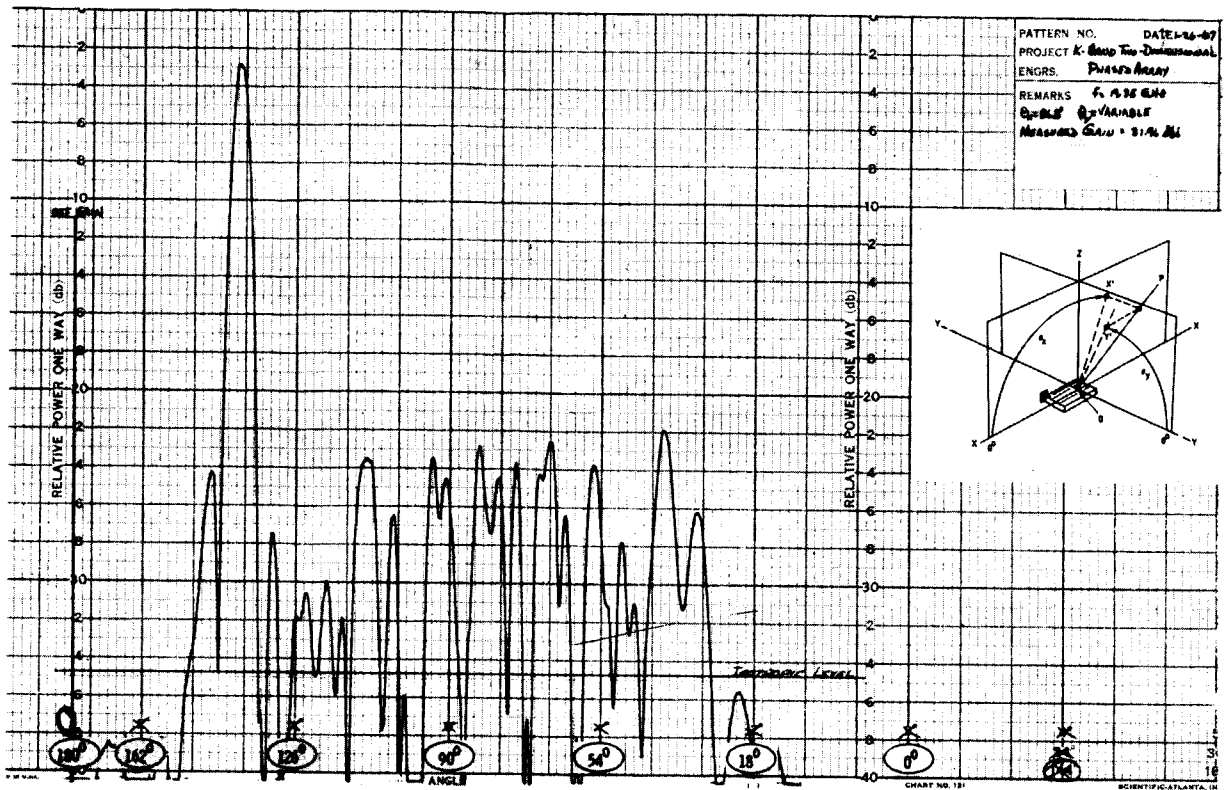
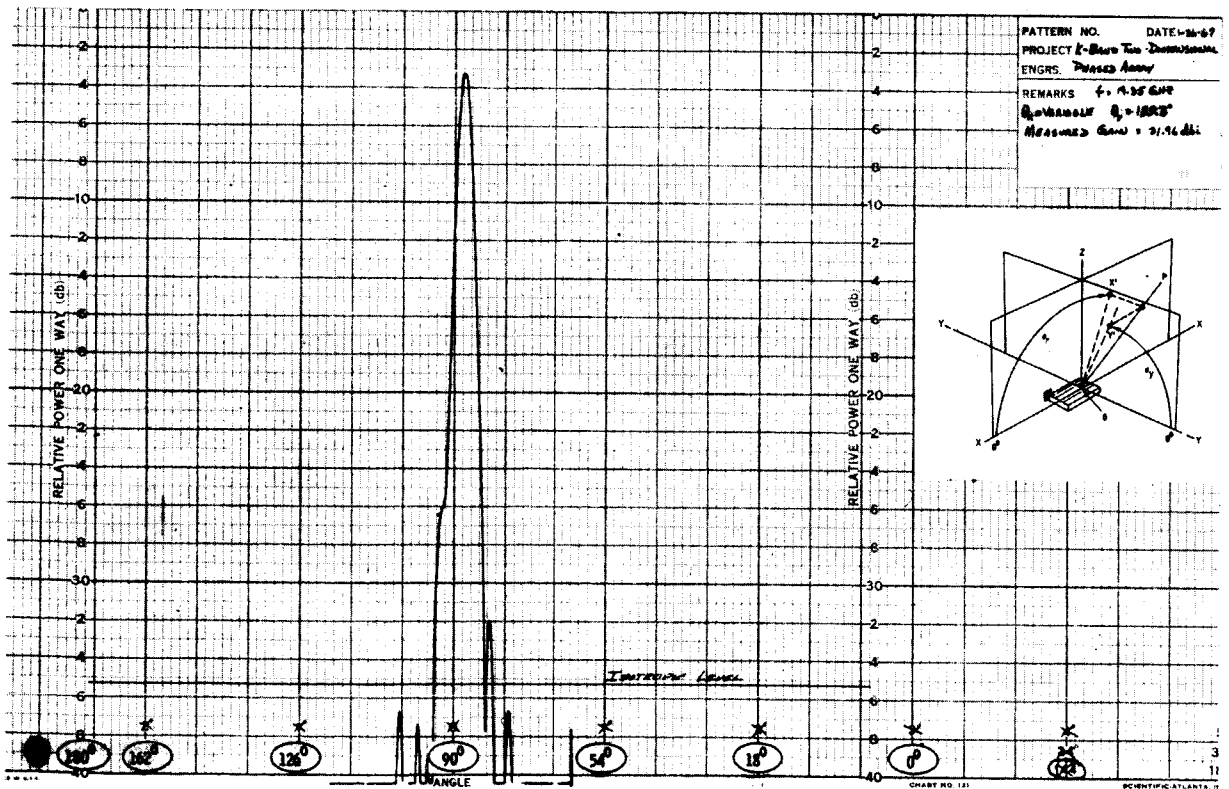


Figure I-4. a. Antenna Pattern, $\theta_x = 86.8^\circ$, θ_y Variable



b. Antenna Pattern, θ_x Variable, $\theta_y = 139.3^\circ$

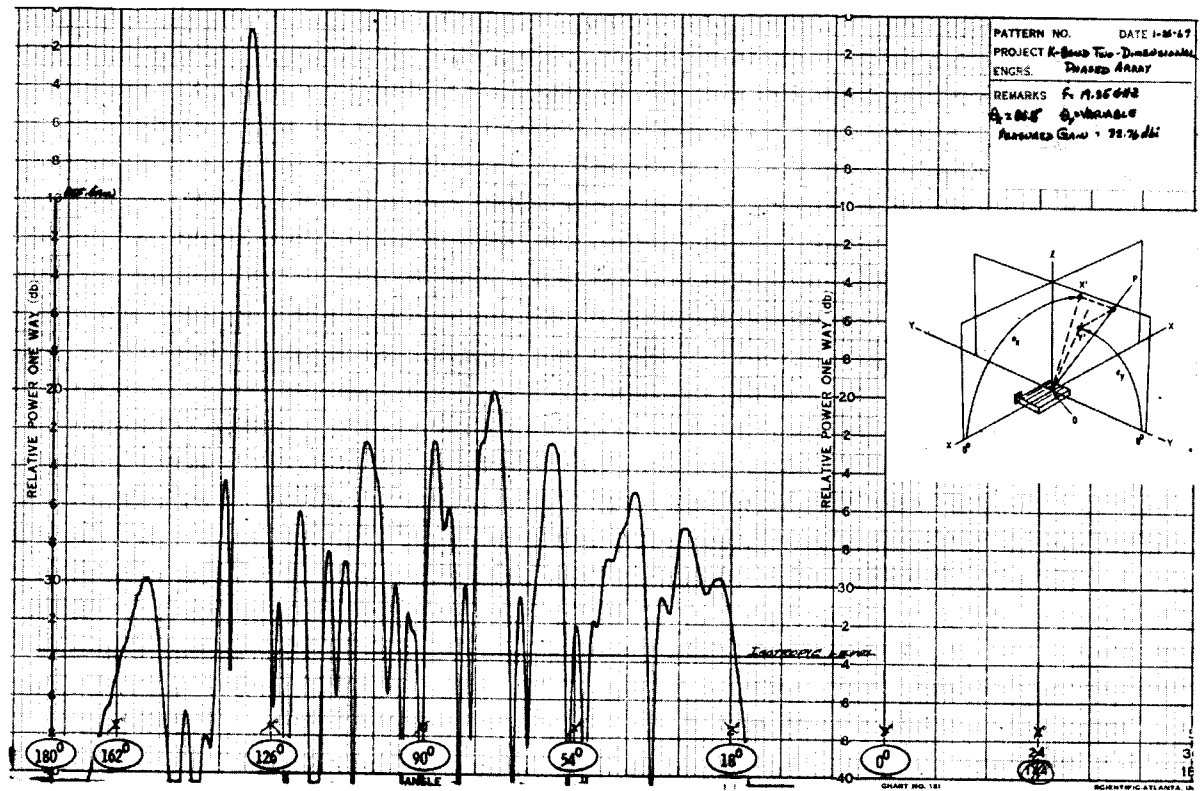
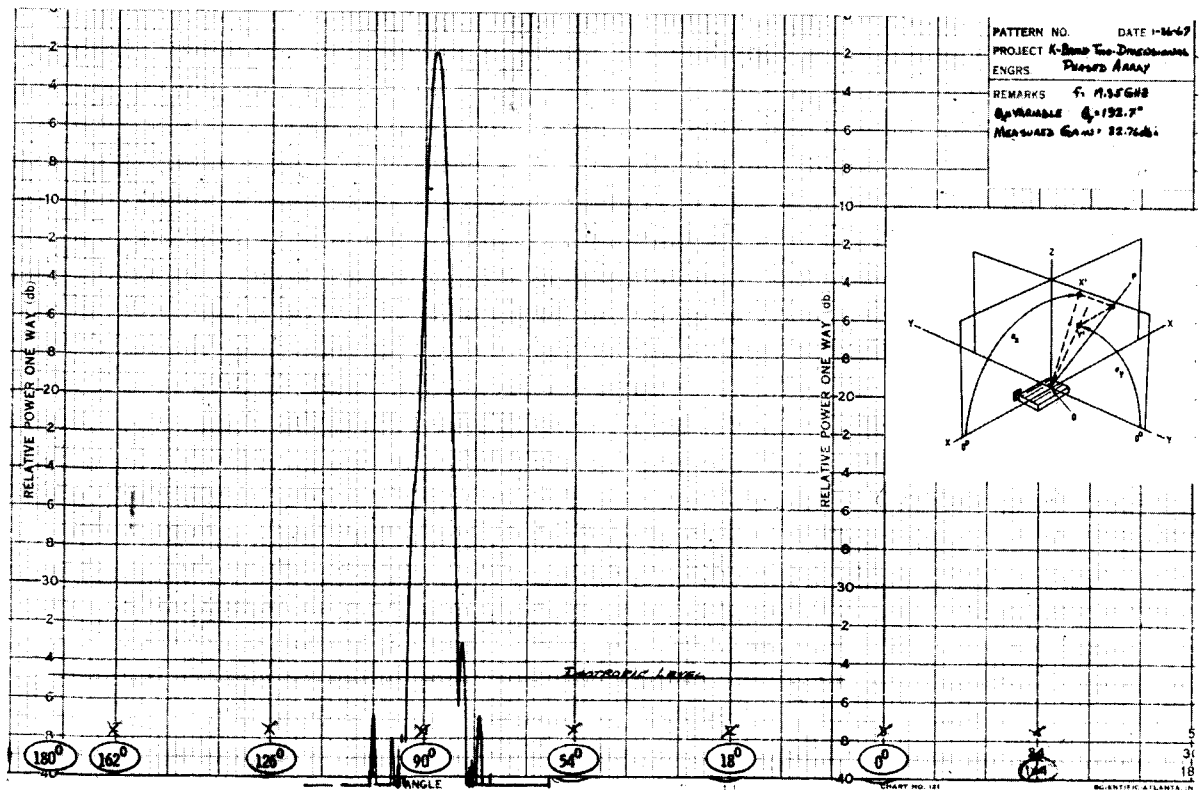


Figure I-5. a. Antenna Pattern, $\theta_x = 86.8^\circ$, θ_y Variable



b. Antenna Pattern, θ_x Variable, $\theta_y = 132.7^\circ$

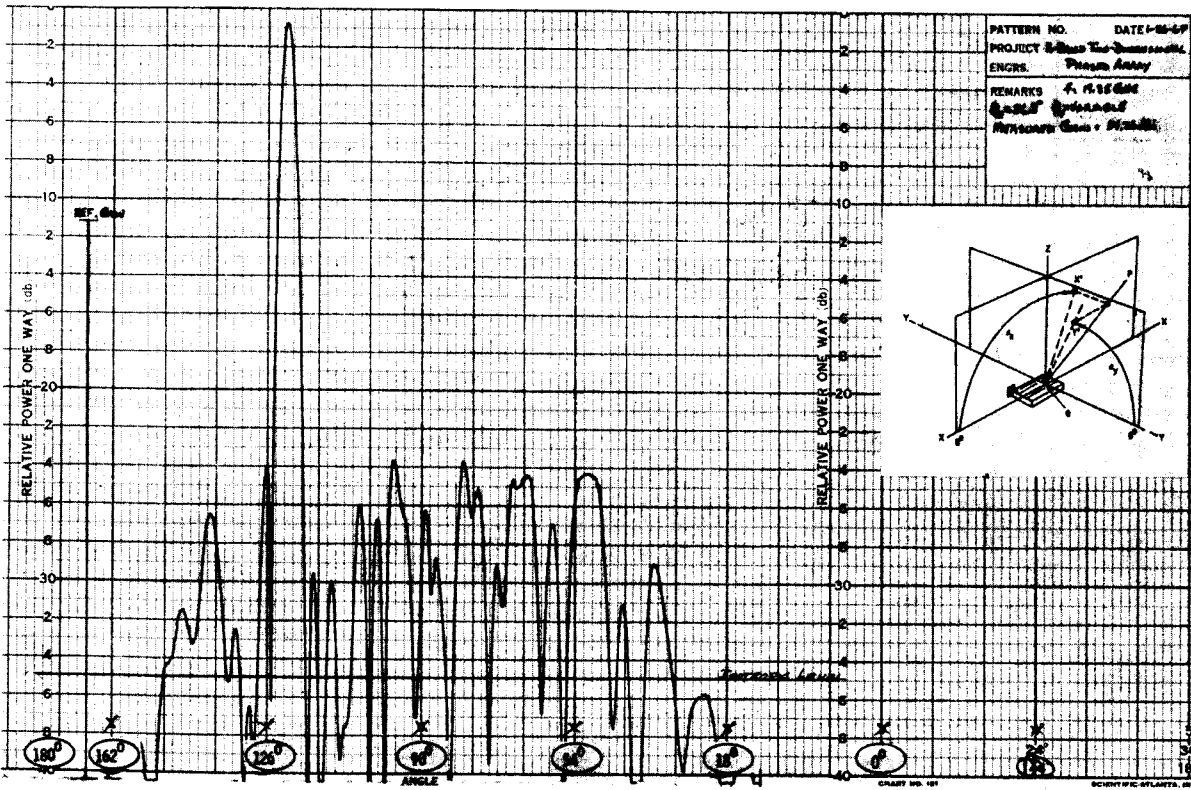


Figure I-6. Antenna Pattern, $\theta_x = 86.8^\circ$, θ_y Variable

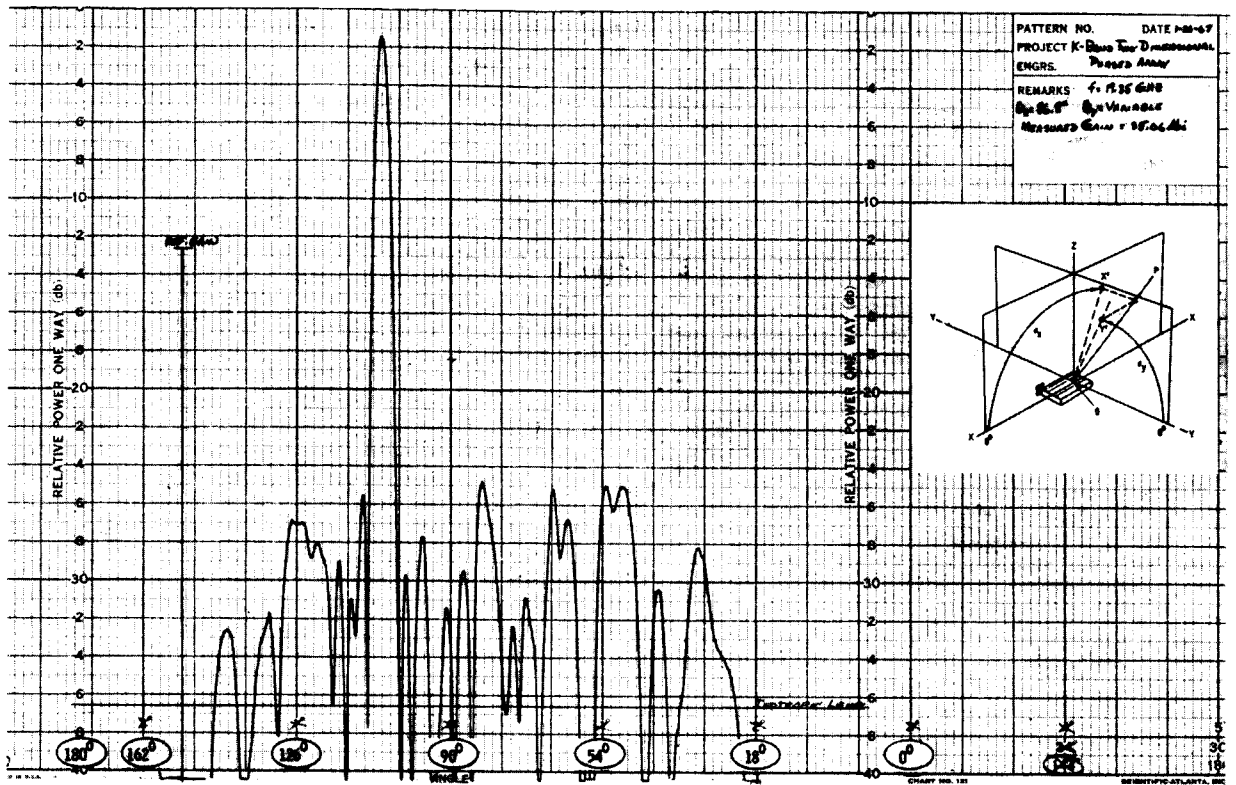
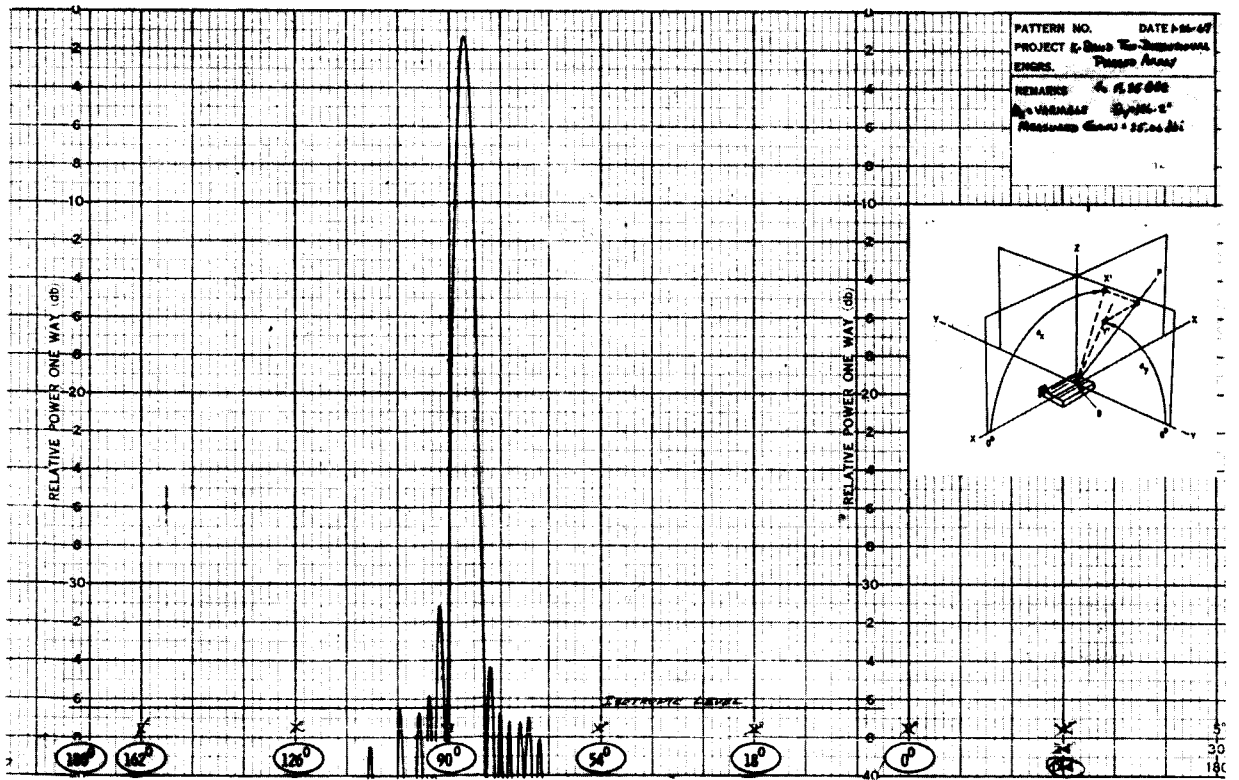


Figure I-7. a. Antenna Pattern, $\theta_x = 86.8^\circ$, θ_y Variable



b. Antenna Pattern, θ_x Variable, $\theta_y = 106.2^\circ$

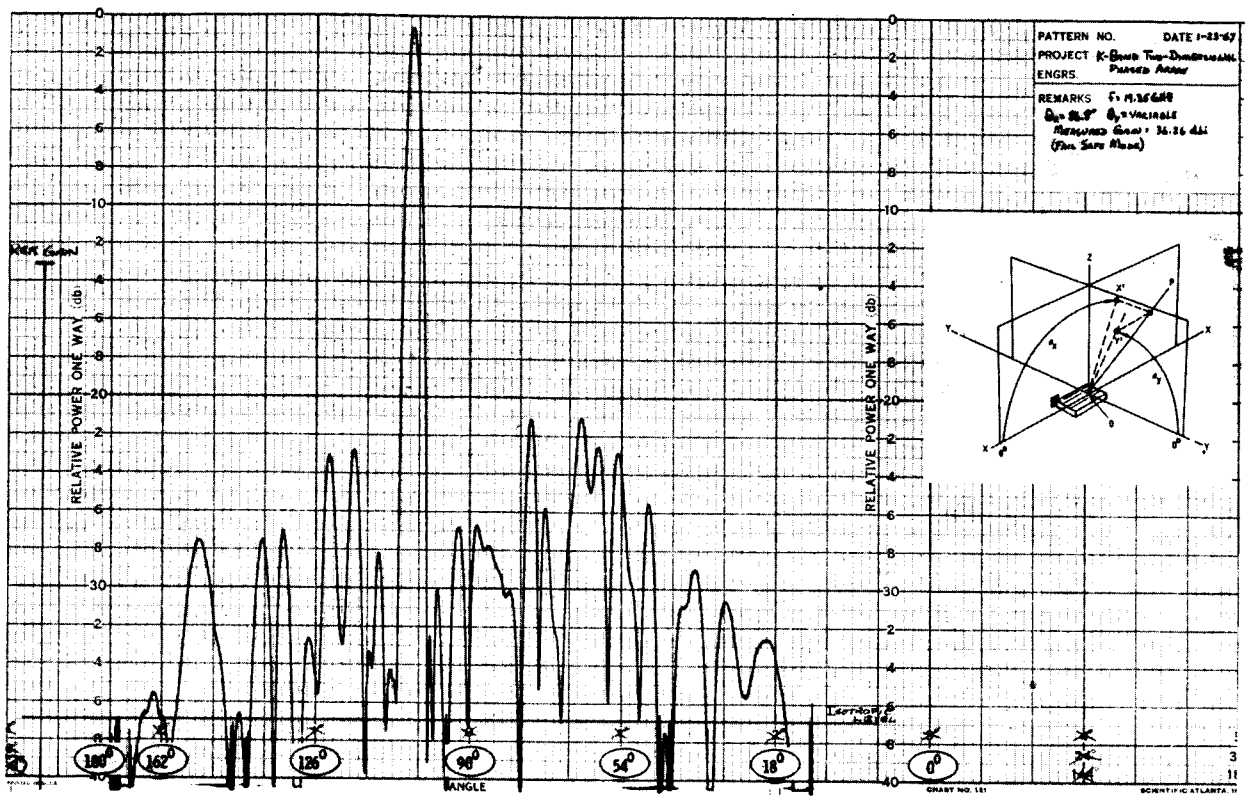
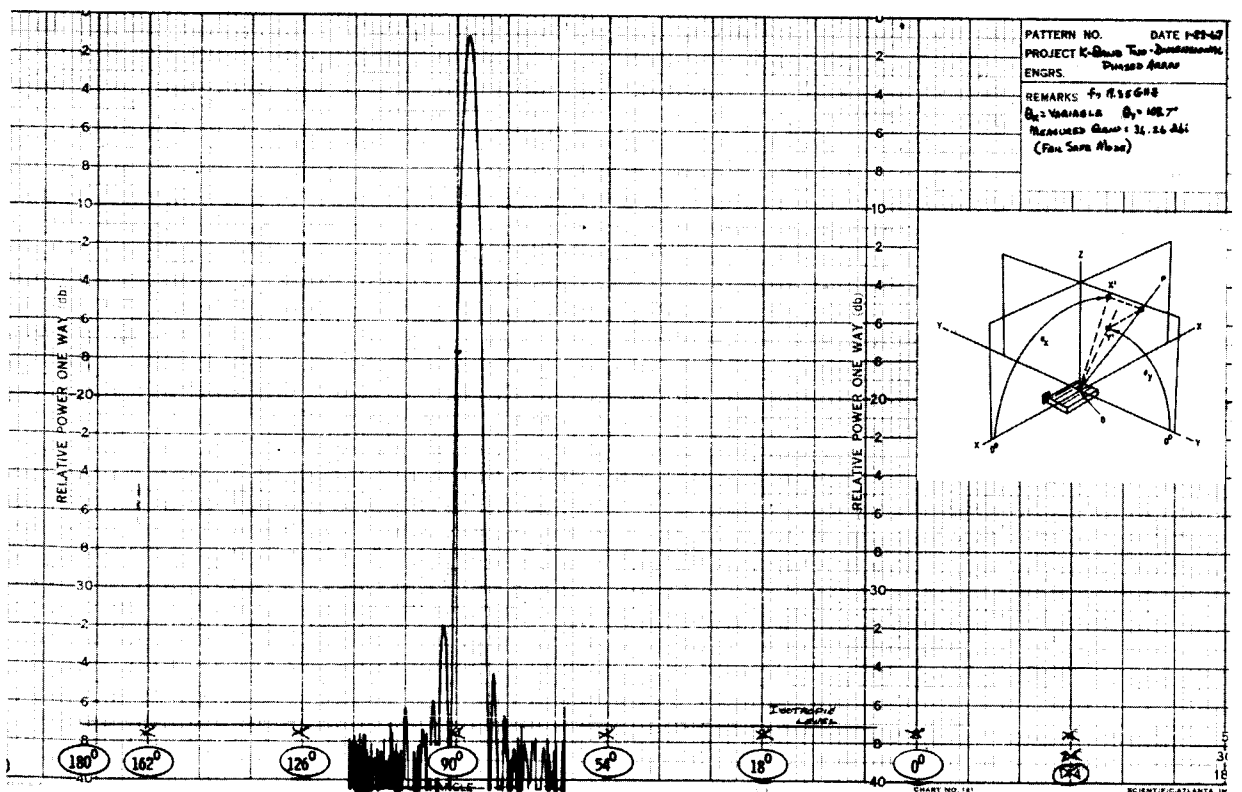


Figure I-8. a. Antenna Pattern, $\theta_x = 86.8^\circ$, θ_y Variable
 (Fail Safe Mode)



b. Antenna Pattern, θ_x Variable, $\theta_y = 103.7^\circ$
 (Fail Safe Mode)

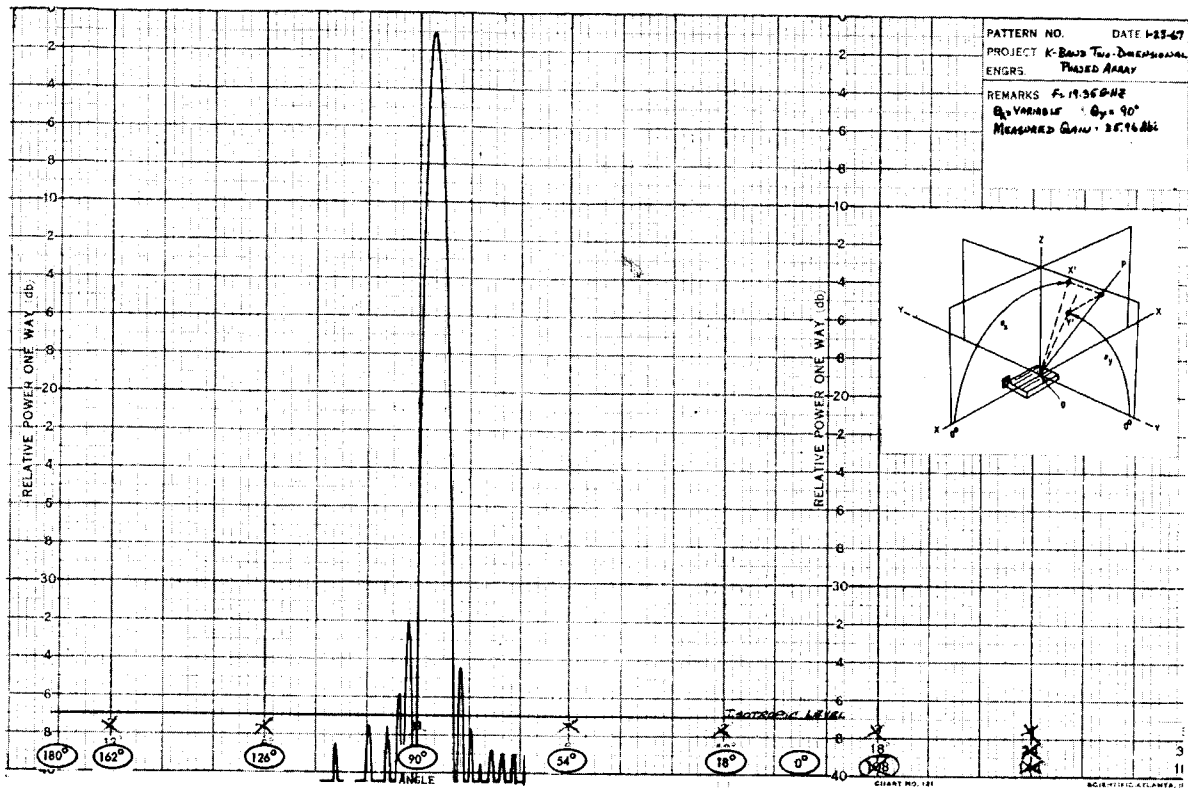
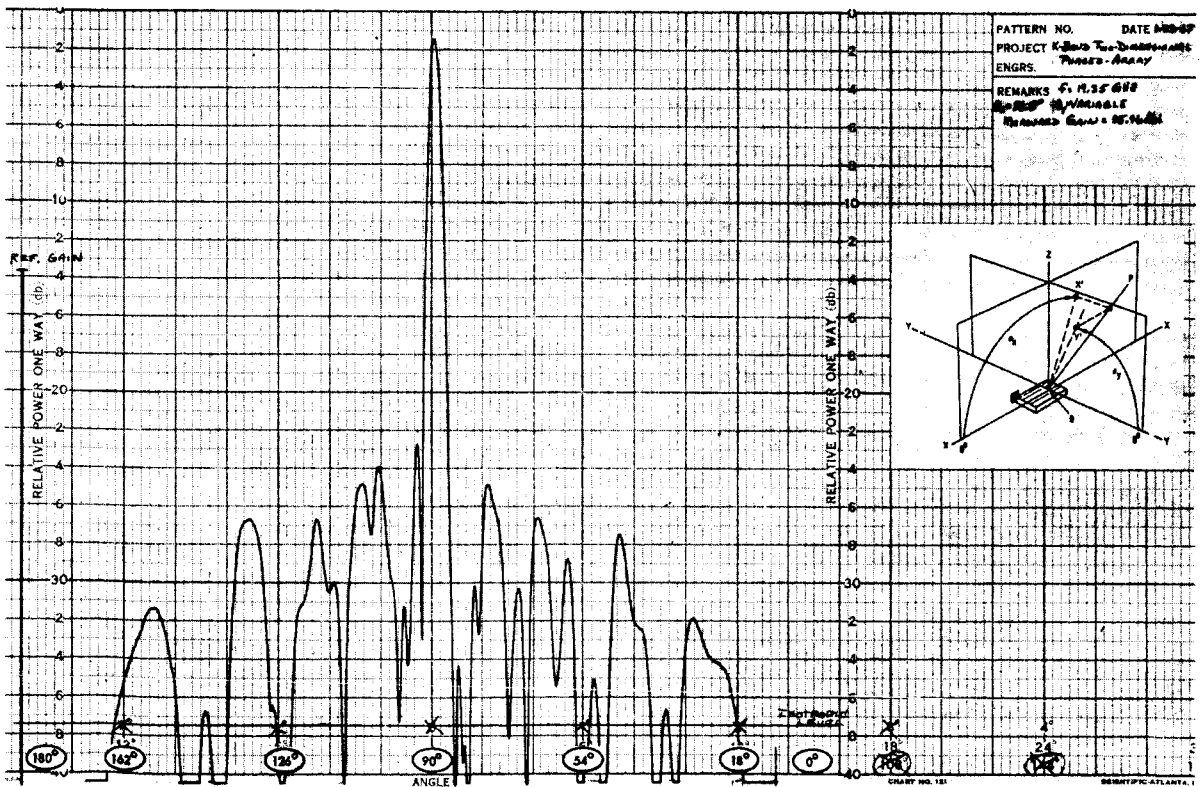


Figure I-9. a. Antenna Pattern, $\theta_x = 86.8^\circ$, θ_y Variable



b. Antenna Pattern, θ_x Variable, $\theta_y = 90^\circ$

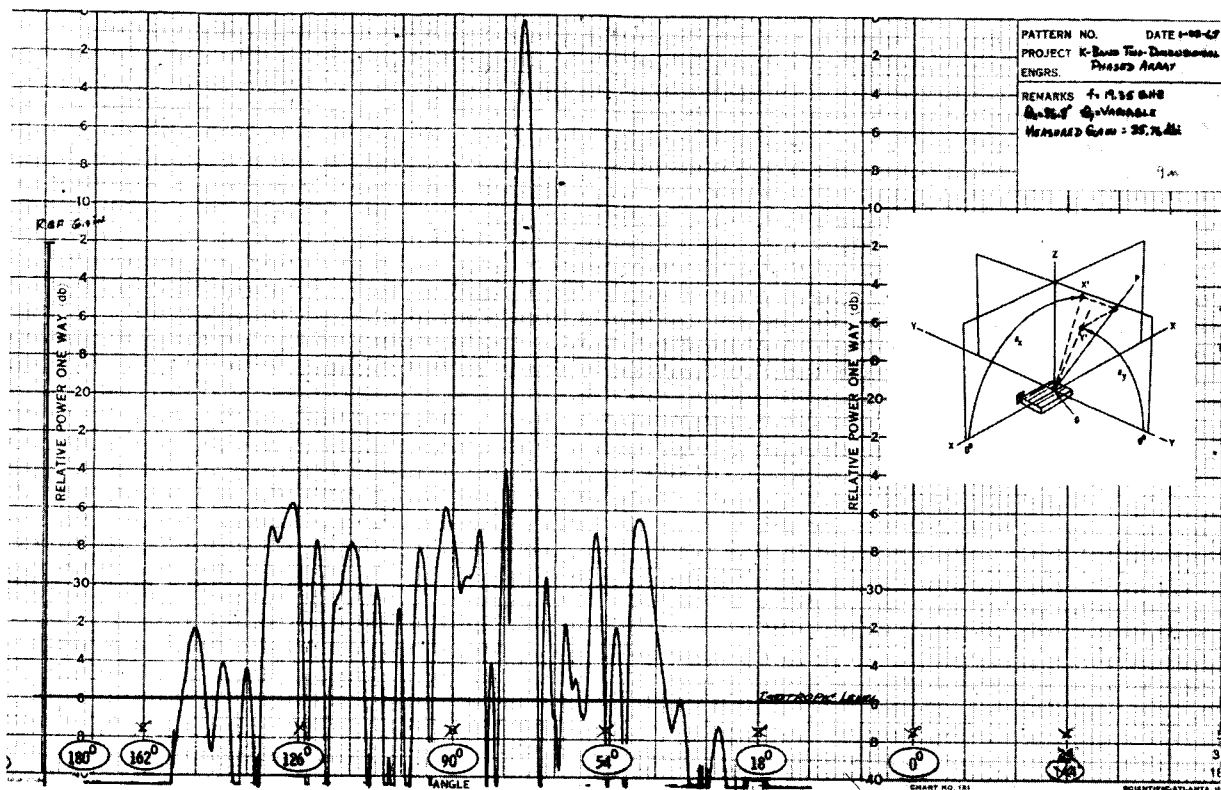
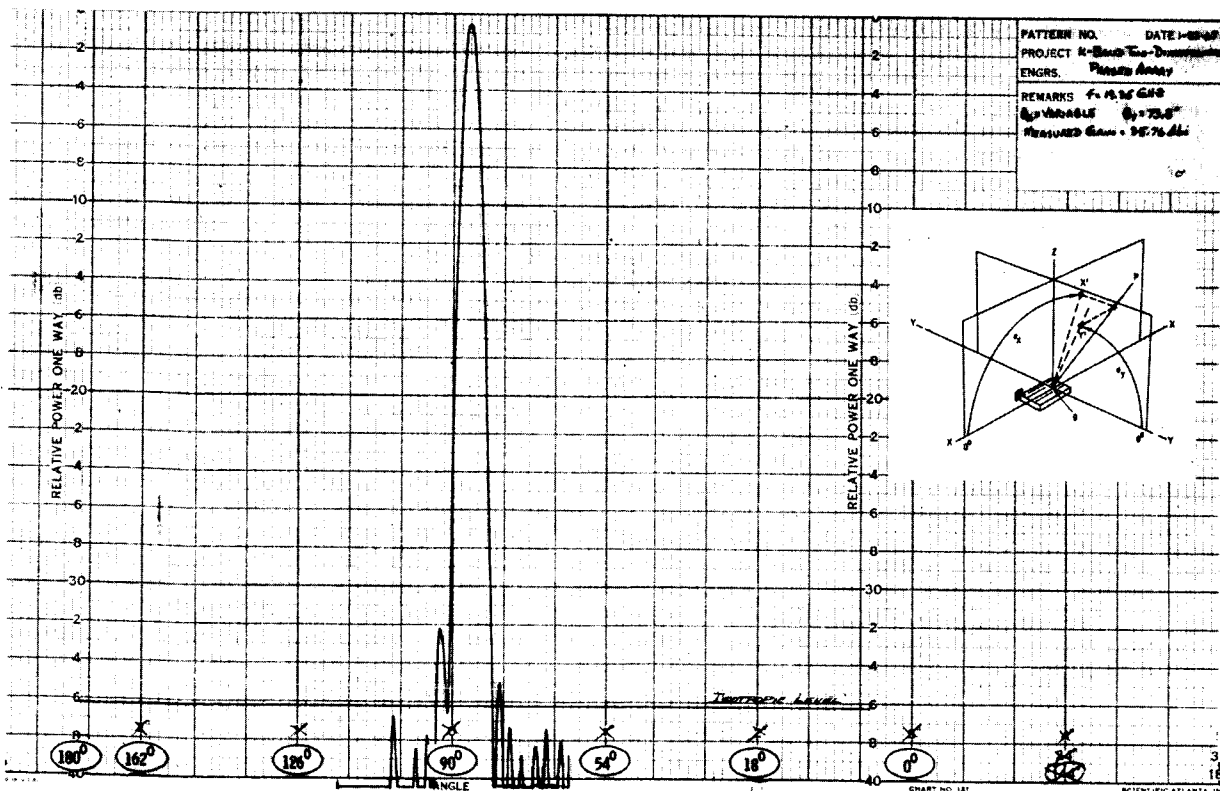


Figure I-10. a. Antenna Pattern, $\theta_x = 86.8^\circ$, θ_y Variable



b. Antenna Pattern, θ_x Variable, $\theta_y = 73.8^\circ$

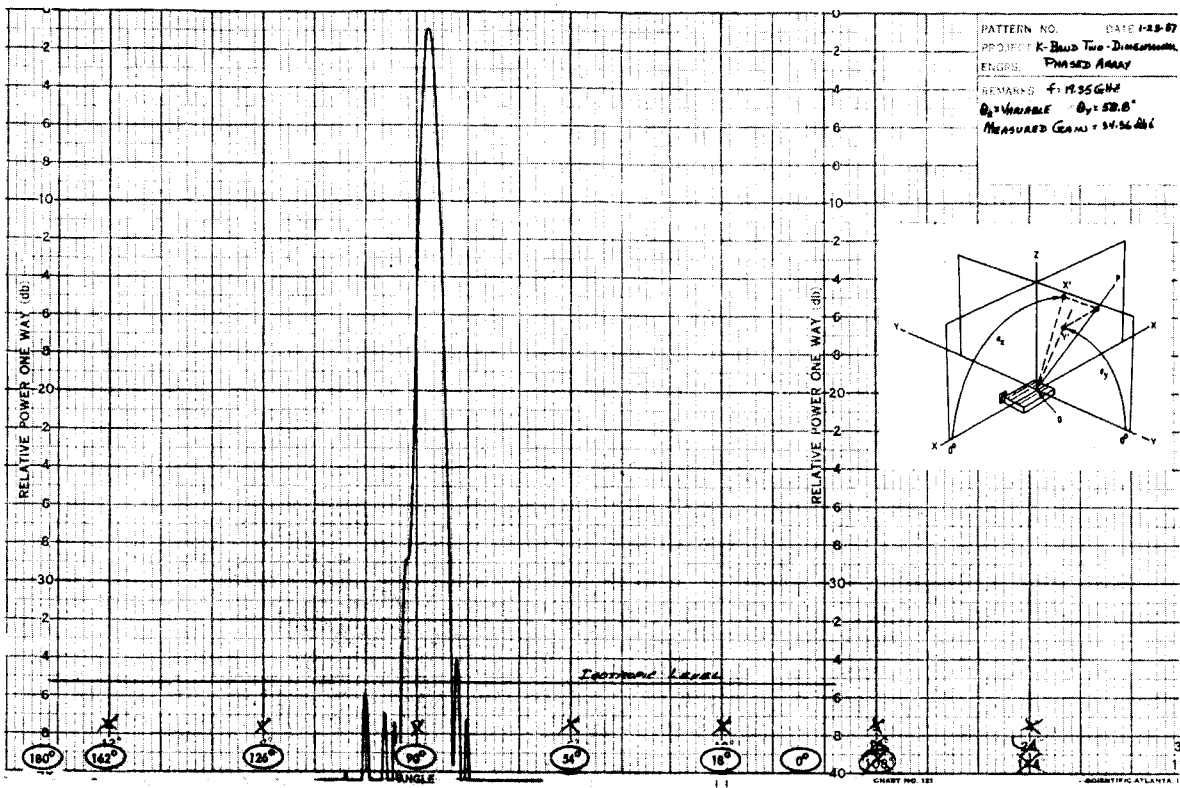
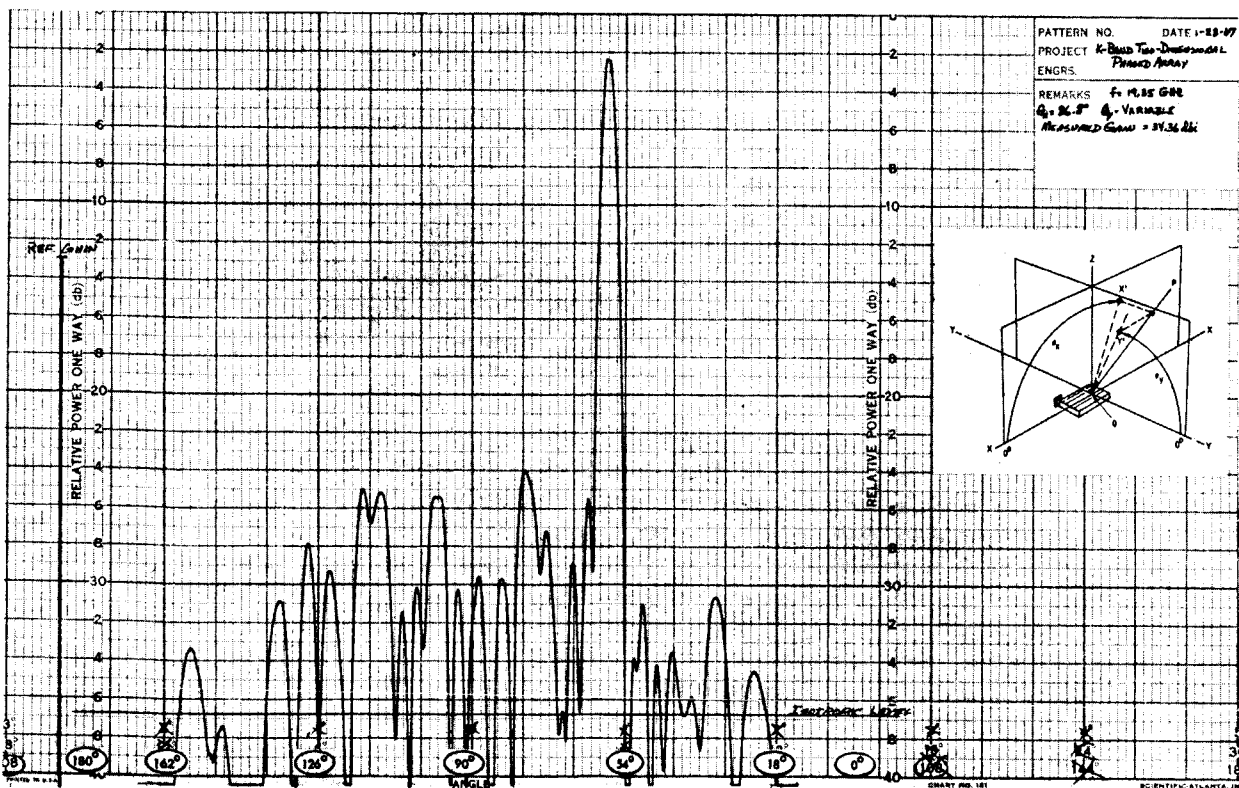


Figure I-11 = Antenna Pattern, $\theta_x = 86.8^\circ$, θ_y Variable



b. Antenna Pattern, θ_x Variable, $\theta_y = 58.8^\circ$

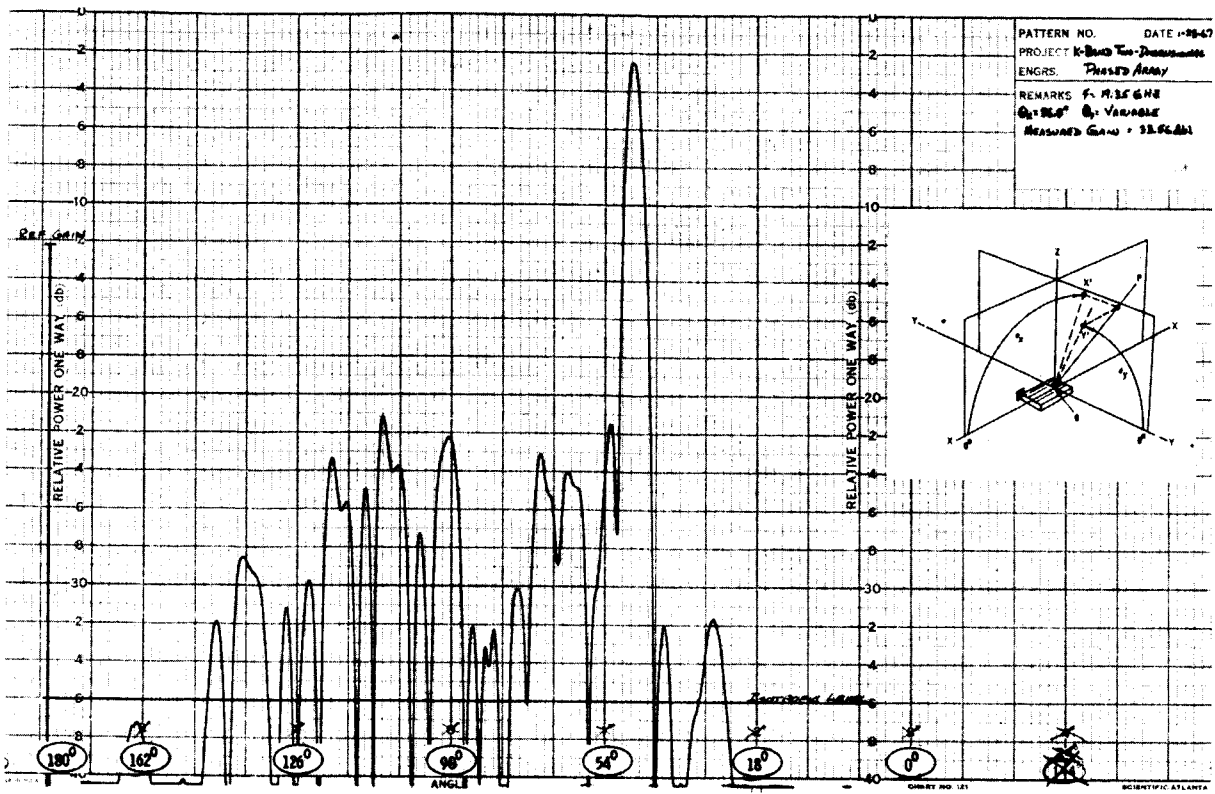
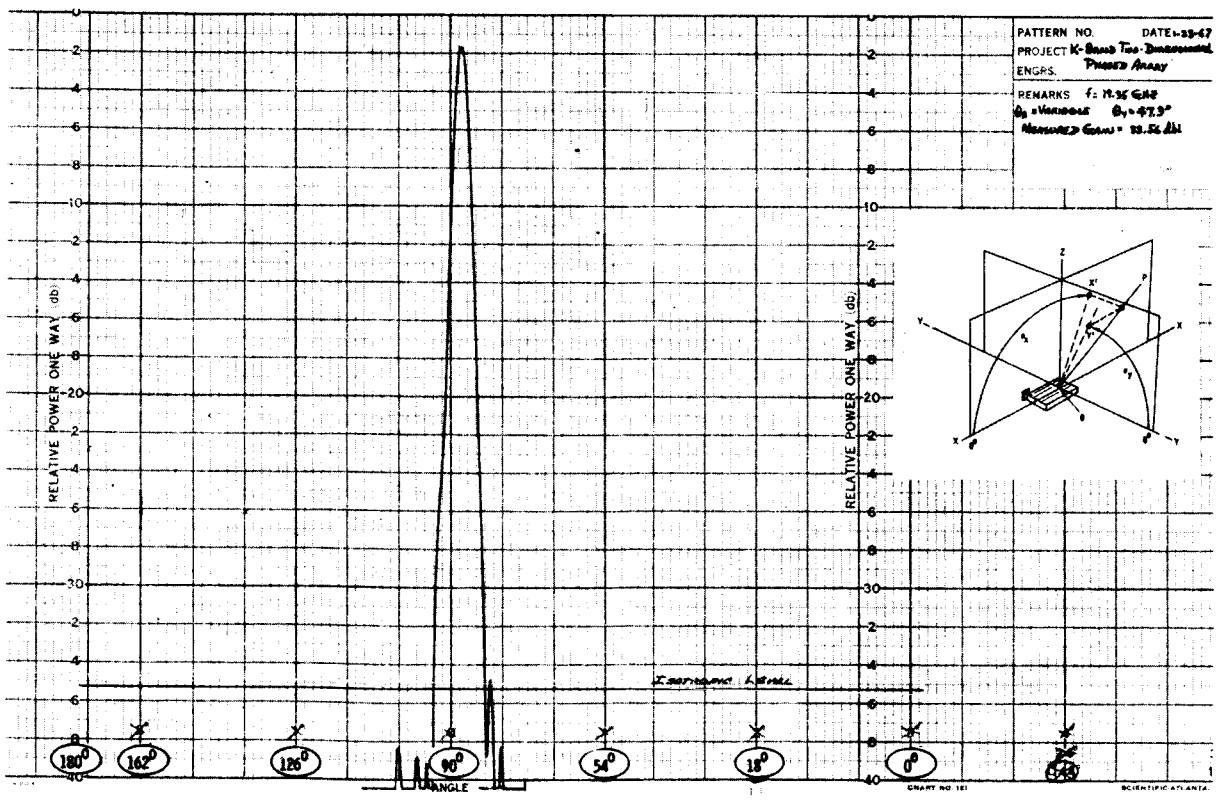


Figure I-12. a. Antenna Pattern, $\theta_x = 86.8^\circ$, θ_y Variable



b. Antenna Pattern, θ_x Variable, $\theta_y = 47.3^\circ$

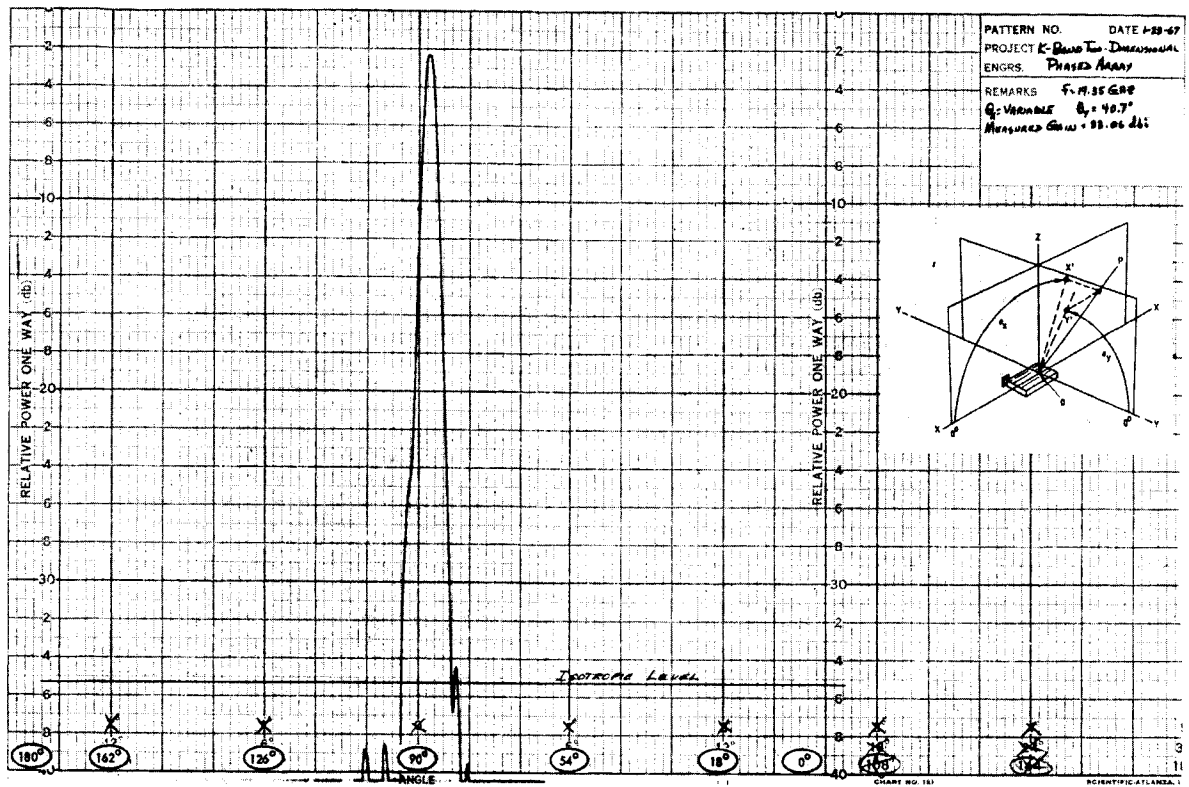
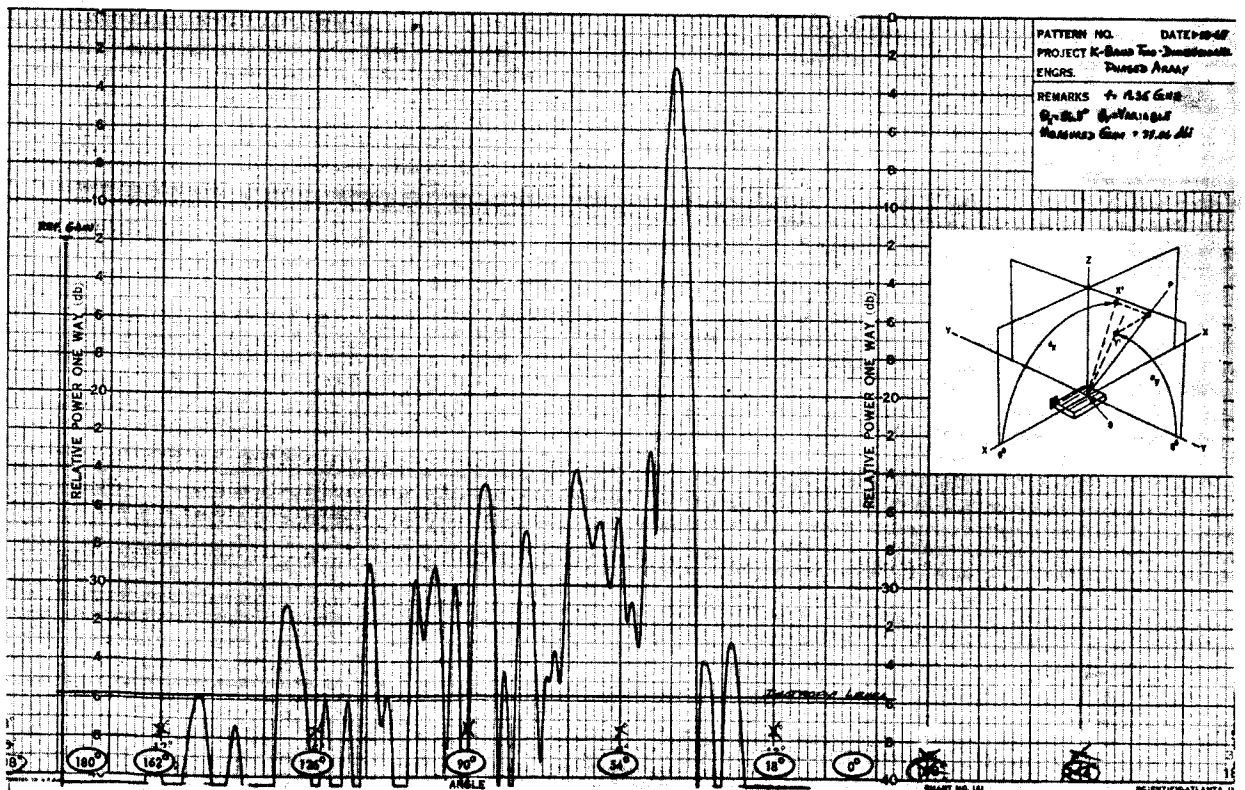


Figure I-13. a. Antenna Pattern, $\theta_x = 86.8^\circ$, θ_y Variable



b. Antenna Pattern, θ_x Variable, $\theta_y = 40.7^\circ$

Appendix II

FERRITE CIRCULATOR-SWITCHES

This appendix describes the r-f switches to be used on the 19 Gc/s radiometer proposed for possible use on the Nimbus satellite. It is also intended that one may better understand circulators in general, and will be able to see the tradeoffs one must make when specifying a circulator or a circulator-switch for a systems application.

INTRODUCTION

A Y-junction circulator is a non-reciprocal device providing energy transmission from one port to an adjacent port while decoupling the signal from all other ports. The circulator symbol in Figure 1 indicates that r-f energy incident on P_1 emerges from P_2 , energy entering P_2 emerges from P_3 , and energy entering P_3 emerges from P_1 . Circulator action is obtained by properly biasing a ferrite element placed in a transmission line, the ferrite being located in the center of three symmetrical junctions spaced 120° apart. In order for a circulator to operate as a switch, one need only have the capability of reversing the sense of the biasing magnetic field.

19 Gc RADIOMETER SWITCH

The switch to be used for Nimbus is a three position-single pole waveguide switch which consists of two double-throw single-pole ferrite Y-junction circulator switches, as shown in Figure 2. Switch No. 1 is a modulated or continuously operated switch which requires approximately 100 ma of current through a coil positioned so as to provide the necessary biasing field. In order to conserve drive power, switch No. 2 is not continuously switched but is biased with a permanent magnet. Periodically, a pulse of current is passed through a coil in order to override the field of the permanent magnet and thus cause switching action. The switch is referred to as a half-latch type switch. The specifications for this switch are given in SP AAD 1001.

CIRCULATOR SPECIFICATIONS

The major electrical parameters to be specified when calling out a particular circulator are isolation, VSWR, and insertion loss. For switched circulators, included are parameters such as coil current, switch rise time, etc., which are a function of the RF frequency as well as the switch rate and available switching power and are not often difficult to specify. Practical and theoretical circulator isolations are very often confused, however. Systems engineers generally accept specified isolations without thought to loading, while component engineers generally do not specify the conditions under which specified isolations are measured. The following is intended to clarify this matter. Referring to Figure 1, the direction of energy travel is shown by the arrow.

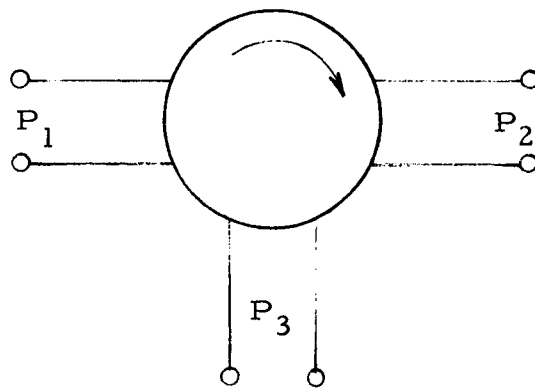


Figure 1. Y-Junction Circulator Symbol

By definition energy into P_1 prefers to go to P_2 , energy into P_2 prefers to go to P_3 and so on. Isolation is defined as follows: when energy goes in P_1 a major portion goes to P_2 , but since no three port device is perfect, some portion of the incoming energy does arrive at P_3 even under conditions

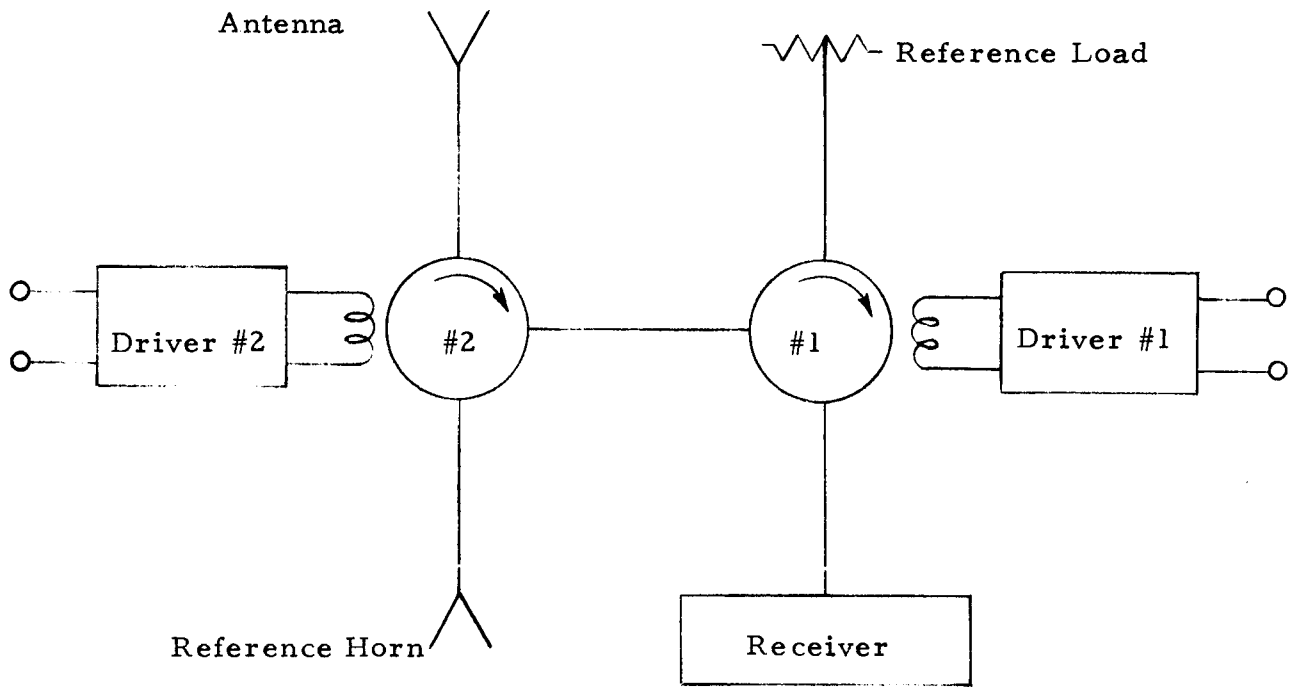


Figure 2. Two Double-Throw Single-Pole Ferrite Y-Junction Circulator Switches

of perfect impedance match at each port. The ratio of the input energy to the amount appearing at P_3 is then defined as the isolation. These statements assume perfectly matched ports (VSWR = 1). The maximum value of isolation under this perfectly matched condition is called the intrinsic isolation. The isolation one normally encounters or measures is under conditions when the loads are not matched and is called the observed isolation. How the observed isolation differs from the intrinsic isolation is explained in detail below.

Energy enters P_1 and travels to P_2 . When the VSWR of P_2 is greater than 1.0 some energy is reflected and is circulated on to P_3 . Thus, the energy level at P_3 is above that of the intrinsic value. How much higher this energy level is may be easily calculated. The intrinsic isolation in db may be converted to an equivalent reflection coefficient term Γ_1 by the simple relationship

$$\text{Isolation (db)} = 20 \log |\Gamma_1| \quad (1)$$

Likewise, the VSWR of P_2 may be converted to a reflection coefficient term Γ_2 by the well known relation

$$|\Gamma_2| = \frac{1 - \text{VSWR}}{1 + \text{VSWR}} \quad (2)$$

Each of these terms adds to the energy level at P_3 to yield a resultant term, Γ_3

$$\Gamma_3 = \Gamma_1 + \Gamma_2 \quad (3)$$

where

$$\Gamma_n = |\Gamma_n| e^{j\theta_n}$$

θ_n = phase angle.

The cases of interest are when

$$|\Gamma_3| = |\Gamma_1| \pm |\Gamma_2| \quad (4)$$

or when the two energy components add in phase or out of phase. When they are added in phase, the observation isolation is a minimum value and for this reason is the condition of major importance here.

At 19 Gc the maximum obtainable isolation (intrinsic) with perfectly matched ports has been found to be on the order of 27 - 30 db (corresponding to a 1.1 - 1.07 VSWR ferrite disc). When the VSWR of the ports increases, this value will decrease as shown in the table below:

<u>Observed Isolation (db)</u>	<u>VSWR</u>
27 (Intrinsic)	1.00
25	1.02
22.5	1.06
21	1.10
18	1.15
17	1.20
16	1.25
15	1.30
12	1.50

In order to insure a minimum isolation value of 25 db over a 200 mc band, a maximum allowable VSWR of 1.02 was selected. Likewise to insure a minimum value of 21 db isolation over a 600 mc band, a maximum VSWR of 1.10 was allowed. The other specifications such as insertion loss were specified to be values thought to be within the present state-of-the-art.

Appendix III

POSITION OF HORIZONTALLY-POLARIZED GRATING LOBES

This appendix discusses the spacing and number of linear array elements needed to satisfy the Job 939 antenna array contractual requirements. To ensure the suppression of all horizontally-polarized grating lobes when the main beam is scanned ± 30 degrees from broadside and still have maximum spacing between elements for coil windings, the spacing should be 0.380 inches (or 0.62λ). It is the purpose of this appendix to show the position of these grating lobes as the main beam is scanned to ± 60 degrees.

The position of the main beam and extraneous grating lobes can be determined from the expression

$$\sin \theta = \frac{\lambda}{\lambda_g} - \frac{n\lambda}{2d} + \frac{\Delta\phi \lambda}{2\pi d} \quad (1)$$

where θ is the angular position of the beam relative to broadside, λ and λ_g are the free-space and waveguide wavelength respectively, n is an odd integer (i. e., $\pm 1, \pm 3$, etc.), and $\Delta\phi$ is the phase delay introduced by the ferrite phase shifters. The significance of n is that there may be more than one value of n yielding real values of θ . These additional solutions correspond to grating lobes. In the present situation, $N = +1$ corresponds to the main beam, $n = +3$ to the grating lobe. These are the only values of n that will yield real values of θ . This is based on the assumption that the main beam is not scanned beyond ± 60 degrees.

For RG-53/U waveguide (0.170 x 0.420 inches) spaced at 0.380 inches, Equation (1) reduces to

$$\sin \theta = 0.688 - 0.804n + \frac{\Delta\phi}{224} \quad (2)$$

For any position of the main beam, there is related to it some phase delay $\Delta\phi$ and at times some grating lobe. Two independent simultaneous equations can therefore be generated from Equation (2), one describing the position of the main beam, the other the position of the grating lobe (if it exists).

$$\sin \theta_M = 0.688 - 0.804 + \frac{\Delta \phi}{224}$$

or

$$\sin \theta_M = -0.116 + \frac{\Delta \phi}{224} \quad (3a)$$

and

$$\sin \theta_{GL} = 0.688 - (0.804 \times 3) + \frac{\Delta \phi}{224}$$

or

$$\sin \theta_{GL} = -1.724 + \frac{\Delta \phi}{224} \quad (3b)$$

where the subscripts M and GL refer to the main lobe and the grating lobe, respectively.

From Equations (3a) and (3b), it is possible to determine the position of the grating lobe (if it exists) when the main lobe position is given, or vice versa.

Some typical results of interest are given in the table below:

Main Lobe Position	0°	± 30°	± 37.4°	± 47.7°	± 50°	± 57.1	± 60°
Grating Lobe Position	--	--	± 90°	± 60°	± 57.4°	± 50°	± 48°

Appendix IV

EFFECT OF WAVEGUIDE TOLERANCES ON PHASE FRONT OF PORTED-ARRAY ELEMENTS

In order to suppress the orthogonally-polarized energy of the linear edge-slotted array elements, auxiliary sections of waveguide (or ports) can be placed over each slot of the linear array element. Standard size RG-53/U waveguide, however, cannot be used for these ports because of the required spacing between adjacent linear elements in the planar array. A waveguide with a reduced wide dimension must be used. This requires, therefore, that the operating frequency be much closer to the cutoff frequency of this reduced-size waveguide. As a result, small changes in the internal dimensions of this waveguide may radically change the phase velocity in the guide. This, in turn, reflects a change in the phase of the wave radiating from the port aperture. It is the purpose of this memorandum to investigate this variation in phase as a function of the tolerance on the waveguide internal dimensions.

The spacing between the adjacent linear elements of the planar array should be 0.380 inch in order to suppress all horizontally-polarized grating lobes when the beam is scanned to ± 30 degrees from broadside. Assume now that the spacing between adjacent ports, dimension A in Figure 1, is 0.010 inch and that the wall thickness T of the ports is 0.020 inch. The maximum wide dimension of the port waveguide is therefore limited to 0.330 inch. (This same dimension results if the spacing is set at 0.030 inch and the wall thickness is 0.010 inch.)

Before the phase variation can be computed, the waveguide wavelength must first be determined from the expression:

$$\lambda_g = \frac{\lambda_o}{\sqrt{\epsilon - \left(\frac{\lambda_o}{\lambda_{c_o}}\right)^2}} \quad (1)$$

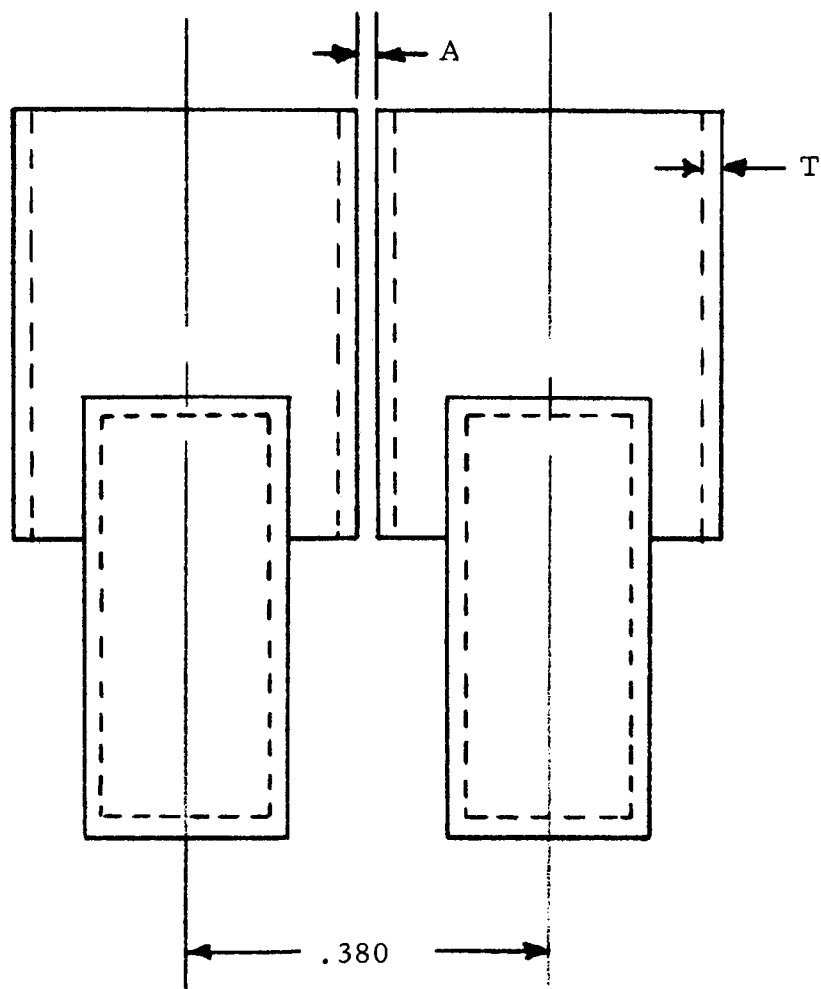


Figure 1. End View of Two Ported Linear Array Elements

where λ_g , λ_o and λ_{c_o} are the waveguide, free-space and cutoff wavelengths respectively, and ϵ is the relative dielectric constant of the medium filling the waveguide. Since the waveguide is air-filled and since $\lambda_{c_o} = 2a$ for the TE_{10} mode, where a is the wide dimension of the guide, Equation (1) reduces to

$$\lambda_g = \frac{\lambda_o}{\sqrt{1 - \left(\frac{\lambda_o}{2a}\right)^2}} \quad (2)$$

It is obvious from Equation (2) that the greatest changes in λ_g , and hence in phase, will be caused by negative tolerances, i. e., the size of the waveguide is smaller than the nominal. Also, the rate of change of λ_g becomes greater as the cutoff wavelength approaches the operating or free-space wavelength. Only the negative tolerances will therefore be considered. The waveguide wavelength has been computed and compiled in Table 1 for a nominal wide dimension of 0.330 inch and for tolerances of -0.001, -0.002 and -0.003 inch. The cutoff frequency, incidentally, for the 0.330 inch case is approximately 17.9 Gcps.

Waveguide Width (inch)	Tolerance	λ_g (inch)	$\Delta\phi$ (degrees)	
			Port Length = $\lambda/2$	Port Length = $\lambda_g/2$
.330	.000	1.5964	0	0
.329	-.001	1.6256	-1.26°	-3.30°
.328	-.002	1.6568	-2.26°	-6.81°
.327	-.003	1.6901	-4.04°	-10.57°

Table 1

WAVEGUIDE WAVELENGTH AND PHASE ERROR
VS WAVEGUIDE TOLERANCE

The resulting phase errors can now be computed as a function of waveguide tolerance for various port lengths. The two cases considered here are port lengths equal to $\lambda / 2$ and $\lambda_g / 2$ where λ and λ_g are based on a frequency of 19.35 Gcps and a waveguide width of 0.330 inch. It should be realized that the phase errors shown are the result of variations in the width of the waveguide only. Variations in the length of the ports introduce additional errors; however, these are less than two degrees for a $\pm .003$ inch tolerance.

All non-standard waveguide procured to date has been extruded as precision waveguide to a ± 0.001 inch tolerance on the inside dimensions. At present it appears that the length of the ports can be made a half free-space wavelength. (This will be verified by laboratory measurements.) Therefore from Table 1 it appears that the tolerance effects on the phase distribution across the array aperture will present no major problem. The principle problem envisioned is that of getting a ground plane in the small spacing between adjacent ports. This will be investigated further.

Appendix V

REVIEW OF BASIC RF PREAMPLIFIER GAIN REQUIREMENTS FOR THE NIMBUS RADIOMETER RECEIVER

The purpose of this appendix is to review the basic r-f preamplifier gain requirements for the Nimbus radiometer receiver. Included is a short discussion on amplifier gain instability due to source impedance variations along with a physical description of the tunnel diode preamplifier.

Gain Requirement

In order that an antenna signal be distinguishable from the noise of the post detection amplifier, sufficient gain must be provided by the r-f preamplifier. The noise voltage at the input of the post detection amplifier is

$$e_n = (4K T_o B_L R F_L)^{1/2} \quad (1)$$

where

K = Boltzman's constant, 1.38×10^{-23} joules/watt

T_o = 290° K

B_L , F_L = post detection amplifier noise bandwidth and noise figure.

R = post detection amplifier source resistance, which is equal to the square-law detector output impedance.

In the case of an integrate and dump type of integrator following the post detection amplifier,

$$B_L = \frac{2}{\tau} \quad (2)$$

where τ = integration time.

Thus,

$$e_n = (8K T_o R F_L \tau^{-1})^{1/2} \quad (3)$$

The detector output voltage corresponding to the minimum detectable change of antenna temperature, ΔT_{\min} , is equal to the minimum signal output voltage, $(e_s)_{\min}$. To ensure negligible degradation of the radiometric signal by the post detection noise, $(e_s)_{\min}$ is chosen to be ten times e_n .

The detector's minimum input power, P_{\min} is related to $(e_s)_{\min}$ by

$$P_{\min} = \frac{(e_s)_{\min}}{\gamma} = \frac{10(e_n)}{\gamma} \quad (4)$$

where γ = the square law detector's voltage responsivity. P_{\min} is also related to the minimum detectable antenna temperature, ΔT_{\min} .

$$P_{\min} = \Delta T_{\min} K B_H G_H \quad (5)$$

where B_H , G_H = preamplifier noise bandwidth and gain.

The equation for ΔT_{\min} is (see SGC P-6308)

$$\Delta T_{\min} = 2 (T_e + T_A) \left(\frac{1}{B_H \tau} \right)^{1/2} \quad (6)$$

where

T_e = excess noise temperature of the receiver

T_A = antenna temperature, 290°K for mapping applications

Combining equations 4, 5, and 6 and solving for G_H (and noting that $F_R T_o = T_e + T_A$) yields

$$G_H = \frac{10}{F_R \gamma} \left(\frac{2R F_L}{B_H K T_o} \right)^{1/2} \quad (7)$$

For the receiver under discussion the following values apply

$$F_L = 3 \text{ db} = 2$$

$$R = 100 \text{ ohms}$$

$$B_H = 2 \times 10^8 \text{ cps}$$

$$\gamma = 800 \text{ volts/watt}$$

$$F_R = 7.7 \text{ db} = 5.8$$

$$T_o = 290^\circ\text{K}$$

Substituting these values into equation 7 yields the required amount of predetection gain. $G_H = 47 \text{ db}$ for $(e_s)_{\min} = 10 e_n$.

The filter which will be inserted between the first and second stages of amplification will result in a 3 db insertion loss so the required tunnel diode amplifier gain is $(47 + 3) = 50 \text{ db}$. Since a signal-to-noise ratio of 10 was assumed (20 db) a value somewhat less than 50 db will yield satisfactory results. For this reason a gain of 48 db was specified.

Gain Instability

Gain of a tunnel diode amplifier is commonly expressed by

$$G = \left| \frac{1 - \frac{Z_d}{Z_o}}{1 + \frac{Z_d}{Z_o}} \right|^2 \quad (8)$$

where

Z_d = the tunnel diode amplifier circuit impedance

Z_o = the impedance presented to the amplifier circuit by the circulator

At resonance this becomes simply,

$$G_o = \left[\frac{1 - \frac{R_d}{R_o}}{1 + \frac{R_d}{R_o}} \right]^2 \quad (9)$$

where R_d , R_o = the real parts of Z_d and Z_o .

If a mismatch $|\Gamma|$ is introduced external to the circulator the equation for gain is modified. It has been shown [1] in the case of a negative resistance, reflection type circulator-coupled parametric amplifier, that the gain becomes approximately

$$G = \frac{G_o}{\left[1 - \frac{|\Gamma| \sqrt{G_o + 1}}{2\sqrt{I}} \right]^2} \quad (10)$$

where

I = the circulator isolation

Since the tunnel diode amplifier is also a negative resistance, reflection type, circulator-coupled amplifier, it would appear that this equation also applies. Assuming that it does, one can then determine the amount of isolation required to maintain a given level of gain instability.

Under conditions of switching, the reflection coefficient of the circulator switch may be as high as 0.4. For a gain stability of 0.1 db the denominator must not be less than 0.98 or, in other words

$$\frac{|\Gamma|}{2} \frac{\sqrt{G_o + 1}}{\sqrt{I}} = .01 \quad (11)$$

For the preamplifier under discussion the gain will be provided by three stages of amplification. Each stage must be considered separately. Thus, when $|\Gamma| = 0.4$ and $G_o = 16$ db, I must be approximately 43 db.

For a single amplification stage, normally a 5-port circulator coupling arrangement, as shown in Figure 1, provides adequate load and source stability. This arrangement usually gives isolations on the order of 40 to 50 db with reasonably well matched ports. In order to ensure the degree of isolation necessary to maintain much better than a 0.1 db gain stability, an additional circulator will be required, resulting in a 6-port circulator-coupled amplifier with a configuration as shown in Figure 2. The specified isolation value is 65 to 70 db.

Since each stage of a TD amplifier is inherently stable, increased gain can be obtained by cascading stages. Normally the remaining stages of a cascaded amplifier need only be 4 port-circulator coupled amplifiers. For the Nimbus radiometer receiver a bandpass of approximately 200 mc is required. This bandpass characteristic is to be achieved by inserting a filter between the first and second stages of amplification. This is done in order that the filter insertion loss have only a small affect on system noise figure. For additional amplifier stability the second stage will consist of a 5-port circulator-coupled amplifier, while the third stage will consist of a 4-port. The overall configuration is shown in Figure 3.

Reference 1. Kenneth M. Johnson, "Improving the Gain Stability of Parametric Amplifiers," Microwave Journal, December, 1961, pp-86-91.

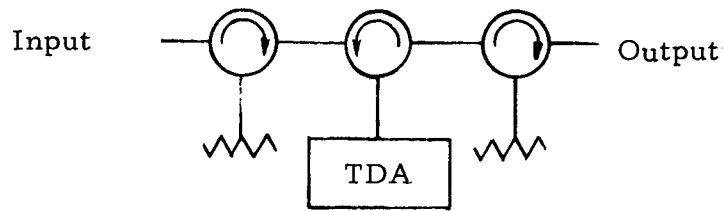


Figure 1. 5-Port Circulator Coupled TDA

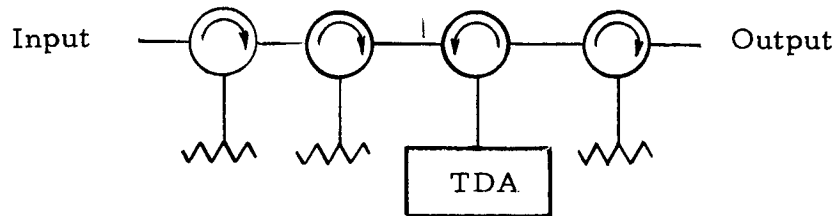


Figure 2. 6-Port Circulator Coupled TDA

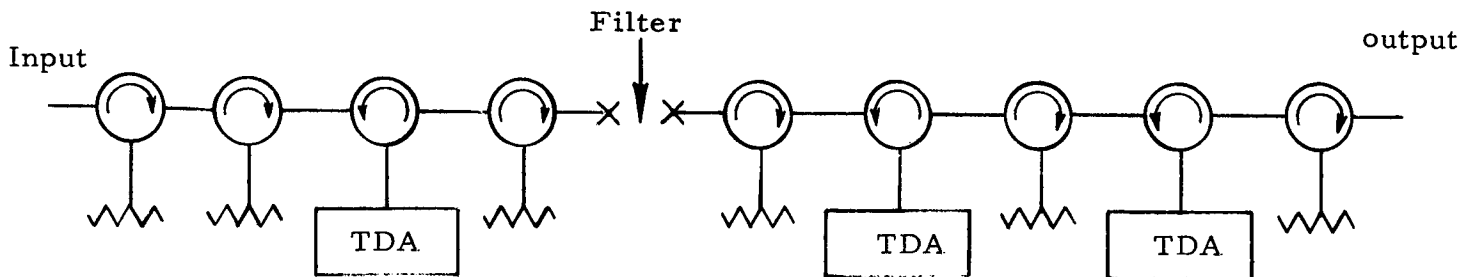


Figure 3. Nimbus Tunnel Diode Preamplifier Arrangement

Appendix VI

PHASE-SHIFTER COIL REQUIREMENT

Preliminary measurements of the performance of a Reggia-Spencer type ferrite phase-shifting device designed for use in the Nimbus phased-array antenna subsystem have been made. The principle object of these measurements was to investigate the phase shift of the device as a function of applied magnetic field so that the control coil parameters could be specified. The results of these measurements are shown in Figure 1 for a frequency of 19.35 Gcps. A rod of 0.120 inch diameter and 2.0 inch length, stepped at the ends for impedance matching, was used. The rod was made from Trans-Tech TT 2-111 nickel ferrite and was placed at the geometric center of a section of RG-53/U waveguide. Supporting the rod inside the waveguide was a block of teflon that was tapered at the ends.

From Figure 1, it is apparent that if a total phase variation of approximately 400 degrees is required and that if operation is restricted to the linear portion of the curve, the magnetic field must be changed between approximately 5 and 20 oersteds. The "average" applied field is therefore approximately 12.5 oersteds. If a constant bias field of 5 oersteds is applied to the device by either a second coil or permanent magnets, the range of magnetic field variation is reduced to 0-15 oersteds and the "average" field is reduced to 7.5 oersteds. The advantages and disadvantages of applying this constant bias field will be discussed in detail later in this appendix.

In terms of the total number of turns in the coil (N), the length of the coil (L) and the current flowing in the coil (I), the magnetic field generated by the coil is

$$H = \frac{NI}{L} \text{ ampere-turns/inch} \quad (1a)$$

or

$$H \approx \frac{NI}{2L} \text{ oersteds} \quad (1b)$$

The total number of turns N is equal to the product of the turns per layer and the number of layers. That is

$$N = nM \quad (2)$$

where

$$n = \frac{L}{2r} \text{ turns per layer}$$

$$M = \frac{h}{2r} \text{ number of layers}$$

$$2r = \text{wire diameter}$$

$$h = \text{coil thickness}$$

By substituting into Equation (1b), one can see that the magnetic field is given by the expression

$$H = \frac{hI}{2(2r)^2} \quad (3)$$

Since there is a physical limit on the coil thickness and the coil current, the only remaining variable in Equation (3) is the wire diameter. The required wire size can, therefore, be determined once the remaining parameters are specified. Therefore, assume that 1) $H_{\text{avg}} = 12.5$ oersteds; 2) $I_{\text{avg}} = 5$ ma; and 3) $h = 0.140$ inch. (The required average field is derived from Figure 1; the average current is limited by the current capacity of the transistors in the drive and control network and is approximately 5 ma*; the maximum coil thickness is limited by the spacing between adjacent array elements (.380 inch) and the size of the waveguide (.210 inch) in the narrow dimension.)

From Equation (3) it is possible to now determine the wire size that is needed. The required diameter is 0.0053 inch, i. e., a 37 gauge wire. A total

*Since the rated current capacity of the transistors being used is 300 ma, an average coil current of 5 ma sets the total current for the 44 coils at 220 ma. Some derating of the transistors can, therefore, be designed into the network.

of 26 layers yields a coil thickness of 0.143 inch. The total number of turns is, therefore, equal to 9450. If the coil is made from copper wire, the weight and resistance per coil are 0.0969 pounds and 675 ohms respectively. Forty-four (44) coils, therefore, weigh 4.26 lbs. By using aluminum wire the total coil weight is reduced to 1.29 lbs and the resistance per coil is increased to 1240 ohms. The use of aluminum wire, however, introduces soldering difficulties and other minor problems which may effect the reliability of the system. Therefore, if the additional weight of the copper coils can be tolerated, it is recommended that this approach be taken.

Since the coils and drive-control network are powered by a 24.5 volt supply, the total power requirement for the coil-drive network combination is approximately

$$\begin{aligned} P &= 24.5 \times 5 \times 10^{-3} \times 44 \\ &= 5.39 \text{ watts} \end{aligned}$$

As mentioned previously, there are two alternate approaches that one might take. In both cases the weight of the coil can be reduced appreciably. A constant bias field of approximately 5 oersteds is applied to the phase shifter in one case by a second coil and in the other approach by one or more permanent magnets. The "average" variable field is, therefore, reduced from 12.5 oersteds and the size of the coil is reduced proportionately. The power consumed in the control coil and drive network combination, however, is unchanged. When a second coil is used to obtain this bias, the total power that is required by the antenna subsystem is increased slightly over that shown above. Such is not the case when permanent magnets are used, however. Alternately, if the weight of the coils is tolerable so that a large number of turns can be used, the use of either magnets or a second coil to achieve the field bias will lower the total system power-requirement below that shown above.

The biggest problem that may be encountered with the permanent magnets are 1) obtaining magnets with identical field strengths, and 2) the unknown effect of temperature, and possibly time, on the field strength. A more detailed investigation in this area is certainly in order.

A comparison of the required power and coil weight for each of the three above-mentioned approaches to the phase shifter control coil problem is shown in Table 1. The tradeoffs between weight and power are obvious. One of the big questions not answered in this Table is whether or not it is possible to wind a coil with 9450 turns of 37 gauge wire within the thickness limitation that has been imposed. Conversations with Turbo-jet, Inc., the small company that is doing the Job 934 coils, indicate that there is no real problem. They have been given a purchase order to wind a 7660 turn coil of 36 gauge wire for us for feasibility demonstrations. The thickness of this coil is identical to that of the 9450 turn coil.

Additional phase shift measurements will be made as the development of the phase shifter progresses. Slight modifications in the field requirements may be required. However, it is felt that the data presented here will be quite close to the final requirements.

Some thought should be given to the trade-off between weight and power by the project office and/or system personnel. In the original proposal the total power required by the antenna beam steering network was 9.0 watts. It may, therefore, be possible to negotiate a change in scope to reduce this power requirement, particularly since power is at a premium but weight apparently is not.

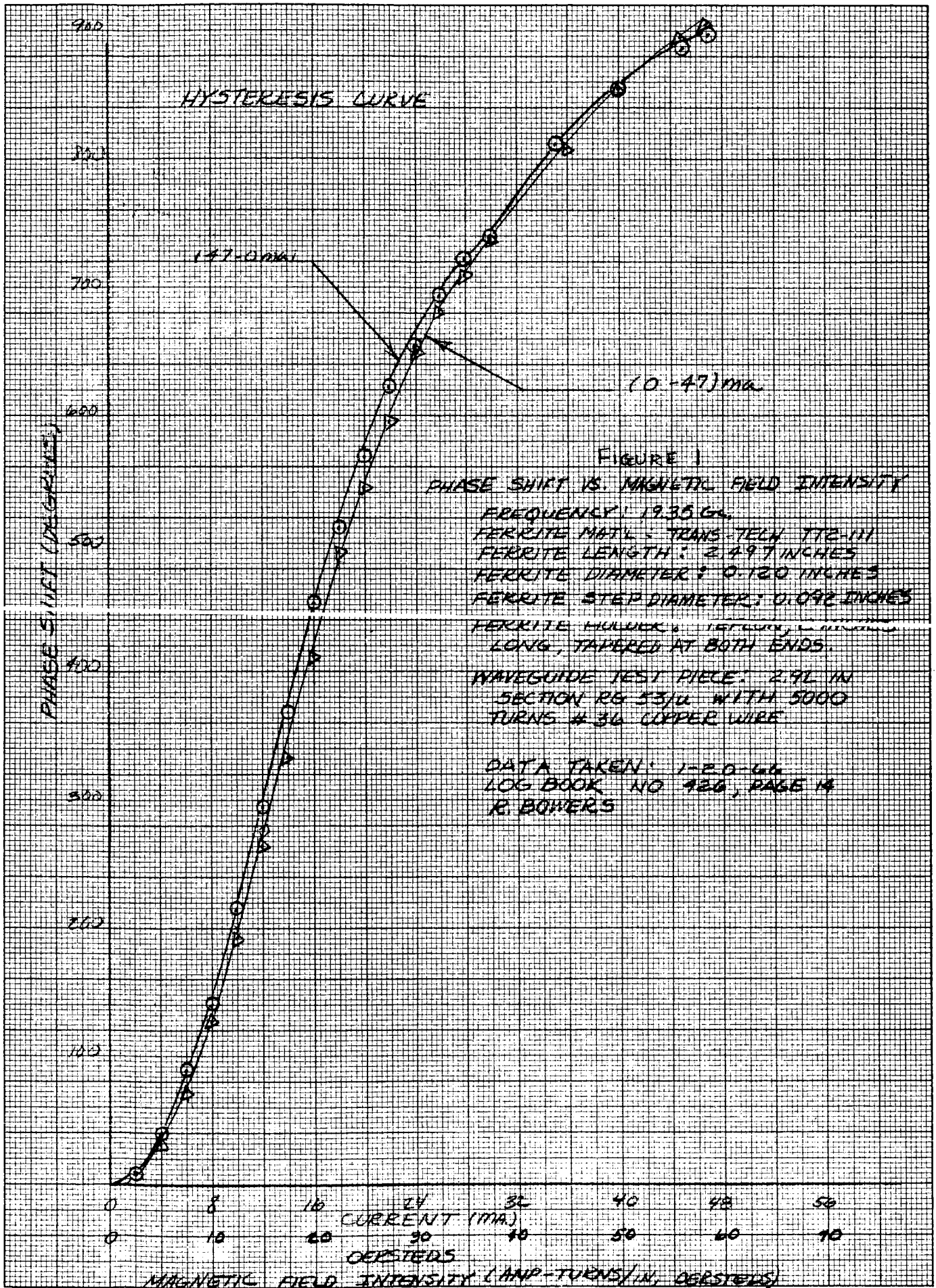
Table 1

COMPARISON OF SYSTEM PARAMETERS FOR
VARIOUS COIL CONFIGURATIONS

	No Fixed Bias	Method of Achieving Constant Bias			
		Second Coil*		Permanent Magnets	
Total Turns/coil	9450	365/5650	365/9450	5650	9450
Total Power (watts)	5.39	5.47	3.30	5.39	3.22
*Total Weight (lbs)	4.26	2.72	4.42	2.55**	4.26**

*Weights are based on the use of copper wire. A 0.303 multiplication factor should be applied if aluminum wire is used. The weight of shielding material is not included.

**This weight does not include the weight of the magnets.



Appendix VII

BEAM ANGLE FOR 94 PERCENT CROSSOVER

For a linear ground track velocity of $V_{GT} = 3.33$ nmi/sec and Radiometer parameters

$$\tau_I = 200 \text{ ms}$$

39 beam + 1 "other" positions

the total forward ground distance traveled in 1 scan is approximately 26.6 nmi.

At the sub-orbital point of a 600 nmi orbit, a 2.78° beam (3 dB width) gives a beam intercept with a 29.1 nmi forward length. Thus, the forward travel to 3 dB beamwidth is about 92%.

Results of a computer program by G. A. Poe indicate 39 beam with adjacent beam crossovers at 94% of the 3 dB width will give the center positions of the end scans at $\pm 49.3^\circ$ from broadside (49.1° required for no gap coverage assuming 27° rotation of Earth in one orbital period). The end of the 3 dB widths will cover $\pm 50.6^\circ$.

BEAM (-) ANGLE

BEAM (+) ANGLE

1	49.3 ^o	39
2	45.9	38
3	42.7	37
4	39.6	36
5	36.7	35
6	33.9	34
7	31.2	33
8	28.6	32
9	26.0	31
10	23.5	30
11	21.0	29
12	18.6	28
13	16.2	27
14	13.8	26
15	11.5	25
16	9.2	24
17	6.9	23
18	4.6	22
19	2.3	21
20	0.0	20

BEAM ANGLE FOR 94% CROSSOVER

Appendix VIII

PHASE SHIFTER AND DRIVE REQUIREMENTS

Additional measurements have been made of the performance of the Reggia-Spencer type ferrite phase-shifter device. These measurements were used to aid in the elimination of resonances from the operating range of frequencies. In addition, measurements were made to determine the effects of temperature variations on the performance of the phase shifter. It is these latter measurements that are pertinent to this appendix.

Measurements of the phase variation of the device as a function of the applied magnetic field for various temperatures were made. A total of six different temperature values was used, these being -25°C , 0°C , 28°C (ambient temperature), 50°C , 75°C and 100°C . A rod of 0.130 inch diameter and 2.0 inch length, stepped at the ends for impedance matching, was used. The rod was made from Trans-Tech TT 2-111 nickel-zinc ferrite and was placed at the geometric center of a section of RG-53/U waveguide.

The data obtained during the above measurements have been plotted in three different manners as seen in Figure 1, 2, and 3. In Figure 1, the phase reference was taken for the condition of zero applied field and ambient temperature (28°C). All phases were then referenced to this set of conditions. The result is a plot of absolute phase variations as a function of applied magnetic field and temperature. From this figure, however, it is difficult to get easily an accurate picture of the effects of temperature. This same raw data was therefore replotted using the phase for the zero field condition for the reference for all values of temperature. This plot is shown in Figure 2. It is apparent in this figure that the slope of the various curves are quite different over an appreciable portion of the curves, particularly in the low and high field regions. However, in the central portion the slopes are almost identical. In Figure 3 the reference phase point for all temperatures was taken at an applied field of 17.5 oersteds and the data was again plotted. The identicalness of the slopes is quite apparent in this figure.

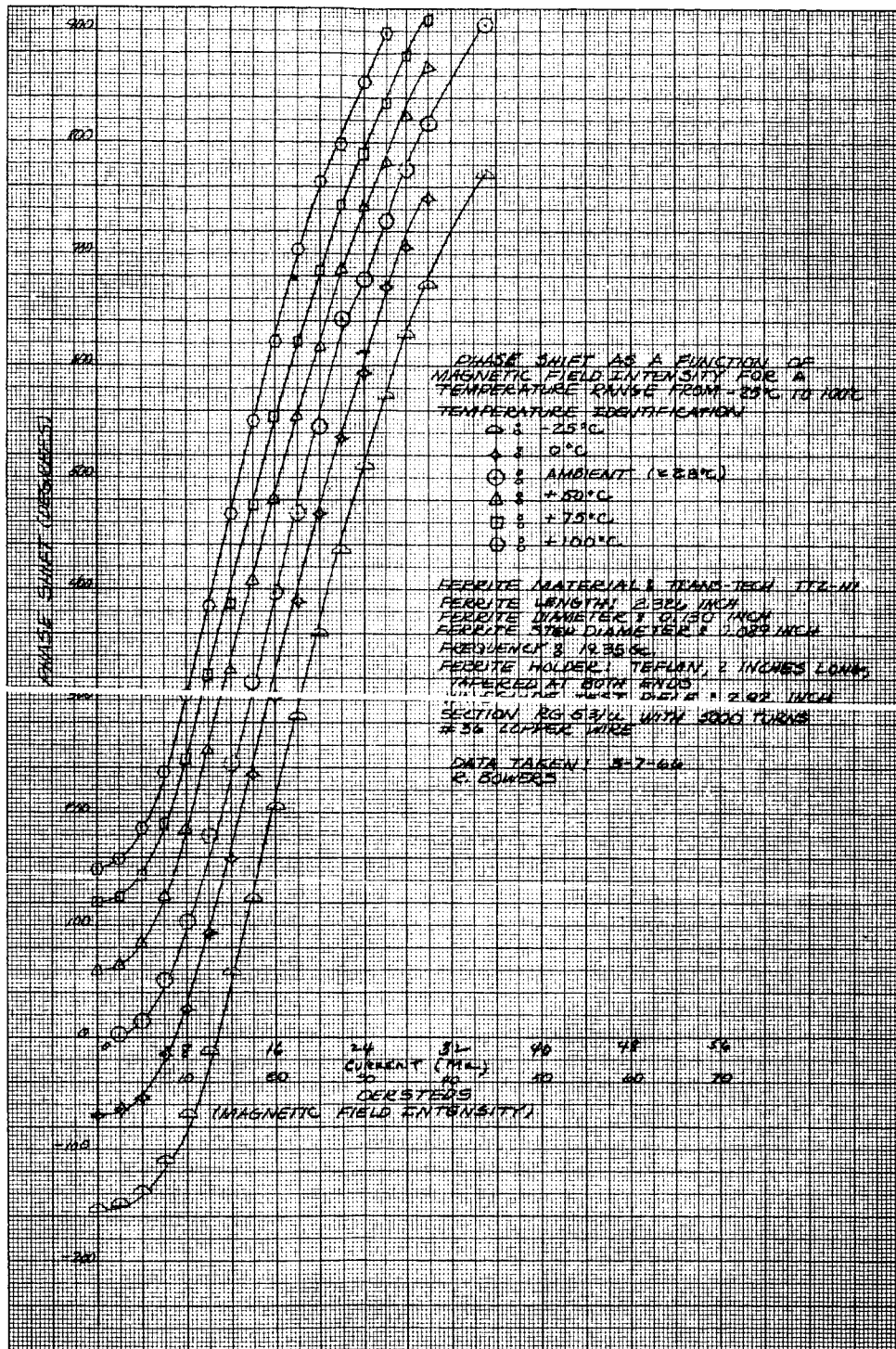


FIGURE 1

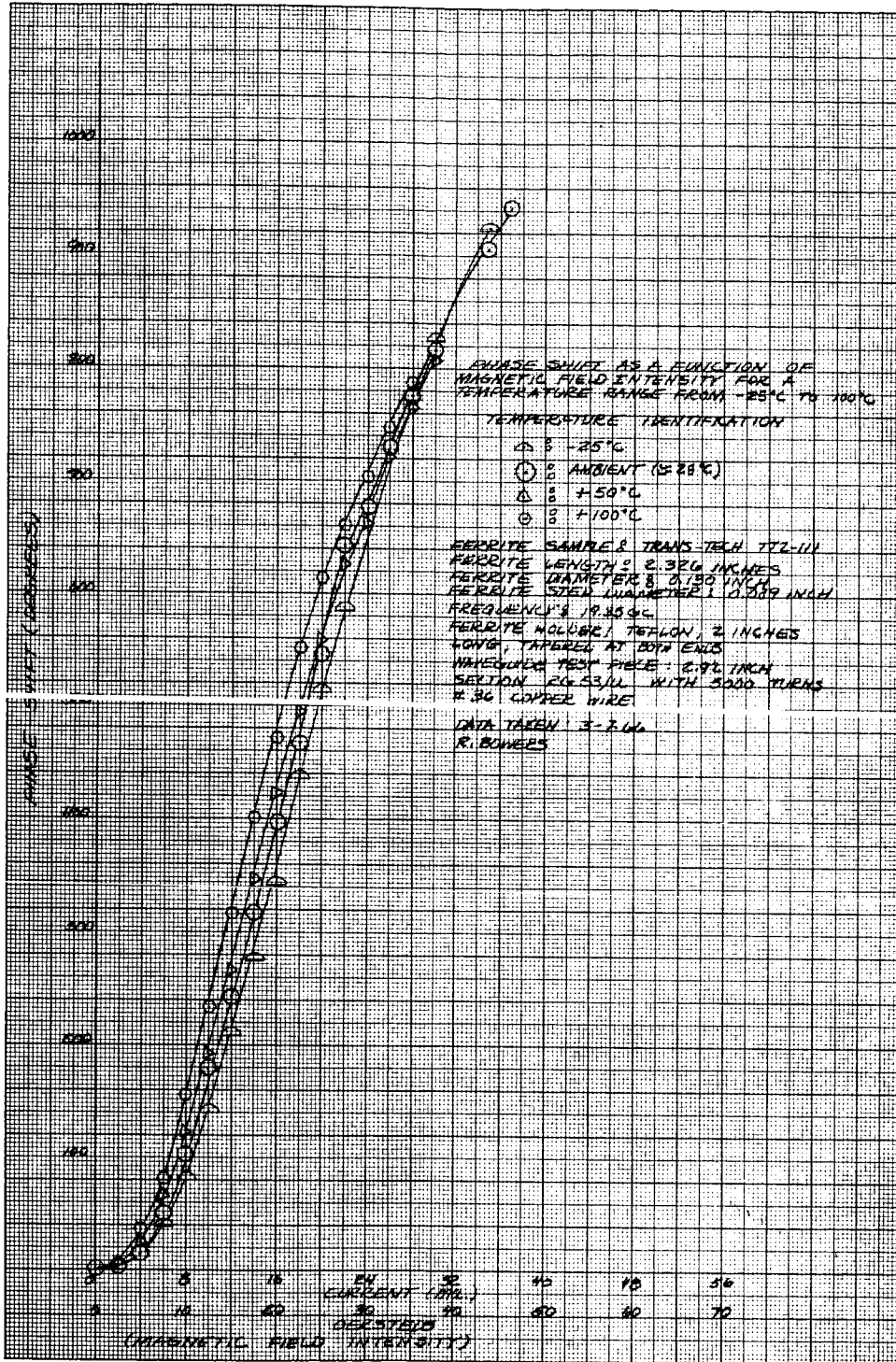


FIGURE 2

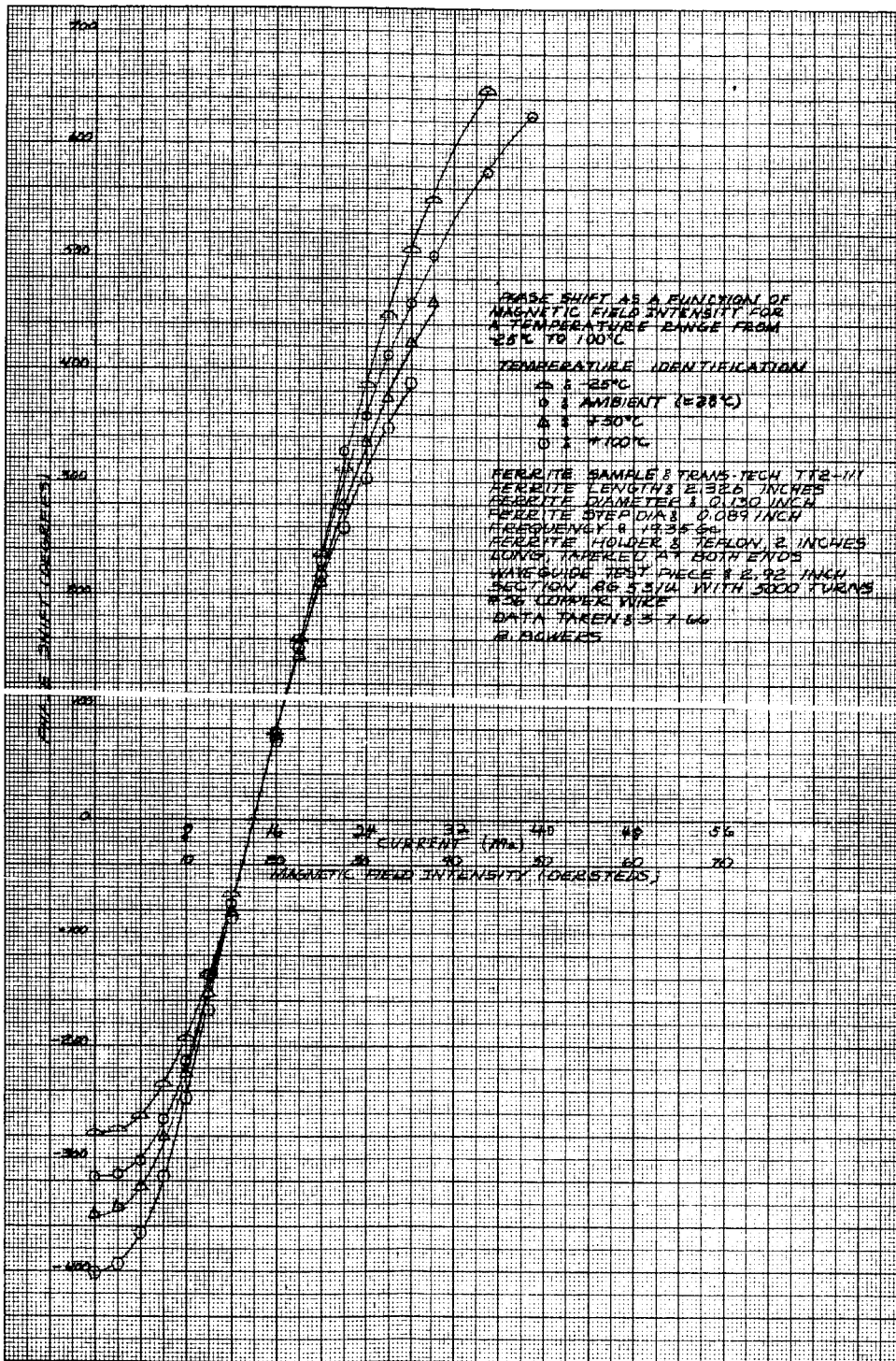


FIGURE 3

The drive coil is connected into the drive control network as shown in Figure 4a. In order to reduce the power required to drive the bias coils, these coils should ideally be connected in series across some voltage source. However, since the voltage requirement becomes unrealistic and because the overall reliability of the network is reduced by this series operation, a series-parallel network will be used as shown in Figure 4b. A 7 x 7 network will be used in order to minimize the required power. (A reduction in the number of linear elements in the planar array from 51 to 49 increases the beamwidth at the $+30^\circ$ scan point from 2.80° to 2.89° if the spacing between elements is unaltered. This is still within the given beam specifications. A reduction in weight and power is therefore achieved.) Such a configuration of bias coils can be connected directly across the output terminals of a -24.5 volt power supply.

The total power required to bias and drive the phase shifter elements in a 49 element array is 9.29 watts. This includes the power required in the drive and control network. A listing of the various coil parameters is given below in Table 1.

Table 1
COIL CHARACTERISTICS

<u>Parameter</u>	<u>Bias Coil</u>	<u>Drive Coil</u>
Turns (total)	2000	6000
Layers	6	18
Resistance (ohms)	127	381
Magnetic Field (oersteds)	12.5	0-12.5
Coil Current (ma)	25	4.17 avg; 8.33 max.
Voltage Across Coil	22.26*	3.17 (max)
Power (watts)	4.28**	5.01**
Total Coil Weight (lbs)	5.25***	

*This is the voltage across the series-parallel network of Figure 4b.

**Power required for a 49 element array.

***Includes shielding material.

In the event that the currently-pursued technique of ground plane suppression of cross-polarized fields does not work out and the ported configuration is used, the number of array elements will be reduced to 44. In this event the total power requirement will be reduced slightly. The bias power will be unchanged, but the drive power will be reduced proportionately.

A 7660-turn coil of 36 gauge wire has been wound for us by Turbo-jet, Inc., for a feasibility demonstration. This coil has 23 layers of windings (one less than that required herein) and is two inches in length. The measured resistance of this coil is 486 ohms; the measured inductance is 199 millihenrys. From a volumetric standpoint this coil is acceptable. It is intended that various environmental tests will be run on it to further check its electrical and mechanical construction and performance.

In order that the NIMBUS planar array be least affected by temperature variations, it is most essential that the slope of the curve of phase shift versus applied magnetic field be constant over a specified range of fields for all temperatures encountered. If such a condition is satisfied, variations in temperature will not alter the relative phase distribution across the array aperture, and hence will not degrade the array performance, i. e., neither the position, width and gain of the main beam nor the level of the sidelobes will be altered. This assumes, of course, that all phase shifting elements are at the same temperature, a temperature which can vary however.

Because each phase shifter must be capable of varying the phase by 360° , in order to take advantage of the temperature characteristics of the device, it is necessary to vary the applied magnetic field between approximately 12.5 oersteds and 25.0 oersteds. The problem that must now be solved is that of the efficient generation of this field. The use of a single coil, or two separate coils, or possibly a coil and a permanent magnet should be considered.

However, before this problem is attacked the drive control network should be analyzed to determine what restrictions, if any, must be imposed on the coil design. A schematic diagram of one leg of the drive control network is shown in Figure 4a. The principal restrictions are two in number:

1. The maximum current that can flow through switching transistor Q_1 is approximately 250 ma. Therefore, if approximately 50 elements are used in the array, the average current in all of the coils cannot exceed 5 ma.
2. In order to achieve the accuracy that is required in the setting of the various drive currents, the voltage across the drive coil should not exceed 5 volts.

In view of the magnetic field requirements and the volumetric limitation on the size of the coil, the above-mentioned restrictions dictate the use of a drive coil in combination with an external bias. This bias can be derived from either a second coil or from a permanent magnet. Because of the attendant time and cost schedule and the question of the reliability of the permanent magnet approach, the use of a bias coil will be pursued. (The magnet approach will be pursued on a reduced priority basis. It is suggested, however, that the customer may be interested in a change in scope to support such an undertaking in order to lower the total system power requirements.)

After having considered the various tradeoffs associated with a specific coil design, i. e., number of turns, wire size, volumetric requirements, resistance, reliability, ease of fabrication, etc., it appears that the use of a 2000-turn bias coil wound on top of a 6000-turn drive coil represents the best solution at this time. Both coils would be wound from 36 gauge copper wire and would be 2.0 inches in length. The drive coil therefore has 18 layers of windings, the bias coil 6 layers.

Appendix IX

SUPPRESSION OF CROSS-POLARIZED FIELDS WITH A GROUND PLANE

In addition to its obvious mechanical value, the use of a conducting metallic plate to tie the various linear array elements together into a planar array assembly has several electrical advantages. As mentioned previously in another report, a properly-located ground plane can serve to enhance the directivity of the individual radiating slots, thereby tending to increase the gain of the planar array assembly and to reduce somewhat the mutual interaction or coupling between the individual slots. It appears that a properly-located ground plane can also serve as a choke-section to suppress the flow of the currents associated with the cross-polarized fields of the edge slotted array and thereby also suppress these fields. It is this latter advantage that is of interest here.

How the currents which give rise to the cross-polarized fields are suppressed can be best understood by referring to Figure 1. The physical placement of the linear array elements relative to the conducting ground plane is shown in Figure 1(a). The outside cross-sectional dimensions of the linear array elements are 0.460 inches by 0.210 inches. Center-to-center spacing between adjacent elements is 0.330 inches (this is based on an antenna subsystem scan requirement of +50 degrees).

As shown in Figure 1(b) the electric field vector E across any slot of the linear array element can be broken into two orthogonal components E_H and E_V respectively, E_H being the desired polarization. Associated with these electric fields are orthogonally-oriented magnetic fields. These magnetic fields, in turn, give rise to currents flowing on the external walls of the waveguide in directions that parallel those of the electric fields. Suppression of the cross-polarized electric field vector therefore will also suppress the associated current and vice versa. Therefore, by preventing the external current I_V from flowing, it is possible to eliminate theoretically the cross-polarized electric field.

By using the ground plane in conjunction with the broad walls of the linear array elements, it is possible to form a choke section to suppress the flow of the current I_v . This section operates in much the same manner as does a choke joint in a waveguide connector, i. e., the short circuit at point A of Figure 1(c) is an open-circuit at point B which is a quarter wavelength from A. The current is therefore zero at point B and the cross-polarized field is substantially reduced. Although the current is zero at point B it does have some small value at point B'. Hence there will exist a very small cross-polarized electric field component.

It is interesting to note that the suppression of this cross-polarized field is dependent only on the position of the ground plane relative to the current source. There is no specific phase relationship required between adjacent array elements, i. e., the current of one does not cancel that of the other. Therefore, as the phase distribution across the array aperture is changed and the beam is scanned from broadside, the degree of suppression of the cross-polarized fields should not change.

Measurements have been made on the antenna pattern range to verify the theories presented above and to determine the degree of suppression that can be achieved. A model similar to that shown in Figure 1(a) was used. Initially only one edge-slotted element was used (element 3 in Figure 1(a)) along with four dummy sections of waveguide (elements 1, 2, 4, and 5). Radiation pattern measurements were then made in the plane of the linear array element for both the desired and the crossed polarization as a function of the depth of the choke section. The frequency of operation was 19.35 GHz. Maximum suppression of all cross-polarized fields in the plane of the linear array element was achieved when d was equal to 0.150 inches. The highest cross-polarized lobe was 21 dB below the desired polarization for this configuration. This is illustrated in Figure 2. Since from a radiometric system standpoint the effects of the cross-polarized energy in the main lobe can be compensated for, it is more desirable to suppress the cross-polarized lobes outside the main beam as much as possible and to accept whatever level occurs in the main beam. "Optimum" results were achieved with a depth d of 0.129 inches and are shown in Figure 3. A 32 dB suppression of the cross-polarized fields outside the main beam was achieved. For comparison

purposes the radiation pattern of the linear array element without a ground plane is shown in Figure 4.

All of the above measurements will be repeated using edge-slotted array elements in lieu of the dummy waveguide sections. No change in the results is anticipated.

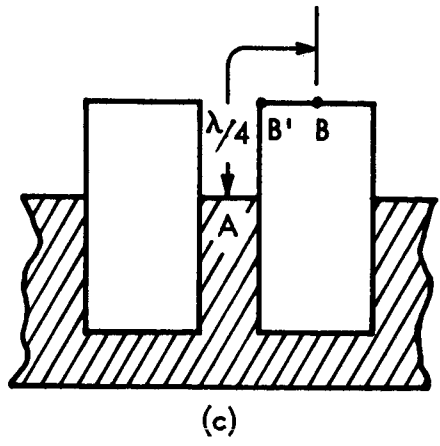
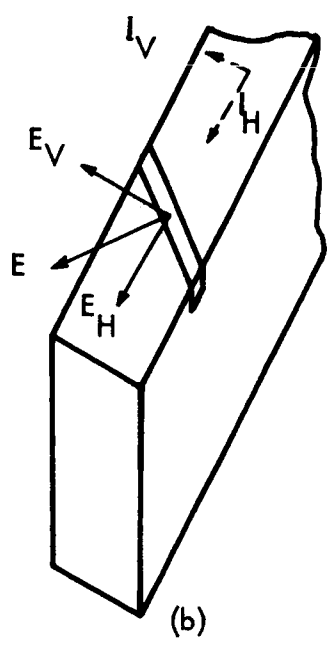
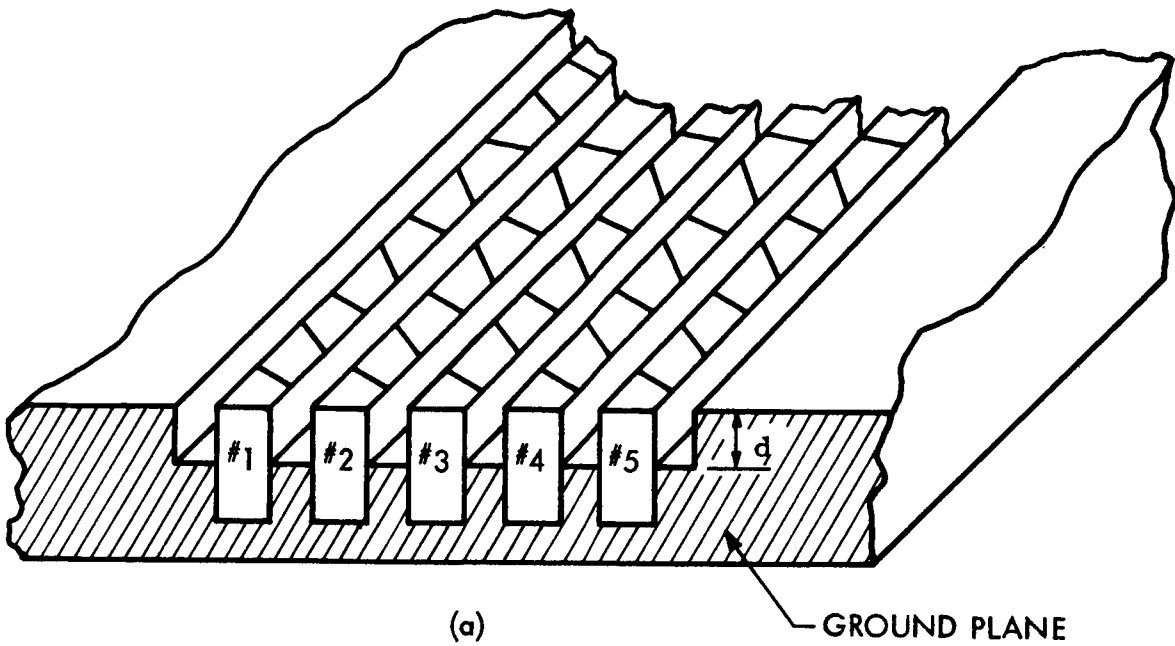


Figure 1

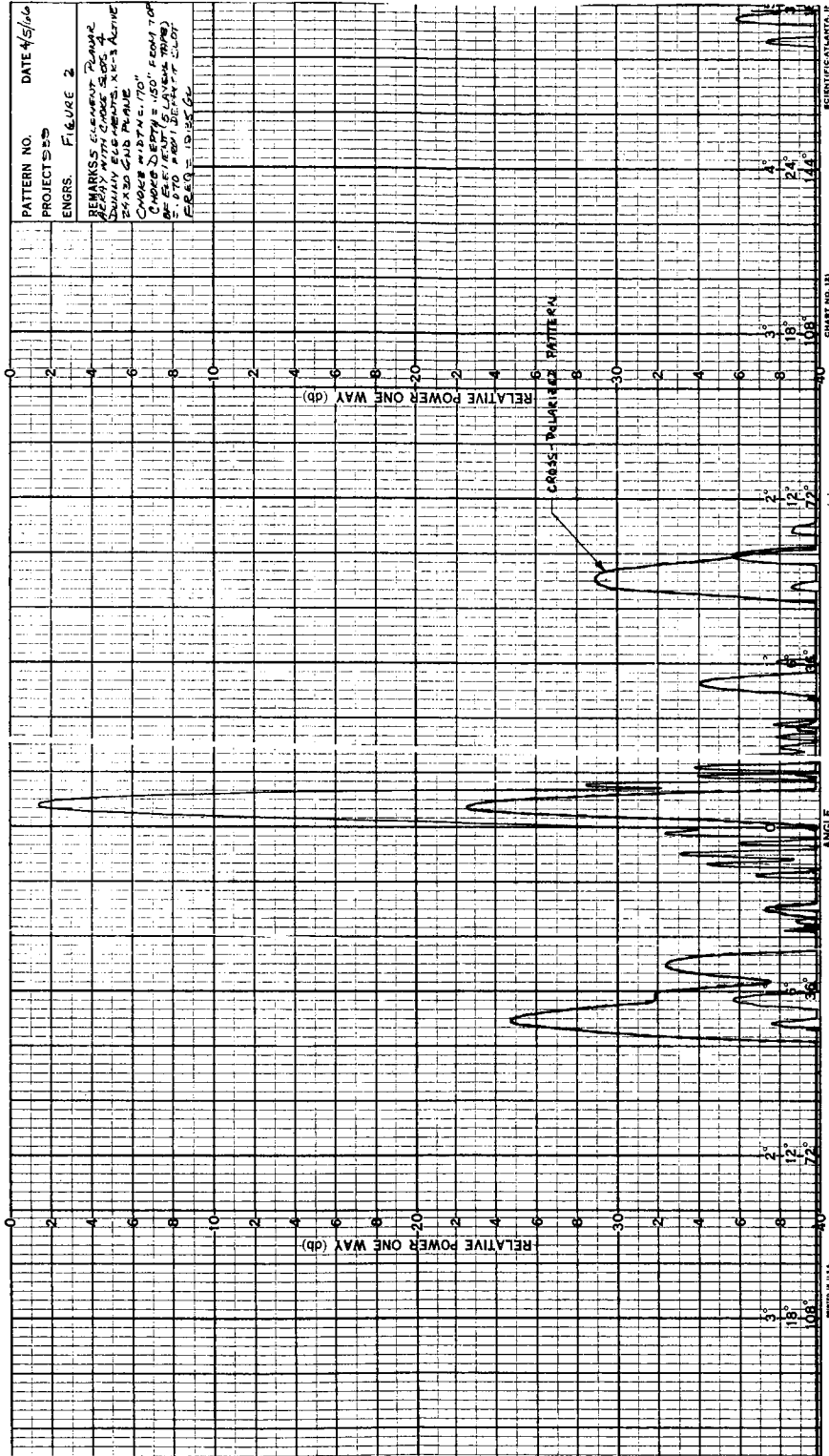


Figure 2

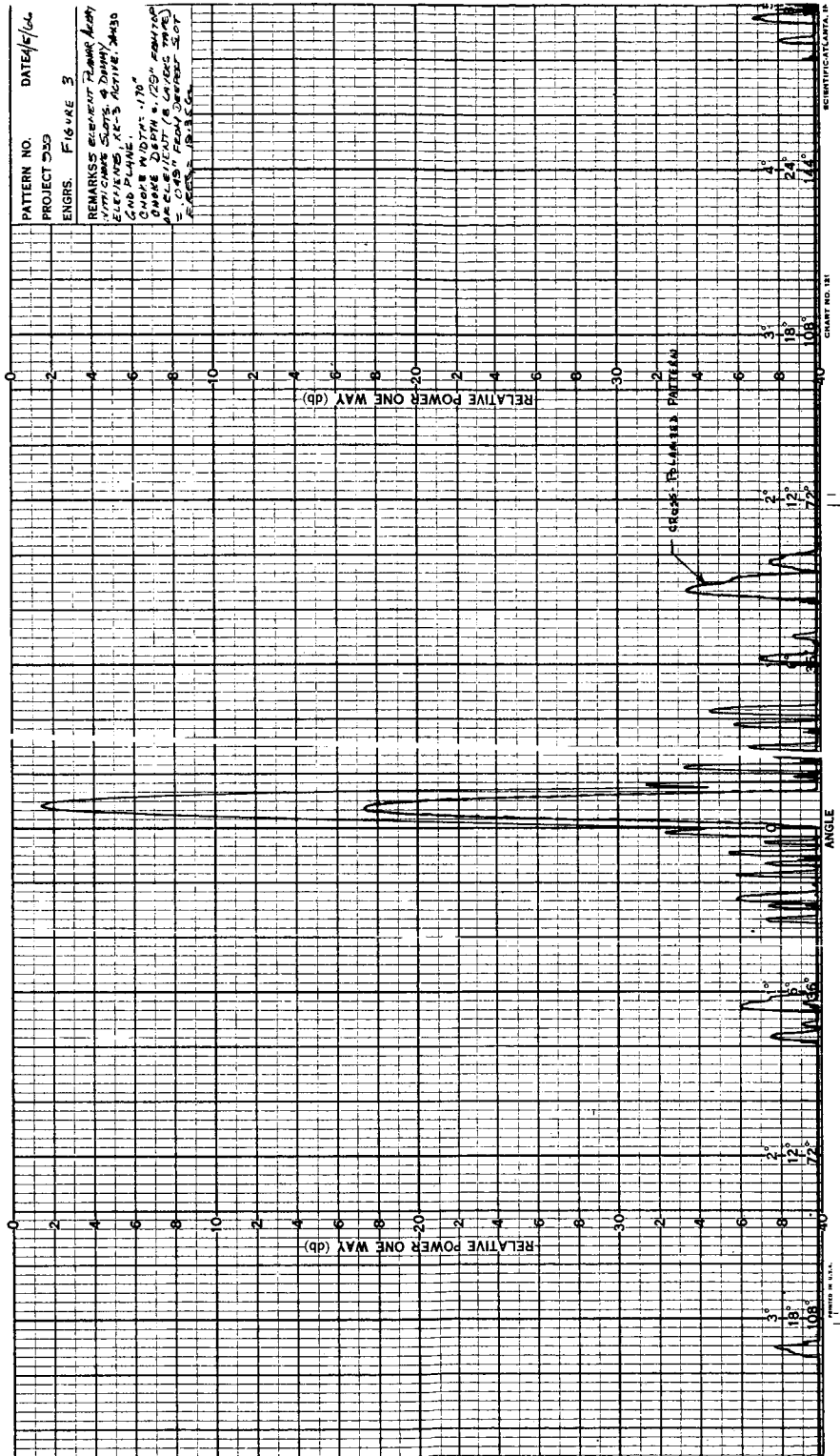


Figure 3

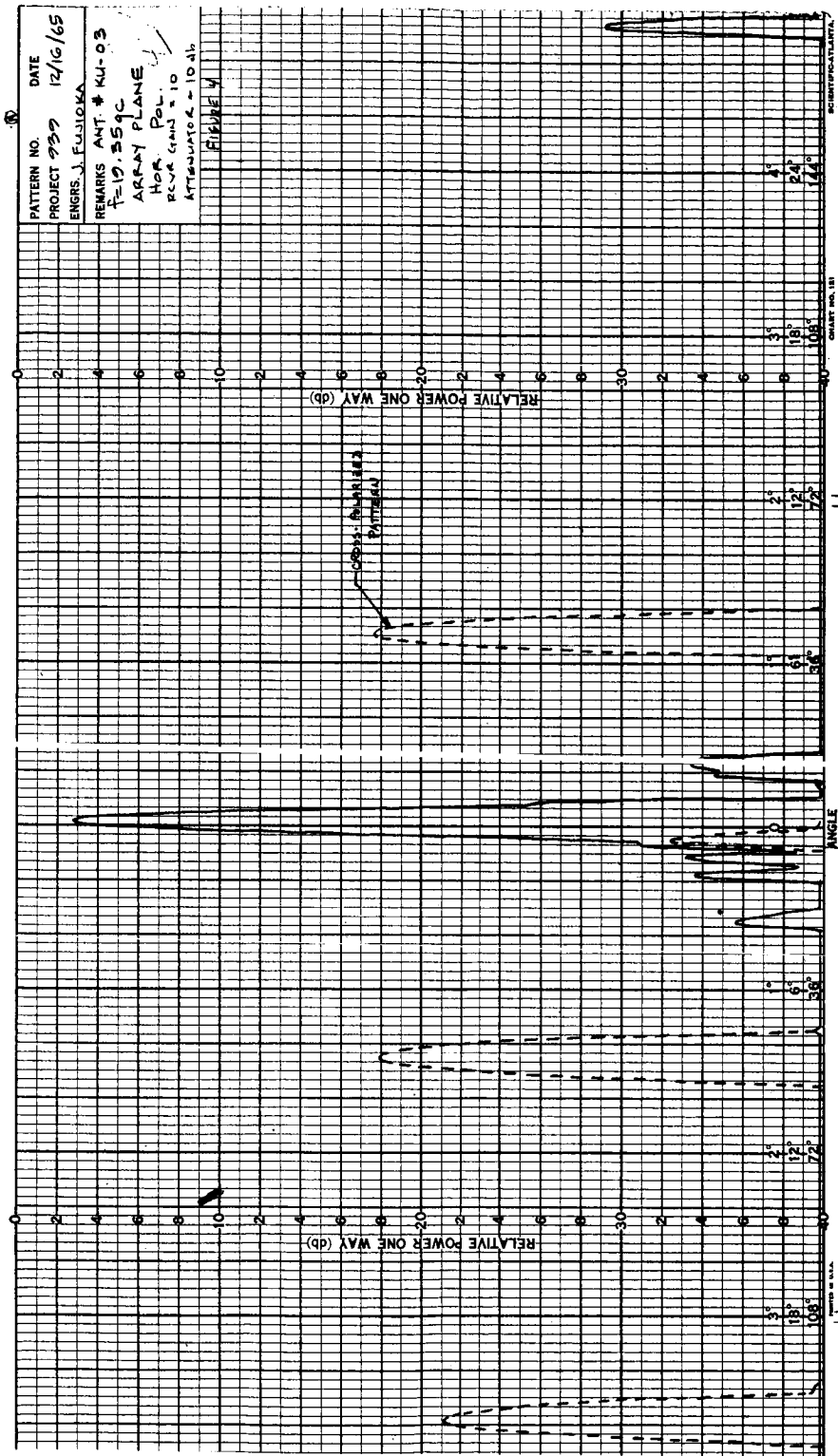


Figure 4

Appendix X

MONTE CARLO ANALYSIS

As part of the work performed by the Space-General Corporation on in-house research and development funds and under contract NOw-65-0135c with the Navy Bureau of Weapons, an analysis was made to determine the effects of phase and amplitude perturbations from a predetermined nominal on the performance of a planar array. The details of this analysis have been published in SGC Summary Report 779R-12⁽¹⁾ and have been used herein to aid in the determination of the tolerances to which the phase and amplitude distributions across an array aperture must be held in order to assure that the resultant radiation pattern will meet all specifications in a suitably high percentage of assembled arrays.

There exist two general classes of phase and amplitude perturbations. The first is random perturbations, i. e., the deviation in phase and amplitude on a particular element of the array does not depend on the state of the other elements in the array. Manufacturing tolerances in the slot spacing, slot angle and depth of cut, etc., are the principal source of these random perturbations. The second class is a constant bias on the phase and amplitude distribution. Mutual coupling between individual elements is the most apparent bias error mechanism. Whereas amplitude perturbations tend to increase sidelobes symmetrically, phase perturbations disturb the symmetry of the pattern, transferring energy from one side to the other. The gross effect of mutual coupling is to flatten the amplitude taper and to put a phase bias on the outermost elements. A first order correction to mutual coupling, therefore, is to design a harder taper into the amplitude distribution. Measurements made on a single linear array element have shown that this first order correction is sufficient.

(1) "Missile Guidance Array Antenna," SGC 779R-12, 15 December 1965
(Confidential).

As mentioned above, the problem at hand is to determine to what tolerance must the random phase and amplitude perturbations be held so that the resulting radiation pattern will meet all specifications in a suitably high percentage of assembled arrays. From a more practical standpoint, the question centers on the mechanical tolerances required in the manufacture of the array. To answer this question a Monte Carlo computer program was written. This program, in effect, selects an appropriate quantity of elements from a large supply of radiating elements which have predetermined statistically-defined deviations from nominal and assembles an array. The structure of this array is identified and its detailed radiation pattern is determined. The entire sequence is then repeated until a statistically significant number of arrays has been assembled and evaluated. Ultimately, the program yields compilations of data relating phase and amplitude tolerances to various radiation pattern parameters.

In simple language, a Monte Carlo program consists of a random number subroutine, the output of which is a string of random numbers equally likely in the interval $0 \leq x \leq 1$. This output from the random number generator is passed on to a second subroutine which weighs the numbers according to an assigned probability density function. The output from this second subroutine, which acts as a filter for the first is a set of numbers the values of which obey the assigned probability distribution. A Gaussian probability density function with mean zero for phase and amplitude has been used.

A one-sigma value of 0.0033 inches was assigned as the tolerance on the slot spacing and slot depth and 0.33 degrees on the slot angle. These dimensional tolerances were in turn converted into phase and amplitude perturbations. Both the probability density function and the scatter were Gaussian and the assigned one-sigma values were as mentioned above. It is felt that these error values represent the extreme worst case in that the associated peak tolerance errors of 0.005 inch and 0.5 degrees are rather sloppy tolerances that are easily and economically realized in the actual manufacturing of an array.

Twenty-five linear array elements were "built" by the computer using the above-mentioned errors. The nominal array pattern that was chosen had a -35 dB sidelobe level. Results of this Monte Carlo analysis are summarized in the form of histograms in Figures 1 through 4.

Beam position error is negligible (Figure 1)

Beam broadening is negligible (Figure 2)

The loss in gain is almost negligible (Figure 3)

Sidelobe level is the most affected parameter (Figure 4).

The mean value of the highest sidelobe has been raised to -39.2 dB, with 96% of all arrays below -27 dB.

An obvious conclusion to be drawn from these data is that the randomness in the phase and amplitude perturbations tends to cancel out their effects on the array gain, beam width and beam position. If these perturbations were systematic or periodic, this would no longer be true. This can be better understood by analyzing the mechanism required to change the various array parameters.

For example, the gain of the array is determined by vectorally summing the contribution from each element in the array. Random perturbations would therefore tend to cancel one another and therefore not affect the gain of the array. Since the width and position of the main lobe are primarily functions of the relative amplitude and phase distributions, respectively, and since random perturbations would not change the relative amplitude and phase across the array aperture, then neither of these two array parameters should be affected. In the case of sidelobes, however, this cancellation of effects is not experienced. This is due to the fact that amplitude and phase perturbations both cause an increase in the sidelobe level, amplitude errors tending to increase the sidelobe structure symmetrically, phase errors asymmetrically. The net effect is a change in the total sidelobe structure.

In the orthogonal or scanned plane of the array, in addition to the phase and amplitude errors that are introduced by the mechanical tolerances in the feed element additional phase and amplitude errors may be introduced by the ferrite phase shifting elements. Phase errors are the direct result of the accuracy to which the individual phase shifter drive currents can be set. Amplitude errors can occur if the insertion loss in the phase shifter varies as a function of the applied magnetic field. By properly matching the device, however, any amplitude variation can be made negligibly small.

Because of the additional possible phase errors that can occur in the scanned plane, a separate Monte Carlo analysis was performed for this plane. The probability density function and the scatter were again assumed to be Gaussian. A one-sigma value of 0.0033 inches was assigned to the tolerance on the slot spacing and slot depth and 0.33 degrees on the slot angle. In addition a tolerance was assigned to the phase shifter settings. A one-sigma value of 3 degrees was used in one program, 6 degrees in a second, and 10 degrees in a third. The results of these Monte Carlo analyses were again printed in histogram form and are tabulated in Table 1 for easy reference.

It should be pointed out that the sidelobe level tabulated in Table 1 is the highest sidelobe that occurred in the particular radiation pattern. The average sidelobe level is much lower.

The results of the Monte Carlo analysis indicate the effects that might be expected on the various array parameters as a function of certain assumed maximum perturbations. It should be restated that the tolerances assumed are quite loose and easily satisfied from a manufacturing standpoint. Tighter tolerances will obviously improve the system performance.

In another memorandum an analysis is made to determine the amount of energy that is contained in side and backlobe radiation as a function of the sidelobe level in the plane of the linear, array element and in the scan plane. This analysis, in conjunction with the Monte Carlo analysis of this section, can then be used to specify the mechanical tolerances required in the fabrication of the planar array.

Table 1
Effect of Mechanical Tolerances on Radiation Pattern Parameters

Slot Spacing and Slot Depth (Inches)	Assumed Tolerance	Main Lobe Position (Degrees)			Main Lobe Level (db)			Main Lobe Width (Degrees)			Highest Sidelobe Level (db)			
		σ	μ	σ	σ	μ	σ	σ	μ	σ	σ	μ	σ	
														Phase Shifter (Deg.)
.0033	0.33	0*	-3.230	-3.224	-3.220	-0.00	-0.08	-0.15	2.728	2.740	2.752	-30.4	-29.2	-28.2
.0033	0.33	3	-3.240	-3.226	-3.214	-0.00	-0.08	-0.18	2.728	2.740	2.752	-28.4	-27.5	-26.5
.0033	0.33	16	-3.256	-3.228	-3.204	+0.06	-0.02	-0.09	2.728	2.740	2.753	-27.0	-25.6	-24.1
.0033	0.33	10	-3.276	-3.236	-3.196	+0.13	+0.03	-0.07	2.725	2.738	2.752	-24.5	-22.8	-21.0

*This condition applies for both the plane of the linear array element and for the scan plane when no phase error is introduced by the ferrite phase shifters

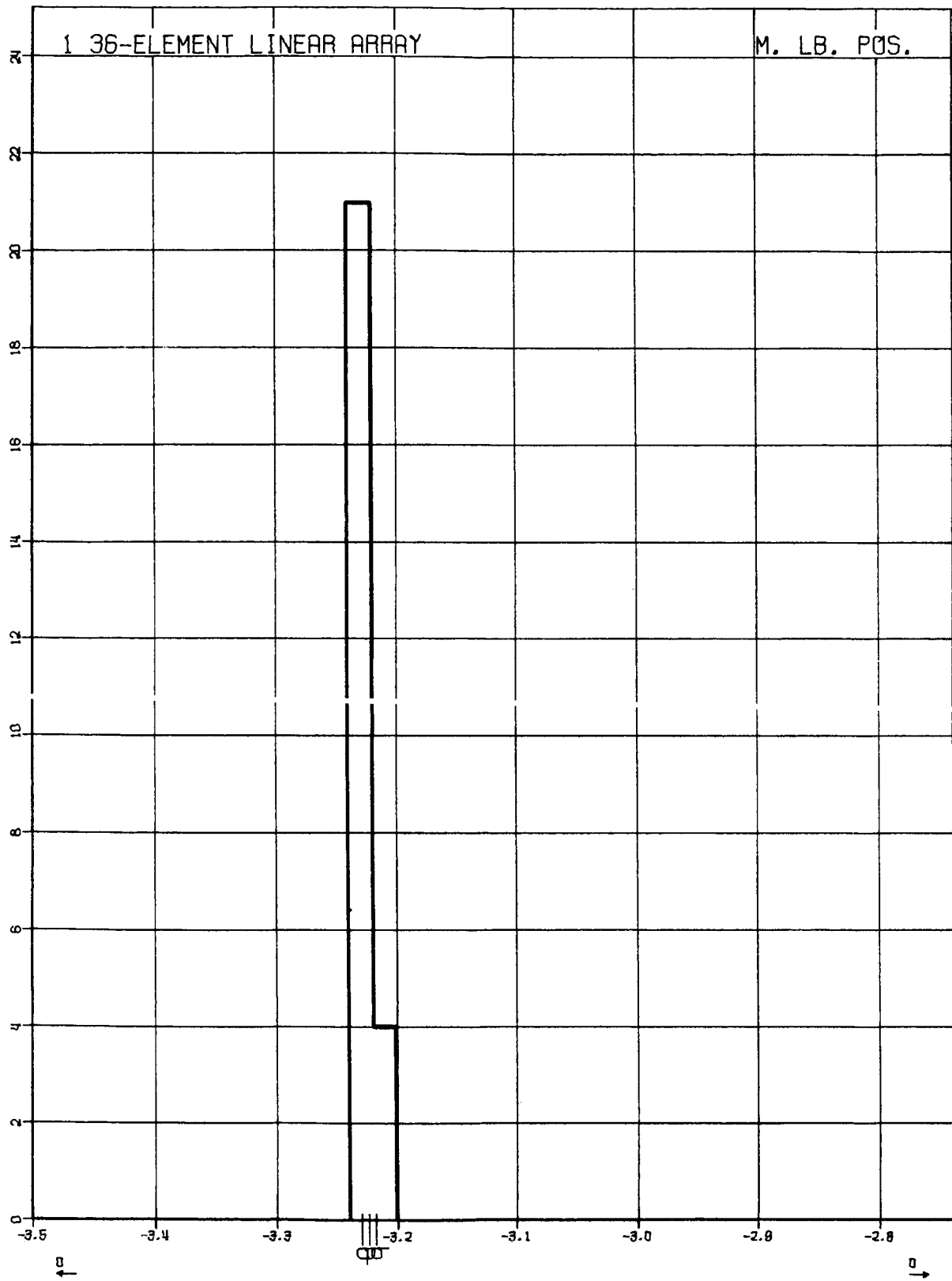


Figure 1

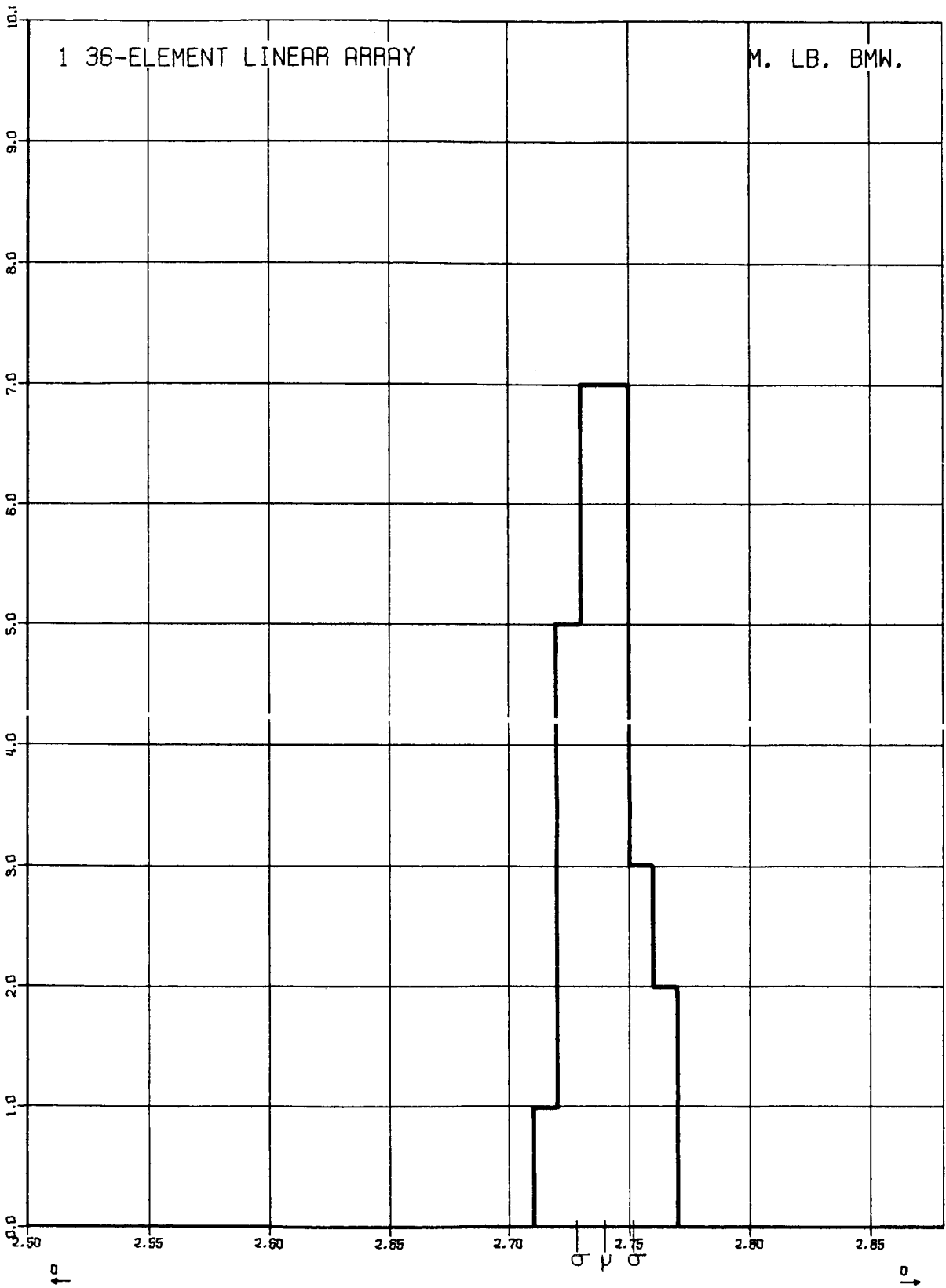


Figure 2

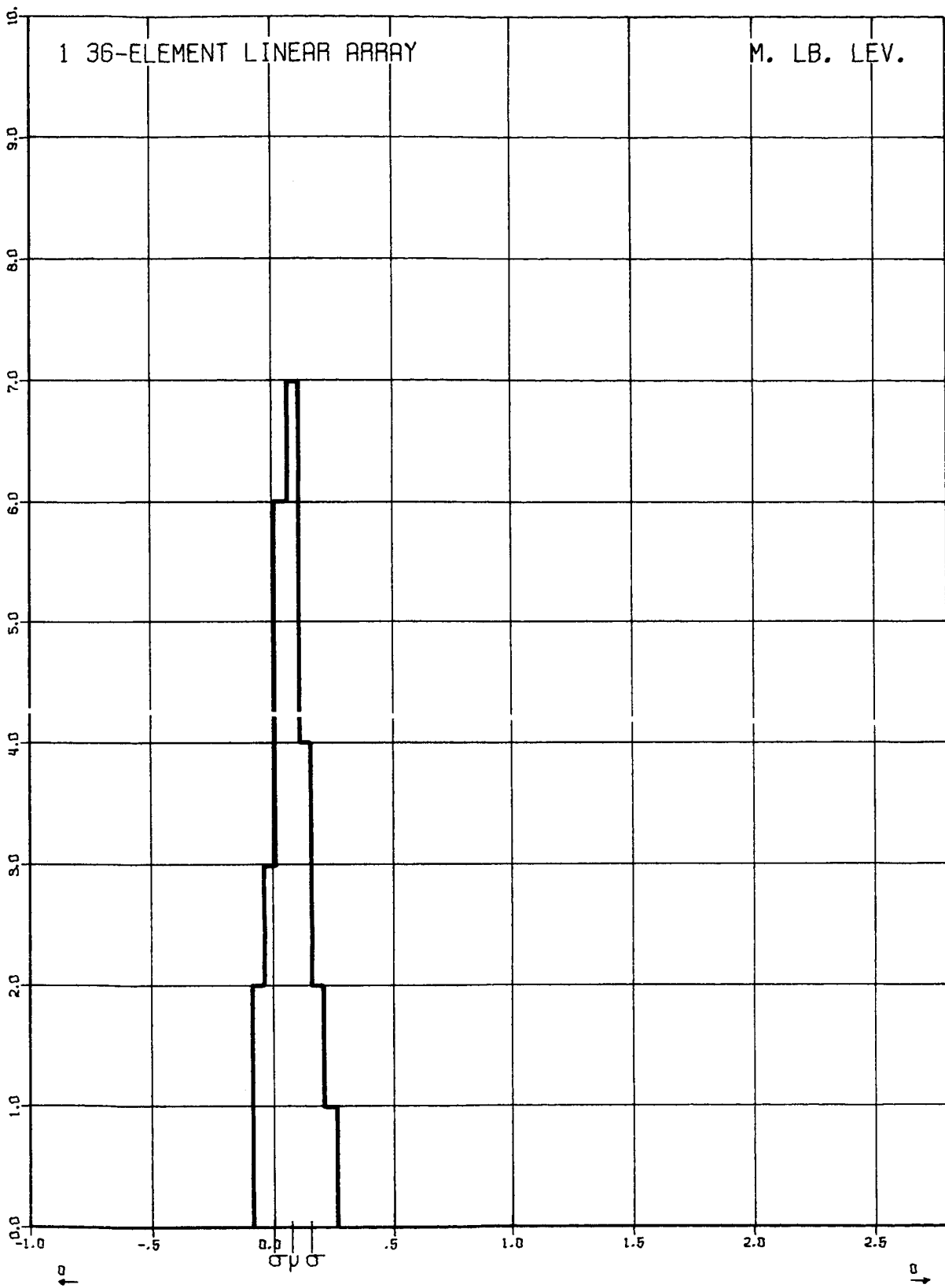


Figure 3

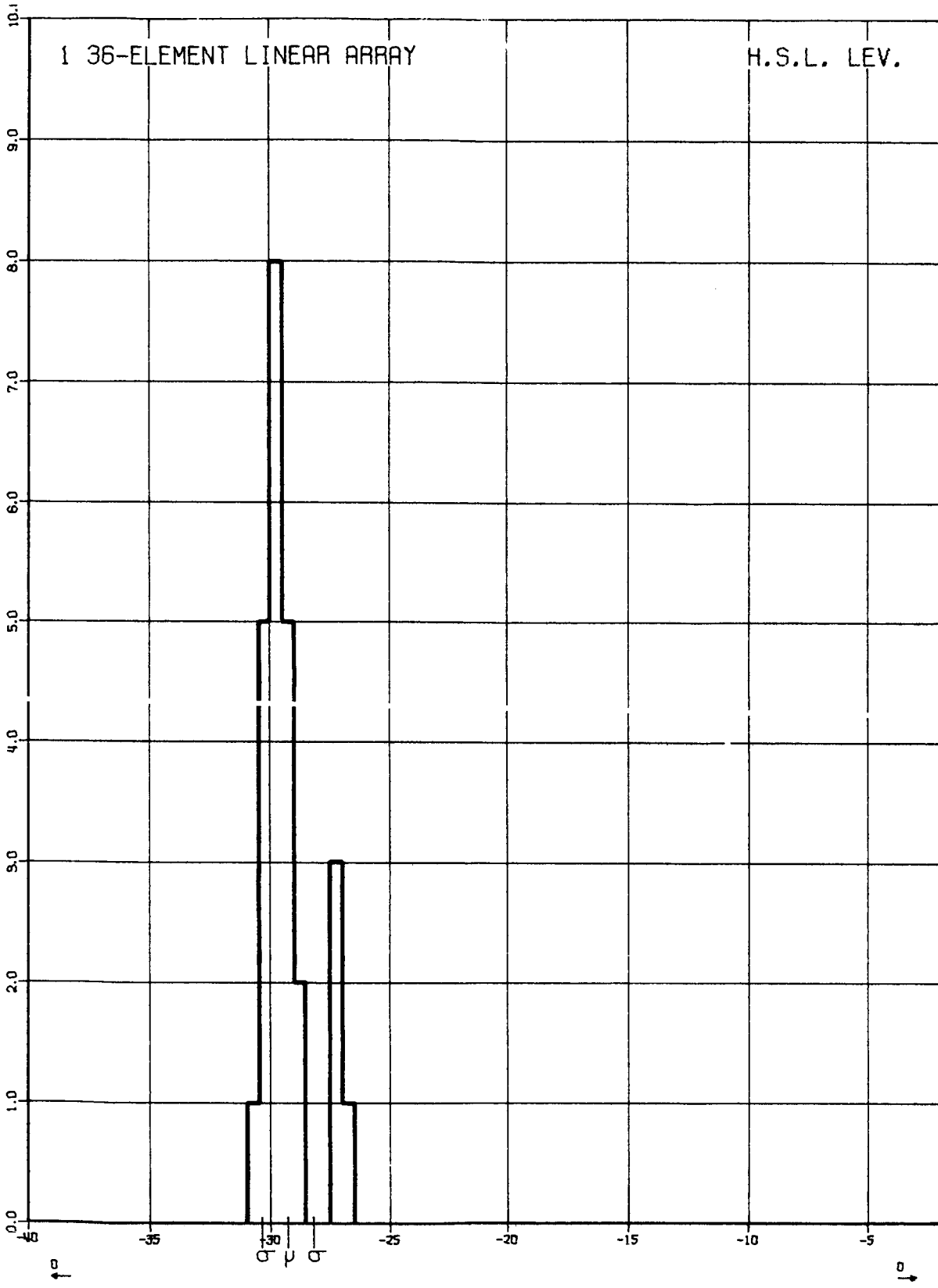


Figure 4

Appendix XI

BEAM POSITIONS FOR SCANNING AND OTHER MISCELLANEOUS TOPICS

The original beam incrementing scheme for the radiometer used a constant increment in angle, even though the beamwidth was increasing with scan angle. The specified integration time (200 ms) and number of steps, when combined with the orbital parameter, showed redundant coverage in the direction transverse to travel, and gaps in the direction of travel.

Some of the desired features (all of which are not simultaneously obtainable) for a new scanning arrangement are:

1. The base 200 millisecond timing should be retained.
2. 40 beam positions or some multiple thereof should be used per telemetry frame. This actually allows 39 antenna beam positions with the other slot used for calibration and other multiplex parameters.
3. Equal overlap of beams in the forward direction and also in the traverse direction.
4. Coverage in the transverse direction should be wide enough so successive passes over the equator will scan adjacent areas with no gaps in coverage.
5. As much non-redundant data as possible.

When the effect of beam broadening is included, the beam steps must be one of increasing size as the beam is pointed away from the array normal. For narrow beams (when not scanning too close to endfire) the increase in beamwidth is given approximately by the reciprocal of the scan angle. The beam is broadened only in the direction of the scan. Effects of the beam tilt due to the non-resonant array are not considered (see Attachment I).

For the 39 beam positions plus 1 "other" time slot, the total time per scan is 40×0.2 or 8 seconds. In 8 seconds, the forward distance traversed (on the ground track) is 26.6 nautical miles. At the sub-orbital point a 2.78° beam will give a ground intercept 29.1 nautical miles in diameter. This means

beams of sequential scans will overlap by about 9%, or another way of saying this is the crossovers in the forward direction occur at .92 beam widths.

Tables II and III of Attachment II give the results of a computer run for differing amounts of overlap. Only the case of .92 and .94 beamwidths overlap are shown. With this scheme, the overlap in the transverse direction will be uniform. The overlap in the direction of travel will however, increase with increase in scan angle. This is due to the uniform scanning speed in the forward direction while the beam spot size is not uniform with scan angle. The increase in the linear dimension of the spot in the forward direction with scan angle is due to the increase in slant range between the antenna and the ground. The ordinate is proportional to the down track size of the beam intercept size, and the abscissa is the scan angle (this is not proportional to the cross-track distance).

The incidence angle is important for radiometric reasons, the central angle has no particular importance here except in the computations. In Attachment V it is shown that a scan of $\pm 49.1^\circ$ for β will give complete mapping of the earth by the radiometer. Notice that the incidence angle θ varies from 0° to 62° in this scan range. The tangent ray ($\theta = 90^\circ$) is about 58° from this figure.

Attachment I to Appendix XI

The use of a non-resonant array causes a beam offset from normal, in the down range direction. For the present array this offset is about 3°. This is accounted for in the mechanical mounting to make the resultant beam look straight down. The direction of the transverse scan is perpendicular to the down range track only for a "broadside" array, and will scan a cone for any other tilted array. For the 3° tilt, the angular error is given in Table III of Attachment II. Larger offsets are approximately proportional to the 3° case. The actual scan angle θ is determined from

$$\sin \theta = \frac{\sin 3^\circ}{\cos \beta}$$

TABLE I

<u>Transverse Scan Angle (β)</u>	<u>Angle From Broadside To Array (θ)</u>	<u>Error</u>
0	3.0°	0.0°
10	3.03	0.03°
20	3.20	0.20
30	3.45	0.45
40	3.95	0.90
50	4.65	1.65
55	5.2	2.20
60	6.0	3.00

Attachment II to Appendix XI

The beam positions were computed by assuming the beam broadening is accurately given by the broadside beamwidth divided by the cosine of the scan from broadside, and making the adjacent beams tangent to each other at some constant fraction of the 3 dB beamwidth. Since the beamwidth is determined by the scan angle and the scan angle position is dependent on the beamwidth, an iterative method was used to compute them. The Fortran program along with a short interpretation, is given here. Tables II and III are samples of the output when the spacing between adjacent beam positions is 0.92 and 0.94 of the 3 dB width at that location.

INTERPRETATION

Statement

5. Converts beamwidth "BO" from degrees to radians
6. Set initial beam position to 0 (straight down)
11. The first fractional beamwidth "BW(1)" is set equal to the broadside beamwidth "BO" times the beam fraction "V1".
13. The first estimate of the second beam position "POINT(2)" is made.
- 14-16. A DO loop that refines the estimate of beam size and then of the pointing angle.
21. Converts the pointing angle into degrees. The program continues this procedure for the other beam positions.

FORTRAN SOURCE LIST

```
1      DIMENSION POINT (100), BW(100), PONTD (100), BWD(100)
2      1  READ (5, 500) BO, VI, NBEAM
4      500  FORMAT (5X, F3. 1, 10X, F6. 5, 32X, 14, 18X)
5      BO=BO/57. 2958
6      POINT(1) = 0. 0
7      PONTD (1)=0. 0
10     BWD (1)=BO*57. 2958
11     12  BW (1) =BO*V1
```

```

12      DO 200 M=2, NBEAM
13      POINT (M)=POINT M-1)+BW(M-1)
14      DO 201 K=1, 5
15      BW (M)=BW(1)/COS(POINT(M))
16  201  POINT (M)=POINT (M-1_+0.5*(BW(M-1) + BW(M)
20      BW(M)=BW(M)*57.2958/V1
21  200  PONTD (M)=POINT (M)*57.2958
23      WRITE (6, 601) V1, (K, BWD(K), PONTD(K), K=1, NBEAM)
30  601  FORMAT (1H1, 20X, 3HV1=, F8.5, ///, 10X, 8HPOSITION, 3X,
              10HBEAM WIDTH, 13X, 14H POINTING ANGLE//100(13X, 13,
              7X, F7.3, 9X, F7.3/))
31      1F(0.8-V1)10, 11, 11
32  10   V1=V1-0.020
33      GO TO 12
34  11   END

```

TABLE II

VI = 0.92000

<u>Position</u>	<u>Beamwidth</u>	<u>Pointing Angle</u>
1	2.430	0.000
2	2.432	2.236
3	2.437	4.476
4	2.447	6.723
5	2.460	8.980
6	2.478	11.252
7	2.499	13.541
8	2.526	15.853
9	2.558	18.191
10	2.595	20.562
11	2.639	22.970
12	2.691	25.422
13	2.750	27.924
14	2.820	30.487
15	2.901	33.118
16	2.997	35.832
17	3.111	38.642
18	3.248	41.567
19	3.415	44.631
20	3.622	47.868
21	3.888	51.323
22	4.243	55.064
23	4.746	59.199
24	5.528	63.925
25	7.000	69.688
26	12.120	78.483

TABLE III

 $V_1 = 0.94000$

<u>Position</u>	<u>Beamwidth</u>	<u>Pointing Angle</u>
1	2.430	0.000
2	2.432	2.285
3	2.438	4.574
4	2.448	6.870
5	2.462	9.177
6	2.480	11.500
7	2.503	13.841
8	2.531	15.207
9	2.564	18.601
10	2.603	21.030
11	2.650	23.499
12	2.704	26.015
13	2.767	28.587
14	2.842	31.223
15	2.929	33.935
16	3.032	36.737
17	3.156	39.645
18	3.306	42.682
19	3.490	45.876
20	3.724	49.267
21	4.029	52.911
22	4.449	56.896
23	5.072	61.371
24	6.127	66.634
25	8.577	73.545
26	12.857	83.619

Attachment III to Appendix XI

The linear beam dimension on the ground in the forward direction can be approximated by

$$b_y = L \times B.W.$$

where

b_y is the length of the ground intercept of the 3 dB beam dimension in the direction of travel.

L is the distance from the satellite to the ground intercept. $B.W.$ is the 3 dB antenna beamwidth in the forward direction expressed in radians.

Since the beamwidth $B.W.$ is fixed, it remains only to determine L . Take the satellite as being located at the origin of the coordinate system and located a height H above an earth with radius R_o . P is the intersection of the beam (scanned to an angle β) and the earth. The equations of the beam and earth are

$$Y = \frac{X}{\tan \beta}$$

and

$$X^2 + (y - y_o)^2 = R_o^2$$

combine the two (substitute for X)

$$y^2 \tan^2 \beta + y^2 - 2yy_o + y_o^2 = R_o^2$$

solve for y

$$y = \frac{+ 2y_o \pm \sqrt{4y_o^2 - 4(1 + \tan^2 \beta)(y_o^2 - R_o^2)}}{2(1 + \tan^2 \beta)}$$

$$y = \cos \beta \left[y_o \cos \beta + \sqrt{R_o^2 - y_o^2 \sin^2 \beta} \right]$$

$$L = -\frac{y}{\cos \beta} = -\left[y_0 \cos \beta + \sqrt{R_0^2 - y_0^2} \sin^2 \beta \right]$$

since $y_0 = (R_0 + H)$

$$L = (R_0 + H) \cos \beta - \sqrt{R_0^2 + H^2} \sin^2 \beta$$

This also allows the determination of the central angle ϕ and the incidence angle θ as functions of the scan angle β . Since

$$\theta = \beta + \phi$$

$$\text{Let } \gamma = 180 - \theta = 180 - (\beta + \phi)$$

The sine law gives

$$\begin{aligned} \frac{\sin \beta}{R_0} &= \frac{\sin \gamma}{R_0 + H} \\ &= \frac{\sin(\beta + \phi)}{R_0 + H} = \frac{\sin \beta \cos \phi + \cos \beta \sin \phi}{R_0 + H} \end{aligned}$$

or

$$\tan \beta = \frac{\sin \phi}{\frac{R_0 + H}{R_0} \cos \phi}$$

Attachment IV to Appendix XI

GROUND TRACK VELOCITY AND PERIOD

The gravitational attraction of the earth is

$$a_g = \frac{\gamma M}{R^2} \quad \gamma = 6.67 \times 10^{-11} \frac{\text{Newton-Meter}^2}{\text{Kilogram}^2}$$

$$M = 5.98 \times 10^{24} \text{ Kilograms}$$

$$R_o = 6.378 \times 10^6 \text{ Meters}$$

The centripetal acceleration is

$$a_r = R \omega^2$$

Equating the two

$$a_r = a_g$$

$$R \omega^2 = \frac{\gamma M}{R^2}$$

$$\omega = \frac{\gamma M}{R^3} = \frac{6.67 \times 10^{-11} \times 5.98 \times 10^{24}}{R^3}$$

For a 600 nautical mile high orbit (\approx 1112 kilometers)

$$\omega = \frac{39.86 \times 10^{13}}{(6378 + 1112)^3 \times 10^3} = \frac{39.9 \times 10^{13}}{42.0 \times 10^{19}}$$

$$= 95.3 \times 10^{-8} = 9.74 \times 10^{-4} \text{ rad/sec}$$

The ground track has a surface speed of

$$V_{GT} = R_o \omega = 6.371 \times 10^6 \times 9.77 \times 10^{-4} \text{ meters/sec}$$

$$= 62.0 \times 10^2 \text{ meters/sec}$$

$$V_{GT} = 3.34 \text{ NM/Sec}$$

The period T of the orbit

$$T = \frac{2\pi}{9.77 \times 10^{-4}} = 6.43 \times 10^3 \text{ sec}$$

$$T = 107.4 \text{ minutes}$$

Earth rotation rate

$$\omega_E = \frac{2\pi}{24 \times 60} = 4.37 \times 10^{-3} \text{ rad/minute}$$

Earth rotation/period of orbit

$$\begin{aligned} \phi &= T \omega_E = 1.075 \times 10^2 \times 4.37 \times 10^{-3} \\ &= .470 \text{ radians} = 27.0^\circ \end{aligned}$$

Attachment V to Appendix XI

MAXIMUM SCAN ANGLES

The tangent point for the largest scan angle β that just grazes the earth, can be obtained from the expressions in Attachment III, although it is much more easier done by considering the right triangle with sides R_o , $R_o + H$ and L . All we want to know is β

$$\sin \beta = \frac{R_o}{R_o + H} = \frac{6378}{6378 + 1112} = .852$$

$$\beta = 58.4^\circ \text{ for scanning of earth only.}$$

The other criteria for determining a maximum scan is to avoid scanning an area redundantly. Actually with a polar orbit and a fixed scan range it is obvious that the area close to the poles will be scanned many more times than the equatorial regions. It is thus impossible to have both non-redundant data and complete coverage under the present conditions.

In order to provide a complete coverage in the equatorial regions, we can provide a scan with a total width equal to the displacement of the orbit along the equator in one revolution of the satellite. This displacement is just the amount of the earth's rotation in one orbital period (if we neglect nodal regression). The earth central angle change per period is 27.0° (from Appendix IV).

$$\tan \beta = \frac{\sin \left(\frac{27^\circ}{2} \right)}{\frac{R_o + H}{R_o}} \cos \left(\frac{27^\circ}{2} \right)$$

$$= \frac{.2334}{\frac{7490}{6378} \cdot .972} = 1.154$$

$$\beta = 49.1^\circ \text{ for total coverage at the equator.}$$

Appendix XII

BEAM EFFICIENCY OF A SCANNING PLANAR ARRAY ANTENNA

1.0 INTRODUCTION

The beam efficiency of an antenna, defined as the ratio of the power radiated into the main lobe to the total power radiated by the antenna, is an important parameter in any radiometric antenna system. It describes the degree of concentration of power in the main lobe and is useful in the determination of brightness temperature from antenna temperature measurements. The main beam is defined to be that part of the power pattern enclosed by the first null.

The beam efficiency is expressed as

$$\eta = \frac{\int_{\Omega_0} F(\theta, \phi) d\Omega}{\int_{4\pi} F(\theta, \phi) d\Omega} \quad (1)$$

where

$F(\theta, \phi)$ = relative antenna power pattern

$d\Omega$ = incremental solid angle = $\sin \theta d\theta d\phi$

Ω = main beam solid angle

The assumption is made that the amplitude distribution of this rectangular array of radiators is such that $F(\theta, \phi)$ is separable. Also, the relative antenna power pattern, $F(\theta, \phi)$ will be assumed to be transformable into a new coordinate system; the two new variables being the directional angle α_x and α_y as shown in Figure 1. The antenna power pattern can then be expressed as:

$$F(\alpha_x, \alpha_y) = F_x(\alpha_x, \alpha_y) F_y(\alpha_x, \alpha_y) \quad (2)$$

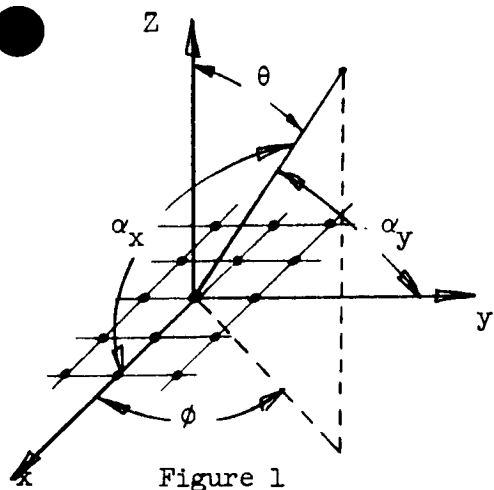


Figure 1
System Coordinates

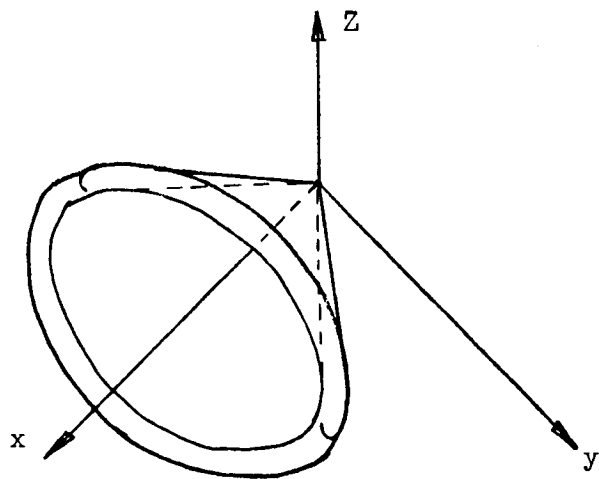


Figure 2a Main beam pattern of linear array of isotropic radiators laid along x axis

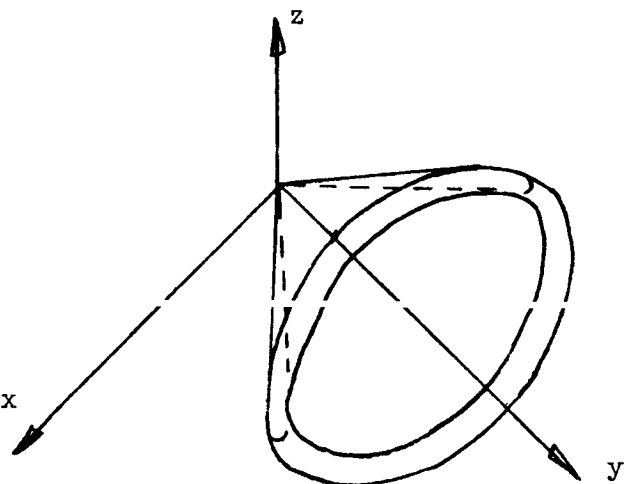


Figure 2b Main beam pattern of linear array of isotropic radiators laid along y axis

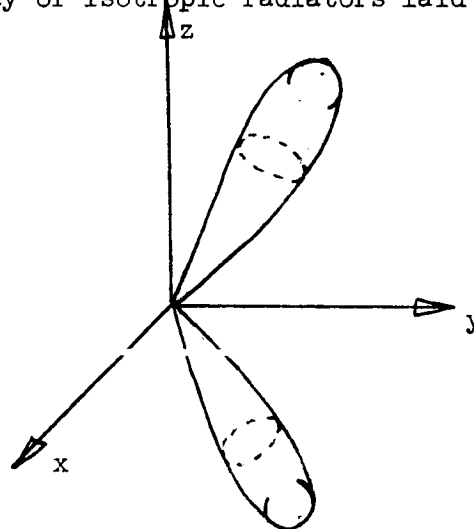


Figure 2c Main beam pattern of planar array

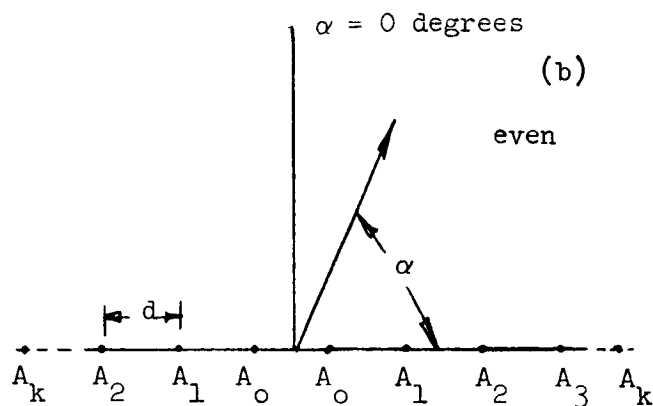
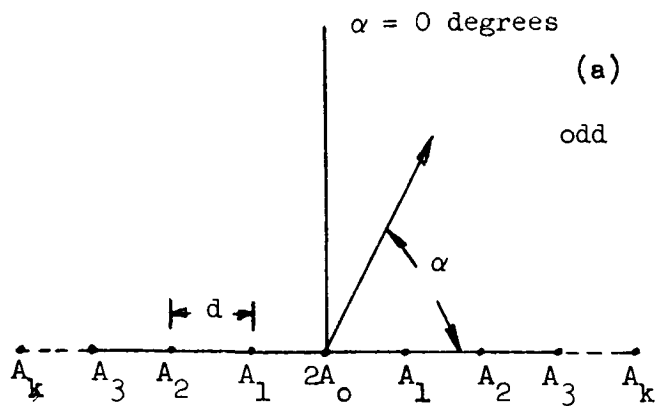


Figure 3

Linear broadside array of isotropic radiators with uniform spacing

The reason for the transformation to this new coordinate system is that for many antennas and particularly for the antenna system of concern, both F_x and F_y will be known as a function of α_x and α_y .

As a result of pattern multiplication the power pattern of the planar array will be a product of the power patterns of two linear arrays, one laid along the x-axis and the other along the y-axis. The power pattern of the linear array laid along the y-axis we call $F_y(\alpha_x, \alpha_y)$, and the power pattern of the array laid along the x-axis $F_x(\alpha_x, \alpha_y)$. The planar array can now be described in terms of these two linear arrays.

The main lobe of F_x in three dimensional space consists of a hollowed cone with cone angle equal to α_{x0} , the beam pointing angle. The power pattern of F_x , if entirely symmetric about the x-axis, will be independent of α_y . The main lobe of F_y is similar to that of F_x , with the exception that its symmetry is about the y-axis. The main lobes of F_x and F_y are shown in Figures 2a and 2b. The intersection of these two cones give rise to two pencil beams, one pointing into the $z > 0$ space, the other in the $z < 0$ space (Figure 2c). These two pencil beams are then, the main lobes of the planar array. We consider only the beam and its associated sidelobes in the $z > 0$ space since utilization of a ground plane will surpress any power from radiating into the $z < 0$ space.

The beam efficiency, η , can now be expressed as

$$\eta = \frac{\iint_{\Omega_0} F_x(\alpha_x, \alpha_{x0}) F_y(\alpha_y, \alpha_{y0}) d\Omega}{\iint_{2\pi} F_x(\alpha_x, \alpha_{x0}) F_y(\alpha_y, \alpha_{y0}) d\Omega} \quad (3)$$

where α_{x0} = beam pointing angle of F_x

α_{y0} = beam pointing angle of F_y

The direction of the pencil beam, and also the orientation of the entire power pattern of the planar array is then dependent on the beam pointing angles, α_{x0} and α_{y0} . Let us see now how these angles are incorporated in both F_x and F_y .

The far-field due to a linear array of isotropic radiators with symmetric amplitude distribution can be written as¹.

$$E = 2 \sum_{k=0}^{k=(N-1)/2} A_k \cos \left(2k \frac{\psi}{2} \right) \quad \text{for } N \text{ odd} \quad (4)$$

$$E = 2 \sum_{k=0}^{k=\frac{n}{2}} A_k \cos \left(\frac{2k+1}{2} \psi \right) \quad \text{for } N \text{ even} \quad (5)$$

where

N = number of radiators

A_k = amplitude of the k^{th} radiator

$$\psi = \frac{2\pi d}{\lambda} \cos \alpha + \gamma$$

γ = phase shift between radiators

Figure 3 shows the coordinate configuration for both the even and odd case. The phase shift γ will determine how far the main beam is shifted off broadside for a linear array of isotropic radiators. From equation 4 and 5, we see that the maximum value of the far field will exist at an angle, α_o , such that ψ becomes identically equal to zero.

$$\frac{2\pi d}{\lambda} \cos \alpha_o + \gamma = 0 \quad (6)$$

and

$$\gamma = -\frac{2\pi d}{\lambda} \cos \alpha_o \quad (7)$$

where α_o = the beam pointing angle of the linear array

$$\text{therefore } \psi = \frac{2\pi d}{\lambda} (\cos \alpha - \cos \alpha_o) \quad (8)$$

For a broadside array, α_o is equal to 90 degrees. It would be more convenient at this time to make a change of variables and consider

$$\alpha' = \frac{\pi}{2} - \alpha \quad (9)$$

then

$$\psi = \frac{2\pi d}{\lambda} (\sin \alpha' - \sin \alpha_o') \quad (10)$$

Now, for a broadside array, α_o' is equal to zero degrees and the far field pattern is symmetric about this point. In the remainder of this discussion, the primes on the variables will be dropped, and the new variables referred to as α and α_o .

The beam efficiency can then be expressed as

$$\eta = \frac{\iint \Omega_o F_x (\sin \alpha_x - \sin \alpha_{xo}) F_y (\sin \alpha_y - \sin \alpha_{yo}) d\Omega}{\iint 2\pi F_x (\sin \alpha_x - \sin \alpha_{xo}) F_y (\sin \alpha_y - \sin \alpha_{yo}) d\Omega} \quad (11)$$

2.0 EVALUATION OF THE BEAM EFFICIENCY

In order to evaluate equation 11, $d\Omega$ must be expressed in the α_x, α_y coordinate system. In the spherical coordinate system $d\Omega$ is equal to $\sin \theta d\theta d\phi$. The transformation from the θ, ϕ system can be accomplished by using the Jacobian, defined as the determinant

$$J(\alpha_x, \alpha_y) = \begin{vmatrix} \frac{\partial f}{\partial \alpha_x} & \frac{\partial f}{\partial \alpha_y} \\ \frac{\partial g}{\partial \alpha_x} & \frac{\partial g}{\partial \alpha_y} \end{vmatrix} \quad (12)$$

where

$$\theta = f(\alpha_x, \alpha_y)$$

$$\phi = g(\alpha_x, \alpha_y)$$

The incremental solid angle can be expressed as

$$d\Omega = \sin \theta \left| J(\alpha_x, \alpha_y) \right| d\alpha_x d\alpha_y \quad (13)$$

The Jacobian is derived in the Appendix and from the results obtained there, we have

$$d\Omega = \frac{\cos \alpha_x \cos \alpha_y}{(1 - \sin^2 \alpha_x - \sin^2 \alpha_y)^{1/2}} \quad (14)$$

The power pattern of the planar array will only be defined in the region bordered by lines connecting the $-\frac{\pi}{2}$ and $\frac{\pi}{2}$ intercepts on both axes of the α_x and α_y plane as shown in Figure 4. Assuming a unit radius, each point in this region corresponds to a point on a unit hemisphere symmetric about the origin. The region is divided into several sectors and each sector given an appropriate number as shown in Figure 4. The integration to obtain the total radiated power can be separated into 9 integrals which are evaluated in the respective sectors previously defined. The integral evaluated in sector 1 is defined as $I(1)$, the integral evaluated in sector 2, $I(2)$ and so forth.

The total radiated power can then be expressed as

$$W_t = \sum_{k=1}^9 II(k) \quad (15)$$

the power in the main beam as

$$W_{mb} = I(5) \quad (16)$$

$$W_{sl} = W_t - W_{mb} \quad (17)$$

The power pattern in sectors 6, 7, 8, and 9 can be thought of as being products of the sidelobe power patterns of two linear arrays, one laid out along the x-axis, and the other along the y-axis. For low sidelobe antennas, the integrals evaluated in these sectors will be small compared to the sidelobe power contained in sectors 1, 2, 3, and 4, and in fact, are assumed negligible. In the appendix an attempt is made to show that under certain conditions this assumption is quite valid.

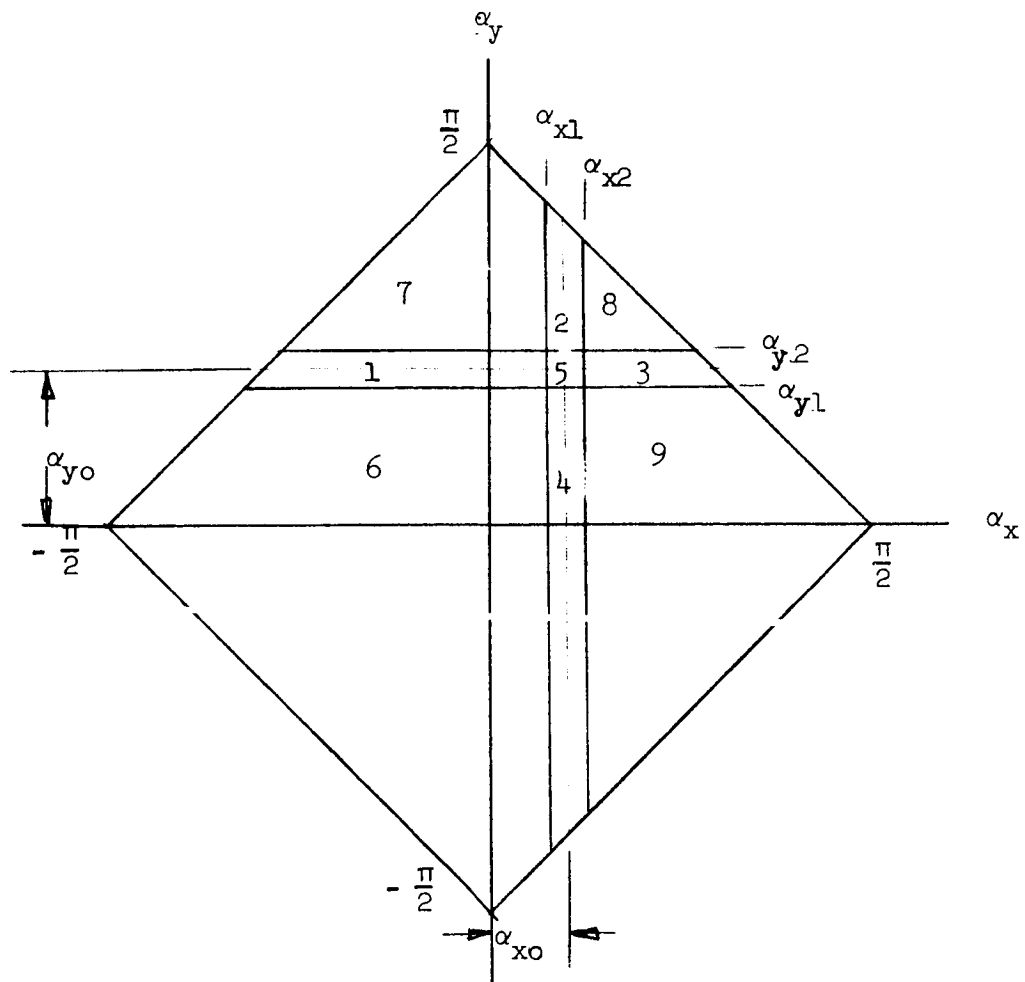


Figure 4

α_x α_y Plane

then

$$W_{mb} = I(5) = \int_{\alpha_{y1}}^{\alpha_{y2}} \int_{\alpha_{x1}}^{\alpha_{x2}} \left[\frac{F_x (\sin \alpha_x - \sin \alpha_{x0}) F_y (\sin \alpha_y - \sin \alpha_{y0}) \cos \alpha_x \cos \alpha_y}{(1 - \sin^2 \alpha_x - \sin^2 \alpha_y)^{1/2}} \right] d\alpha_x d\alpha_y \quad (18)$$

In order to shorten the notation we express the function enclosed by the brackets as F_{xy} , and so

$$W_{mb} = \int_{\alpha_{y1}}^{\alpha_{y2}} \int_{\alpha_{x1}}^{\alpha_{x2}} F_{xy} d\alpha_x d\alpha_y \quad (19)$$

where α_{y1} , α_{y2} , α_{x1} , α_{x2} are null positions as shown in Figure 4. For a broadside beam, of course,

$$\alpha_{y1} = \alpha_{y2}$$

and

$$\alpha_{x1} = \alpha_{x2}$$

The power in the sidelobes is then

$$W_{sl} = \sum_{k=1}^4 I(k) = \int_{\alpha_{y1}}^{\alpha_{y2}} \int_{-\frac{\pi}{2} + \alpha_y}^{\alpha_{x1}} F_{xy} d\alpha_x d\alpha_y + \int_{\alpha_{x1}}^{\alpha_{x2}} \int_{\frac{\pi}{2} - \alpha_x}^{\alpha_{y2}} F_{xy} d\alpha_x d\alpha_y + \int_{\alpha_{y1}}^{\alpha_{y2}} \int_{\frac{\pi}{2} - \alpha_y}^{\alpha_{x2}} F_{xy} d\alpha_x d\alpha_y + \int_{\alpha_{x1}}^{\alpha_{x2}} \int_{\frac{\pi}{2} + \alpha_x}^{\alpha_{y1}} F_{xy} d\alpha_x d\alpha_y \quad (20)$$

and therefore

$$\eta = \frac{W_{mb}}{W_{mb} + W_{sl}} = \frac{I(5)}{\sum_{k=1}^5 I(k)} \quad (21)$$

3.0 BROASIDE APPROXIMATION

The determination of equation (2) may require the evaluation of several complicated integrals, the complexity of which, of course, would depend on the complexity of the power pattern. It is the purpose of this portion of the discussion to approximate those integrals under certain assumed conditions. A broadside, narrow beamwidth, low sidelobe planar array will be assumed. Under these assumptions then,

$$d\Omega \approx 1 \quad -\alpha_{x1} \leq \alpha_x \leq \alpha_{x1}$$

$$d\Omega \approx 1 \quad -\alpha_{y1} \leq \alpha_y \leq \alpha_{y1}$$

and

$$W_{mb} = I(5) = \int_{-\alpha_{x1}}^{\alpha_{x1}} F_x d\alpha_x \int_{-\alpha_{y1}}^{\alpha_{y1}} F_y d\alpha_y \quad (22)$$

and

$$W_{sl} = \sum_{k=1}^4 I(k) = 2 \int_{-\alpha_{y1}}^{\alpha_{y1}} F_y d\alpha_y \int_{\alpha_{x1}}^{\frac{\pi}{2}} F_x d\alpha_x + 2 \int_{-\alpha_{x1}}^{\alpha_{x1}} F_x d\alpha_x \int_{\alpha_{y1}}^{\frac{\pi}{2}} F_y d\alpha_y \quad (23)$$

and

$$\eta = \frac{W_{mb}}{W_{sl} + W_{mb}} \quad (24)$$

The approximations have now reduced a set of double integrals to several much simpler products of single area integrals. Thus, by knowing the area under the power patterns in both planes the beam efficiency can be easily computed.

4.0 SUMMARY

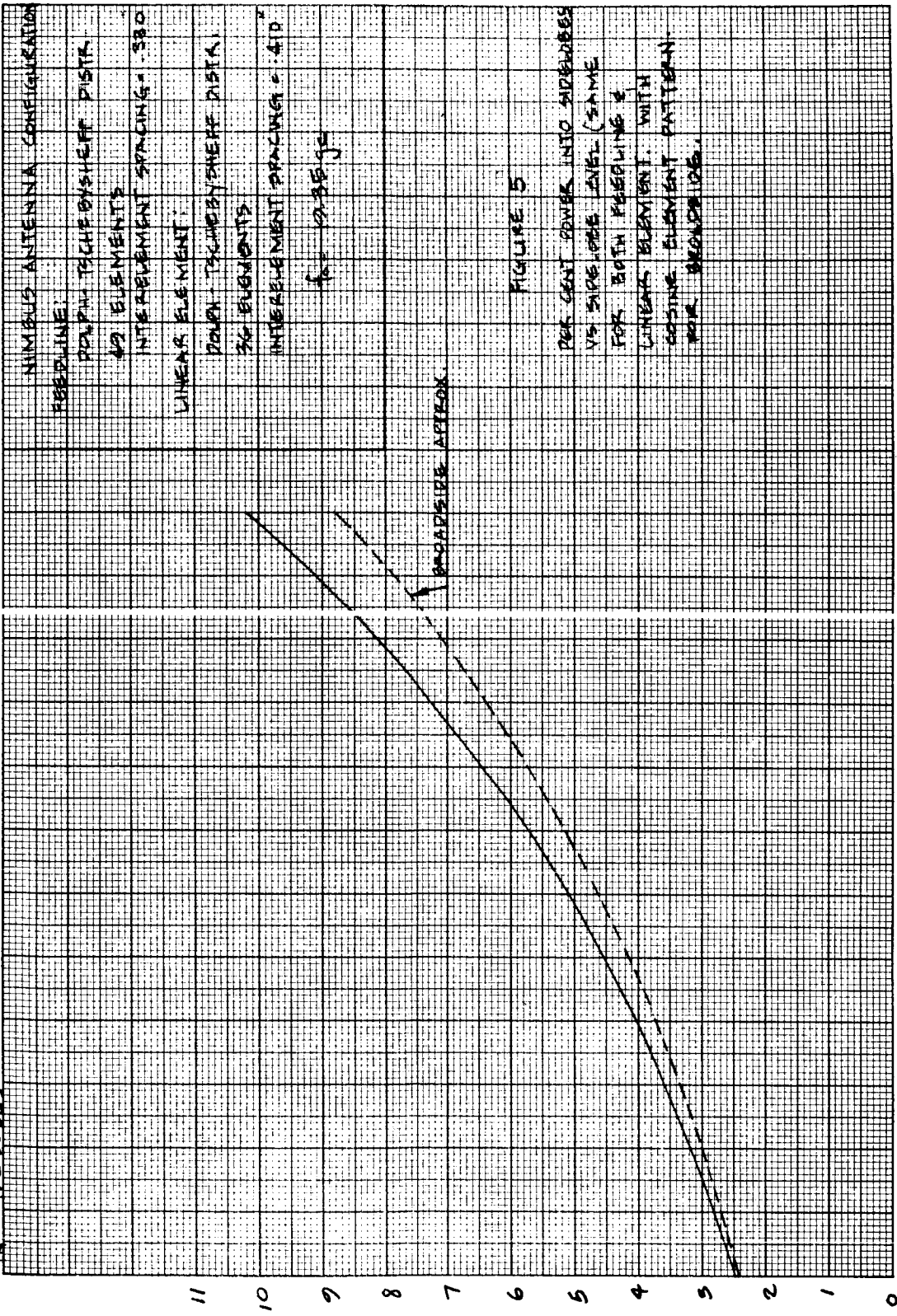
The beam efficiency was computed for a specific antenna configuration. This was the proposed 50 degree scan Nimbus radiometer. The amplitude distribution was Dolph-Tschebysheff in both planes, the element field pattern of the individual slots cosinusoidal, and the interelement spacing .330 inches for the feed line and .410 inches for the linear elements. The two parameters that were varied were the sidelobe level in both the feedline and linear element, and the scan angle in the plane of the feedline. The results are graphical shown in Figures 5 to 9.

In Figure 5 the sidelobe levels in both planes were equal and varied from 31 to 25 dB. Both equation 21 and the broadside approximation was used and a comparison made between them. The approximation was quite good for high sidelobe levels but deteriorated as the sidelobes were raised.

In Figure 6, 7, 8 and 9, the sidelobe level in the linear element was kept constant and the sidelobe level of the feed line varied for several values of scan angle. As the angle of scan is increased a greater percentage of the power is radiated into the sidelobes. This increase in relative sidelobe power is mainly due to the directive element pattern which decreases the peak value of the main beam as it is scanned off broadside.

All computations were made on the SGC 7040 computer.

PER CENT POWER IN SIDE LOBES

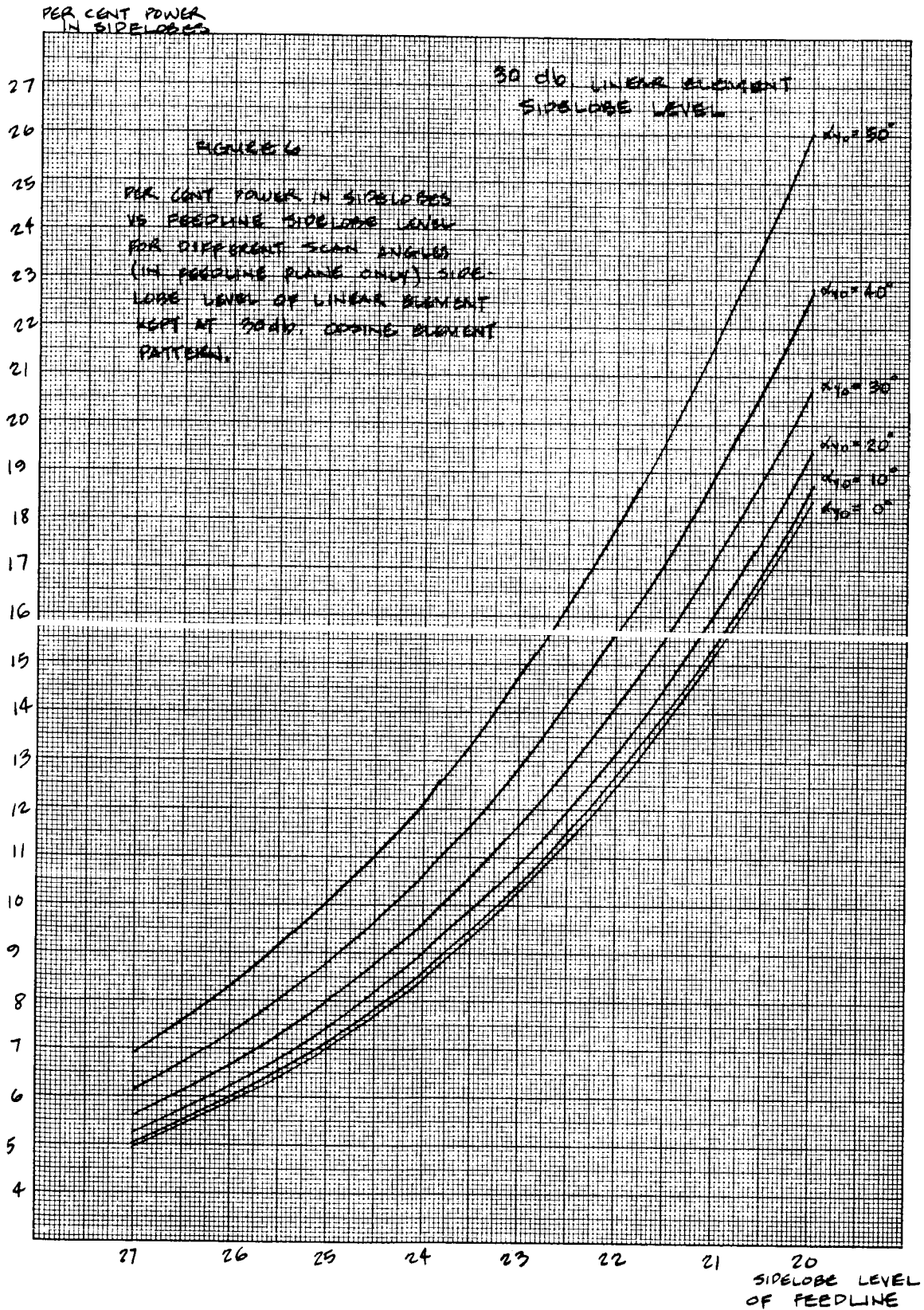


NIMBUS ANTENNA CONFIGURATION
 REEPLINE:
 PARABOLIC BY SHEFF DISTA
 49 ELEMENTS
 INTERELEMENT SPACING = .380
 LINEAR ELEMENT:
 PARABOLIC BY SHEFF DISTA
 30 ELEMENTS
 INTERELEMENT SPACING = .410
 for change

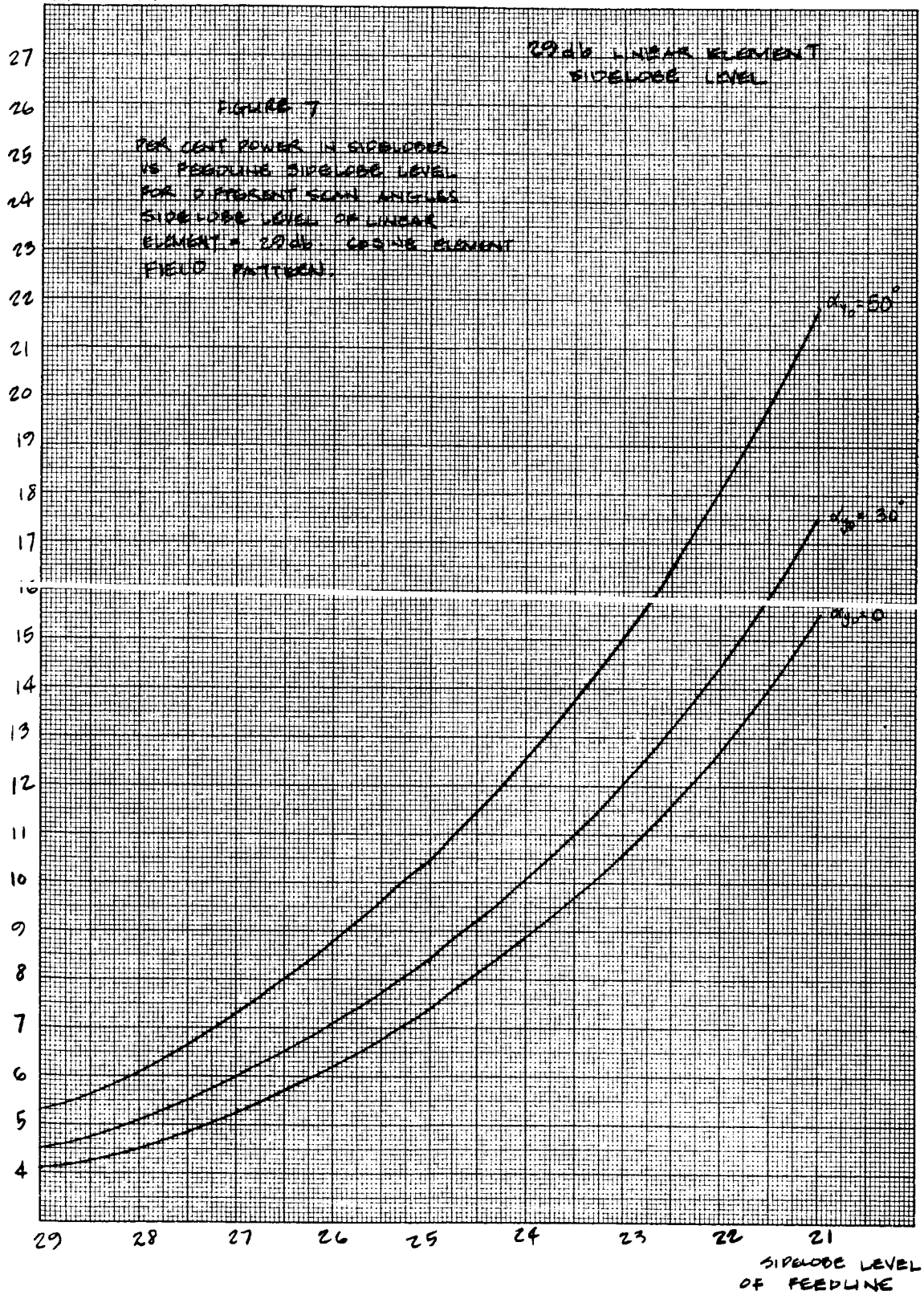
FIGURE 5

PER CENT POWER INTO SIDELOBES
 VS. SIDE LOBE LEVEL (SAME
 FOR BOTH REEPLINE &
 LINEAR ELEMENT WITH
 COSINE ELEMENT PATTERN
 FOR PARABOLIC)

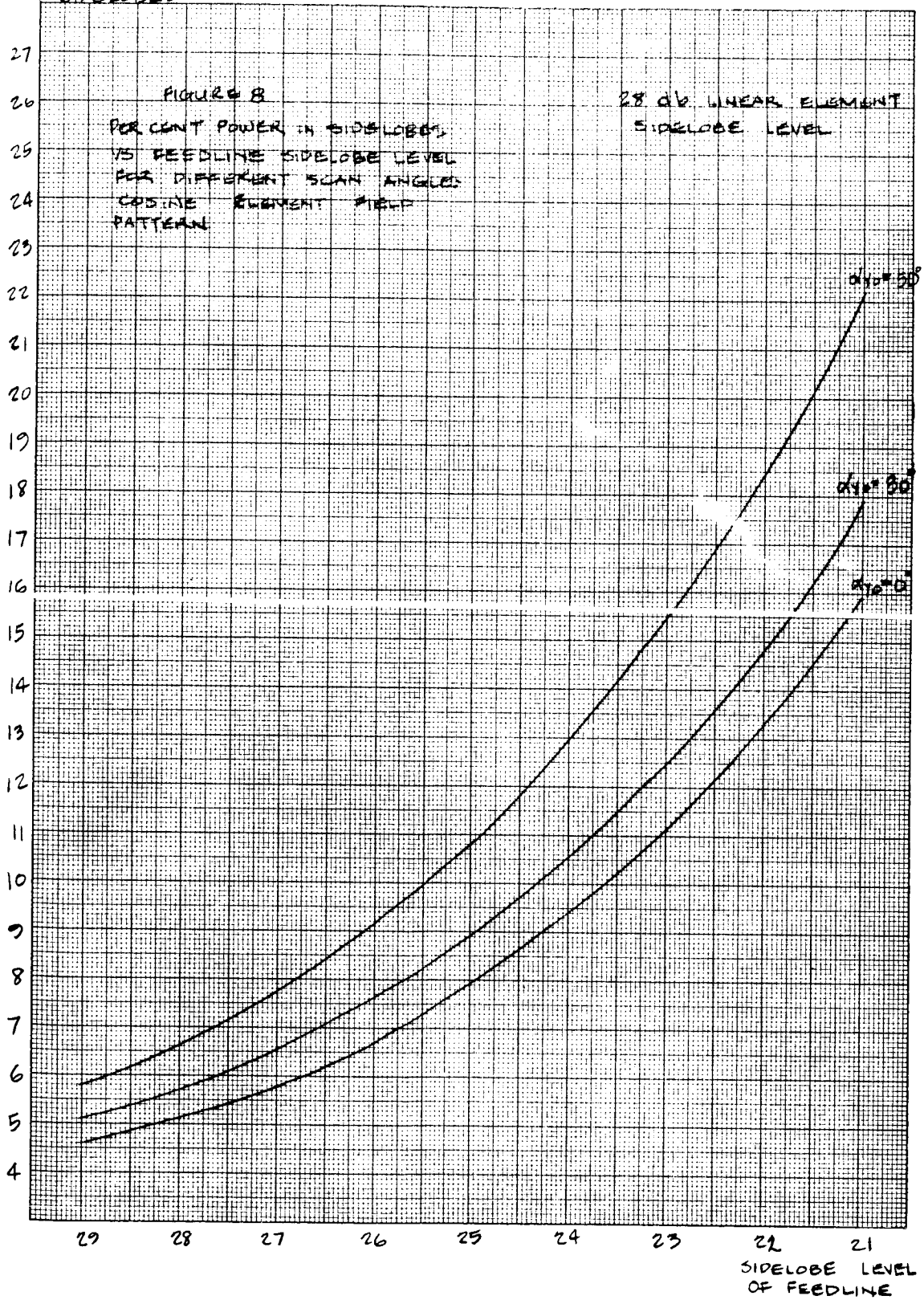
SIDE LOBE LEVEL
 DEIBELS



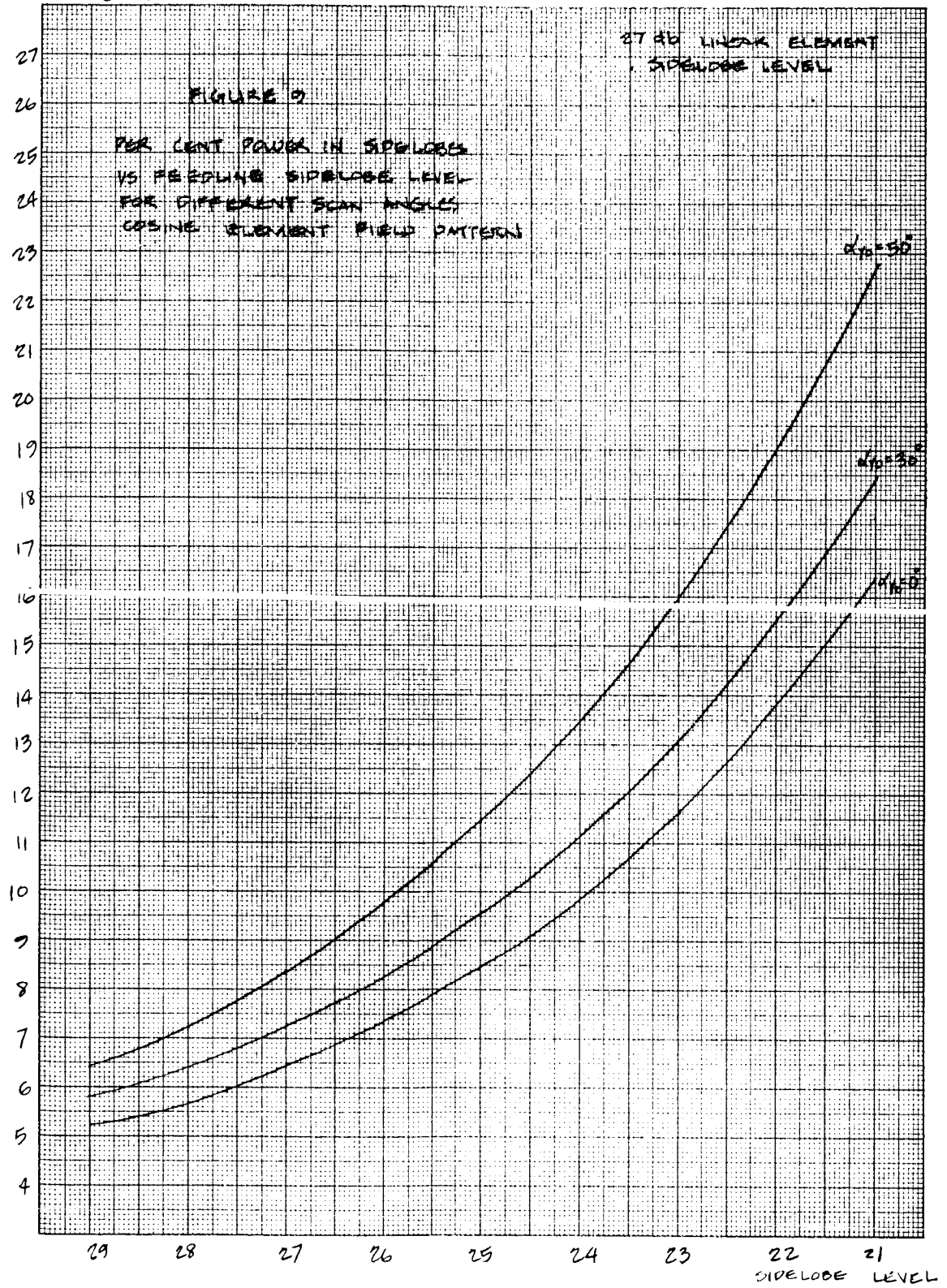
PER CENT POWER
IN SIDELOBES



PER CENT POWER
IN SIDELOBES



PER CENT POWER
IN SIDELOBES



REFERENCES

1. John D. Kraus, Antennas, McGraw-Hill, Inc., New York, 1950, pp 97-100.
2. Angus Taylor, Advanced Calculus, Ginn and Company, New York, 1955.

Appendix XIII

CONTINUOUS ONE-PIECE WAVEGUIDE FLANGE FOR THE NIMBUS ANTENNA

Because of the small separation between ports along the feedline of the Nimbus Antenna, the connection from feed port to phase shifter and from phase shifter to the linear array elements could not be made using standard waveguide flanges. A new flange configuration had to therefore be specified. Two basic configurations were suggested. The first was a narrower version of the standard waveguide flange, with two bolting holes instead of the standard four, as shown in Figure 1. In a 49 element array a total of 196 of these flanges would be required. The second flange configuration suggested was a continuous one-piece type made from a rectangular cylinder with 49 rectangular holes. The two waveguide ends to be connected together would be placed in each hole, butted together, and held in place by a conducting epoxy as shown in Figure 2. Only two of these one-piece flanges would be needed in a single planar array. One to connect the waveguide feed ports to the phase shifters, the other to connect the phase shifters to the linear array elements.

From a mechanical viewpoint, the one-piece type flange was obviously the better of the two configurations. First of all the simplicity of its design made fabrication much easier. Only two pieces would be needed as opposed to 196 pieces for the single flange case. No bolts and nuts would be required. The assembly and alignment of the planar array could be accomplished with less effort and with greater accuracy using this type flange. The one-piece flange could also be used as part of the support structure of the array, thereby reducing somewhat the weight of the total package.

Before agreeing on the use of the one-piece type flange on the Nimbus Antenna, it was necessary to demonstrate in the laboratory first that the amount of deterioration, if any, on the transmission of energy through a flange of this type was tolerable. The two parameters measured were the return loss (VSWR) and insertion loss of a junction of this kind in comparison with that of a standard

flange. The gap spacing between waveguide ends was varied from 0.000 to 0.070 inches. The results are graphically shown in Figures 3 and 4. The VSWR with the waveguide ends butted against each other is about 1.05 and insertion loss about .12 dB, which is as good as one would expect from a narrow-type single flange, and is within the tolerable range with respect to the total package requirements. Considering both the electrical and mechanical characteristics, it was then obvious that the continuous one-piece flange was the better type for use in the Nimbus planar array antenna.

NOT TO SCALE

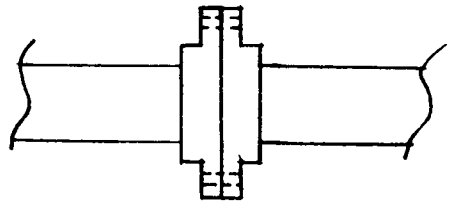
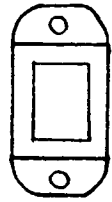


Figure 1. Single Flange Configuration

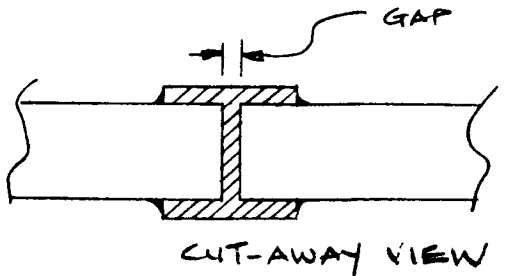
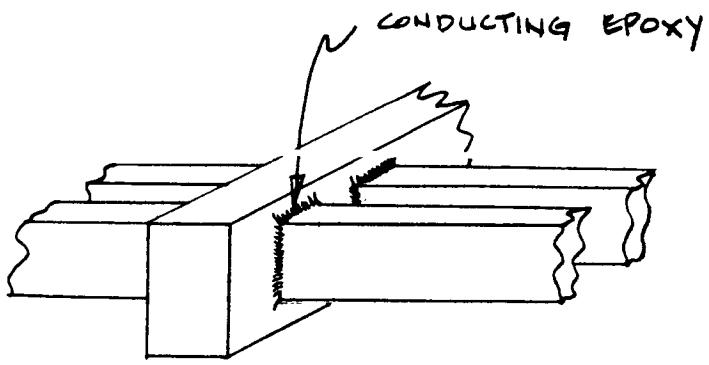
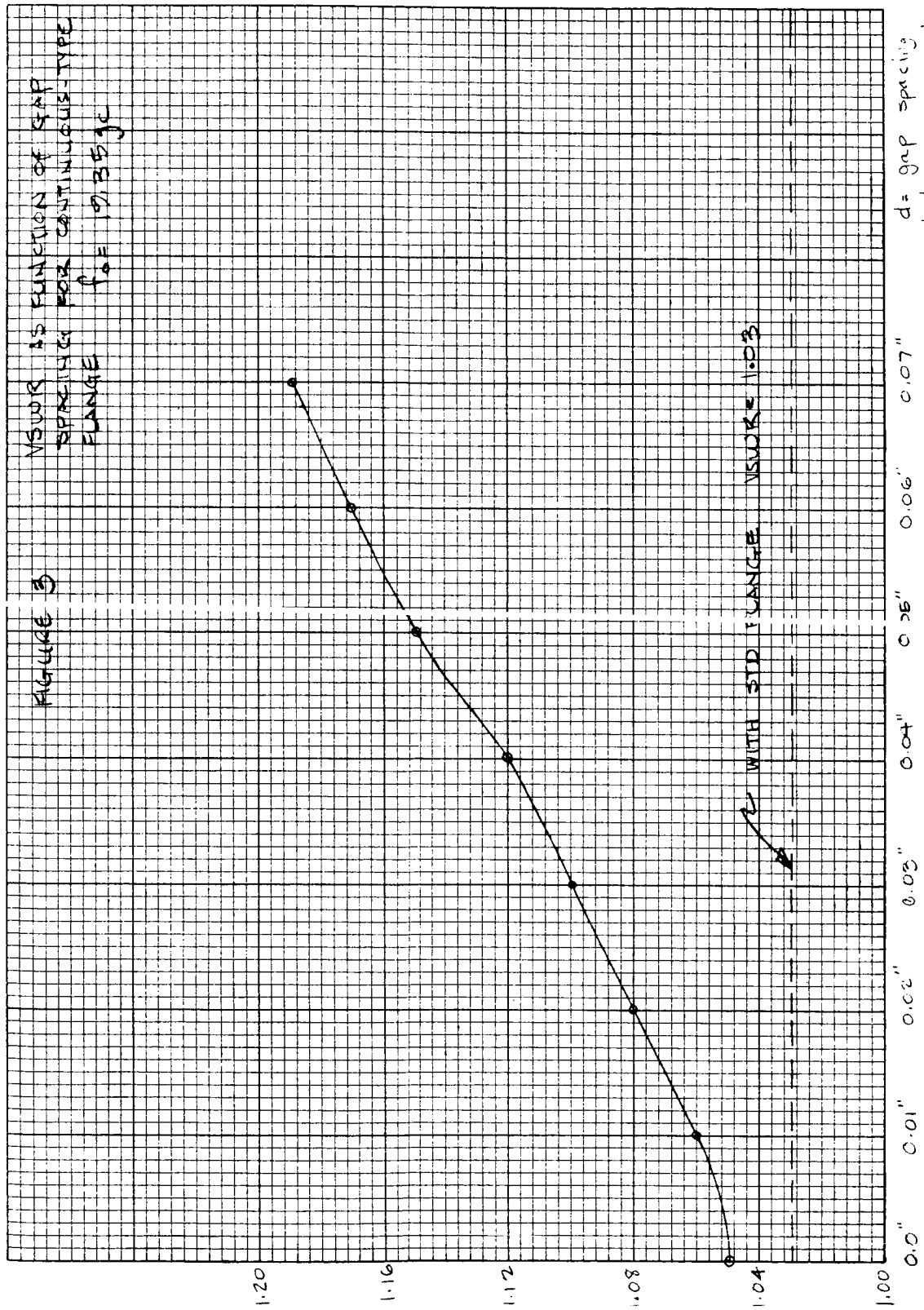


Figure 2. Continuous One Piece Configuration

15WR



Insertion Loss (db)

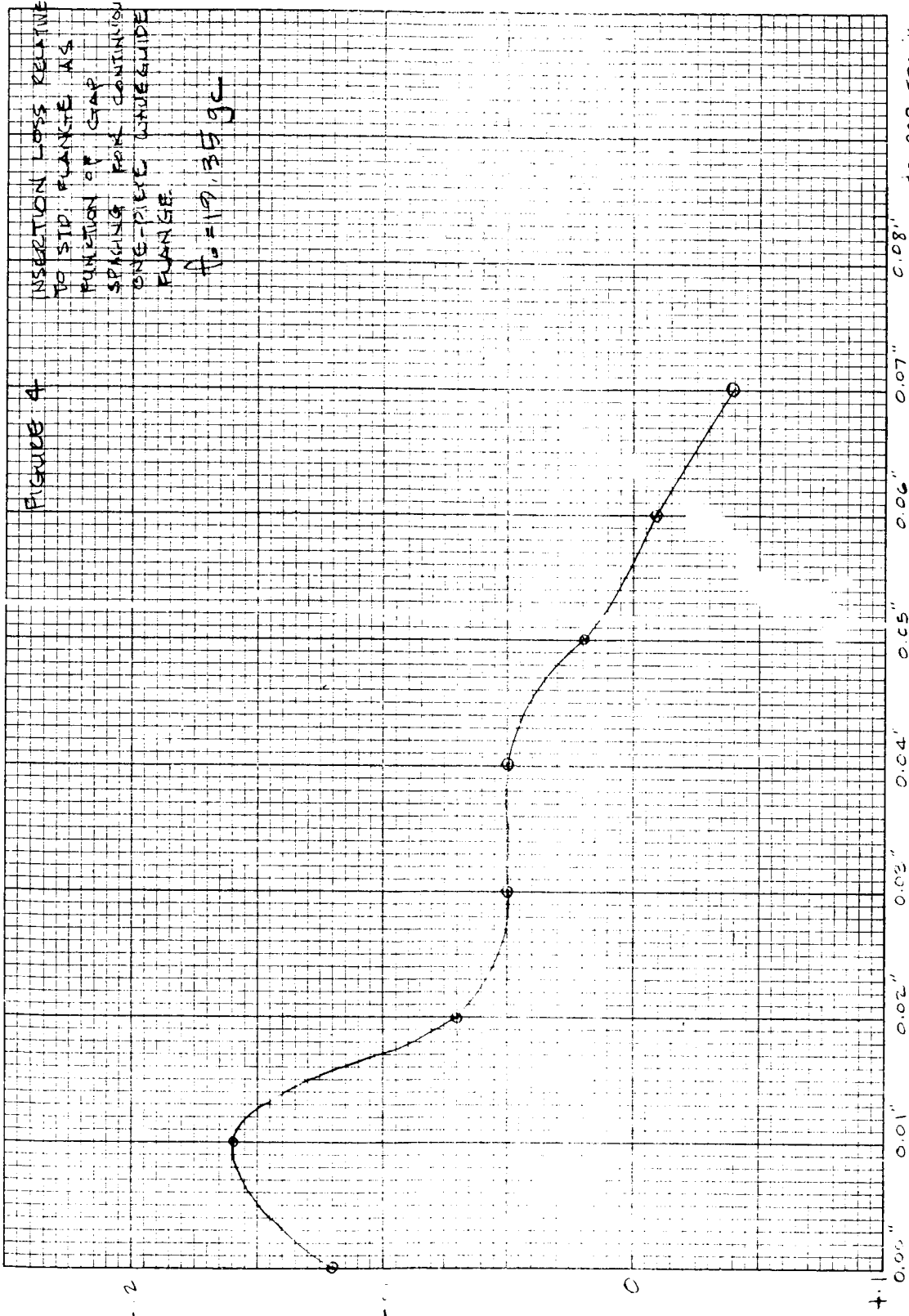


FIGURE 4

INSERTION LOSS RELATIVE
TO STD. FLANGE AS
FUNCTION OF GAP
SPACING FOR CONTINUOUS
ONE-PIECE WAVEGUIDE
FLANGE.

$$f_0 = 11.9, 3.5 \text{ gc}$$

d = gap spacing
between waveguide ends

Appendix XIV

PHASE SHIFTER DRIVE/BIAS COIL, FUNDAMENTAL DESIGN

Essential Coil parameters are as follows:

	<u>Drive Coil</u>	<u>Bias Coil</u>
Wire Size	No. 39	No. 35
No. of Layers	12	5
No. of Turns	5736	1480
Resistance (ohms)	711	66
Inductance (mh)	76.8	3.7
L/R (μ s)	108	56.3

These coils give rise to the following drive/bias circuit parameters:

Average Current in Drive Coil	4.36 ma
Total Array Avg. Drive Current	214 ma
Max. Voltage Across Drive Coil	6.93 volts
Bias Coil Current	33.8 ma
Voltage Drop Across Bias Coil	2.23 ma
Bias Coil Configuration	5 rows of 10 coils each
Total Bias Power	4.18 watts
Total Drive Power	5.23 watts
Total Array Power	9.41 watts

Appendix XV

AN ELECTRONICALLY-SCANNED K-BAND PHASED ARRAY FOR SPACE-BORNE RADIOMETRIC APPLICATIONS

SUMMARY

The development of a small, lightweight electronically-scanned passive phased array suitable for use in space-borne systems is considered. Conventional edge-slotted linear elements are assembled into a planar array, the beam of which is scanned in one plane by Reggia-Spencer type ferrite phase shifting elements.

A brief discussion of array theory as it applies to the problem is presented. Emphasis, however, is given to the practical aspects of achieving the high beam efficiency required in radiometric applications.

INTRODUCTION

Included among the possible experiments to be conducted in the near future on the Nimbus meteorological satellite system is one which is devoted to microwave radiometry. A two-dimensional radiometric map of the brightness temperature of the earth is to be generated by inertialessly scanning the beam of the radiometer antenna in the plane orthogonal to the direction of vehicular motion. The motion of the vehicle itself provides the scan capability in the second orthogonal plane. This paper is devoted to a discussion of the development of the antenna subsystem that is to be used in this K-band radiometric sensor.

In the radiometric applications, as in radio telescoping, the beam efficiency of the antenna, i. e., the ratio of the power radiated within the main beam to the total power radiated, is quite important. Power contained in side and back lobes can substantially reduce the absolute accuracy of the temperature measurement. Because of this, a more stringent control of

side and back radiation is required. In lieu of limiting the peak side and back lobes to some specified level, as is done in most radar systems, radiometric applications require that the total power contained in the side and back lobes be less than some percentage of that contained in the main lobe, the percentage depending on the accuracy required in the measurements to be made. Emphasis will be given herein to the practical aspects of achieving the high beam efficiency that is required.

A summary of system performance requirements will be presented. This will be followed by a brief discussion of array theory as it applies to the problem and a detailed description of the antenna array configuration. Experimental results will be presented where appropriate.

DESIGN CONSIDERATIONS

System Performance Parameters

The antenna system is a 19.35 GHz two-dimensional phased-array. The main beam of this array is electrically-scanned in one dimension over an angle of ± 50 degrees relative to the array nadir. Scanning is effected in the direction perpendicular to the direction of vehicular motion and between the specified limits is accomplished in 39 incremental steps. Crossover points between adjacent beam positions occur at approximately the half-power beam width level.

Between ± 30 degrees relative to the array normal the half-power beamwidth of the main lobe is less than three degrees. Over the full scan range it is less than four degrees. The total power, including cross-polarized power, received by the side and back lobes over the full scan range is less than 18 percent of that received by the main lobe; between ± 30 degrees it is less than eight percent.

Maximum loss in the antenna, exclusive of the reduction in gain that occurs as a result of the decrease in the effective aperture of the array as the beam is scanned from broadside, is less than 1.3 dB. This includes the loss in the phase shifting devices, waveguide walls, and array terminations.

The volume occupied by the array is approximately 18 x 18 x 3 inches. Weight of the array, including the phase shifting devices, is approximately seven pounds. The total power required to drive the phase shifting devices and to control the position of the main beam is approximately 9.5 watts.

General Approach

The antenna described here consists of a group of 49 parallel edge-slotted waveguide elements arranged to form a two-dimensional planar array as shown in Figure 1. Each linear array element contains 36 radiating slots. A ground plane, which cannot be seen in this figure, is located behind and external to the radiating slots to aid in both the reduction of mutual coupling and the suppression of cross-polarized energy, as well as to tie the array together mechanically. To reduce the weight of the array substantially, thin-wall aluminum waveguide (0.020 inch) of WR-42 internal dimensions (.170 x .420 inch) is used.

Both the phase and the amplitude distribution along the linear array elements, and hence also the radiation pattern, are readily controlled by proper spacing and angling of the slots in the elements. For reasons to be given later, a -35 dB Dolph-Tchebyscheff amplitude distribution is designed into these elements.

The planar ensemble of linear edge-slot array elements is fed by a similar edge-slot array in the manner indicated in Figure 1. However, in this application a Reggia-Spencer type ferrite phase shifting element is interposed at each junction at a linear element and the feed so that a differential phase bias can be introduced between the linear arrays. This differential phase shift is achieved by applying a variable magnetic field to the ferrite elements. Physical location of these phase shifting elements is in the region of the scale in Figure 1. At the time this photograph was taken, however, the control coils had not yet been assembled in place.

Although it is desirable that the beam of the linear array elements be broadside to the array, the use of resonant arrays presents several undesirable features. For example, the input standing wave ratio of this type

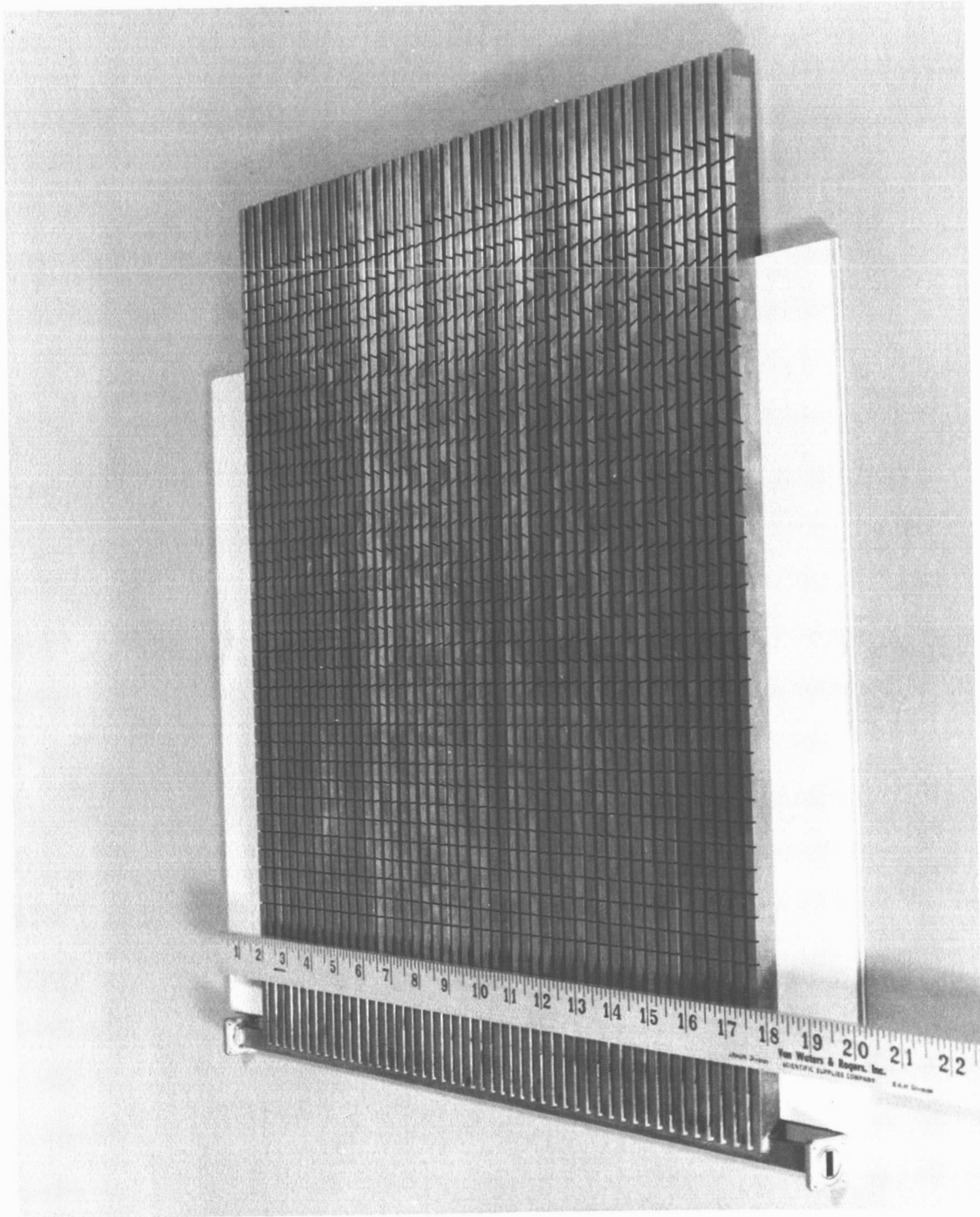


Figure 1. Two-Dimensional Edge-Slotted Electrical Scanned Array

array is quite high, approximately 3:1, resulting in an intolerable reflection loss of approximately 1.25 dB at the array input. In addition the resonant array is very frequency-sensitive, both the input impedance and the radiation pattern changing radically with frequency. A non-resonant array in which the beam is positioned within a few degrees of broadside was therefore designed. A small percentage of the input power, approximately three percent, must be wasted in a dummy load at the far end of the array, however. This gives rise to a loss of approximately 0.15 dB.

An additional loss that must be considered is the loss due to the finite conductivity of the waveguide walls. This is independent of the type array used. In aluminum WR-42 waveguide, this attenuation amounts to approximately 17 dB per 100 feet of waveguide. Silver plating the inside of the waveguide and/or increasing the size of the waveguide would both serve to lower the attenuation. The total reduction, however, is slight for the lengths used herein.

Beamwidth and Sidelobe Level

In general, the beamwidth and the gain of an array are dependent on several factors. Among these factors are: (1) the wavelength at the operating frequency, λ ; (2) the length of the array, L ; (3) the amplitude distribution across the array aperture; and (4) the squint angle of the beam, i. e., the position of the beam relative to the array normal. Although it is possible to compute a beam broadening factor that is dependent only on the array amplitude distribution, the other factors must all be considered simultaneously when the beamwidth of the array is computed. The sidelobe level, however, is determined primarily from the phase and amplitude distribution along the array.

Since the required amplitude distribution is dependent on the desired sidelobe level, it is necessary to translate the percent power contained in the side and back lobes into a maximum allowable peak sidelobe level. This can be accomplished through the process of pattern multiplication in which the total power pattern of the planar array is obtained by taking the product of the radiation patterns of the two orthogonal planes of the array. This multiplication can be separated into three groupings: (1) main beam

in one plane times the main beam in the orthogonal plane, (2) main beam in one plane times the sidelobes of the other and vice versa, and (3) sidelobes times sidelobes. The total radiated power in the main lobe is derived from the product of group 1, that in the sidelobes from the sum of the remaining three products. Fujioka¹ has shown, however, that if the average value of the power gain-beamwidth product (modified by the cosine of the beam pointing angle) in both planes is much greater than unity, then the contribution to the sidelobe power made by the product of the sidelobes in the two orthogonal planes is negligibly small and can be neglected. Such is the case for the array described here.

A computer program was generated to determine the beam efficiency, and hence also the power in the sidelobes, as a function of scan angle for the array considered herein. A Dolph-Tchebyscheff amplitude distribution was used in both planes. The element pattern of the individual slot radiators was assumed to be cosinusoidal. Computations of the percent energy in the side lobes were made for various assumed sidelobe levels in each of the two orthogonal planes and also as a function of the array scan angle.

Typical of the results that were achieved are those shown in Figure 2. The percent power contained in the side and back lobes is shown in the vertical axis as a function of feed-plane sidelobe level and scan angle. The assumed level of the sidelobes in the plane of the linear array elements is -30 dB. As an example of the interpretation of these curves, to limit the power in the sidelobes to 8 percent when the beam is scanned to either ± 30 degrees, the highest sidelobe in the feed plane cannot exceed -25 dB when the highest sidelobes in the linear array plane equal -30 dB. After having analyzed the radiation patterns of a large sampling of linear array elements, it appears that the assumed -30 dB level is a realistic and representative number. It should be noted that the level of the sidelobes indicated in these curves is that which occurs as a result of the combined effects of the designed amplitude distribution, mechanical tolerances, and mutual coupling.

The curves of Figure 2 serve only to aid in the setting of design goals. To allow for the deleterious effects of mechanical tolerances in

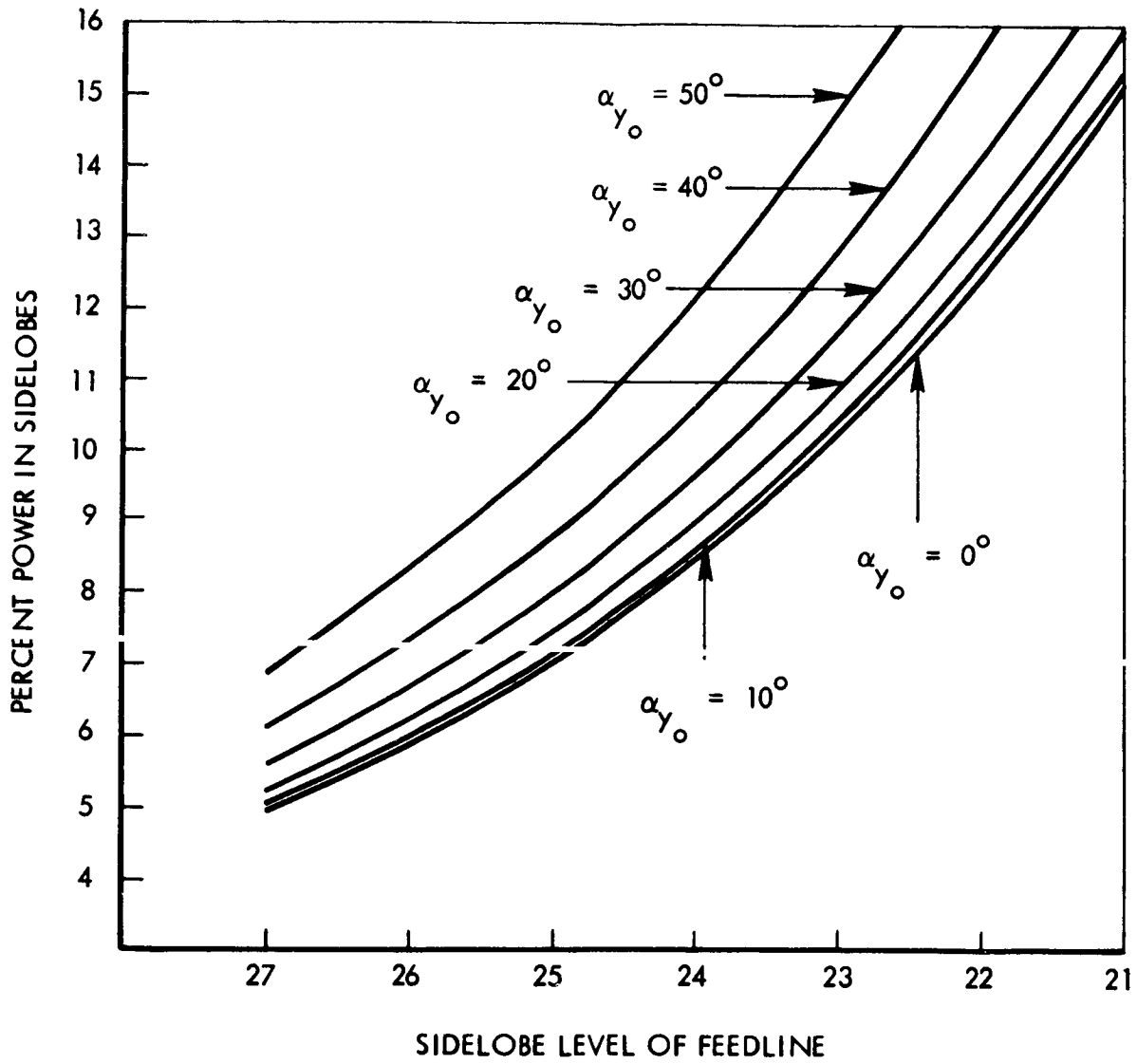


Figure 2. Beam Efficiency Versus Feed Plane Sidelobe Level and Scan Angle

the fabrication of the array and mutual coupling effects between elements of the array, an average sidelobe level of -35 dB has been designed into both the linear array elements and the feed element.

As mentioned above, both the beamwidth and the sidelobe level are dependent on the amplitude distribution across the array. A Dolph-Tchebyscheff amplitude distribution is used since it will produce the narrowest beamwidth for a given sidelobe level and vice versa. The effect of this distribution, or any tapering of the amplitude distribution from uniform, is to broaden the beamwidth of the main lobe. In addition, as the beam is scanned from broadside, there is a further increase in the beamwidth due to the reduction in the effective aperture of the array. Stegen² has derived an expression relating the beamwidth of the Tchebyscheff array to the sidelobe level and array length. This expression, modified to include the beam broadening factor for scanned arrays, is

$$\Theta = \frac{A \lambda}{L} \sec \theta \quad (1)$$

where Θ is the beamwidth in degrees, λ is the free-space wavelength, L is the length of the array, θ is the position of the main beam relative to broadside, and A is a factor dependent on the sidelobe level r . For $r = -35$ dB, $A = 65.0$ degrees.

Slot and Linear Element Spacing

To minimize the number of elements in the array, it is desirable that the spacing between elements be as large as possible. However as the spacing between elements is increased, a point is soon reached where grating lobes appear.

The required spacing to suppress grating lobes at any angle θ can be approximated from the expression

$$\frac{d}{\lambda} = \frac{1 - \frac{1}{N}}{1 + \sin \theta} \quad (2)$$

where d is the element or slot spacing, N is the number of elements, and θ is the scan angle. Since the required number of elements can be determined from

$$N = \frac{L}{d} + 1 \quad (3)$$

it is possible to substitute the latter equation into the former and determine the maximum allowable element spacing. The result is

$$d^2 + Ld - \frac{L \lambda}{1 + \sin \theta} = 0 \quad (4)$$

It should be mentioned in passing that thinning techniques normally used in large arrays to reduce the number of elements considerably are not applicable to the present configuration due to the beam scanning and low sidelobe requirements.

Amplitude Distribution

The required relative amplitude distribution for both the linear array element and the feed element can be determined from exact expressions developed by Stegen³. Typical of these distributions is that shown in Figure 3 for the 36-element linear array. Design sidelobe level is 35 dB for this Tchebyscheff distribution.

In the design of a slotted array antenna, it is quite important that the power radiated from each slot in the array be sufficiently predictable in order that a specific amplitude distribution can be designed into the array. Numerous measurements were therefore made by conventional means⁴ to determine slot coupling as a function of slot angle and wall thickness. Measurements were also made to determine the resonant length of these slots as a function of these same two parameters. Separate measurements had to be made for the linear array elements and the feed element.

Cross-Polarization and Mutual Coupling Reduction

In addition to its obvious mechanical value, the use of a conducting metallic plate to tie the various linear array elements together into a planar array assembly has several very important electrical advantages. For example, a properly-located ground plane can serve to enhance the directivity of the individual radiating slots, thereby tending to increase the gain of the planar array assembly and to reduce somewhat the mutual interaction or coupling between the individual slots. In addition it has been

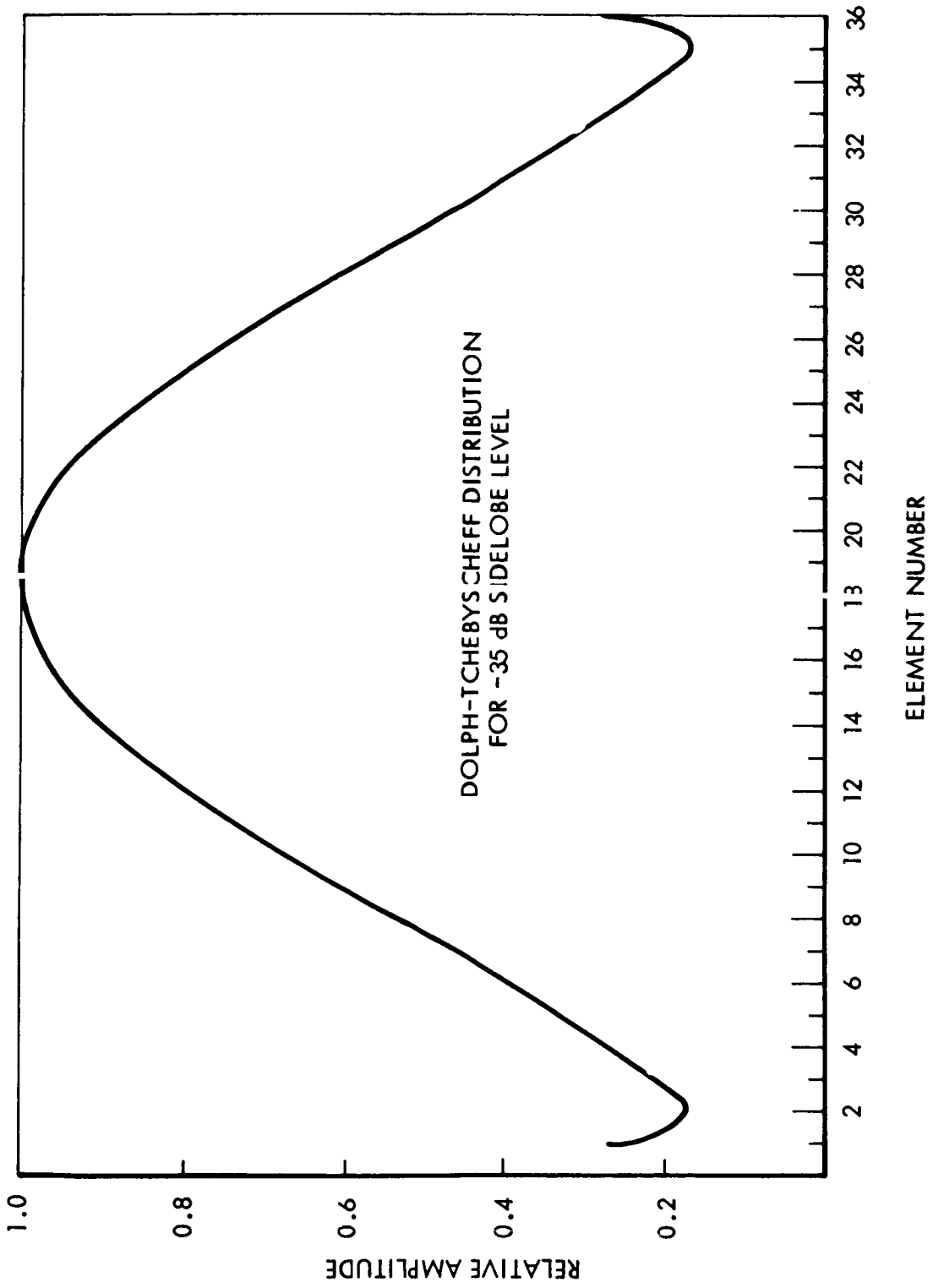


Figure 3. Relative Amplitude: Distribution for 36-Element Linear Array

demonstrated that such a ground plane can also serve as a choke-section to suppress the flow of currents associated with the cross-polarized fields of the edge-slotted array and thereby also suppress these fields. In suppressing or reducing these cross-polarized fields, the ground plane can also further reduce the mutual coupling between adjacent linear elements.

Measurements were made on an antenna pattern range to determine the degree of reduction that one can achieve in the cross-polarized field through the use of a properly-positioned ground plane. The reduction was substantial. With no ground plane, for example, the cross-polarized fields were only approximately 15 dB below the desired polarization. As one might expect, maximum suppression of all cross-polarized lobes in the plane of the linear array element was achieved when the ground plane was approximately a quarter wavelength behind the slot. The highest cross-polarized lobe was 21 dB below the desired polarization for this configuration. However, since, from a radiometric system standpoint, compensation can be made for the effects of cross polarized energy in the main beam, it is more desirable to suppress those cross-polarized lobes outside the main beam as much as possible and to accept whatever level occurs in the main beam. "Optimum" results were achieved with a depth of approximately 0.21λ . A 32 dB suppression of cross-polarized fields outside the main beam was achieved.

Because of its effectiveness in reducing both the mutual coupling between adjacent linear elements and the energy contained in undesired cross-polarized lobes, the ground plane represents the key element in the satisfaction of the system performance requirements.

Beam Steering and Phase Control

To steer the beam of a scanned antenna array, it is necessary to alter the effective phase distribution across the array aperture in a prescribed manner. In an edge-slotted array, for example, the phase distribution that is required along the array to position the beam at a given angle θ can be determined from the expression.

$$\sin \theta = \frac{\lambda}{\lambda_g} - \frac{\lambda}{2d} + \frac{\Delta\phi\lambda}{360d} \quad (5)$$

where λ and λ_g are the free-space and waveguide wavelengths respectively, d is the element spacing and $\Delta\phi$ is the phase difference introduced between adjacent apertures to scan the beam. It should be noted that the beam can be positioned to either side of the array normal by properly selecting the value of $\Delta\phi$. That is, if a leading or positive phase difference $\Delta\phi$ is used, $\sin \theta$ can be made positive and the beam will be positioned on one side of the array normal. Similarly, by using a negative or lagging phase difference $\Delta\phi$, $\sin \theta$ can be made negative and the beam will be positioned on the other side of the array normal.

For large beam steering angles and for long arrays, the required phase difference between the first element and the i th element will exceed 2π . However, physically, there is no difference between $\Delta\phi$ and $\Delta\phi - 2n\pi$ for an integer n . Therefore, it is only necessary that each phase shifting element be able to change the phase in its respective element by 360 degrees. This is readily accomplished by the phase shifting elements that are being used.

As mentioned previously, the phase distribution across the aperture is varied by means of Reggia-Spencer type ferrite phase shifting elements. Other type devices were considered but were rejected for various reasons. Diode devices, for example, were considered too lossy. Because of the relatively large number of bits required in a digital or latching ferrite device to scan the beam in the desired fashion, the length and cost of this type device were considered unrealistic.

Several aspects of the phase shifter design deserve specific comments. These areas are the material selection, the matching of the device, the insertion loss, and the temperature sensitivity. Because the figure of merit, or phase shift per dB of loss, of the nickel ferrites is higher in the frequency region of interest, a Trans-Tech TT2-111 nickel-zinc ferrite material is used in the phase shifting device. This material has a saturation magnetization of 5000 Gauss and a loss tangent of 0.001. By using a "rolling-pin" design, excellent matching is achieved in a minimum length. The VSWR and insertion loss of the device, for example, are 1.10 ± 0.1 and 0.5 ± 0.1 dB

respectively. In order to achieve uniformity among the phase shifters in the system, the material for all of the devices has been mixed and sintered as a single batch. This approach has proved to be quite satisfactory.

Measurements have been made on the phase shifter to determine the temperature sensitivity of the device. In order that the array performance be least affected by temperature variations, it is most essential that the slope of the curve of phase shift versus applied magnetic field to constant over a specified range of fields for all temperatures encountered. If such a condition is satisfied, variations in temperature will not alter the relative phase distribution across the array aperture, and hence will not degrade the array performance. This assumes, of course, that all phase shifting elements are at the same temperature, a temperature which can vary, however, Proper heat sinking will ensure this.

The phase shift has been measured as a function of both applied magnetic field and temperature. Plots of these data are shown in Figures 4a and 4b. In figure 4a the phase reference was taken for the condition of zero applied field and ambient temperature (28°C). All phases were then referenced to this set of conditions. From this figure, however, it is difficult to get easily an accurate picture of the effects of temperature. At the low and high field regions the slopes of the various curves are quite different. However in the central position the slopes are almost identical. In Figure 4b the reference phase point for all temperatures was taken at an applied field of 17.5 oersteds and the data replotted. The identicalness of the slopes is quite apparent in this figure.

Because each phase shifter must be capable of varying the phase by 360° to take advantage of the temperature characteristics of the device, it is necessary to vary the applied magnetic field between approximately 12.5 oersteds and 25.0 oersteds. Two coils are used, one to provide the 12.5 oersted bias, the other to provide the 12.5 oersted variation. The total power required to drive and control each phase shifter is less than 0.2 watt. With 49 elements in the array, the total power consumption is approximately 9.4 watts.

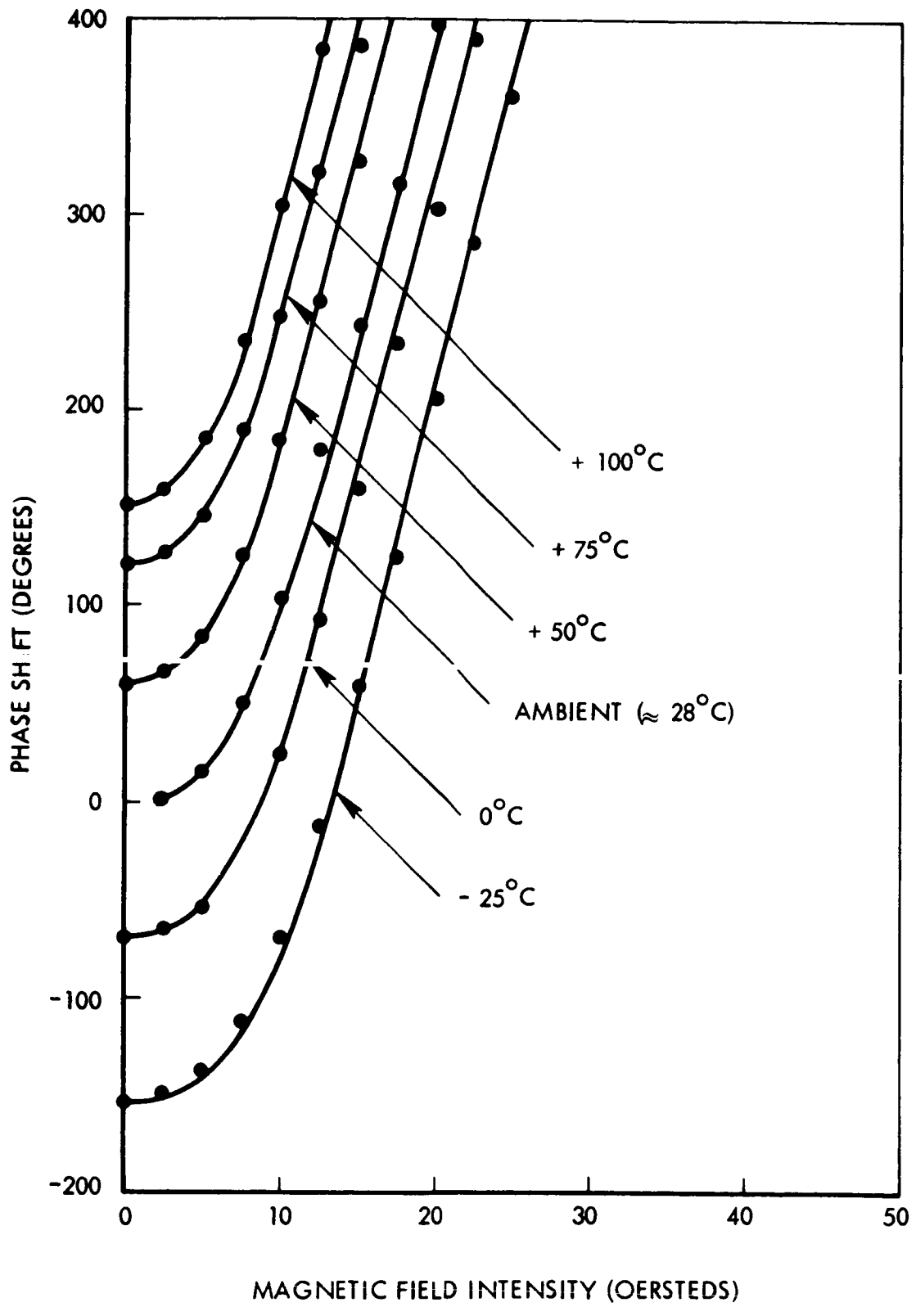


Figure 4a. Phase Shift Versus Applied Field (Reference Condition: Zero Field, Ambient Temperature)

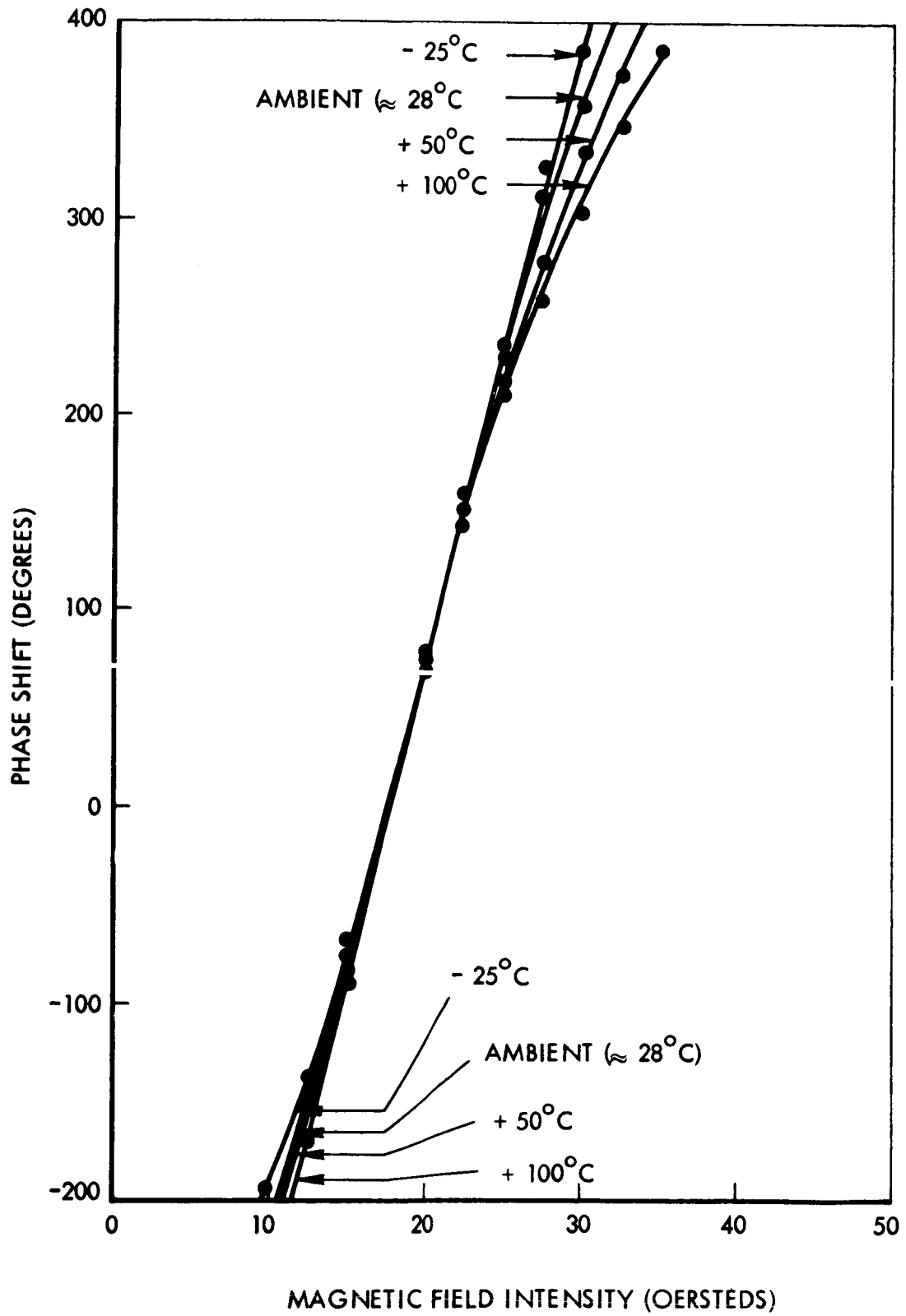


Figure 4b. Phase Shift Versus Applied Field (Reference Condition: Applied Field = 17.5 Oersteds)

Array Performance

The radiation pattern of a single linear array element is shown in Figure 5. The difference in the measured side lobe level of -31 dB and the designed -35 dB level is attributed to mutual coupling effects. Mechanical tolerances that were maintained in the manufacture of the element were ± 0.001 degree on all linear dimensions and ± 0.1 degree on the slot angles.

Assembly of the entire array is just nearing completion and complete radiation patterns are therefore not available at this time. Because of the effectiveness of the ground plane in reducing the mutual coupling between adjacent linear elements and reducing the cross-polarized energy, satisfaction of all performance requirements is expected.

ACKNOWLEDGEMENT

The work presented in this paper has been performed under Contract Number NAS 5-9680 sponsored by the Goddard Space Flight Center, Greenbelt, Maryland. Appreciation is extended to James Fujioka and Robert Bowers who have collected the data presented herein.

REFERENCES

1. J. K. Fujioka, "Beam Efficiency of a Scanning Planar Array Antenna," Space-General Corporation Memorandum NBSD TM-11, April, 1966.
2. R. J. Stegen, "Excitation Coefficients and Beamwidths of Tchebyscheff Arrays," Proc. IRE, Vol 41, pp 1671-1674, Nov. 1953.
3. R. J. Stegen, *ibid.*
4. W. M. Watson, "Waveguide Transmission and Antenna Systems," Clarendon Press, Oxford, 1947.

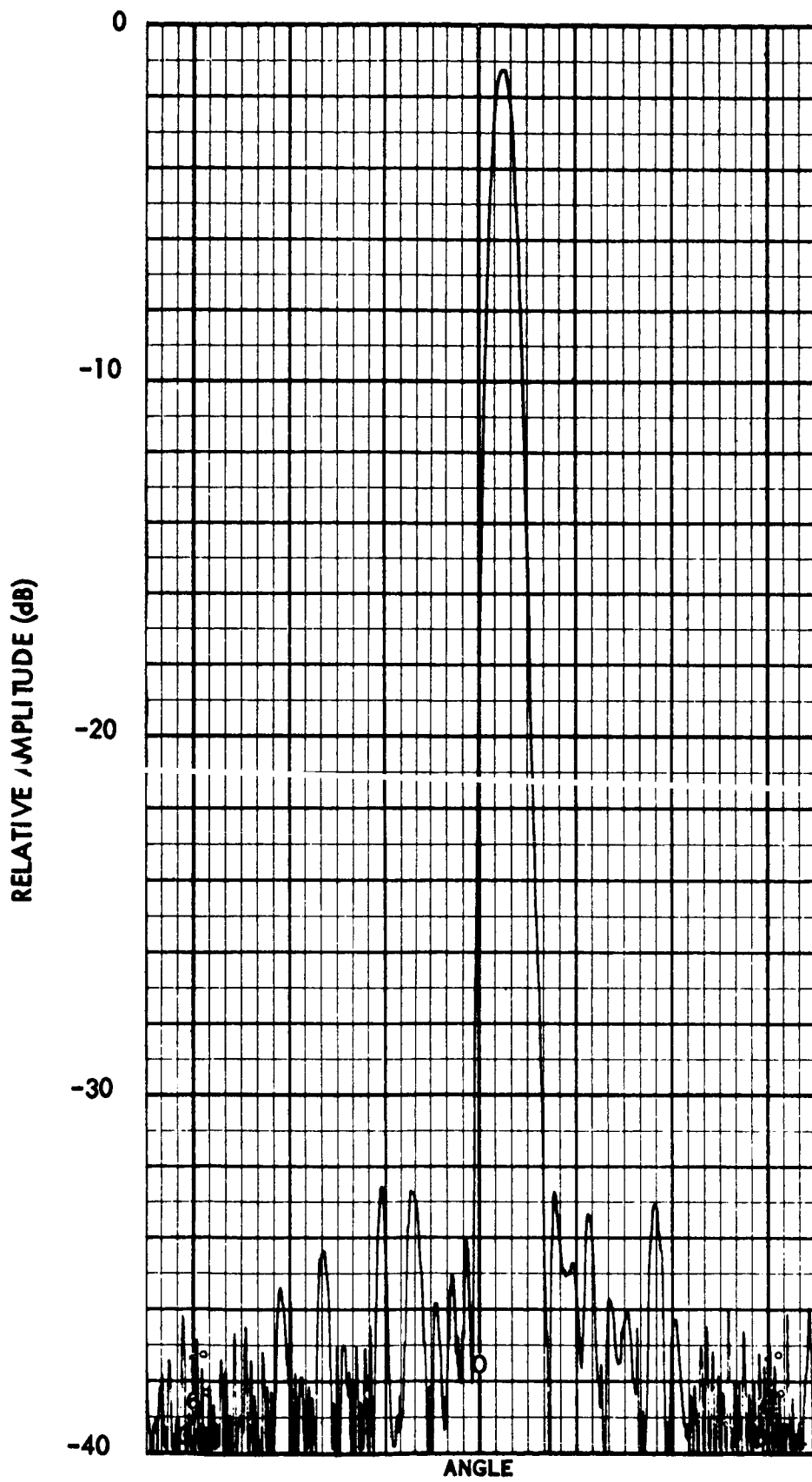


Figure 5. Radiation Pattern of a Single Linear Array Element

Appendix XVI

ANTENNA PATTERN RANGE FOR SPACE-GENERAL

INTRODUCTION

The present Space-General antenna range is located between the Engineering and Administration facility, where the pedestal and recording equipment is located, and the SEF building where the transmitting equipment is located. The range is 450' long and approximately 40' high. It is bounded on the east side by Bldg. 4 and a long 8' high chain link fence. Between buildings the main employee parking lot is located.

The building, fence and parked cars are sources of considerable reflection. The magnitude of the reflection is evident from patterns shown in Figure 1(a) and 1(b).

The patterns are of a 19 GHz dipole showing both the E and H plane cuts. There appears to be a consistent distortion of approximately 3 dB in the E plane cut, the H plane cut shows some shadowing at 180° due to the mixer. To show how the pattern behaved with a single "stick" of the Nimbus array, patterns were cut with transmitter and receiver on the same roof. Next, the present range was used. The transmitter was then moved to the roof of Bldg. 4. The elimination of the near-in side lobe is immediately evident in the latter situation. This was due to the removal of the reflections from the parking lot. It is certain that if lower frequency antennas were to be tested on the present range, the distortion would be considerably worse.

The error in gain measurement due to a single reflection can be calculated from the expression

$$\text{gain error} = 20 \log \left[1 \pm \frac{|E_r|}{|E_d|} \right],$$

where

E_r = reflected voltage

E_d = direct voltage

Since the side lobes are out of phase with the main beam, the worst condition can have the main beam gain reduced and the side lobe height increased. Considering the half-wave diaphragm tested (with a resulting gain difference of 3 dB) the reflection could be causing about 1.5 dB of gain error. Thus, the relative reflected power is only down 15 dB from the direct power.

Calculations on the NIMBUS antenna show that for 8 percent power in the side lobes, the side lobe level should be 26 dB down. An error of +1 percent would allow the side lobes to vary from 26-1/2 dB to 25-1/2 dB. This variation of 1 dB in the worst case would indicate that the range reflections causing the error should be down by 25 dB from the direct power received. Our present range therefore has reflections that are at least 10 dB too large to meet the Nimbus requirement.

Because of the large errors caused by the present antenna range, it is felt necessary that a new site be obtained so that we might properly meet our contractual obligations.

GENERAL FEATURES OF THE RANGE

- a. The range should be designed for future expansion as the work load increases.
- b. Should handle a large variety of antennas.
- c. Should operate over a wide range of frequencies.
- d. Should be efficient -- easy to operate and maintain.
- e. Provide user with accurate results.

SITE SELECTION

The present buildings with the exception of the SEF building are so designed that heavy loading of the roof is not permissible unless reinforced. Such reinforcement would be difficult and costly to achieve at the present time. Therefore, a separate antenna site containing transmitting and receiving buildings was considered. A rough sketch and verbal instructions concerning the proposed site was presented to the Plant Engineering people (M. Riley) to enable them to draw plans and to estimate costs. Without elaborating on the details, it can be seen that the cost of a separate facility would be extremely high and therefore this plan was abandoned.

A second site was considered utilizing the SEF building as the recorder site. At present there is a supported roof section where the SGC helix is maintained with a vacant room beneath, capable of housing the recording equipment. There is a stairway leading to the roof in this area. The photo lab is located between the empty room and the outside wall. We have been told that it is possible to move this photo lab to give us access to the outside. This site will allow for a 200' range, a tower height of 55', as well as a model tower range of approximately 20' in height and approximately 100' long.

Distances involved from the towers to the south wall of Building No. 4 are on the order of 180'. Between the towers and the SEF building are a field approximately 150' long, an asphalt road, cyclone fence and an empty asphalt pavement which occupy the remaining 50' of the range. The angle of incidence for these objects is shallow, thereby, reflections from these objects will not impinge on the test antenna.

AMPLITUDE VARIATIONS

If the amplitude variation over the aperture is limited to 1/4 dB, measurement errors from this source will be negligible for practically all applications⁽¹⁾. Cutter, et al⁽²⁾⁽³⁾ has shown that the field variation over an aperture of width d_r will be limited to about 1/4 dB if the transmitting antenna has a width

$$d_t \leq \frac{R\lambda}{4 d_r} \quad (1)$$

Where R is the range between the two antennas, λ is the free-space wavelength, and d_r and d_t are measured in the same plane.

It should be emphasized that the 1/4 dB criterion is sufficient for practically all antenna measurements, those considered herein included. In some instances it may be desirable, however, to accept a greater taper in order

(1) C. C. Montgomery, "Techniques of Microwave Measurements," Radiation Laboratory Series, Vol. 11, McGraw-Hill Book Co., New York, 1949, p 903.

(2) C. C. Cutter, A. P. King and W. E. Kock, "Microwave Antenna Measurements," Proc. IRE, Vol. 35, No. 12, December 1947, pp 1462-1471.

(3) D. R. Rhodes, "On Minimum-Range for Radiation Patterns," Proc. IRE, Vol. 42, No. 9, September 1954, pp 1408-1410.

to eliminate more serious distortions of the pattern from ground reflections. Such is not the case here since other methods, such as the use of absorbing panels or diffraction screens, can be used to eliminate or sufficiently reduce these reflections.

PHASE VARIATIONS

The phase front from a radiating aperture at a distance that is large compared to the wavelength is spherical in shape. At very large distance it is of course considered planar. In order that the spherical curvature not cause a phase error greater than $\lambda / 16$, it is easy to show that the minimum separation is

$$R = \frac{2d_r^2}{\lambda} \quad (2)$$

The major effect of this small deviation is to produce minor distortions of the sidelobe structure. Larger values will cause appreciable errors in both the measured gain and sidelobe structure. For a well-formed antenna, phase deviation of $\lambda / 16$ will cause a gain error of about 0.1 dB and negligible change in the pattern shape.

In order to minimize the errors caused by both phase and amplitude errors, an acceptable rule of thumb is

$$R = \frac{(d_t + d_r)^2}{\lambda} \quad (3)$$

At 19.35 GHz, the required range when $d_t = 12$ inches and $d_r = 16$ inches is, from Equation (3), approximately 108 feet.

EFFECTS OF REFLECTIONS

The error in gain measurement due to a single reflection can be calculated from the expression

$$\text{Gain Error} = 20 \log \left[1 + \frac{|E_r|}{|E_d|} \right] \quad (4)$$

Fujioka⁽⁴⁾ has shown for the Nimbus planar array antenna for 8 percent power in the sidelobes, the sidelobe level should be approximately 26 dB down. An error of ± 1 percent would allow the sidelobes to vary from 26.5 dB to 25.5 dB. From Equation (4) it is possible to show this 1 dB variation in the worst case (when the main beam gain is reduced and the sidelobe height increased) would require that the range reflections causing the error be down by 19 dB from the direct voltage.

In reducing the errors due to ground reflections it is desirable to have the point of specular reflection at the first null of the transmitting antenna radiation pattern. This condition cannot be satisfied for all antenna aperture sizes and frequencies, however. For example, in the range under consideration (model tower height of 23 feet and a 110 feet distance between transmit and receive sites), the angular position of the first null in the transmit antenna pattern would have to be at approximately 25 degrees. In the case of a parabolic dish of 1 foot diameter, the first null is at an angle of only 2 degrees. A range of approximately 1320 feet is required if the first null is to be at the specular point for this system. Therefore for the 1 foot dish the specular point will be illuminated only by the sixth or seventh sidelobes. The level of these sidelobes relative to that of the main beam is well below the 19 dB requirement.

To further minimize the error that can be introduced by reflections, absorbing panels and diffraction screens will be placed at strategic locations on the range. It should be noted that because of the relatively remote position of the surrounding buildings and structures, reflections from these structures will be negligibly small.

In summary, the range now under construction will satisfy all the requisites for good radiation pattern measurements for the Nimbus antenna program. Calibration measurements of the quality of the range will be made by using a standard antenna, the radiation pattern of which is well known. A dipole or slotted cylinder will be used.

(4) J. K. Fujioka, "Beam Efficiency of a Scanning Planar Array Antenna," Space-General Corporation Memorandum NBSD TM-11, April 1966.

Appendix XVII

NIMBUS BREADBOARD LINEARITY MEASUREMENTS

Linearity measurements conducted on the Nimbus breadboard 12-2-66 and 12-5-66 indicate a worst case non-linearity from signal input to the post detection amplifier to count output of the analog to digital converter of $\pm .06\%$ and an average non-linearity of $\pm .024\%$. These measurements include the composite non-linearities of the post detection amplifier, stepped AGC attenuator, synchronous detector, analog multiplexer, integrate and dump filter and analog to digital converter. Figure 1 is a block diagram of the linearity measuring set up. The signal generator in the upper left hand corner provides a 600 cycle square wave signal simulating the square law detector output. The signal generator consists of a stable 6.8 volt reference supply, a linear 10 turn potentiometer, a 600 cycle chopping circuit and an output attenuator. The 10 turn potentiometer divides the stable reference supply providing a variable input voltage of zero to 6.8 volts to the 600 cycle chopper circuit. The chopper circuit consists of field effect transistors which alternately switch the attenuator input between the potentiometer output and ground at a 600 cycle rate. The 600 cycle rate is supplied by the radiometer timing and control counter and is synchronous to the synchronous detector 600 cycle reference. The output of the chopper circuit is, therefore, a 600 cycle square wave signal of ER amplitude. During the calibration period, as described by the calibrate period pulse from the timing and control counter, the field effect transistors of the chopper circuit switch between the 6.8 volt stable reference and ground providing a full scale (6.8 volt) signal appropriate for the calibrate period. The 600 cycle chopper output is attenuated by 106 dB, and fed to the post detection amplifier input. The signal at the post detection amplifier input simulates the normal square law detector output in all aspects except for the noise component.

A digital voltmeter is used to monitor the chopper input voltage (E_R). Since this voltage is equal to the chopper peak to peak output amplitude, it provides an accurate indication of the signal amplitude into the post detection amplifier.

Linearity measurements indicate signal amplitude linearity from the post detection amplifier input to count linearity at the analog to digital converter output.

The radiometer breadboard receives its input power and timing signals from the radiometer test set directly, simulating the spacecraft telemetry interface. Radiometer output signals are received, processed and displayed by the test set. Three sets of linearity measurements were made; one at 23.5 volts, minimum supply voltage, one at 24.5 volts, nominal supply voltage and one at 25.5 volts, maximum supply voltage. All three sets of measurements were made at an ambient temperature of 25°C. Measuring intervals are every four counts of the analog to digital converter except for count zero to sixteen in which two count intervals were used. The three sets of data follow. Periodic calibration counts indicate to some degree the radiometer gain variation during these measurements.

Count	E_R (mv)	Count	E_R (mv)	Count	E_R (mv)	Count	E_R (mv)	Count	E_R (mv)
486	- Calib	104	- 1470	224	- 3164	344	- 4856	464	- 6551
2	- 27	108	- 1527	228	- 3218	348	- 4915	468	- 6605
4	- 56	112	- 1583	232	- 3276	352	- 4970	472	- 6664
6	- 84	116	- 1641	236	- 3335	356	- 5028	476	- 6721
8	- 115	120	- 1695	240	- 3390	360	- 5083	480	- 6777
10	- 141	124	- 1751	244	- 3447	364	- 5139	484	- 6834
12	- 168	128	- 1809	248	- 3503	368	- 5194	488	
14	- 200	132	- 1864	252	- 3556	372	- 5253	492	
16	- 227	136	- 1921	256	- 3617	376	- 5309	496	
485	- Calib	140	- 1978	260	- 3671	380	- 5365	500	
20	- 283	485	- Calib	485	- Calib	485	- Calib		Calib
24	- 337	144	- 2035	264	- 3728	384	- 5422		
28	- 396	148	- 2091	268	- 3786	388	- 5481		
32	- 452	152	- 2144	272	- 3839	392	- 5535		
36	- 510	156	- 2207	276	- 3898	396	- 5590		
40	- 567	160	- 2261	280	- 3954	400	- 5647		
44	- 621	164	- 2318	284	- 4011	404	- 5705		
48	- 675	168	- 2374	288	- 4066	408	- 5758		
52	- 735	172	- 2429	292	- 4126	412	- 5816		
56	- 792	176	- 2487	296	- 4182	416	- 5870		
60	- 847	180	- 2543	300	- 4237	420	- 5929		
485	- Calib	484	- Calib	485	- Calib	485	- Calib		
64	- 901	184	- 2600	304	- 4292	424	- 5988		
68	- 961	188	- 2656	308	- 4352	428	- 6041		
72	- 1017	192	- 2713	312	- 4408	432	- 6096		
76	- 1076	196	- 2771	316	- 4463	436	- 6156		
80	- 1134	200	- 2825	320	- 4517	440	- 6213		
84	- 1185	204	- 2882	324	- 4577	444	- 6270		
88	- 1242	208	- 2939	328	- 4632	448	- 6323		
92	- 1300	212	- 2996	332	- 4684	452	- 6382		
96	- 1355	216	- 3050	336	- 4748	456	- 6437		
100	- 1410	220	- 3107	340	- 4800	460	- 6492		
485	- Calib	485	- Calib	485	- Calib	485	- Calib		

Count	E_R (mv)	Count	E_R (mv)	Count	E_R (mv)	Count	E_R (mv)	Count	E_R (mv)
485	- Calib	104	- 1470	224	- 3163	344	- 4863	464	- 6556
2	- 27	108	- 1525	228	- 3223	348	- 4917	468	- 6611
4	- 55	112	- 1581	232	- 3283	352	- 4973	472	- 6668
6	- 86	116	- 1640	236	- 3334	356	- 5036	476	- 6725
8	- 113	120	- 1696	240	- 3392	360	- 5088	480	- 6782
10	- 139	124	- 1753	244	- 3448	364	- 5143	484	
12	- 172	128	- 1809	248	- 3505	368	- 5199	488	
14	- 195	132	- 1864	252	- 3562	372	- 5256	492	
16	- 225	136	- 1922	256	- 3620	376	- 5312	496	
484	- Calib	140	- 1977	260	- 3674	380	- 5369	500	
20	- 282	484	- Calib	484	- Calib	484	- Calib		Calib
24	- 336	144	- 2035	264	- 3733	384	- 5425		
28	- 395	148	- 2093	268	- 3787	388	- 5482		
32	- 449	152	- 2150	272	- 3844	392	- 5538		
36	- 508	156	- 2207	276	- 3901	396	- 5594		
40	- 568	160	- 2260	280	- 3955	400	- 5653		
44	- 621	164	- 2318	284	- 4014	404	- 5709		
48	- 678	168	- 2376	288	- 4070	408	- 5763		
52	- 735	172	- 2432	292	- 4128	412	- 5819		
56	- 790	176	- 2489	296	- 4181	416	- 5876		
60	- 847	180	- 2546	300	- 4239	420	- 5934		
485	- Calib	484	- Calib	484	- Calib	484	- Calib		
64	- 903	184	- 2602	304	- 4294	424	- 5995		
68	- 963	188	- 2657	308	- 4352	428	- 6050		
72	- 1017	192	- 2713	312	- 4406	432	- 6104		
76	- 1073	196	- 2773	316	- 4463	436	- 6162		
80	- 1132	200	- 2829	320	- 4523	440	- 6215		
84	- 1187	204	- 2884	324	- 4581	444	- 6272		
88	- 1243	208	- 2942	328	- 4634	448	- 6330		
92	- 1300	212	- 2997	332	- 4693	452	- 6386		
96	- 1355	216	- 3054	336	- 4750	456	- 6443		
100	- 1415	220	- 3110	340	- 4806	460	- 6498		
484	- Calib	484	- Calib	484	- Calib	484	- Calib		

25°C

Count	E_R (mv)	Count	E_R (mv)	Count	E_R (mv)	Count	E_R (mv)	Count	E_R (mv)
83	- Calib	104	- 1480	224	- 3177	344	- 4879	464	- 6585
2	- 27	108	- 1531	228	- 3237	348	- 4935	468	- 6641
4	- 54	112	- 1587	232	- 3290	352	- 4992	472	- 6694
6	- 82	116	- 1647	236	- 3350	356	- 5050	476	- 6749
8	- 111	120	- 1703	240	- 3405	360	- 5106	480	- 6809
10	- 140	124	- 1758	244	- 3461	364	- 5163	484	-
12	- 166	128	- 1816	248	- 3514	368	- 5220	488	-
14	- 197	132	- 1875	252	- 3573	372	- 5277	492	-
16	- 227	136	- 1929	256	- 3632	376	- 5335	496	-
483	- Calib	140	- 1987	260	- 3690	380	- 5390	500	-
20	- 284	483	- Calib	482	- Calib	482	- Calib		Calib
24	- 338	144	- 2044	264	- 3746	384	- 5445		
28	- 395	148	- 2100	268	- 3799	388	- 5504		
32	- 451	152	- 2157	272	- 3860	392	- 5559		
36	- 510	156	- 2213	276	- 3915	396	- 5616		
40	- 570	160	- 2266	280	- 3969	400	- 5672		
44	- 621	164	- 2328	284	- 4030	404	- 5730		
48	- 680	168	- 2387	288	- 4084	408	- 5784		
52	- 737	172	- 2442	292	- 4142	412	- 5842		
56	- 794	176	- 2496	296	- 4200	416	- 5898		
60	- 851	180	- 2555	300	- 4255	420	- 5955		
483	- Calib	483	- Calib	483	- Calib	483	- Calib		
64	- 906	184	- 2610	304	- 4311	424	- 6012		
68	- 966	188	- 2667	308	- 4366	428	- 6068		
72	- 1022	192	- 2722	312	- 4423	432	- 6126		
76	- 1078	196	- 2781	316	- 4480	436	- 6184		
80	- 1134	200	- 2837	320	- 4539	440	- 6238		
84	- 1191	204	- 2896	324	- 4594	444	- 6294		
88	- 1245	208	- 2952	328	- 4653	448	- 6351		
92	- 1304	212	- 3007	332	- 4707	452	- 6411		
96	- 1360	216	- 3065	336	- 4765	456	- 6470		
100	- 1419	220	- 3121	340	- 4822	460	- 6523		
483	- Calib	483	- Calib	483	- Calib	482	- Calib		

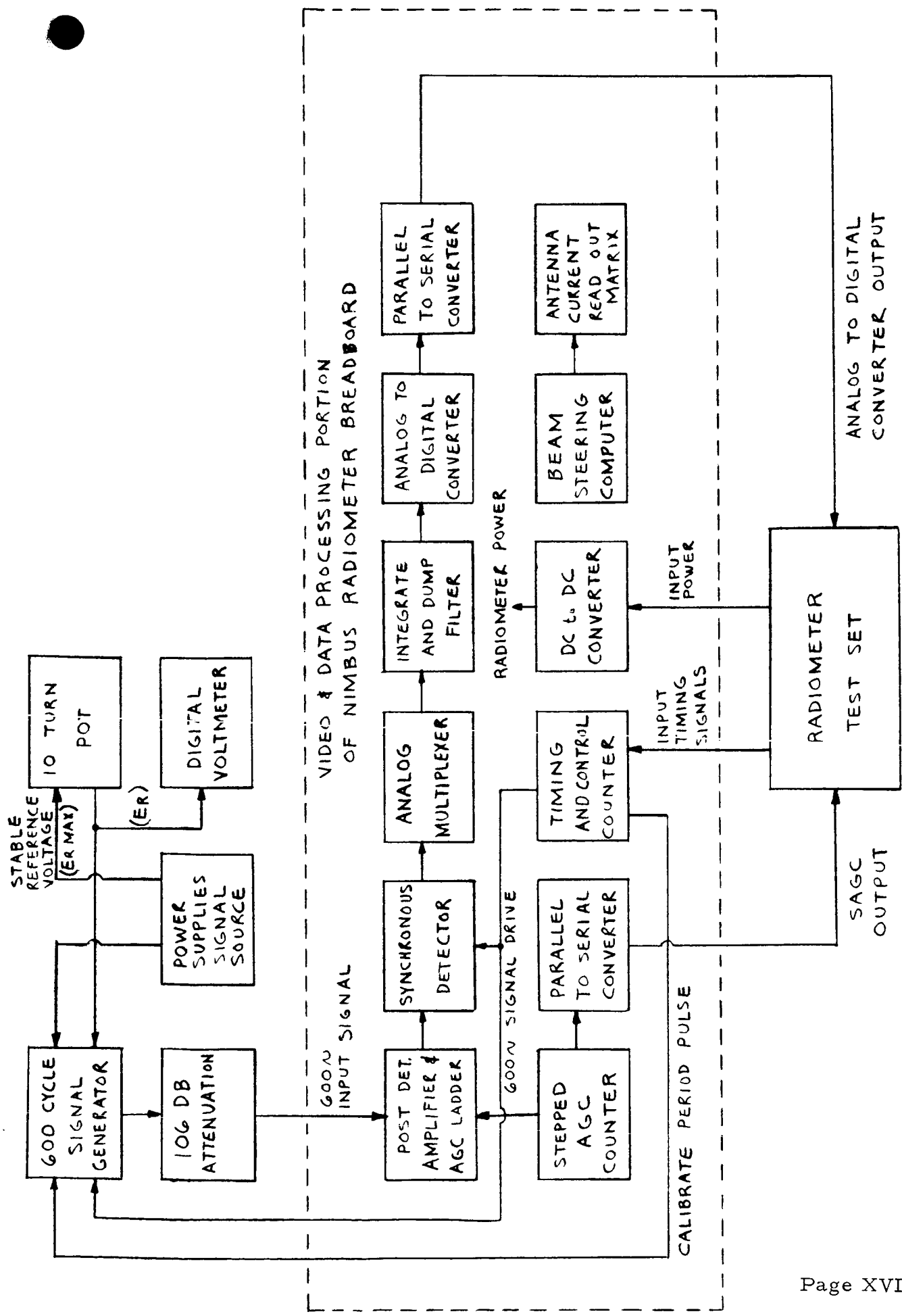


Figure 1. Block Diagram of Linearity Measurement Set Up

Appendix XVIII

THE MEASUREMENT OF ΔT

The sensitivity, ΔT , is the root mean square deviation of the input noise temperature of the radiometer. This can be measured by recording the radiometer output signal on a chart recorder and estimating the rms value of the fluctuations and introducing a known temperature, T , to calibrate the chart recorder. When the radiometer output is sampled and printed out digitally ΔT can be calculated directly by determining the rms of the recorded values of the noise.

Record the radiometer output, a , for N samples. Change the temperature at the input of the radiometer by a known amount T , ($^{\circ}K$) and record the radiometer output for N additional samples. The two sets of samples can now be plotted as a histogram with the number of counts plotted vs. the count value. This will give an indication of the shape of the distribution.

The average of each set of samples is now computed from

$$\bar{a} = \frac{1}{N} \sum_{n=1}^N a_n$$

where

a_n = the value of the n^{th} sample

N = number of samples

\bar{a} = average of a

taking the first set of readings the rms deviation of \bar{a} is calculated from

$$\begin{aligned} \Delta a &= \sqrt{\frac{(\bar{a} - a_1)^2 + (\bar{a} - a_2)^2 + \dots + (\bar{a} - a_n)^2}{N}} \\ &= \sqrt{\frac{\sum_{n=1}^N a_n^2 - N \bar{a}^2}{N}} \end{aligned}$$

where

$$\Delta a = \text{rms deviation of } \bar{a}$$

Now Δa can be related to ΔT by

$$\Delta T = \Delta a \left| \frac{T}{\bar{a} - \bar{b}} \right|$$

where

ΔT = rms deviation of the temperature

\bar{a} = mean value of a at a fixed reference temperature

\bar{b} = mean value of a when an additional temperature, T , is added.

The accuracy of the measurement of ΔT will be proportional to \sqrt{N} and the accuracy of the measurement of \bar{a} or \bar{T} will also be proportional to \sqrt{N} .

By taking $N = 100$ samples the measurement accuracy of ΔT will be $\sim 11\%$, with a 90% confidence level. For other cases, see the following:

The ΔT is the one sigma ($\sigma =$ one standard deviation) of the radiometer noise. Therefore, what we are trying to determine is the standard deviation and its accuracy.

For large number of samples, i. e., ≥ 100 , the sampling distribution for the standard deviation (rms value, ΔT , etc.) is almost normal, and the standard deviation of the standard deviation estimate is given by σ_s , where

$$\sigma_s = \frac{s}{\sqrt{2N}}$$

s is the measured standard deviation ($s = \Delta a$), and N is the number of samples. We can then use the properties of the tabulated normal distributions and the standard deviation can be written as

$$\sigma = s \pm k \sigma_s = s \pm k \frac{s}{\sqrt{2N}}$$

where k is the number of standard deviations from the mean, determined from table of the Areas under the Standard Normal Curve. The value of k determines the confidence level. The confidence level is the probability that the value of the standard deviation is within the confidence limits $(\pm \frac{s}{\sqrt{2N}})$.

For a smaller number of samples, the χ^2 distribution must be used. The range of the standard deviation is given by

$$\sqrt{\frac{ns^2}{x_2^2}} < \sigma < \sqrt{\frac{ns^2}{x_1^2}}$$

where σ is the true value of the standard deviation and s is the estimate. The two variables x_1^2 and x_2^2 are from the Chi squared distribution for $n-1$ degrees of freedom and for whatever confidence level is desired. The confidence level is the difference between the two probabilities associated with the two Chi squared variables.

Figure I shows both the assumption of normal distribution (the curve labeled 1.645) and the Chi squared test. The Chi squared test didn't give values of error symmetrical around the standard deviation, but they are plotted as if the range were around the center value. An example of the closeness of the two methods for large numbers is a range of .238 ($\pm 11.9\%$) for the Chi squared test and .232 ($\pm 11.6\%$) for the normal distribution. It can be seen from Figure I that the error in using the normal distribution leads to greater errors for smaller number of samples.

Figure II shows the error limits (or accuracy) versus the number of samples for various confidence levels. If the graph were extended, it would show that over ten thousand samples are needed to insure the accuracy of the ΔT measurement to 1%, with a 90% confidence. If we would have been satisfied with only a 50% confidence, only slightly greater than 500 samples are required. The 50% confidence indicates that in this case, only half of the time in a large number of different determinations would the ΔT be within 1% of the correct value.

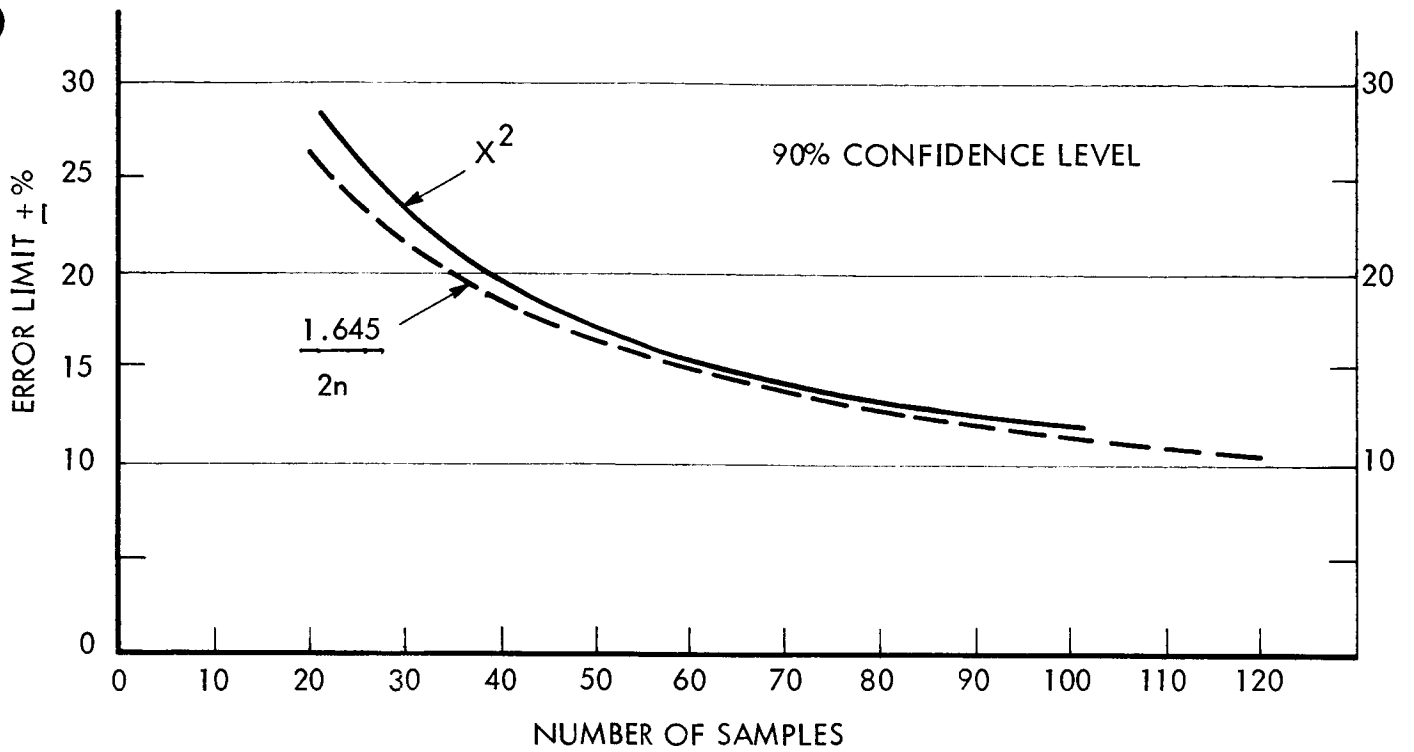


Figure I. Normal Distribution versus the Squared Test

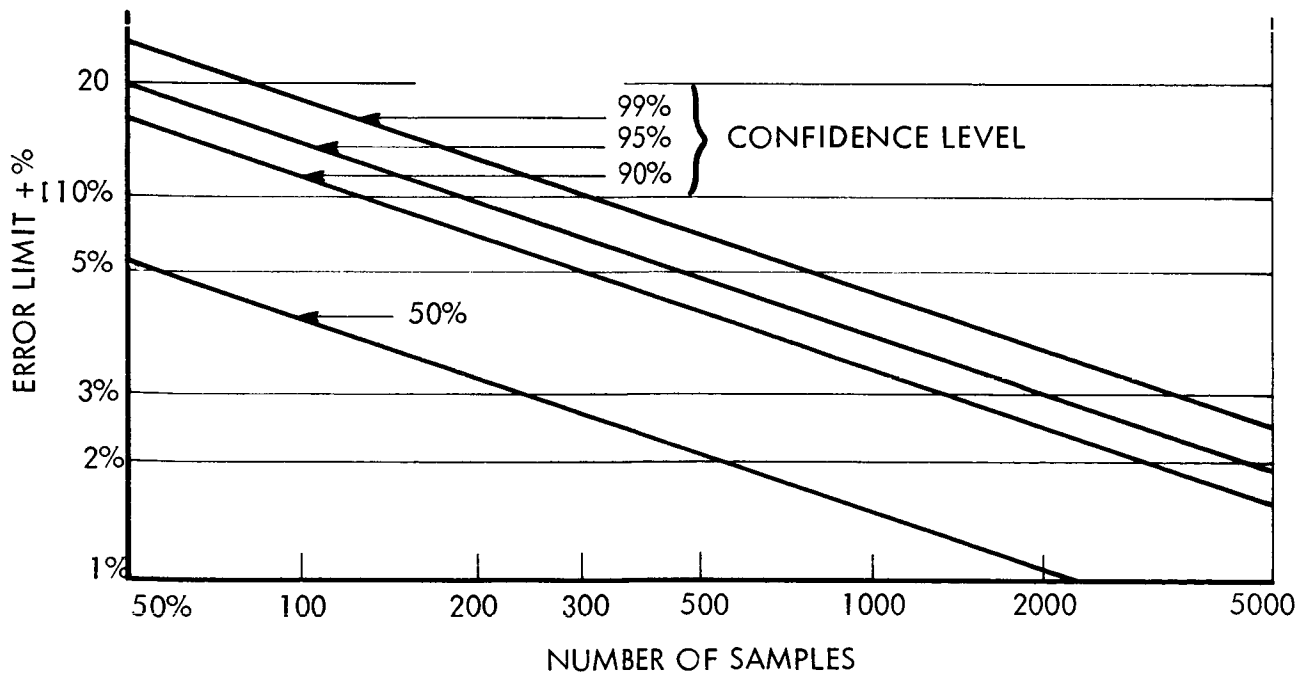


Figure II. Error Limits versus Various Confidence Level

Appendix XIX

CIRCUIT DESCRIPTION OF NIMBUS IF AMPLIFIER, POST DETECTION, AND SWITCH DRIVER CIRCUITS

IF AMPLIFIER AND SQUARE LAW DETECTOR (Refer to Drawing No. DW-AAD3381)

Circuit Description:

The IF amplifier consists of a cascade of six Texas Instruments TIXM101 UHF germanium transistors. The first transistor is selected and biased to obtain minimum noise figure. Latter stages are biased at a value of emitter current that obtains approximately maximum gain over the frequency range of interest. Frequency selective emitter degeneration and shunt current feed back is employed in the design to obtain the required frequency response and stability with temperature variations. It should be noted that, except for input and output networks, R-C circuits are used for interstage coupling and tuning.

In order to minimize the receiver noise figure, data was obtained from curves published by Texas Instruments giving optimum source impedance as a function of frequency. This data, combined with the measured IF impedance of the mixer, enabled the synthesis of a broadband noise-matching network between the mixer and IF amplifier.

A Philco L 4167 back diode detector is incorporated as part of the amplifier design in order to provide the video output. The coupling circuit of the detector to the amplifier output consists of a simple L-C filter in order to obtain a rapid high frequency roll off.

To date, four units have been fabricated: the original breadboard; Nimbus breadboard and flight models; and a unit for the 35 gc receiver being fabricated by W. H. Conway's group. All of the units have been found to be quite uniform with respect to bandwidth, gain and noise figure. It has been found that about 20 minutes to 1/2 hour is required for tuning, once the equipment has been set-up.

Tuning consists of adjustment of the three capacitors shown in drawing number DW-AAD3381 along with minor adjustments of the series inductor in the output (L5).

Measured specifications of a typical unit are as follows:

Bandwidth: 200 mc

Center Frequency: 120 mc

Broadband noise figure: less than 2 dB

Gain: 60 dB \pm 3 dB

Gain variation with temperature: 3 dB over -10°C to $+65^{\circ}\text{C}$

Detector output sensitivity: approximately 20 μV for a 1°K change at IF amplifier input.

IF Amplifier Checkout:

In order to fully checkout and adjust the IF amplifier, it is necessary to use both a sweeper (from about 10 MHz to 250 MHz) and an oscilloscope. However, a very simple functional check is to measure the DC voltage at the output of the square law detector. This voltage should be approximately 10 to 20 millivolts (measured at C26).

Should the amplifier be malfunctioning due to a faulty transistor, this component can be found by measuring the DC voltage on each collector. The proper voltages are as follows (within $\pm 15\%$):

$$Q_1: V_{C_1} = -8 \text{ volts}$$

$$Q_2: V_{C_2} = +0.6 \text{ V}$$

$$Q_3: V_{C_3} = +5.4 \text{ V}$$

$$Q_4: V_{C_4} = +0.6 \text{ V}$$

$$Q_5: V_{C_5} = +5.4 \text{ V}$$

$$Q_6: V_{C_6} = +0.6 \text{ V}$$

The detector diode can be checked by observing its i-v characteristics on a transistor curve tracer.

VIDEO PREAMPLIFIER (Refer to Drawing Number DW-AAD3391)

Circuit Description:

The video preamplifier consists of a General Instruments PC 200 integrated circuit low noise operational amplifier. This amplifier, along with its associated feedback and biasing circuitry, mounts on a printed circuit board that is located in the mixer - IF amplifier box. Zener diode voltage regulator and low frequency filter components to supply DC power to both the IF amplifier and the video preamplifier are mounted on the same board.

Gain adjustment of the video amplifier is accomplished by changing R_4 to an appropriate value (preamp gain is very nearly R_5/R_4).

To adjust the preamp gain to the proper value, the procedure is as follows: (Note: the preamp gain has already been set to approximately that required).

1. Observe setting of AGC after the hot load has arrived at the proper temperature and the AGC computer has stopped stepping the gain.
2. Adjust R_4 by an amount proportional to the difference between 16 dB and the AGC setting observed in step 1. For example, if the AGC setting observed in step 1 was -10 dB, R_4 would be decreased by a factor of 2, thereby increasing the R_4 video gain by a factor of 2 (or +6 dB).

Video Amplifier Checkout:

The video amplifier can be checked by using an audio signal generator and an oscilloscope (an AC millivolt meter must be used for very accurate measurements). A 600 Hz signal from the generator is connected to the amplifier input and the gain can be measured by conventional means. The gain should be equal to the ratio R_5/R_4 .

POST AMPLIFIER / SYNCHRONOUS DEMODULATOR

The post-amplifier and synchronous amplifier designs are essentially unchanged from that discussed on pp 72-73 and pp 79-80 of the first Nimbus Quarterly Report.

The post amp/sync demod is checked out through the use of a square-wave generator, attenuator and microammeter connected as shown in the following block diagram (see Figure 1).

The peak-to-peak voltage at terminal 6 on the circuit board is adjusted by the attenuator to 5 mv. The current read by the microammeter should be approximately 25 to 30 μ a, with the polarity dependent on whether the voltage at terminal 2 leads or lags the voltage at terminal 1. With the signals at 1 and 2 reversed, the polarity of the current into the DC microammeter should also reverse.

With the attenuator disconnected and terminal 6 shorted to ground (terminal 7), the output current should be less than .05 μ a.

PERIODIC SWITCH DRIVER (Refer to Drawing DWG-AAD3351)

Circuit Description:

Q_2 functions as a current source, through which current is flowing continuously. The current path is either through one RF switch coil via pins 4 and 5 for one switch state or through the other coil via pins 3 and 5 for the other RF switch state. The RF switch coil (determining the position of the switch) that is activated is determined by switching transistors Q_1 and Q_5 . With a periodic trigger pulse appearing at pin 1, Q_1 and Q_5 are alternately switched on and off, thereby alternately driving the two switch coils.

In order to enhance the RF switching rise time, an added current pulse is provided via Q_3 and Q_4 each time the RF switch changes position. The pulse is derived from Q_5 and Q_1 via steering diodes CR 8 and CR 7.

The temperature characteristics of zener diodes CR 5 and CR 6 combine with the temperature characteristics of the base - emitter voltage of Q_2 in such a way that adequate stability of the current drive to the RF switch is insured over the specified temperature range.

Circuit Checkout Procedure:

1. Connect 5 ohm (+1%) resistors between terminals 3 and 5 and between terminals 4 and 5.

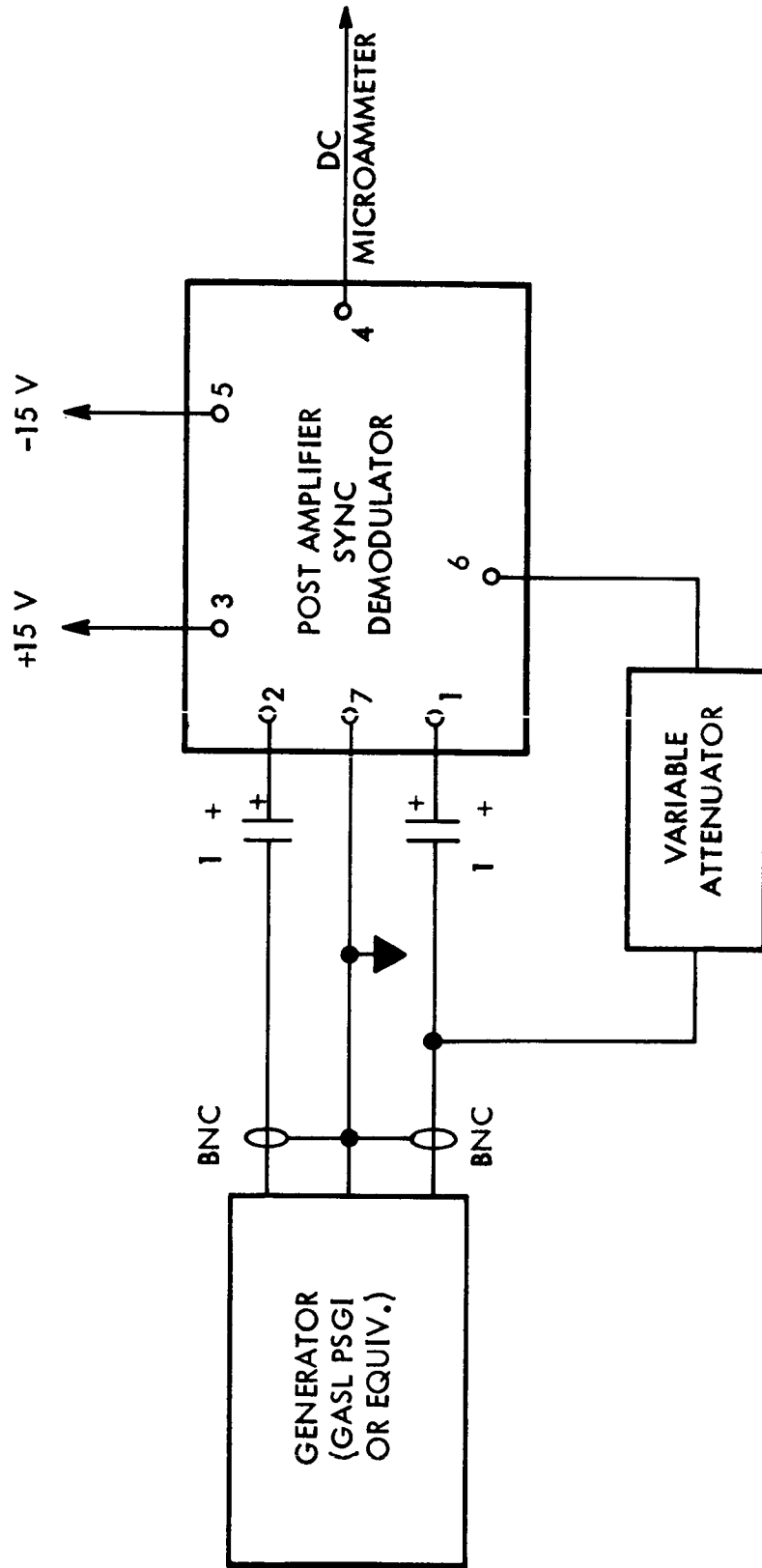


Figure 1. Amplifier/Synchronous Demodulator Checkout Circuit

2. Apply 24.5 volts to circuit via terminals 2 and 6.
3. Connect a voltmeter across the 5 ohm resistor connected to pins 3 and 5.
4. To find the proper value for R_g , select from metal film, 1 watt, 5% resistors (120 ohm nominal) a resistor that will produce 0.34 volt across the 5 ohm resistor (this provides the 68 ma necessary for proper ferrite switch operation. Note that if a ferrite switch is used with slightly different current requirements, R_g can be selected accordingly).
5. Connect a positive going, 2V, 600 Hz symmetrical square wave to pin 1. The resulting waveform across either of the 5 ohm resistors should be as shown below.

Switch Driver Specifications:

Supply voltage: -24.5 V

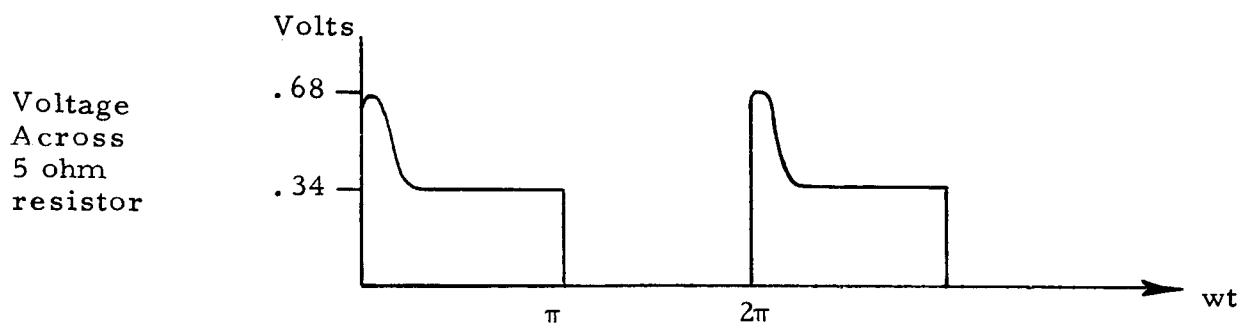
Current requirement: 100 ma

Current supplied to ferrite switch: 68 ma \pm 3%

RF switching rise time: 100 μ sec

Operating temperature range: 0 to 50°C

Trigger requirement: +2 volts min.



NON-PERIODIC SWITCH (Refer to Drawing No. DW-AAD-3341)

Circuit Description:

This circuit provides the driving current for the non-periodic ferrite switch. Terminals 3 and 5 connect to the switch coil; to change the switch state, the driving current is simply reversed by the switch driver. The current sources are Q_3 and Q_5 , one for each switch coil current direction. The current sources and the transistor switches Q_2 and Q_4 are switched when activated by the trigger. For one coil current direction, Q_6 , Q_2 and Q_5 conduct, for the other direction Q_1 , Q_4 and Q_3 conduct.

The zener diodes are the references for the current sources and provide temperature compensation for environmental temperature change. Low drift resistors R7 and R12 are used for long term stability.

Specifications:

1. Voltage Required: 24.5 V
2. Current Required: 28 ma
3. RF switching rise time: 10 m sec
4. Temperature operating range 0 - 50°C
5. Trigger required: +2V min.
6. Current supplied to ferrite switch: 19.5 ma \pm 2%

Preliminary Checkout Procedure:

1. Connect a 50 ohm resistor \pm 1% to terminals 3 and 5.
2. Connect 24.5 volts to terminals 2 and 4.
3. Connect voltmeter across the 50 ohm resistor.
4. Select from metal film resistors (430 ohm nominal) a resistor for R7 that will give .975 volts across the 50 ohm resistor.
5. Apply positive 3V DC to trigger input.
6. Select resistor for R12 to give 0.975 volts across the 50 ohm resistor.

7. Remove voltmeter and connect oscilloscope across 50 ohm resistor.
8. Connect positive trigger (at least 2 volts) to trigger input. Use square wave, 20 cps. Waveform should be $\pm .975$ volts. (1.95Vp-p).

D

NOTES:

- 1. SCHEMATIC TO BE USED IN CONJUNCTION WITH DW AAD3390-1ASSY
- 2. UNLESS OTHERWISE SPECIFIED, RESISTOR VALUES IN OHMS ± 5% 1/4W



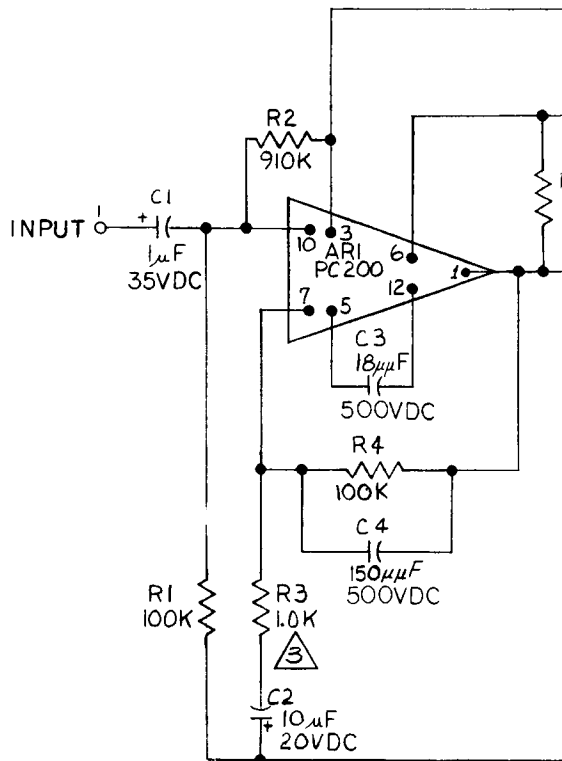
VALUE SHOWN IS APPROXIMATE. EXACT VALUE TO BE DETERMINED AT TEST.

C

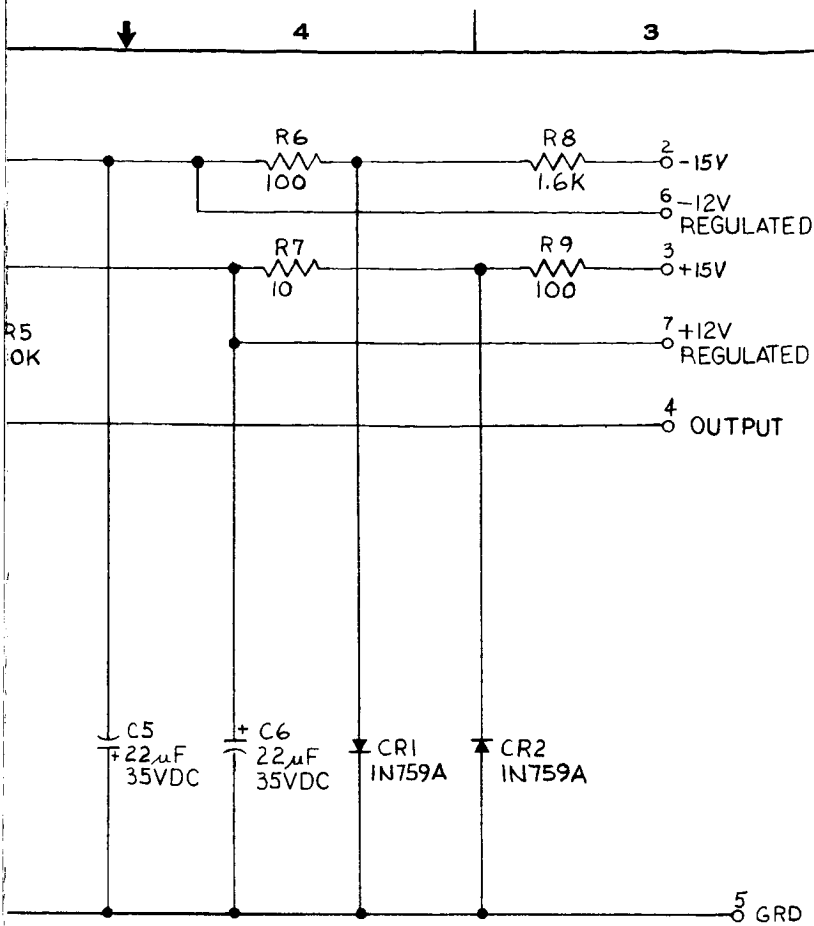


B

A



10-1



REVISIONS				
ZONE	LTR	DESCRIPTION	DATE	APPROVED

D
 C
 B COPY RELEASED
 A

QTY REQD	SYM	CODE IDENT	PART OR IDENTIFYING NO.	NOMENCLATURE OR DESCRIPTION	MATERIAL	SPECIFICATION	UNIT WT.	ZONE	ITEM NO.
LIST OF MATERIALS									
UNLESS OTHERWISE SPECIFIED DIMENSIONS ARE IN INCHES TOLERANCE ON DECIMALS .XX ± .03 XXX ± .010 DO NOT SCALE DRAWING				CONTRACT NO. NAS 5-9680		SPACE-GENERAL CORPORATION <small>10000 CALIFORNIA, A SUBSIDIARY OF AEGYPT GENERAL CORPORATION</small>			
DRAWN <i>E. M. Keener</i> DATE <i>2-2-67</i>				DESIGN <i>H. H. Oudin</i> DATE <i>2/16/67</i>		TITLE ELECTRICAL SCHEMATIC DIAGRAM, PRE AMPLIFIER			
TREATMENT				PRODUCTION		DWG CODE IDENT NO. DWG NO.			
FINISH				DESIGN <i>H. H. Oudin</i> DATE <i>2-20-67</i>		DWG SIZE D		13655 DW-AAD3391	
PART DASH NO. PER ASSY				CUSTOMER		SCALE NONE		REL DATE <i>4-3-67</i>	
DRAWING LEVEL 0				ACT. WT. CALC. WT.		SHEET			

10-2

8

7

6

5

NOTES:

D

- 1. TO BE USED IN CONJUNCTION WITH ASSEMBLY DRAWING DW-AAD3350.
- 2. UNLESS OTHERWISE SPECIFIED:
 - A- ALL RESISTORS VALUES ARE IN OHMS, 1/4WATT, ±5%
 - B- ALL TRANSISTORS ARE TYPE 2N2907
 - C- ALL DIODES ARE TYPE IN457
- 3. SELECTED RESISTOR NOMINAL VALUE 120 OHM 1WATT ±5% ACTUAL VALUE TO BE DETERMINED AT TEST & ENGINEERING NOTIFIED
- 4. CR1 NOT USED.

C

→

B

A

TRIGGER
TO J103-7

CR 2
CR 3
CR 4

R3
1K

R4
100

R2
1.8K,
1/2W ±5%

R1
4.7K

C1

CR5
IN750A
CR6
IN751A

R5
18K

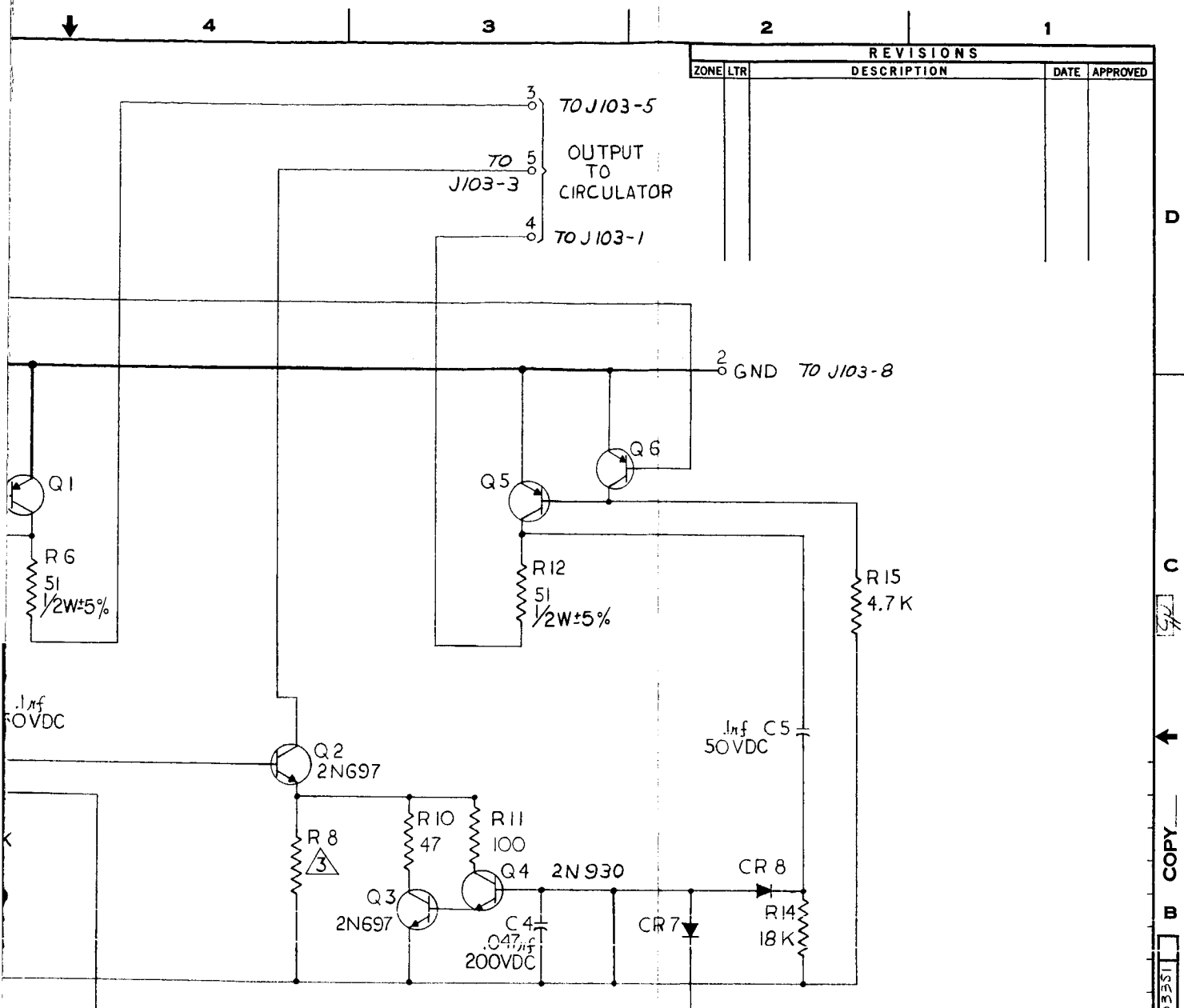
TO J103-9
6
-24.5V

8

7

6

5



REVISIONS				
ZONE	LTR	DESCRIPTION	DATE	APPROVED

D
 C
 B COPY
 A
 DW-AAD3351

QTY REQD	SYM	CODE IDENT	PART OR IDENTIFYING NO.	NOMENCLATURE OR DESCRIPTION	MATERIAL	SPECIFICATION	UNIT WT.	ZONE	ITEM NO.

UNLESS OTHERWISE SPECIFIED DIMENSIONS ARE IN INCHES TOLERANCE ON DECIMALS XX ± .03 XXX ± .010 DO NOT SCALE DRAWING				CONTRACT NO. NA95-9680		SPACE-GENERAL CORPORATION <small>A DIVISION OF GENERAL ELECTRIC CORPORATION</small>		
TREATMENT				DRAWN: <i>W.C. 4/10/67</i> DATE: <i>2-10-67</i> DESIGNED: <i>W.C. 2/10-67</i> CHECKED: <i>W.C. 2-14-67</i>	TITLE ELECTRICAL SCHEMATIC DIAGRAM SWITCH DRIVER #2 PERIODIC			
FINISH				DESIGN APPROVED: <i>W.C. 2/20/67</i>	DWG SIZE: D	CODE IDENT NO. 13655	DWG NO. DW-AAD-3351	
EFFECTIVE SERIAL NO. USAGE DATA				SIMILAR TO	ACT. WT. CALC. WT.	SCALE	RELEASE DATE <i>4-7-67</i>	
ON	THRU	PART DASH NO.	NEXT FINAL QTY REQD PER ASSY	NEXT ASSY	USED ON	DRAWING LEVEL		

8

7

6

5

D

NOTES:

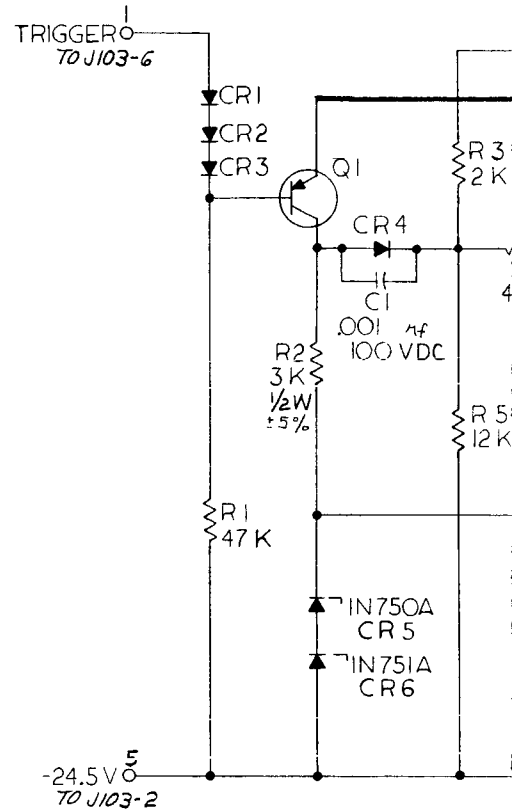
- △ SCHEMATIC DIAGRAM TO BE USED IN CONJUNCTION WITH ASSEMBLY DW-AAD-3340
- 2 UNLESS OTHERWISE SPECIFIED:
 - A. ALL RESISTOR VALUES ARE IN OHMS ±5%
1/4 WATT
 - B. ALL DIODES ARE TYPE IN457
 - C. ALL TRANSISTORS ARE TYPE 2N2907
- △ EXACT RESISTOR VALUE TO BE DETERMINED BY TEST (NOMINAL VALUE 432 OHMS ±1%)
‡ ENGINEERING NOTIFIED.

C

→

B

A



8

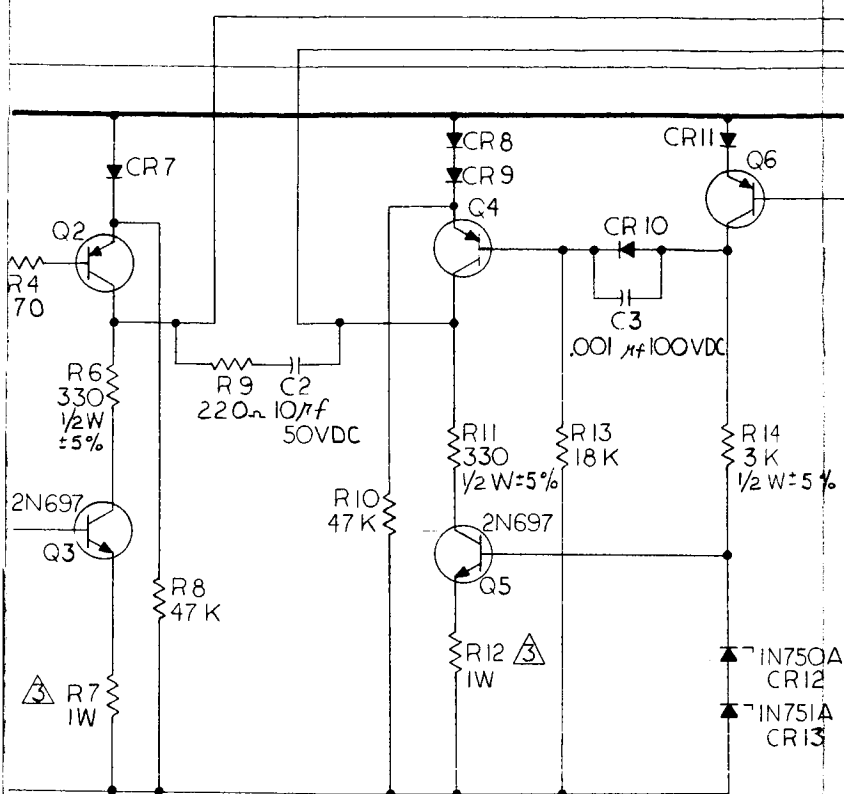
7

6

5

REVISIONS				
ZONE	LTR	DESCRIPTION	DATE	APPROVED

TO J103-4
 3 TO CIRCULATOR
 4 TO J103-9
 2 GROUND TO J103-8



D
C
B
A
DWG AAD 3341

QTY REQD	SYM	CODE IDENT	PART OR IDENTIFYING NO.	NOMENCLATURE OR DESCRIPTION	MATERIAL	SPECIFICATION	UNIT WT.	ZONE	ITEM NO.
LIST OF MATERIALS									
UNLESS OTHERWISE SPECIFIED				CONTRACT NO. NAS-5-9680		SPACE-GENERAL CORPORATION <small>EL SEGUNDO, CALIFORNIA - A SUBSIDIARY OF AEROSOL-GENERAL CORPORATION</small>			
DIMENSIONS ARE IN INCHES				DRAWN <i>W. G. Spence</i> DATE <i>11/29/66</i>					
TOLERANCE ON DECIMALS				CHECKED <i>W. G. Spence</i> DATE <i>12/15/67</i>		TITLE ELECTRICAL SCHEMATIC DIAGRAM SWITCH DRIVER #1 NON-PERIODIC			
XXX ± .03				DESIGN <i>W. G. Spence</i> DATE <i>11/29/66</i>					
XXX ± .010				STRESS		DWG NO. 13655 DWAAD-3341			
DO NOT SCALE DRAWING				STRUCTURE					
TREATMENT				MATERIALS		SCALE NONE RELEASE DATE 4-7-67 SHEET			
FINISH				PRODUCTION					
ON				DESIGN APPROVED <i>W. G. Spence</i> DATE <i>11/29/66</i>		DWG SIZE D			
THRU				CUSTOMER					
EFFECTIVE SERIAL NO. USAGE DATA				SIMILAR TO		CODE IDENT NO. 13655			
PART DASH NO.				ACT. WT. CALC. WT.					
NEXT FINAL				DRAWING LEVEL		DWG NO. DWAAD-3341			
NEXT ASSY				APPLICATION					
USED ON				DRAWING LEVEL		SCALE NONE RELEASE DATE 4-7-67 SHEET			
DRAWING LEVEL				APPLICATION					

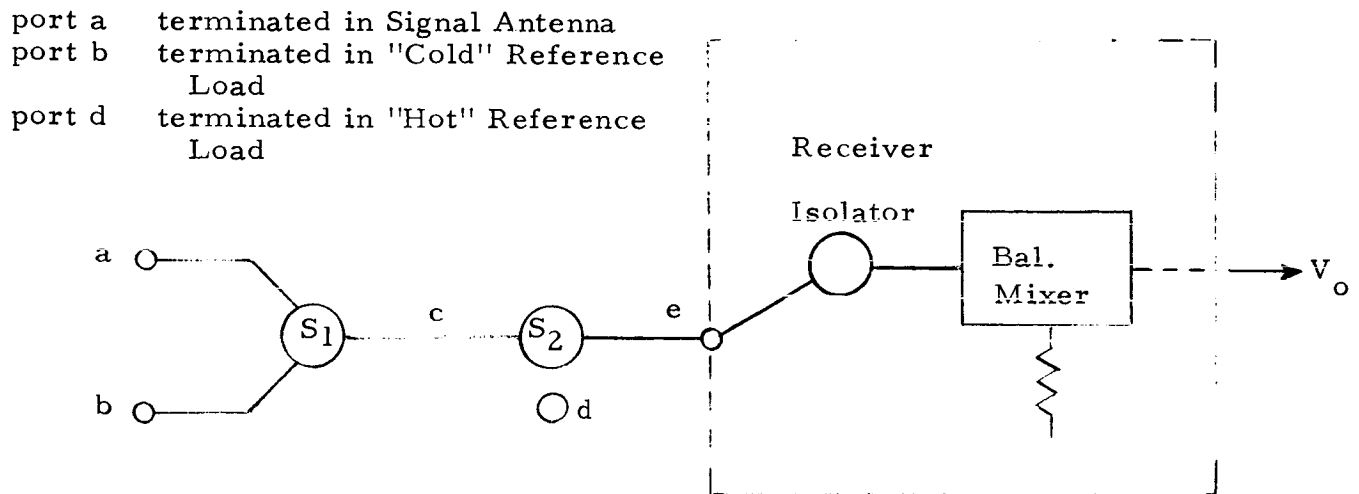
Appendix XX

BENCH CALIBRATION OF METEOROLOGICAL SATELLITE RADIOMETER

INTRODUCTION

The following notes are intended to explore some of the problems associated with the procedures employed in achieving absolute calibration of a microwave radiometer employing both an internal "hot" reference and an external "cold" reference.

The two external microwave input ports of radiometer are connected to a signal antenna and a "cold" radiometric reference load during normal operational use. These two ports together with a third port terminated in a "hot" radiometric reference constitute the three input ports to the microwave switching network located between the signal antenna and the receiver. The configuration is shown in Block Diagram No. 1.



Block Diagram of Microwave Switching and Calibration Network

In the following discussions devoted to the radiometer calibration procedures the following conditions are assumed to be true.

- (1) The voltage reflection coefficients associated with the microwave switches S_1 and S_2 are sufficiently small so that the mismatch insertion losses $\frac{1}{|1 + \Gamma_V|^2}$ are negligibly small compared to the dissipative components of the insertion losses in the forward directions.
- (2) The impedance mismatch of the terminations on ports a, b, d, and e is sufficiently good so that the power reflection coefficient $|1 + \Gamma_V|^2$ is less than 1×10^{-3} .
- (3) The inherent reverse isolation of the switches is sufficiently high so that it is determined by the power reflection coefficient of the third port.
- (4) The input of the receiver as seen at port e appears to have a radiometric temperature equal to the thermometer or ambient temperature of the switches S_1 and S_2 , i. e., the isolator at the input to the receiver balanced mixer has a sufficiently high reverse isolation to attenuate the excess temperature emitted from the signal port of the balanced mixer to less than 1°K at port e.
- (5) The isolation of the receiver input isolator is sufficiently great that the receiver gain is totally independent of any impedance variations seen at port e of the switching network.

With these assumptions satisfied it is possible to relate the radiometric temperature of the switching network output at port e to the thermal temperatures, the terminations at ports a, b and d and the insertion losses of the intervening paths.

The radiometric temperature outputs corresponding to the four combinations of settings for switches S_1 and S_2 are:

$S_1 \quad S_2 \quad T_e$

$$a \quad d \quad T_{ed} = \frac{T_d}{L_{de}} + \left(\frac{L_{de} - 1}{L_{de}} \right) T_o \quad (1)$$

$$b \quad d \quad T_{ed} = \frac{T_d}{L_{de}} + \left(\frac{L_{de} - 1}{L_{de}} \right) T_o \quad (2)$$

$$a \quad c \quad T_{ea} = \frac{T_a}{L_{ae}} + \left(\frac{L_{ae} - 1}{L_{ae}} \right) T_o \quad (3)$$

$$b \quad c \quad T_{eb} = \frac{T_b}{L_{be}} + \left(\frac{L_{be} - 1}{L_{be}} \right) T_o \quad (4)$$

Since switch S_2 is the periodic switch of the radiometer system the output voltage of the radiometer is equal to:

$$S_1 \text{ at } a \quad V_o|_a = G_r \left[\frac{T_d}{L_{de}} + \left(\frac{L_{de} - 1}{L_{de}} \right) T_o - \frac{T_a}{L_{ae}} - \left(\frac{L_{ae} - 1}{L_{ae}} \right) T_o \right]$$

$$S_1 \text{ at } b \quad V_o|_b = G_r \left[\frac{T_d}{L_{de}} + \left(\frac{L_{de} - 1}{L_{de}} \right) T_o - \frac{T_b}{L_{be}} - \left(\frac{L_{be} - 1}{L_{be}} \right) T_o \right]$$

List of Definitions for equations

- G_r - The radiometer gain coefficient, volts change at the output per degree Kelvin change of receiver source temperature at port "e".
- T_d, T_b, T_a - The radiometric temperature of perfectly impedance matched terminations at ports d, b and a respectively.
- L_{ae}, L_{be}, L_{de} - The attenuations (power ratio to port e from ports a, b and d respectively).
- T_o - The ambient thermal temperature of the microwave ferrite switches S_1 and S_2 .

It is intended to use the terminations at ports b and d as radiometric references to establish the radiometer gain and to provide an absolute scale to which to relate the radiometric temperature derived at port a.

Clearly a necessary requirement is that the gain as measured with the switch S_1 in position b be independent of the thermal temperature of the switching network. This necessitates that the attenuations L_{be} and L_{de} be equal.

Since the paths (b-e) and (a-e) extends through two switches while the path d-e goes through only one, it is necessary to add attenuation to L_{de} and either L_{ae} or L_{be} that $L_{de} = L_{be} = L_{ae}$.

With the condition $L_{de} = L_{be}$ established the radiometric gain constant measured with switch S_1 in position b is

$$\frac{G_r}{L_{be}} = \frac{V_o|_b}{T_d - T_b}$$

To insure that over a 330°K temperature range the error in indicated temperature is less than one degree requires that these three attenuations be equalized within 0.03 dB.

With these conditions established the equations for V_o reduce to

$$S_1 \text{ at a} \quad V_o|_a = \frac{G_r}{L_{be}} [T_d - T_a]$$

$$S_1 \text{ at b} \quad V_o|_b = \frac{G_r}{L_{be}} [T_d - T_b]$$

and the measured radiometric temperature T_a is expressed as

$$T_a = T_d - \frac{V_o|_a}{V_o|_b} (T_d - T_b)$$

where T_d and T_b are the hot and cold radiometric temperatures references respectively.

It is also apparent from the above that if the insertion losses from all three ports are equalized, and then ports a, b, and d terminated in equal temperature loads, the radiometer zero set is established, i. e., the radiometer output remains constant independently of the three termination temperatures.

Thus the first stage of the overall calibration consists of establishing the radiometric zero setting and equalizing the switching network insertion losses. This equalization will eliminate the dependence of the radiometer calibration upon the ambient temperature of the switches S_1 and S_2 , provided their insertion losses are sufficiently constant within the required range of ambient temperatures. Even if these insertion losses should vary slightly the temperature dependence is greatly reduced to a point where any corrections required using the switch temperature monitor output data should amount to less than 3°K over the full range of 0° to 50°C ambient temperatures.

STEPS IN BENCH CALIBRATION

1.0 RADIOMETRIC ZERO SETTING AND EQUALIZATION OF MICRO-WAVE SWITCHING NETWORK INSERTION LOSSES

1.1 RADIOMETRIC ZERO SET

The radiometer is brought to an ambient temperature of 35°C together with the matched terminations at ports a, b and d. For this condition the radiometric temperature presented by the switch output port e to the receiver input is independent of the insertion loss associated with a particular selection of ports a, b, and d. Consequently the radiometer output voltages corresponding to S_1 positions a and b should both be equal to zero. This procedure provides an output voltage reference corresponding to a radiometric zero point calibration. The individual steps of this measurement are:

1.1.1 Place the radiometer in an oven stabilized to within $\pm 0.5^\circ\text{C}$ at 35°C . The hot reference load heater is disconnected, Hewlett Packard sliding type matched waveguide loads terminate the two external waveguide ports normally occupied by the signal antenna and the cold reference.

1.1.2 Calibrated thermistors⁽¹⁾ are placed on each of the two external loads and also on the aluminum block housing the two ferrite switches. These three

⁽¹⁾Appendix No. 1 on Thermistor Calibration

thermistors together with the monitor thermistor in the internal reference load are continuously monitored to provide a record of the termination temperatures and the ferrite switches.

1. 1. 3 Sufficient time must be allowed with radiometer operating in the temperature controlled oven to insure that the temperatures of the switches and load become equalized and stabilized to within $\pm 0.2^{\circ}\text{C}$. In this condition the radiometer output voltage is measured at the output of the synchronous detector by means of an operational amplifier integrator housing a 10 second (6 dB per octave) integration time.

This will result in the peak to peak fluctuations of the radiometric output voltage, originating from receiver thermal noise, to correspond to approximately 0.4° peak to peak fluctuations in the radiometer input temperature. It is thus apparent that if the measurement is to be limited only by receiver thermal noise, then the variations in the thermometric temperatures of the source must be smaller, e. g. , $\pm 0.2^{\circ}\text{K}$. The period of time, over which these temperature variations occur, must be long compared to the radiometer integration time.

1. 1. 4 The output voltage is then recorded simultaneously together with the four thermistor bridge output voltages and a timing marker by means of a calibrated six channel chart recorder.

1. 1. 5 With RF switch S_1 set at the signal antenna port (a).

1. 1. 6 With the switch S_1 set at the cold reference port (b).

1. 1. 7 With the 600 cps drive removed from the modulator RF switch S_2 .

Note: The radiometer output voltage (previously measured in the pick up and ground loop tests) with modulator switch S_2 operating but with the receiver input disconnected from the switch output by means of a metal window across the guide connecting the switch S_2 output to the receiver input isolator, gives the component of radiometer output voltage due to electromagnetic coupling between the switch S_2 drive coil and the video amplifier.

1.1.8 The difference between the average of the voltages measured in 1.1.5 and 1.1.6 and the output voltage measured in 1.1.7 gives the magnitude and sign of the radiometer output which is the summation of the voltages resulting from: any slight thermal differences in the switches and terminations, synchronous variation of the reflection coefficients looking into switch S_2 from the receiver direction, and electromagnetic pickup of the 600 cps by the video amplifier due to ground loops and electromagnetic coupling from the drive coil of the modulator switch S_2 . Since this ground loop and pickup voltage has been previously recorded, the remaining difference is the radiometer output component resulting from small differences in the input termination temperatures and the synchronous modulation of the reflection coefficient presented to the receiver.

Although it is anticipated that this quantity will correspond to a temperature difference of less than 1°K it is important to obtain quantitative verification.

The difference of the output voltage magnitudes obtained in steps 1.1.5 and 1.1.6 is indicative of the degree to which the temperatures of the external port terminations differ from each other and any differences in their impedance match.

From a previous approximate calibration of the radiometer it is possible to relate these voltages to relative temperature differences. The voltages obtained in steps 1.1.5 and 1.1.6 and 1.1.7 should each correspond to less than 1°K temperature difference.

The average of voltages 1.1.5 and 1.1.6 then correspond to zero radiometric temperature difference within the limits of the experimental ability to measure temperatures of the three sources and the switches.

With the radiometer zero point established the insertion loss equalization of the switching network can be initiated.

1.2 EQUALIZATION OF INSERTION LOSS FROM PORTS a AND b TO PORT e

Place two 65°C hot loads on ports a and b with the reference hot load remaining at the 35°C ambient temperature of the switches S₁ and S₂. Then observe the radiometer output voltage and observe with switch S₁ set at port a and at port b. Then interchange the loads on ports a and b, and again observe the output voltages with S₁ set at a and at b. Designating the two sets of voltages as v_{a1}, v_{b1}, and v_{a2}, v_{b2} respectively, the radiometer voltage output due to any radiometric temperature difference in the two sources is given by

$$ST = \frac{(v_a - v_b)_1 - (v_a - v_b)_2}{2g}$$

while the radiometer output voltage due to difference in the insertion losses L_{ae} and L_{be} is proportional to

$$\Delta T = \frac{(v_a - v_b)_1 + (v_a - v_b)_2}{2g}$$

where g is the approximate radiometer gain coefficient is expressed in terms of the average voltage output increase 'V' over the previously established radiometer zero output by the relation

$$g = \frac{V}{T_H - T_o} = \frac{V}{(65 - 35)^\circ K}$$

the difference between the two attenuations L_{ae} and L_{be} is determined from the indicated radiometric temperature difference ΔT.

$$\Delta T = \left[\frac{T_H}{L_{ae}} + \left(\frac{L_{ae} - 1}{L_{ae}} \right) T_o \right] - \left[\frac{T_H}{L_{be}} + \frac{L_{be} - 1}{L_{be}} T_o \right]$$

assuming L_{be} = L_{ae} (1 + δ), and (L_{ae} - 1) << 1

$$T_o < T_H$$

The differential attenuation δ equals

$$\delta = \frac{\Delta T}{T_H - T_o}$$

attenuation is added then to the lower attenuation input port until ΔT in the above equation is reduced to 0.2°K . Previous insertion loss measurements indicate approximately 0.08 dB corresponding to an initial value of $S = .02$ and $\Delta T \approx 6^{\circ}\text{K}$.

1.2.1 Equalization of insertion loss from port d with ports a and b with ports a and b giving the same radiometric indication, the heating element in the reference hot load on port d is then activated allowing at least one hour for the temperature to stabilize to the value $T_H = 65^{\circ}\text{C}$ then the radiometer output is observed with the switch S_1 in either position a or b. Now all three ports are terminated in the same temperature to within the accuracy of the monitor thermistors in the three hot loads. If the insertion loss L_{de} equalled $L_{ae} = L_{be}$ the radiometer output voltage would be equal to the previously determined radiometric zero value. The same procedure of interchanging hot loads is used to eliminate the effects of load temperature differences and attenuation is added to port d until the output voltage equals the radiometric zero value within $+0.2^{\circ}\text{K}$.

1.2.2 CHECK OF TEMPERATURE SENSITIVITY OF INSERTION LOSS EQUALIZATION

Maintaining the hot loads on the three ports at 65°C , the ambient temperature of the radiometer is then very slowly over a period of 4 hours reduced to 0°C and the output voltage change observed. If the load monitor thermistors ratings remain unchanged, then any change in the output voltage is a radiometric zero shift resulting either from a gain change in the receiver electronics or more likely from attenuation unbalance resulting from attenuation change with temperature in the ferrites of switches S_1 and S_2 . The same observation should be made with a 50°C ambient for the radiometer. Repeating these measurements should permit correlation of radiometric zero drift with ambient temperature and thus allow the derivation of a radiometric data correction factor for use with the switch monitor thermistor data output record. In the above measurements as the ambient is changing it should be possible to obtain a repeatable curve of radiometric zero shift as a function of the switch temperature monitoring thermistor.

2.0 RADIOMETER CALIBRATION WITH EXTERNAL RADIOMETRIC TEMPERATURE REFERENCES

The radiometric zero setting and the insertion loss equalization of the switching network completed we are now in a position to calibrate the radiometer output voltage vs varying antenna port temperature for several different values of fixed temperature terminations on port a. Interchanging the radiometric sources with the various fixed temperature terminations on the antenna port a and varying the cold reference port b termination should produce the same radiometric output. Repeating these procedures for several different ambient temperatures between 0°C and 50°C and employing if necessary any ambient temperature dependent correction factors previously determined in Section 1.2.2 should establish the absolute accuracy to which the radiometric temperature of the antenna port can be ascertained from the radiometric output voltage and knowledge of the hot and cold reference ports radiometric temperatures and the switching network ambient temperature.

Appendix XXI

MEASUREMENT OF NIMBUS ANTENNA RADIOMETRIC EFFICIENCY

SITE: Table Mountain, California

1.0 INTRODUCTION

The objectives of this series of tests is to establish the radiometric efficiency of the antenna and to quantitatively relate the radiometric temperature at the antenna output to the brightness temperature of an object filling the antenna beam. An ideal antenna is one which receives all of its energy from the primary beam (i. e., sidelobes = 0) and transmits all of this energy to its output. Practical antennas diverge from this ideal in that as a consequence of sidelobes the power received in the main beam is reduced. For a given incident power from a source completely subtended by the main beam, the ratio of the power received with a given antenna compared to the incident power will be referred to here as the radiometric beam efficiency of the antenna. The sum of radiation received from objects intercepted by the sidelobes adds an additional power output to the antenna output which is termed radiometric background temperature. Dissipative loss occurring within the antenna and associated feed structures attenuates both the main beam and sidclobe components of the received radiation and adds a reradiation component to the total power available at the antenna output port. Thus, the power output of a practical receiving antenna may be described as the summation of two components of incident radiation P_{im} , P_{is} , the antenna dissipative insertion loss L_a of the antenna and an associated reradiation component P_{ae} . The incident components are defined as follows:

P_{im} = the power incident from the main beam

P_{is} = the total incident power from the sidelobes.

The three components of power available at the output port to the receiver are:

$$\text{The main lobe component } P_{rm} = \frac{P_{im}}{L_a}$$

$$\text{The side lobe component } P_{rs} = \frac{P_{is}}{L_a} (1 - E)$$

The antenna loss reradiation component P_{ae}

These power components may be related to radiometric brightness temperatures of the objects in the main and side lobes and to the thermal temperature of the dissipative elements in the antenna structure. We assume that the main beam observes a uniform brightness temperature T_{im} and that all of the sidelobes observe a uniform brightness temperature T_{is} , and that the antenna loss elements have a thermal temperature T_{ae} . The total power available to a receiver at the antenna port is then:

$$P_{at} = \frac{E}{L_a} P_{im} + P_{is} \frac{(1 - E)}{L_a} + P_{ae}$$

or

$$P_{at} = kb \left[\frac{E T_{im}}{L_a} + \frac{(1 - E)}{L_a} T_{is} + \frac{L_a - 1}{L_a} T_{ae} \right]$$

where:

B = the receiver predetection bandwidth

k = Boltzmann's constant

L_a = the dissipative insertion loss of the antenna

It will be assumed that within the bandwidth B that the antenna characteristics are initially uniform. Furthermore it is assumed that within this bandwidth both the antenna and the receiver input are sufficiently well impedance matched to the interconnecting transmission line so that any intervening insertion loss is purely dissipative, i. e., negligible power reflection.

The radiometric temperature of the antenna T_{at} output is thus given by

$$T_{at} = \frac{P_{at}}{kB} = \frac{E}{L_a} T_{im} + \left(\frac{1 - E}{L_a} \right) T_{is} + \left(\frac{L_a - 1}{L_a} \right) T_{ae}$$

The objectives of the measurements to be conducted at Table Mountain are to accurately ascertain the values of E and L_a .

The antenna is a two dimensional planar array which is electronically scanned over a range of $\pm 50^\circ$ in approximately 2.5° steps. Thus, it will be necessary to determine the values of L_a and E at a sufficient number of angular portions within this range to permit an accurate determination of their variation as a function of scan angle.

In the following test procedures the radiometer itself is assumed to be calibrated. The calibration of the radiometer exclusive of the antenna is described in a separate document.

The principles underlying the tests and reasoning leading to the particular test approach will now briefly be discussed prior to their detailed description.

From the equation for T_{at} it is apparent that if the incident temperatures T_{is} and T_{im} were both zero then a measurement of T_{at} by the radiometer and T_{ae} by a precision thermometer would permit L_a to be computed as

$$L_a = \frac{1}{1 - T_{at}/T_{ae}} = \frac{T_{ae}}{T_{ae} - T_{at}}$$

Although zero values for $T_{im} + T_{is}$ are impossible since the minimum radiometric brightness temperatures available for the antenna are limited by atmospheric absorption at zenith and the isotropic universal background radiation. Atmospheric absorption can be minimized by locating at a relatively high elevation where water vapor absorption is greatly reduced. For this reason Table Mountain with an elevation of 7200 ft. was selected as the test site. Under clear sky conditions the zenith sky temperature observed will be less than $10^\circ K$ and ascertainable to an accuracy of $\pm 1^\circ K$.

If both T_{is} and T_{im} could be made approximately equal to the zenith temperature T_z then the equation for T_{at} is

$$T_{at} = \left[\frac{E}{L_a} + \frac{(1 - E)}{L_a} \right] T_z + T_{ae} \left(\frac{L_a - 1}{L_a} \right)$$

$$T_{at} = \frac{T_z}{L_a} + \frac{T_{ae} (L_a - 1)}{L_a}$$

In practice $T_{is} + T_{im}$ can be made nearly equal by placing a reflecting surface at the back and flaring out along the sides of the antenna so that the sidelobes are reflected into a cone centered at zenith.

Under clear sky conditions the atmospheric absorption varies only very slightly within this angle.

T_z can also be determined from the atmospheric attenuation obtained by observing the radiometric brightness temperature of the sun as a function of zenith angle, and also under these conditions, the predominant portion of T_{at} will be due to the reradiation from the insertion loss of the array antenna.

The antenna loss L_a can be measured for different thermal temperature of the antenna. The loss L_a should be independent of the thermal temperature of the antenna. The thermal temperature range that can be obtained is 0°C to 30°C by taking advantage of the natural ambient temperature range and using electrical heaters.

The next step is to measure the efficiency E of the antenna. This will be accomplished by placing a disk shaped black body target in the main lobe of the antenna pattern. The disk will be shaped to fill the main lobe of the antenna out to the null points at a distance of 40 feet above the antenna. The thermal temperature of the disk, T_d , will be monitored by a thermistor. By maximizing the radiometer output signal the disk can be centered in the beam. Since the disk fills the beam at the null points the accuracy of the measurement is not a strong function of the disk centering.

The antenna output temperature T_{at} is now given by

$$T_{at} = \frac{E T_d}{L_a} + \frac{(E - 1) T_z}{L_a} + T_{ae} \left(\frac{L_a - 1}{L_a} \right)$$

where

- T_{at} = antenna output temperature
- E = efficiency
- L_a = antenna loss
- T_d = thermal temperature of the disk
- T_{ae} = thermal temperature of the antenna
- T_z = zenith sky temperature

Since the efficiency, E , of the antenna is known from the antenna pattern measurements to be near 0.9, the loss $L_a \approx 1$ dB, and $T_z \approx 10^\circ\text{K}$, the second term in the above equation is $\approx 1^\circ\text{K}$. The loss L_a is known from the previous measurement, and the thermal temperatures of the disk, T_d , and the antenna, T_{ae} , are known. The antenna radiometric output temperature is measured and from the above formula the efficiency can be calculated.

2.0 TEST PROCEDURE

2.1 The radiometer will be recalibrated with the cryogenic bench test set on arriving at Table Mountain before proceeding with the tests of the antenna.

2.2 The radiometer and antenna will now be mounted on the pedestal with the cryogenic load attached to the cold reference waveguide port.

2.3 The antenna coil currents will now be set to produce the 0° beam position and the antenna mechanically oriented to point the beam at the zenith.

2.4 The reflectors will now be placed around the radiometer to shield the antenna from the ground.

2.5 The radiometer output is recorded for two minutes by means of the digital printer.

2.6 During the measurement of Sec. 2.5, the following parameters are also recorded:

Ambient air temperature

Humidity

Barometric pressure

Sky cover

Thermal temperature of antenna

2.7 From the data of Sec. 2.5 and Sec. 2.6, the antenna loss in dB will be calculated.

2.8 By means of towers a disk of absorbing material is positioned over the antenna so that it fills the main lobe out to the null points. The height of the disk above the antenna is 40 feet.

2.9 The radiometer output is now recorded for two minutes by means of the digital printer.

2.10 During the measurement of Sec. 2.9, the following parameters are also recorded:

Ambient air temperature

Humidity

Barometric pressure

Sky cover

Thermal temperature of antenna

Thermal temperature of absorbing disk

Height of disk above antenna

Motion of disk above antenna

Motion of disk (estimated)

2.11 The disk's position is now moved while observing the radiometer output to maximize the temperature recorded at the output of the radiometer, and data taken as discussed in Sec. 2.9 and Sec. 2.10.

2.12 From the measurements in Sec. 2.10 and 2.11 and the antenna loss calculated in Sec. 2.7, the percentage of energy in the main lobe of the antenna is calculated.

2.13 The antenna coil currents are now set to position the antenna at -50° and the measurements described in Sections 2.2 through 2.12 repeated for this beam position.

2.14 The above measurements are now taken for the scan angles of -30° , -15° , $+15^{\circ}$, $+30^{\circ}$, and $+50^{\circ}$ in that order, repeating the steps in Sections 2.2 through 2.12.

2.15 From the above measurements, the antenna loss and percentage of energy in the main lobe of the antenna has been determined for the scan angles of -50° , -30° , -15° , 0° , $+15^{\circ}$, $+30^{\circ}$, $+50^{\circ}$, and this data is now compared to the antenna loss and beam efficiency obtained from the antenna pattern measurements of the loss of individual components.

2.16 Data format sheets will be provided to insure that all of the necessary data is recorded and analyzed in the same way for each of the measurements.

3.0 SUPPORT EQUIPMENT

The support equipment to perform these tests is shown in Figure 1. It consists of an antenna mount which can be scanned in elevation in a north-south direction. The radiometer and cryogenic cold load will be supported on this mount with the antenna fastened above the radiometer positioned to point the main lobe at the zenith. The antenna beam can be mechanically scanned $\pm 45^{\circ}$ from the zenith. A reflecting structure which can be placed about the antenna is

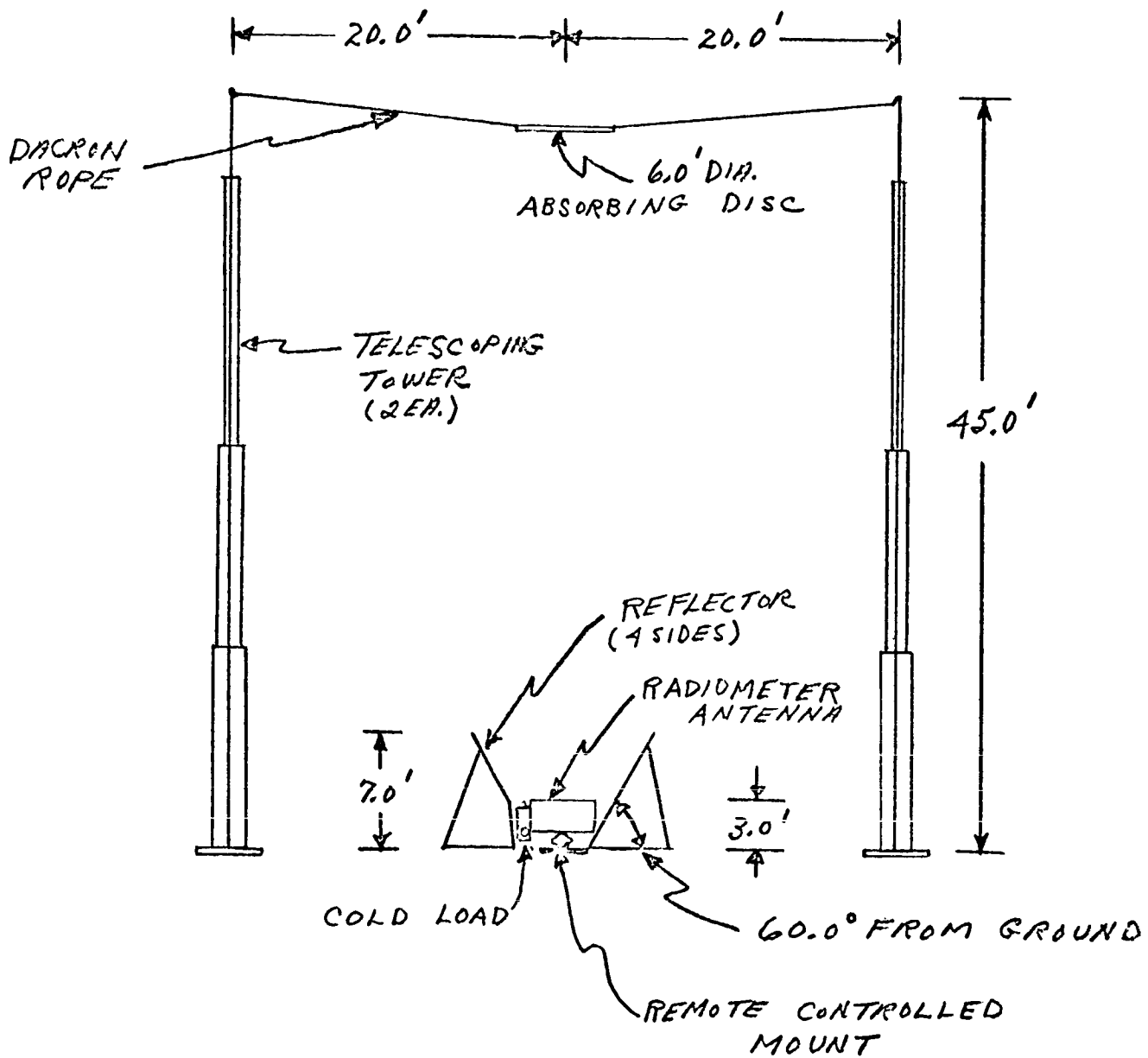


Figure 1. Support Equipment

provided to shield the antenna side and back lobes from the ground and to reflect the sky temperature into the side and back lobes. It is constructed of plywood lined with aluminum. It will be placed approximately one foot from the edges of the antenna and will flare out at an angle of 60° with respect to the ground. They can be moved in or out from the edge of the antenna if desired.

Two guyed 45' steel towers are provided to suspend a target of absorbing material above the antenna. The target will consist of a disk of absorbing material which fills the beam of the antenna out to the nulls of the main lobe. It is about 6 feet in diameter and is 40 feet above the antenna. The target is guyed with nylon ropes to allow it to be moved into position above the antenna. The target can also be adjusted in height.

The ground support equipment will be housed in a truck which can be heated. A small travel trailer will be used for office space.

3.1 TABLE MOUNTAIN TEST SITE

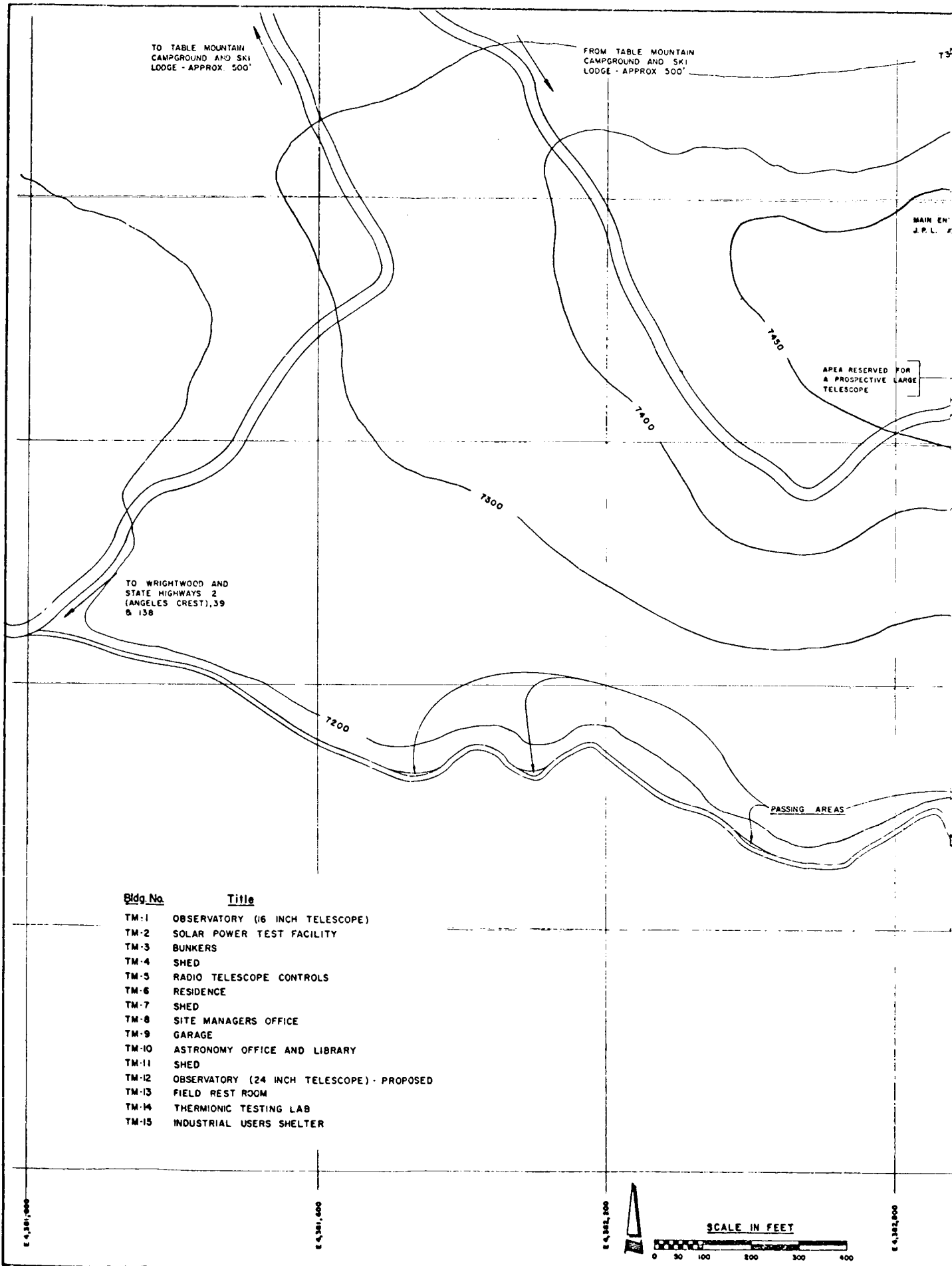
The test site selected is Table Mountain, near Wrightwood, California 65 miles from Space-General, and was chosen because of low humidity, highest convenient altitude available as well as the consideration that this location is operated by JPL for NASA specifically for radiometric type field testing for the above reasons. The altitude of the site is 7200 feet.

The specific locale is an isolated site consisting of a paved level area. The terrain is generally a hillside sloping off to the south, east and west. To the north the hillside rises at an angle of about 30° to the top of the hill about one-half mile away.

The only trees in the vicinity are on this north hillside about 100 ft from the specific test area and are not considered significant interference.

The only proviso accompanying NASA permission of use of this site was that of non-interference with other tests by other NASA contractors proceeding simultaneously, therefore, the towers will be lowered to the ground when needed.

A map of the test site is shown in Figure 2.



10-1

Figure 2. Map of Test Site

Appendix XXII

PRELIMINARY NIMBUS BREADBOARD TEST PROCEDURE (PRELIMINARY TESTING)

A. Ground Loop Checkout of r-f Portion of the Receiver

1. Equipment to be used for initial checkout is as follows: a noise tube and precision attenuator form one reference temp; the two other loads are the hot load and a room temp. load. The periodic switch will be driven by an HP 211A square wave generator at 600 cps. The non-periodic switch will be either turned on/off manually or by a low frequency square wave generator.

2. Initial measurements consist of simply monitoring the video pre-amplifier output on an oscilloscope. This method checks out the r-f portion of the receiver independently of the AGC, synch demodulator and digital portions of the receiver. Ground loops of this portion alone are to be eliminated.

B. Entire System Checkout

1. When the r-f section is felt to be free of ground loops the next step is to tie in with the AGC, Synch demod. and digital portion which are on vector boards. Since each section (the r-f and the digital) has separate ground points, the length of line interconnecting these two points will be kept to a minimum. Since the expected signal level at the video pream output is on the order of 1-3 mv/°K no adverse effect of having the two separate ground points may be encountered. At any rate this is a worst case condition.

2. Once all ground loops are either eliminated or recognized, the AGC and Synch. demod. that are located in the r-f box will be booked up and the system checked again. The signal level output to the integrate and dump circuit should then be on the order of 100 mv/°K or greater and any existing problems due to two separate ground points should be minimized. Should there still be a problem the video amp can be transformer coupled to break the d-c connection.

3. At this time the radiometer is free of ground loops and the insertion loss of the three signal paths to the receiver should be carefully measured if time allows.
4. Calibration of the receiver can begin at this point using cold load test set.
5. In lieu of measuring the insertion loss of each path, a close estimate of the loss can be made using the measured losses of the switch, circulator, and estimating the waveguide losses.

Appendix XXIII

NIMBUS RADIOMETER TEST SET - TELEMETRY INTERFACE CIRCUITRY

The radiometer test set provides interface signals necessary to simulate the Nimbus spacecraft from the antenna port input to the various telemetry outputs. The test set is capable of calibrating and thoroughly testing all functions of the radiometer. The test set consists of a microwave signal source and telemetry interface circuitry. Figure 1 is a functional block diagram of the test set with the microwave source to the left of the radiometer and the telemetry interface circuitry to the right.

The telemetry interface signals consist of the following four categories:

- a. Analog Signals - The analog signals provide the radiometer read out of reference load temperature, antenna sink temperature, temperature of the hottest point in the module and the radiometer supply voltage.
- b. Digital "A" Signals - The digital "A" signals read out serially the state of the analog to digital converter and the stepped AGC counter.
- c. Digital "B" Signals - The digital "B" signals provide the radiometer read out of the state of the power, antenna current read out and fail safe mode command relays.
- d. Command Signals - The command signals are magnetic latching relay drive pulses which set the state of the power, antenna current read out and fail safe mode command relays.

The above information read out of the radiometer is displayed by means of a vacuum tube voltmeter, page printer and front panel indicator lamps. The analog outputs are switch selectable and displayed on a 1 percent, mirrored, vacuum tube voltmeter. The analog to digital "A" output is displayed in decimal format on a page printer. Every 200 milliseconds the count of the analog to digital converter is printed as three decimal digits to the right of the printer page, and the parity bit as a one or zero to the left. The stepped AGC digital "A" output

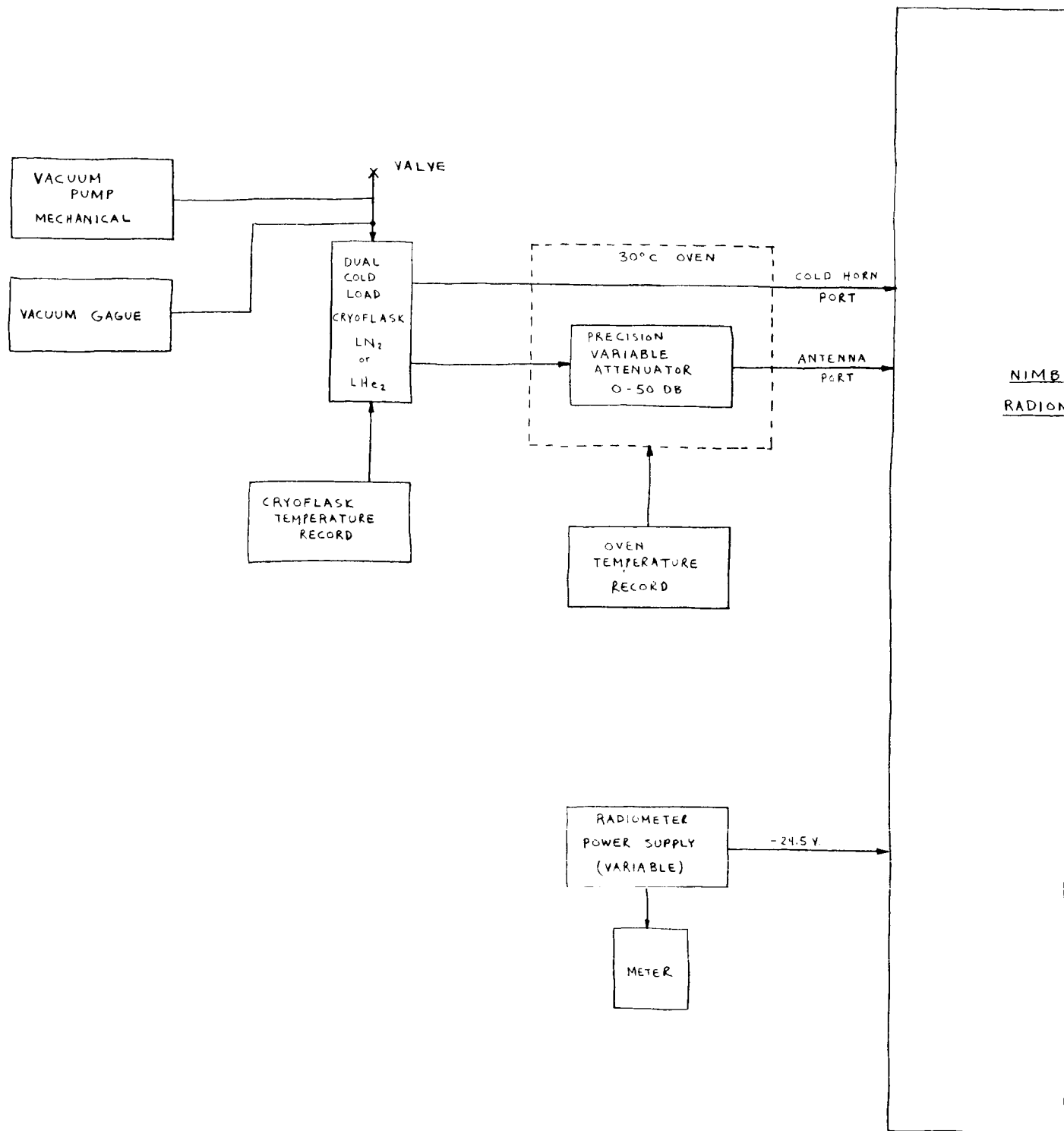
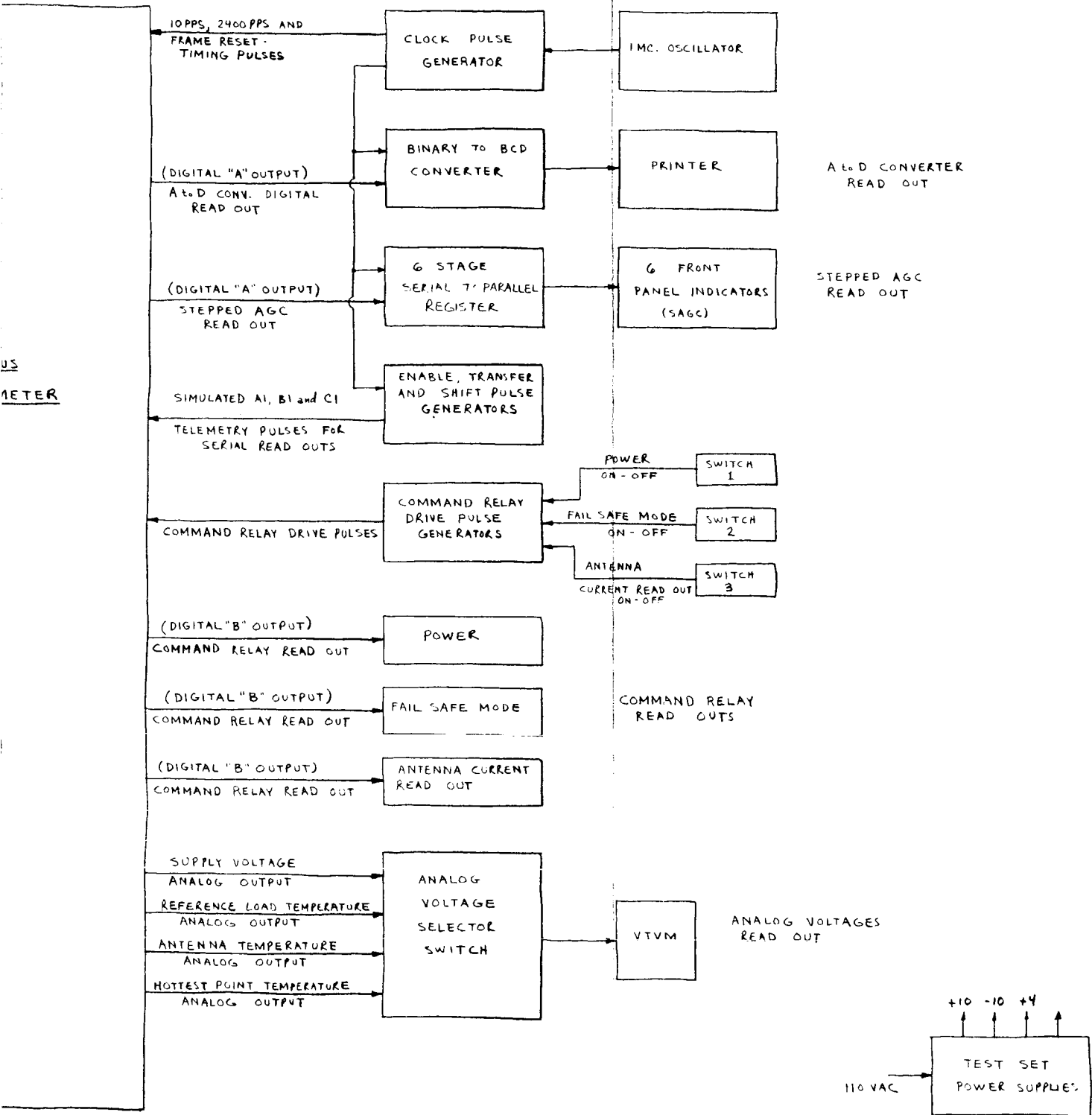


Figure 1. Block Diagram, Nimbus R



Radiometer Test Set

22

is displayed continually by six front panel lamps indicating the state of the six flip flops in the stepped AGC counter; 1/2 dB, 1 dB, 2 dB, 4 dB, 8 dB, and 16 dB attenuation respectively. The command relay read outs (digital "B" outputs) are displayed by means of three front panel lamps. The lamps are physically located in the pushbutton switches that generate the command pulses which set or re-set the relays. The supply voltage to the radiometer is indicated by means of an output voltmeter located on the power supply front panel.

In addition to accepting and displaying the above read out signals the test set provides clock and telemetry timing signals to synchronize the radiometer operations and output format to that of the test set. These signals are indicated as 10 pps, 2400 pps, frame reset timing pulses, A1, B1, and C1 telemetry pulses in the block diagram. The separate 24.5 volt supply to the radiometer allows the radiometer to be tested throughout its specified supply voltage range.

The timing of all signals and functions generated in the test set is derived from a one megacycle crystal oscillator. Through counters and various logic functions shown in Figure 2 the 1 Mc source is logically manipulated to generate clock rates of 2400 pps, 10 pps, 1 pulse/16 seconds and telemetry reference signals "A1," "B1" and "C1". These signals may be observed at test points TP-6, TP-7, TP-11, TP-8, TP-9 and TP-10 respectively. The format and amplitude characteristics of the telemetry digit "A" interface signals "A1", "B1" and "C1" is shown in Figure 3. The amplitude, rise times and impedance characteristics of the clock signals are identical to the "A1", "B1" and "C1" signal characteristics of Figure 3.

Clock pulses and telemetry pulses provide synchronization timing to the radiometer such that the digital "A" outputs may be read out synchronous to the test set timing. The digital "A" outputs read into serial to parallel registers in the test set for data processing and display. The analog to digital converter output is read into the serial to parallel converter of the binary to BCD converter shown in Figure 4. The converter output signal from the radiometer will have a "one" level of $+5 \pm 0.6$ volts and a zero level of 0 ± 0.6 V., an output impedance of 1K or less and rise and fall times of 1 microsecond or less.

NOTES:

CARDS J1 - J14 { +5V PIN E
6VD PIN A

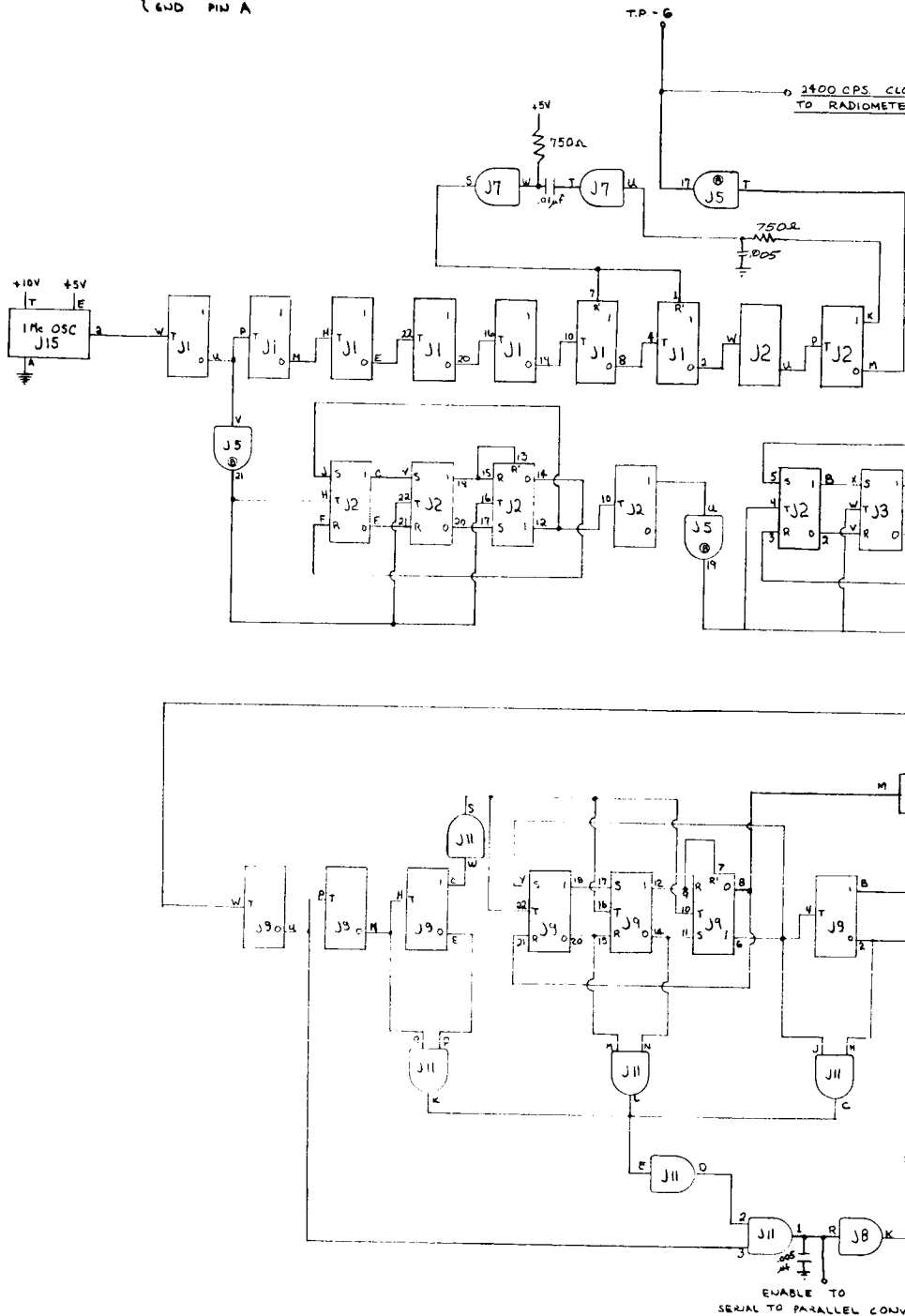
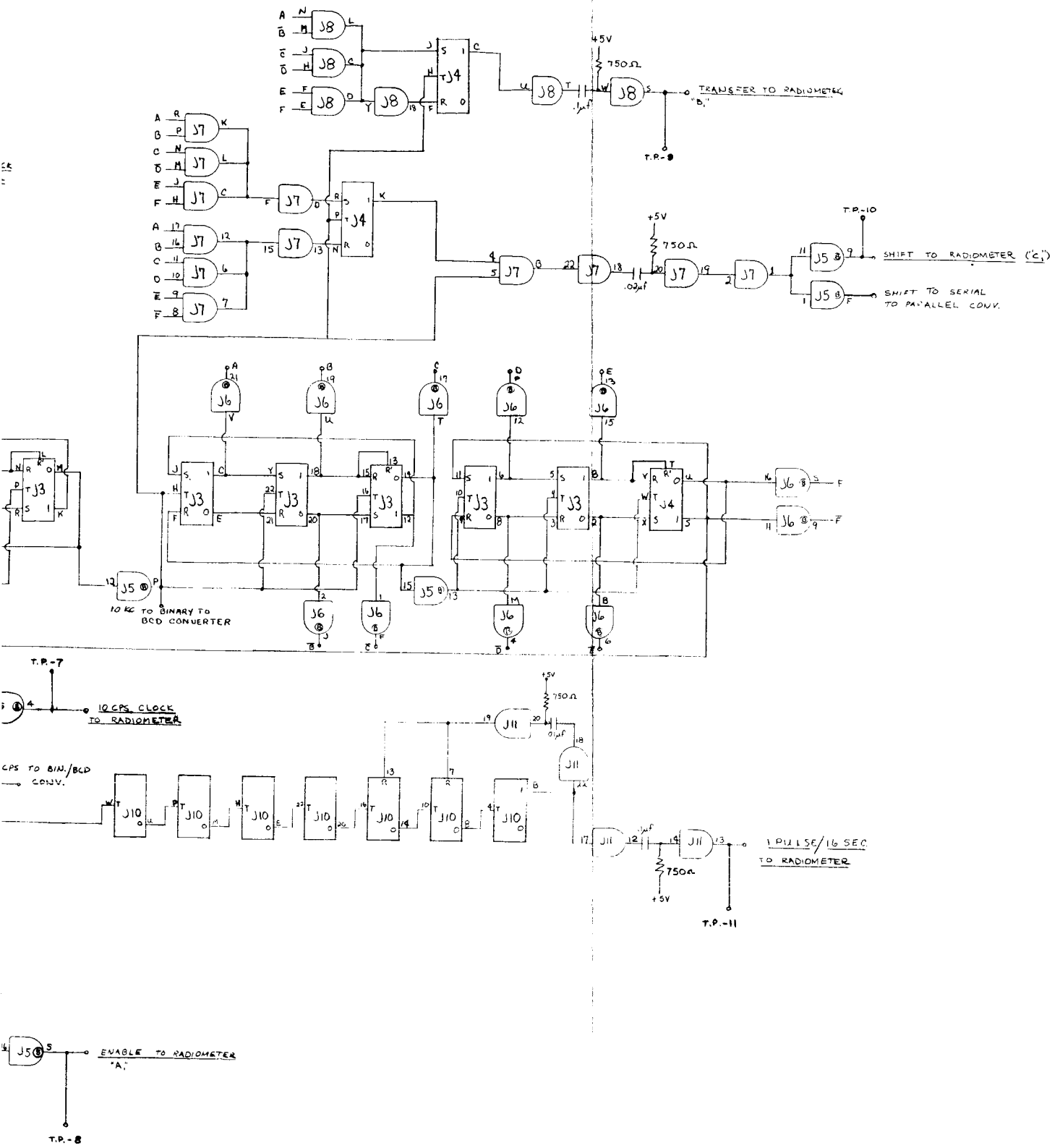


Figure 2. Nimbus Radiometer

4-1



Test Set "B" Rack No. 2

4-2

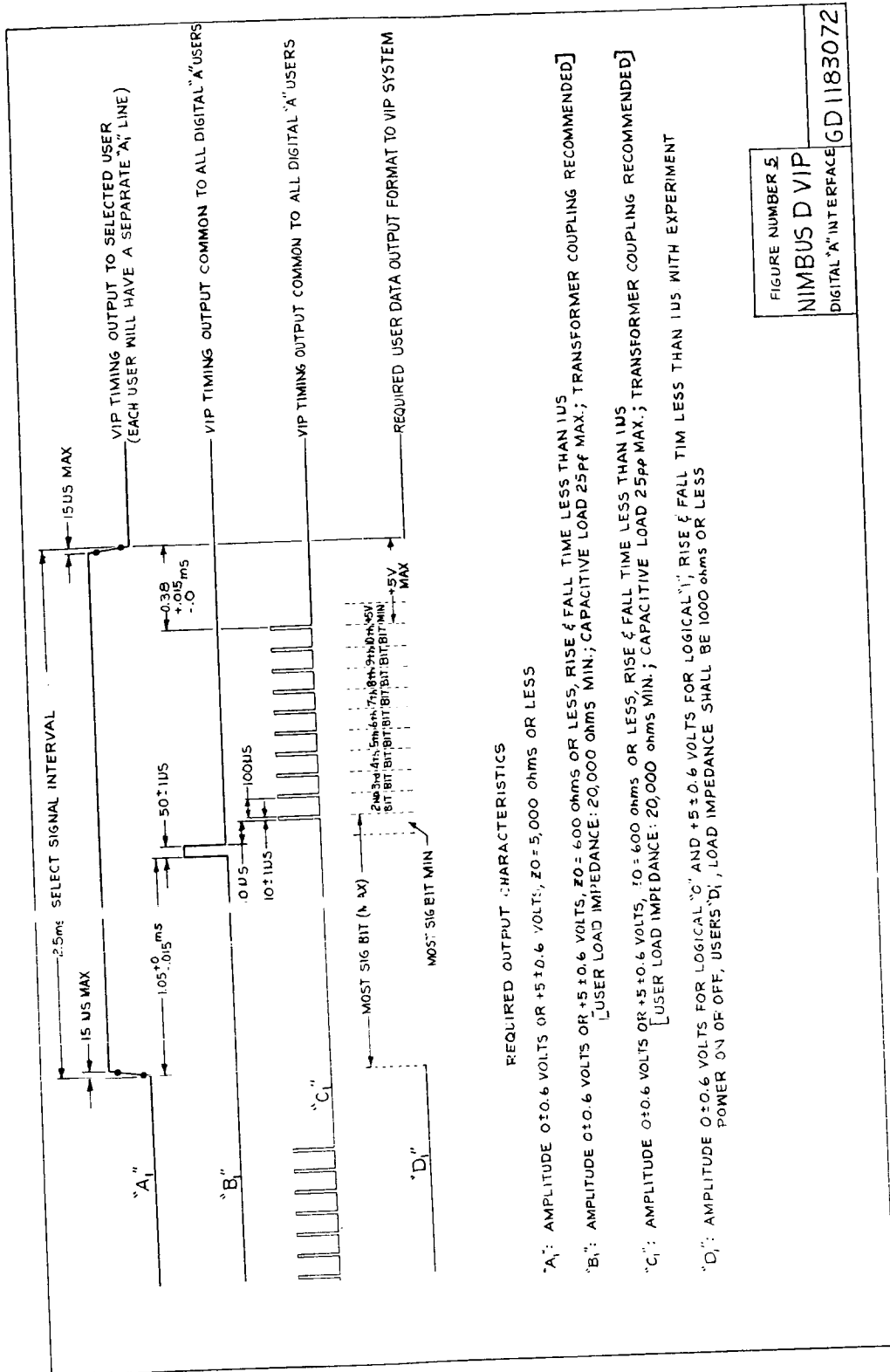


FIGURE NUMBER 5
 NIMBUS D VIP
 DIGITAL "A" INTERFACE
 GD1183072

Figure 3. Nimbus D VIP Digital "A" Interface

CARDS J1-J15 +4V PIN B
 CARD J16 -7.5V PIN B
 ALL CARDS GND PIN A

NOTES:

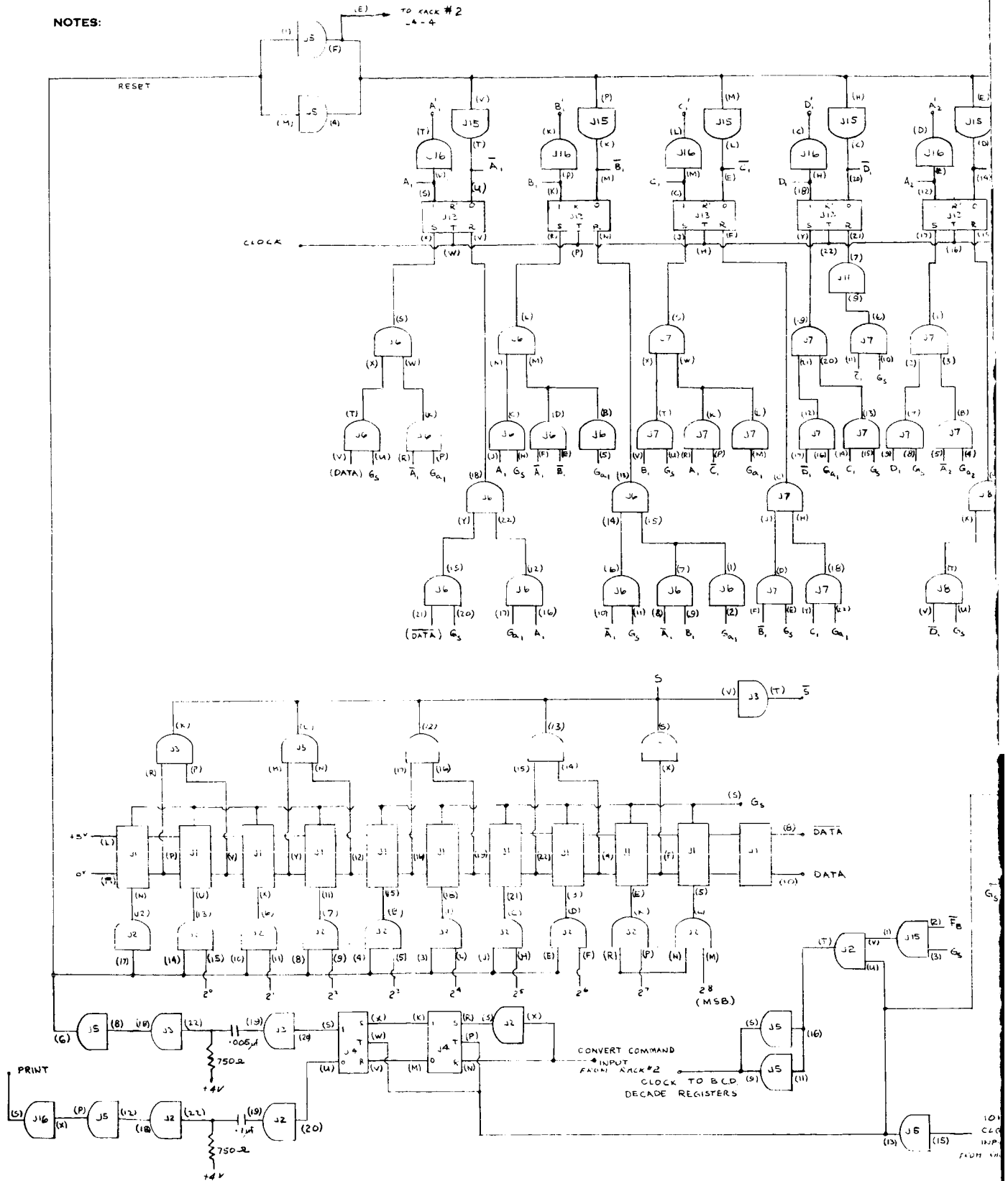


Figure 4. Nimbus Radiometer Test Set
 Rack No

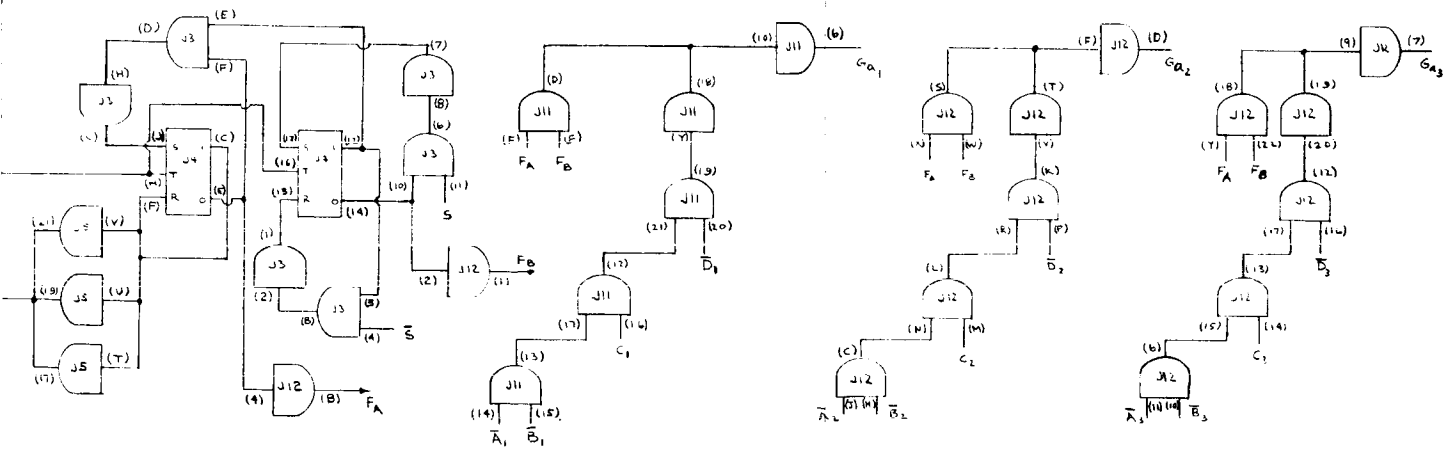
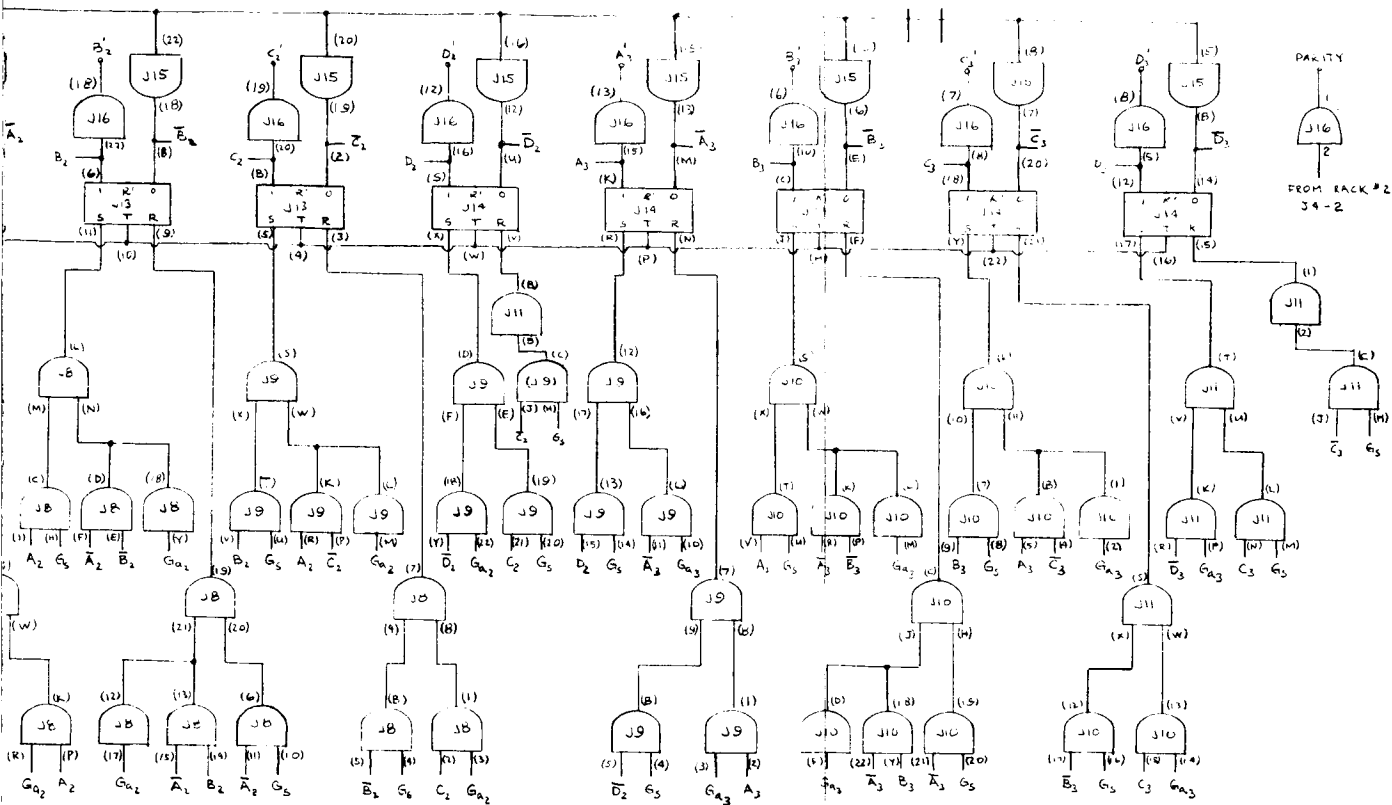


Diagram "A" Binary to BCD Converter

The binary to binary coded decimal converter (Figure 4) is necessary to convert the serial binary output of the A to D converter to BCD form such that the converter count may be displayed decimally and easily interpreted without the use of binary conversion tables. The converter accepts 9 bit parallel data from the serial to parallel input register and converts it, most significant bit first, to binary coded decimal data. The BCD data is stored in a parallel 12 bit 3 decade output register shown at the top of Figure 4. The conversion method used is the double dabble method.

The properties of binary numbers are such that a number may be doubled or halved simply by shifting the number one digit to the right or left with respect to a reference weighting position. A BCD number has the same property, but numbers which have been doubled must be adjusted because a radix of ten has been imposed. Doubling any four bit number greater than four in quantity results in a number 10 or greater which is beyond the limit of the constraint placed on a decimal digit. By adding six to any number greater than 9, as a result of doubling, a two digit number is created within a constrained radix of ten.

A convenient method of implementing the "add 6 correction" is to detect 4 bit digits that are greater than four in quantity and add three before doubling. This is equivalent to adding 6 after doubling but results in less hardware by eliminating the need for carry generation between decades.

The method used entails successive doubling, adding and correcting. The quantity in the BCD register is doubled by shifting the BCD number one place to the right and the next binary bit to be shifted into a particular decade is accumulated to the doubled number in that decade. Between each shift and add cycle the size of the number in each decade register is examined. If the number is greater than 4 an add cycle occurs, adding 3 and thereby generating the necessary correction factor. Each of the three decades are identical. The control logic and shift gate are shared by all decades, but a separate add gate is mechanized for each decade. The BCD three decade output register feeds and the BCD printer input through gates which act as buffer amplifiers to increase the output logic voltage level. A delayed conversion command is used as the print command to the page printer.

The frame format read out of the radiometer in the normal operating mode is shown in Figure 5. The frame reference (noted as frame identification from time increment number 480 in Figure 5) prints out all zeros indicating that the next print out or time period is the beginning of a new frame (period number 1). The frame consists of twelve subframes, each in turn consisting of 40 frame time periods corresponding to 40 decimal print outs. The first 39 frame periods are a read out of the temperature differential between the hot load and the antenna times the radiometer gain factor for the 39 antenna beam positions respectively. The 40th period of every odd subframe is a read out of the temperature differential between the hot load and cold horn references times the radiometer gain factor. Since the temperature of the hot and cold references are known the radiometer gain factor and ultimately the radiometric temperatures seen by the antenna for each beam position may be calculated. The 40th time period of every even subframe is a read out of various parameters time multiplexed into the frame such as antenna sink temperature, hot load temperature, etc. The frame time increments are 200 Ms in duration, therefore the printer reads out at a 5 BPS rate.

The second mode of radiometer operation is a housekeeping mode in which the current levels corresponding to each of the 39 beam positions of all 49 antenna coils are serially read out. This mode of operation is initiated by setting the "antenna current read out" command relay. In this mode the A to D converter quantizes input voltage levels which correspond to the various current levels of the antenna coils and the print out, therefore, is an indication of the beam steering computer operation since the beam steering computer supplies the antenna beam positioning currents. This read out is not meant to be a precise absolute current display, but a relative indication of the 1911 current levels with respect to each other such that any gross error in a particular current level such as zero current or saturating current caused by a catastrophic component failure will be observed.

The frame format of the antenna current read out is shown in Figure 6. As in the normal mode format the frame consists of subframes each 40 frame time periods in length. In the antenna current read out mode, however, a total frame consists of 50 subframes. The first 49 subframes read out 39 coil current

levels corresponding to 39 beam positions and zero current during the 40th time period for the 49 antenna coils. The 50th subframe reads out full scale (saturation) for the purpose of frame identification. Four hundred seconds is required to read out an entire frame since the frame time period again is 200 Ms.

The serial stepped AGC output is synchronously read into the serial to parallel display register shown in the upper left hand corner of Figure 7. The input signal amplitude, rise time and impedance is identical to that of the A to D converter output signal. Although the word read is in ten bits in length only the first six bits are significant information. The last six stages, therefore, of the register feed lamp drivers and front panel lamps which indicate the states of the six flip flops of the stepped AGC counter in the radiometer. The lamps indicate the attenuation of the stepped AGC circuit in binary weighted increments, 1/2 dB, 1 dB, 2 dB, 4 dB, 8 dB and 16 dB, respectively.

The command relay pushbutton switches, one shots and relay driving circuits are shown in the upper right hand corner of Figure 7. Each time a pushbutton is depressed the corresponding flip flop toggles. Each toggle alternately fires the right then left hand one shot which in turn generates pulses alternately to the set and reset coils of the corresponding command relay. Therefore, each time a given pushbutton switch is depressed the corresponding command relay in the radiometer changes states from open to closed and vice versa.

The state of the command relays is indicated by the digital "B" outputs (0 to -7.5 volts) which feed the emitter follower-lamp driven circuits in the lower left hand corner of Figure 7. The lamps are physically located in the pushbutton switches and lit when the function they describe is operative.

Figure 8 is a detailed connector interface schematic showing all interface signals and wires between the radiometer and the test set.

CARDS J1-J14, J19 — +5V PIN E
 CARDS J16 & J17 — { +10V PIN T
 - 24.5V PIN Z
 ALL CARDS — GND PIN A

NOTES:
 LAMPS &
 SWITCHES
 MOUNTED ON
 FRONT PANEL

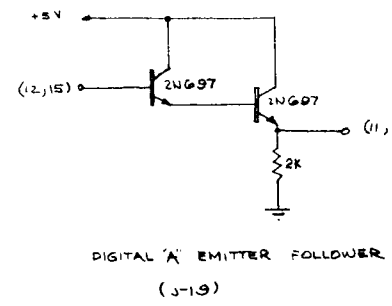
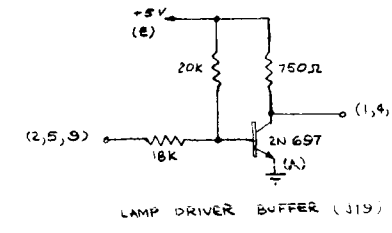
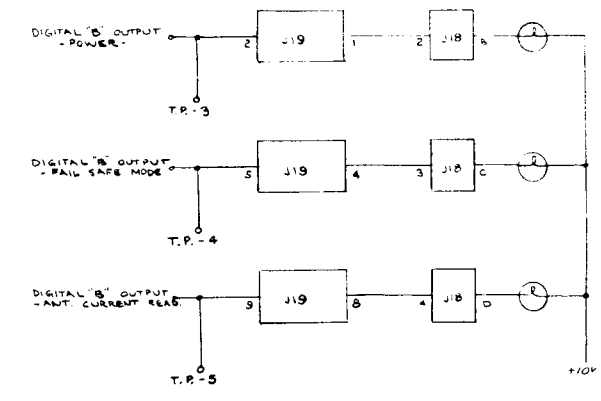
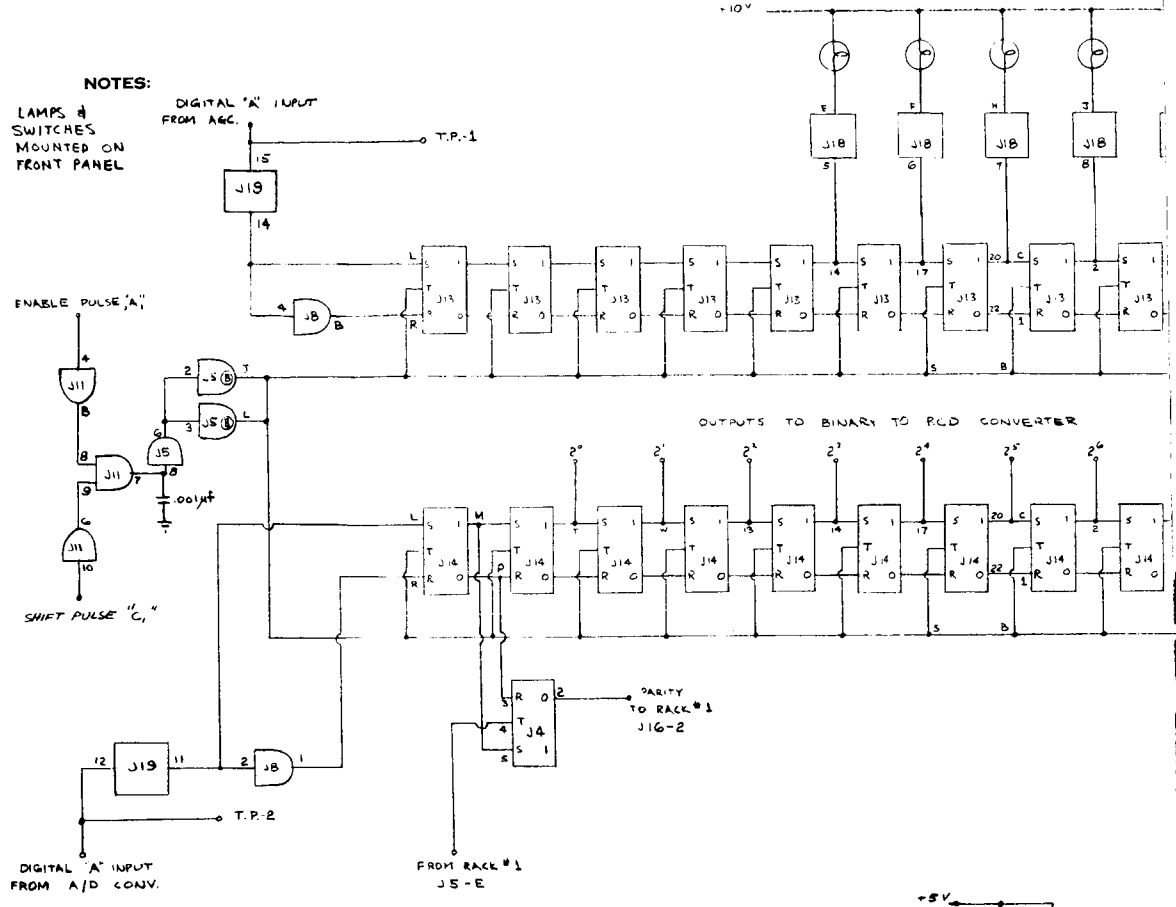
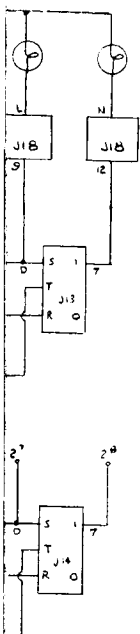
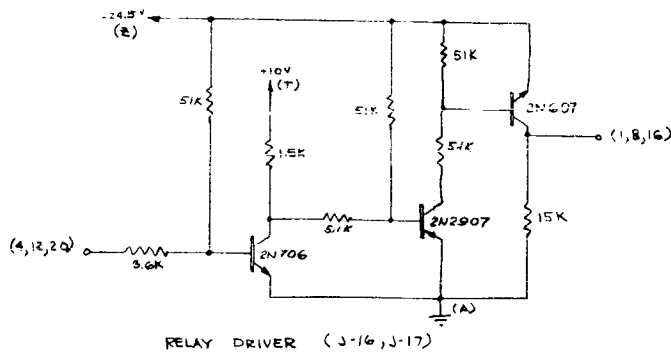
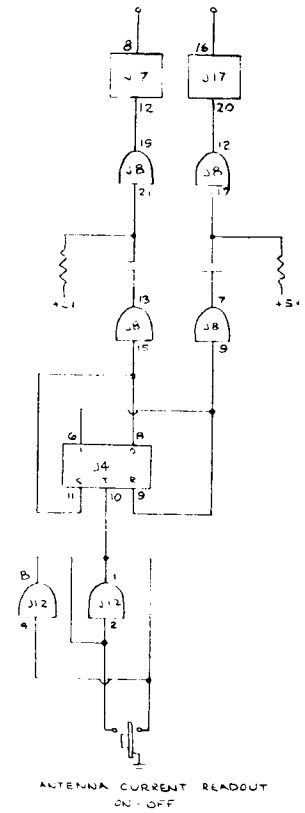
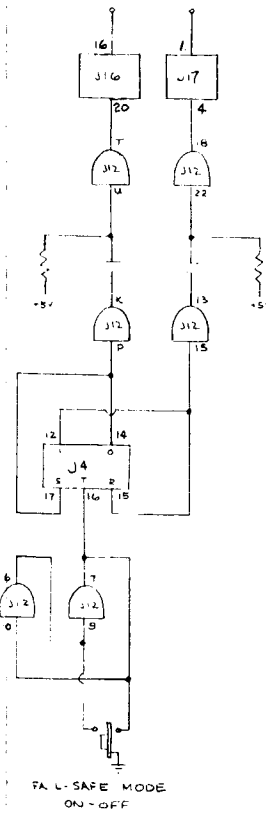
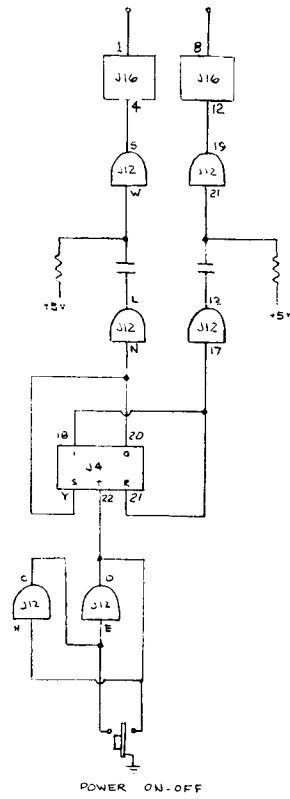


Figure 7. Nimbus Radiometer



PULSES TO COMMAND RELAYS

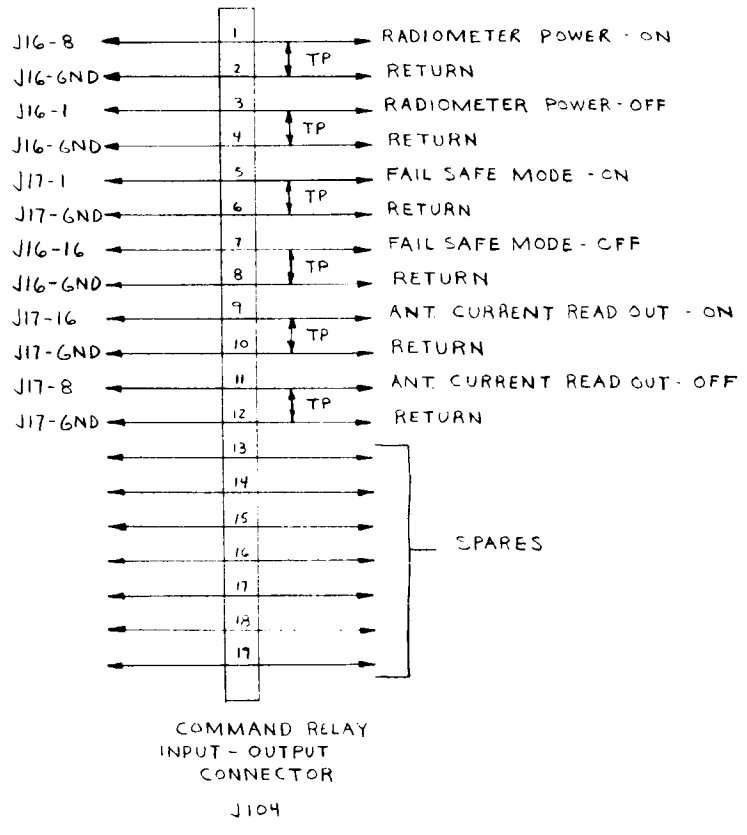


← TO TEST RACK

- ← J5-17
- ← J5-GND
- ← J5-GND
- ← J5-4
- ← J5-GND
- ← J11-13
- ← J11-GND
- ← J5-5
- ← J5-GND
- ← J19-15
- ← J19-GND
- ← J8-5
- ← J8-GND
- ← J5-9
- ← J5-GND
- ← J19-2
- ← J19-GND
- ← J19-5
- ← J19-GND
- ← J19-9
- ← J19-GND
- ← S1-B1
- ← S1-A1
- ← S1-B2
- ← S1-A2
- ← S1-B3
- ← S1-A3
- ← S1-B4
- ← S1-A4
- ← J19-12
- ← J19-GND
- ← J5-5
- ← J5-GND

← TO TEST RACK

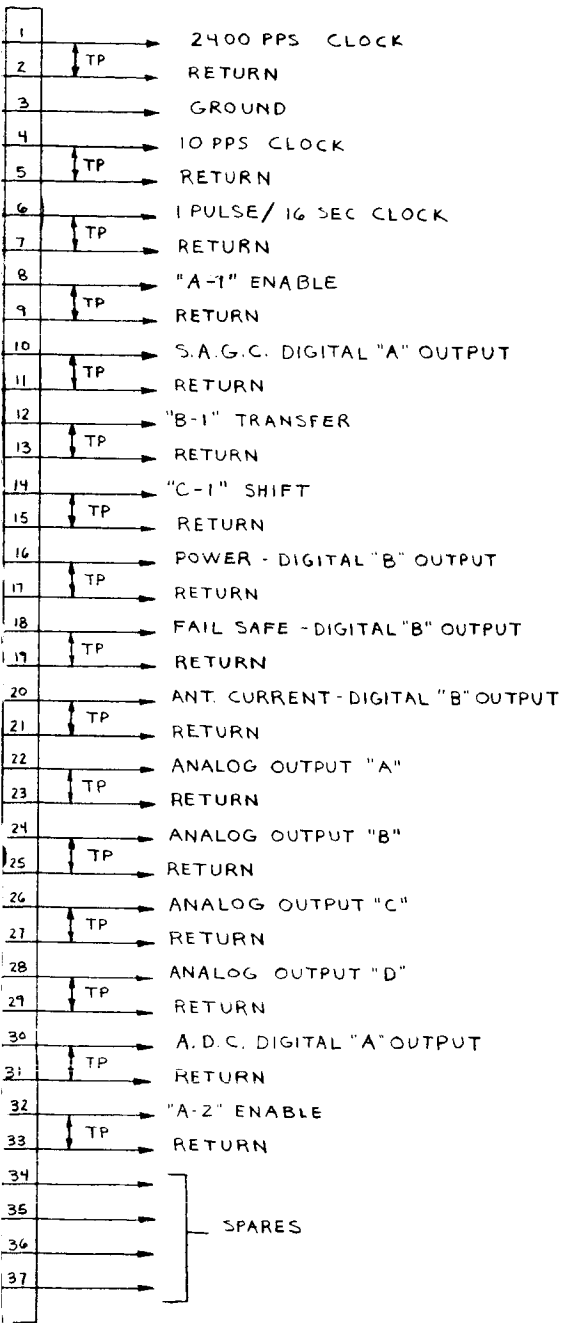
→ TO RADIOMETER



TEL
INPU
CC
J

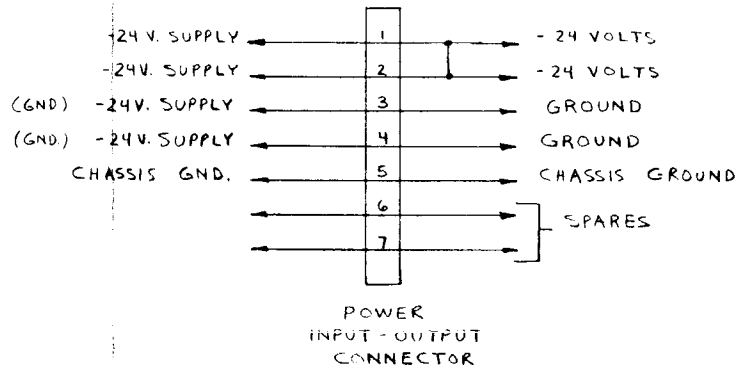
Figure 8. Nimbus Radiometer Test Se

TO RADIOMETER



MEETRY
T - OUTPUT
CONNECTOR
103

TO TEST RACK TO RADIOMETER



Input-Output Connectors

Appendix XXIV

EVALUATION OF THE BREADBOARD MICROWAVE
METEOROLOGICAL RADIOMETER AND SCANNING
ANTENNA

Section 1
INTRODUCTION

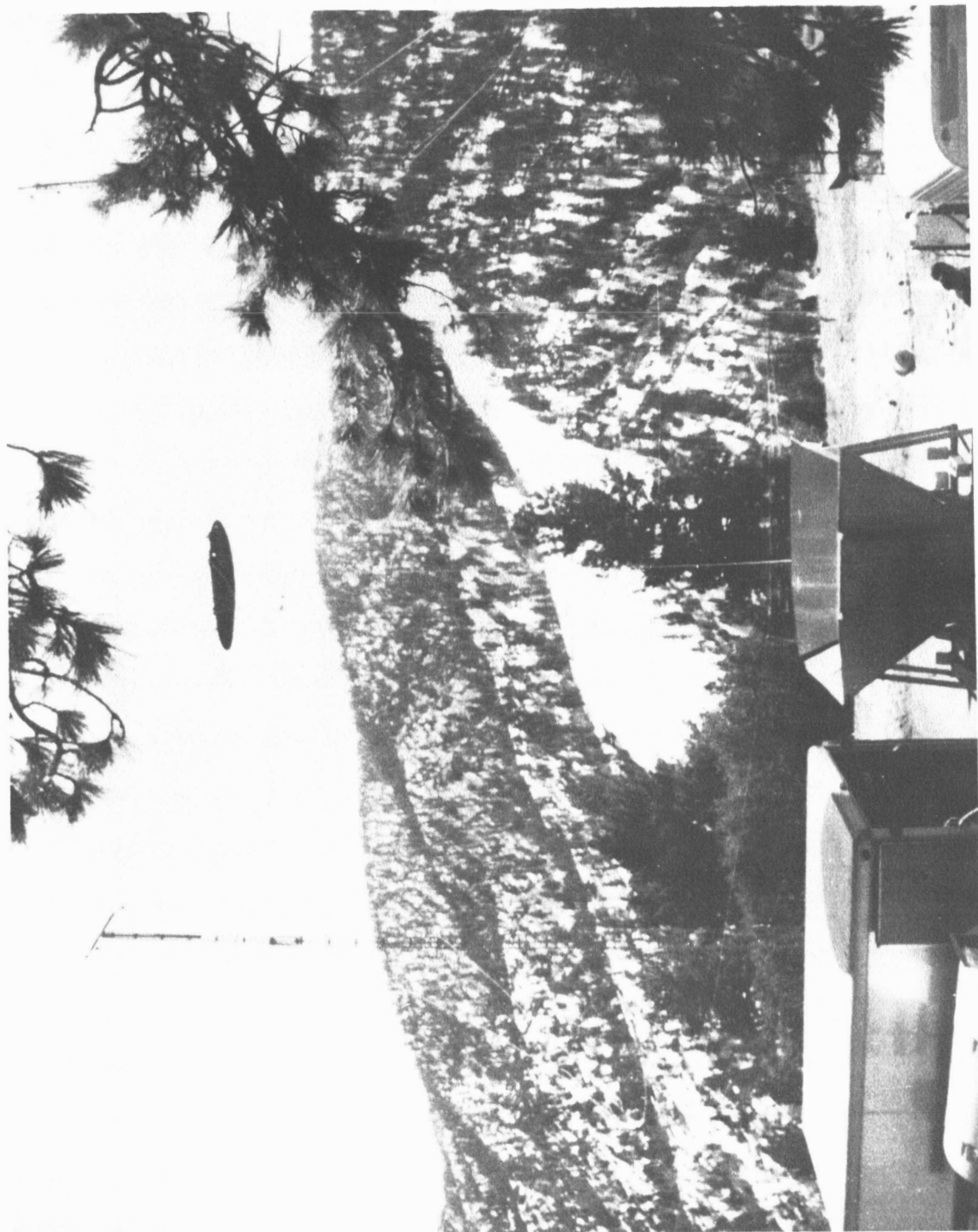
The primary objective of this report is to summarize the results of measurements which were performed on the Nimbus breadboard electronic scanning antenna array. This series of measurements was intended primarily to establish the radiometric beam efficiency and to measure the dissipative loss of the Nimbus array over its range of scan angles, $\pm 50^\circ$. Also, it was desired to quantitatively relate the measured radiometric temperature of an object filling the main beam of the antenna.

Since the radiometer receiver had been accurately calibrated for absolute temperature measurements using the cold load bench test set (see Section 6 and 7), it was the best available instrument for performing the antenna measurement and, also, provided for an overall system functional checkout of the breadboard model.

These measurements were performed at Table Mountain, California, at an altitude of 7200 feet, thus minimizing the atmospheric absorption contributions to the zenith sky temperatures. A photograph of the test site is shown in Figure 1-1.

Details of the theory behind the measurements and of how the measurements were actually performed are discussed in Sections 2 and 3. The results and conclusions of the measurements are discussed in Sections 4 and 5, respectively.

Sections 6, 7, and 8 describe the calibration of the radiometer, the cryogenic bench test site and the zenith sky temperature. Section 9 discusses the sun drift curves which were obtained by allowing the sun to drift through the antenna response, i. e., the antenna pattern.



939/044

Figure 1-1. Photo of Test Site at Table Mountain

Section 2

ANTENNA LOSS AND EFFICIENCY MEASUREMENT TECHNIQUES

2.1 INSERTION LOSS AND EFFICIENCY EQUATIONS

The objectives of this series of tests were to establish the radiometric efficiency of the antenna array and to quantitatively relate the radiometric temperature at the antenna output to the brightness temperature of an object filling the antenna beam. An ideal antenna is one which receives all of its energy from the primary beam (i. e., side lobes = 0) and transmits all of this energy to its output. Practical antennas diverge from this ideal in that, as a consequence of side lobes, the power received in the main beam is reduced. For a given incident power from a source completely subtended by the main beam, the ratio of the power received with a given antenna compared to the incident power will be referred to here as the radiometric beam efficiency of the antenna. The sum of radiation received from objects intercepted by the side lobes adds an additional power output to the antenna output which is termed radiometric background temperature. Dissipative loss occurring within the antenna and associated feed structures attenuates both the main beam and side lobe components of the received radiation and adds a reradiation component to the total power available at the antenna output port. Thus, the power output of a practical receiving antenna may be described in terms of two components of incident radiation, the antenna dissipative insertion loss of the antenna, the antenna beam efficiency, and an associated reradiation component.

List of Definitions

- P_{im} = power incident from main beam
 P_{is} = total incident power from side lobes
 E = antenna main beam efficiency
 L_a = antenna dissipative insertion loss

List of Definitions (Continued)

- P_{rm} = power input to receiver from main beam
 P_{rs} = power input to receiver from side lobes
 P_t = antenna loss power component
 T_{im}, T_{is} = radiometric antenna brightness temperatures
 T_z = zenith sky temperature
 T_R = radiometer output temperature
 t = thermal temperature of antenna
 t_d = thermal temperature of absorbing disk
 k = Boltzman's constant
 B = receiver predetection bandwidth

The three components of power available at the output port to the receiver are (see list of definitions):

- a. The main lobe component $P_{rm} = \frac{EP_{im}}{L_a}$
b. The side lobe component $P_{rs} = \frac{P_{is}}{L_a} (1 - E)$
c. The antenna loss reradiation component $P_t = \left(\frac{L_a - 1}{L_a} \right) t$

These power components may be related to radiometric brightness temperatures of the objects in the main and side lobes and to the thermal temperature of the dissipative elements in the antenna structure. It is assumed that the main beam observes a uniform brightness temperature, T_{im} , and that all of the side lobes observe a uniform brightness temperature, T_{is} , and that the antenna loss elements have a thermal temperature, t . The total power available to a receiver at the antenna port is, then:

$$P_{\Sigma} = \frac{E}{L_a} P_{im} + P_{is} \frac{(1 - E)}{L_a} + P_t$$

or

$$P_{\Sigma} = kB \left[\frac{E T_{im}}{L_a} + \frac{(1 - E)}{L_a} T_{is} + \left(\frac{L_a - 1}{L_a} \right) t \right]$$

It will be assumed that, within the bandwidth B, the antenna characteristics are initially uniform. Furthermore, it is assumed that within this bandwidth both the antenna and the receiver input are sufficiently well impedance-matched to the interconnecting transmission line so that any intervening insertion loss is purely dissipative, i. e., negligible power reflection.

The radiometric temperature of the antenna T_R output is, thus, given by

$$T_R = \frac{P_{\Sigma}}{kB} = \frac{E}{L_a} T_{im} + \left(\frac{(1 - E)}{L_a} \right) T_{is} + \left(\frac{L_a - 1}{L_a} \right) t$$

The primary objectives of the measurements that were conducted at Table Mountain were to accurately ascertain the values of E and L_a using this equation.

The antenna is a two-dimensional planar array which is electronically scanned over a range of $\pm 50^\circ$ in approximately 2.5° steps. Thus, it was necessary to determine the values of L_a and E at a sufficient number of angular positions within this range to permit an accurate determination of their variation as a function of scan angle.

In the following test procedures the radiometer itself is assumed to be calibrated sufficiently well to allow absolute temperature measurements. The calibration of the radiometer is exclusive of the antenna and is described in Section 6.

2.2 BASIC TESTING PRINCIPLES

The principles underlying the tests and reasoning leading to the particular test approach will now briefly be discussed prior to their detailed description.

From the equation for T_R it is apparent that if the incident temperatures T_{is} and T_{im} were both zero, then a measurement of T_R by the radiometer and t by a precision thermistor would permit L_a to be computed as

$$L_a = \frac{t}{t - T_R}$$

Although zero values for T_{im} and T_{is} are impossible, since the minimum radiometric brightness temperatures available for the antenna are limited by atmospheric absorption at zenith and the isotropic universal background radiation, atmospheric absorption can be minimized by locating at a relatively high elevation where water vapor absorption is greatly reduced. For this reason, Table Mountain with an elevation of 7200 feet was selected as the test site. Under clear sky conditions the zenith sky temperature observed was approximately 8°K and ascertainable to an accuracy of $\pm 2^\circ\text{K}$.

If both T_{is} and T_{im} could be made approximately equal to the zenith temperature, T_z , then the equation for T_{at} is

$$T_R = \left[\frac{E}{L_a} + \frac{(1 - E)}{L_a} \right] T_z + \left(\frac{L_a - 1}{L_a} \right) t$$

Then

$$L_a = \frac{t - T_z}{t - T_R}$$

In practice, T_{is} and T_{im} can be made nearly equal by placing a reflecting surface at the back and flaring out along the sides of the antenna so that the side lobes are reflected into a cone centered at zenith. (See Figures 2-1 and 2-2).

Under clear sky conditions the atmospheric absorption varies only very slightly for small angles from the zenith and, thus, $T_{is} \approx T_{im}$. The actual values of T_z used during the course of these measurements were calculated as discussed in Appendix C. T_z can also be determined from the antenna temperatures obtained by observing the radiometer output temperature as a function of zenith angle. Under these conditions, the predominant portion of T_R will be due to the reradiation from the insertion loss of the array antenna.

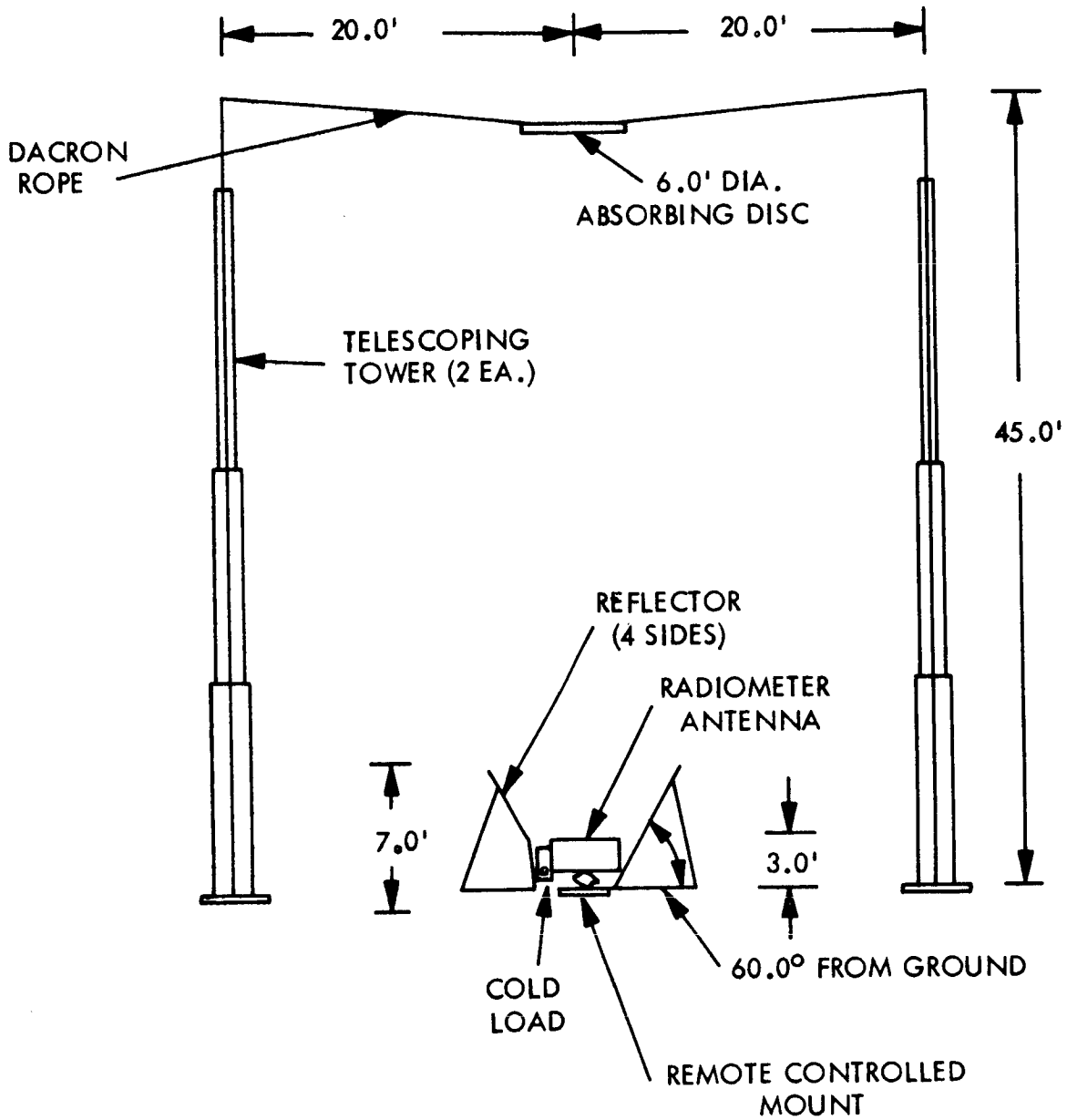
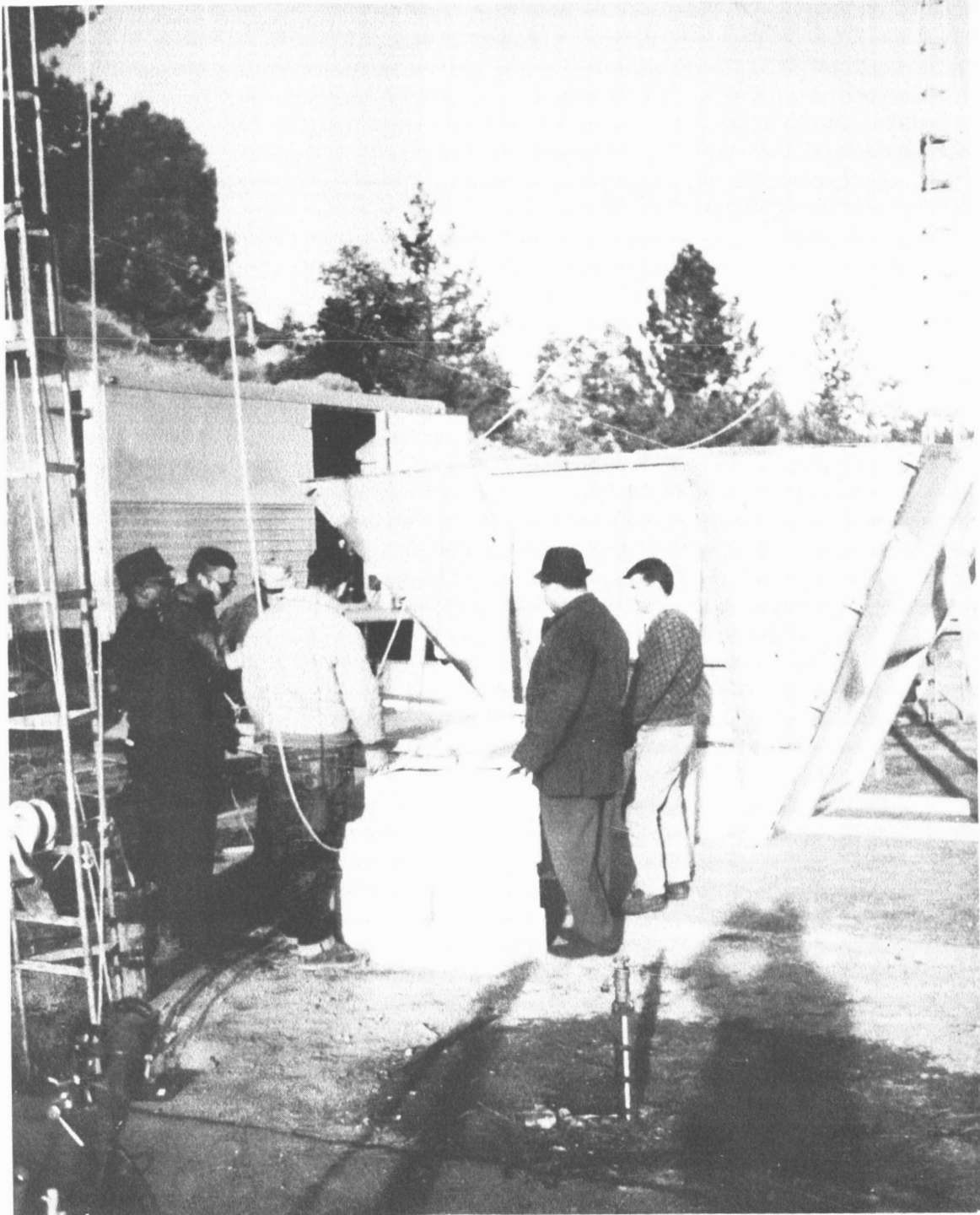


Figure 2-1. Reflector Geometry



930/c1c

Figure 2-2. Reflectors Positioned Around Antenna Array

The antenna loss, L_a , was measured for different thermal temperatures of the antenna at 0° beam position. The loss, L_a , should be somewhat independent of the thermal temperature of the antenna. The thermal temperature range that was obtained is 4°C to 35°C by taking advantage of the natural ambient temperature range and using electrical heaters.

The next step is to find the efficiency E of the antenna. This was accomplished by placing a disk-shaped, black-body target in the main lobe of the antenna pattern. The disk was shaped to fill the main lobe of the antenna out to the null points at a distance of approximately 35 feet above the antenna. (See Figures 2-1 and 2-3). The thermal temperature of the disk, T_d , was monitored by a calibrated thermistor. By maximizing the radiometer output signal, the disk was centered in the beam. Since the disk fills the beam at the null points, the accuracy of the measurement is not a strong function of the disk centering.

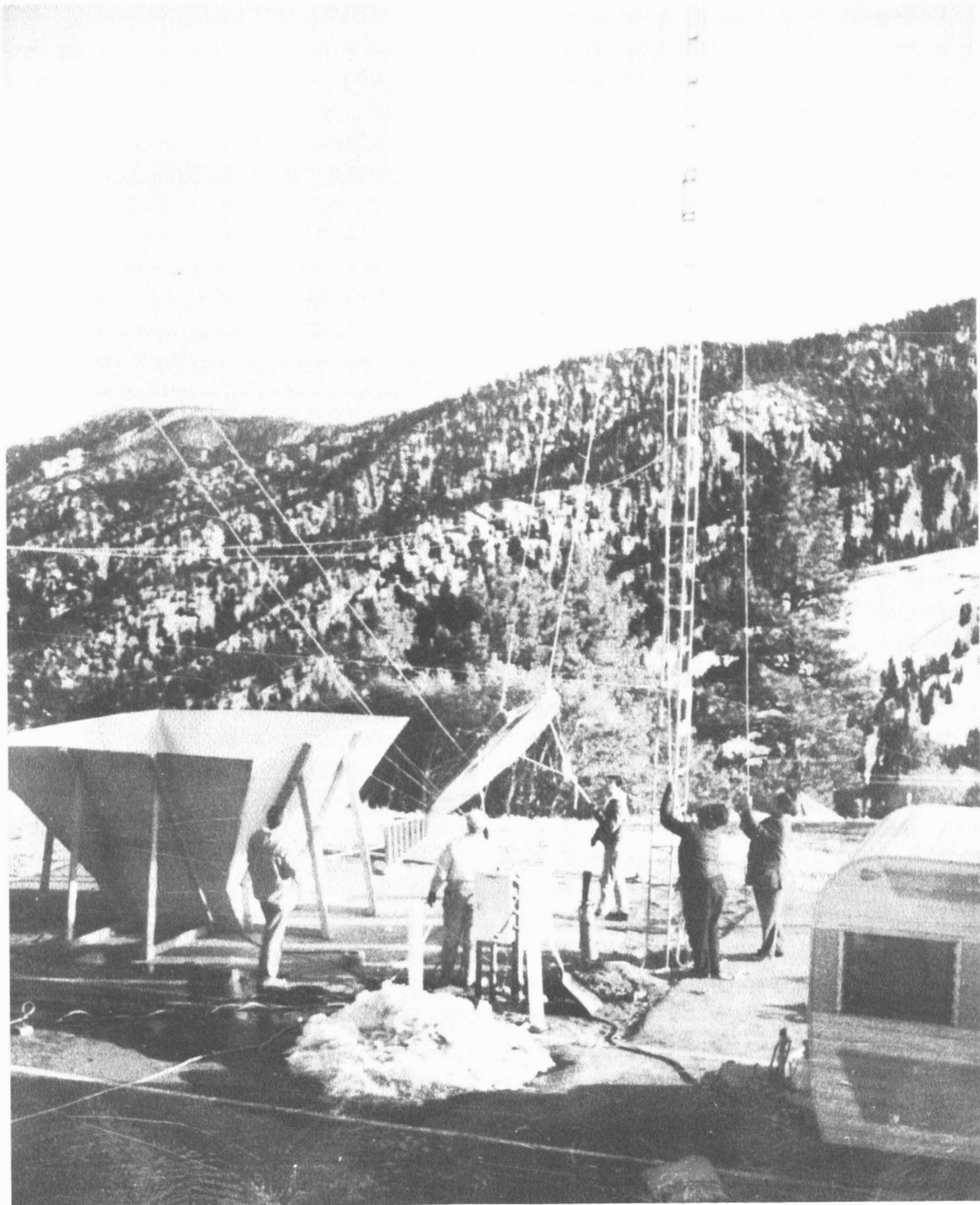
The antenna output temperature, T_R , is now given by

$$T_R = \frac{E t_d}{L_a} + \frac{(1-E) T_z}{L_a} + \frac{t(L_a - 1)}{L_a}$$

Since the efficiency, E , of the antenna is known from the antenna pattern measurements to be near 0.9, the loss $L_a \approx 2\text{ dB}$, and $T_z \approx 8^\circ\text{K}$, the second term in the above equation is $\approx \frac{1}{2}^\circ\text{K}$. The loss, L_a , is known from the previous measurement, and the thermal temperatures of the disk, t_d , and the antenna, t , are monitored. The antenna radiometric output temperature is measured and from the above formula the efficiency calculated. Section 3 contains a description of the test procedure which was followed during the course of these measurements.

2.3 SKY HORN MEASUREMENT

The antenna loss at several beam positions may also be measured by comparing a standard gain horn (Scientific Atlanta, Model No. 12-18S/N36) with the antenna array. This was done at two beam positions by connecting the standard gain horn and a precision variable attenuator on the calibration port and the antenna array on the antenna port (see Figure 2-4). Then the attenuator was positioned so as to present equal readings on the calibration readout and antenna readout. This was performed at both 0° and $+16^\circ$ beam positions.



939/048

Figure 2-3. Absorbing Disks Positioned Above Antenna Array

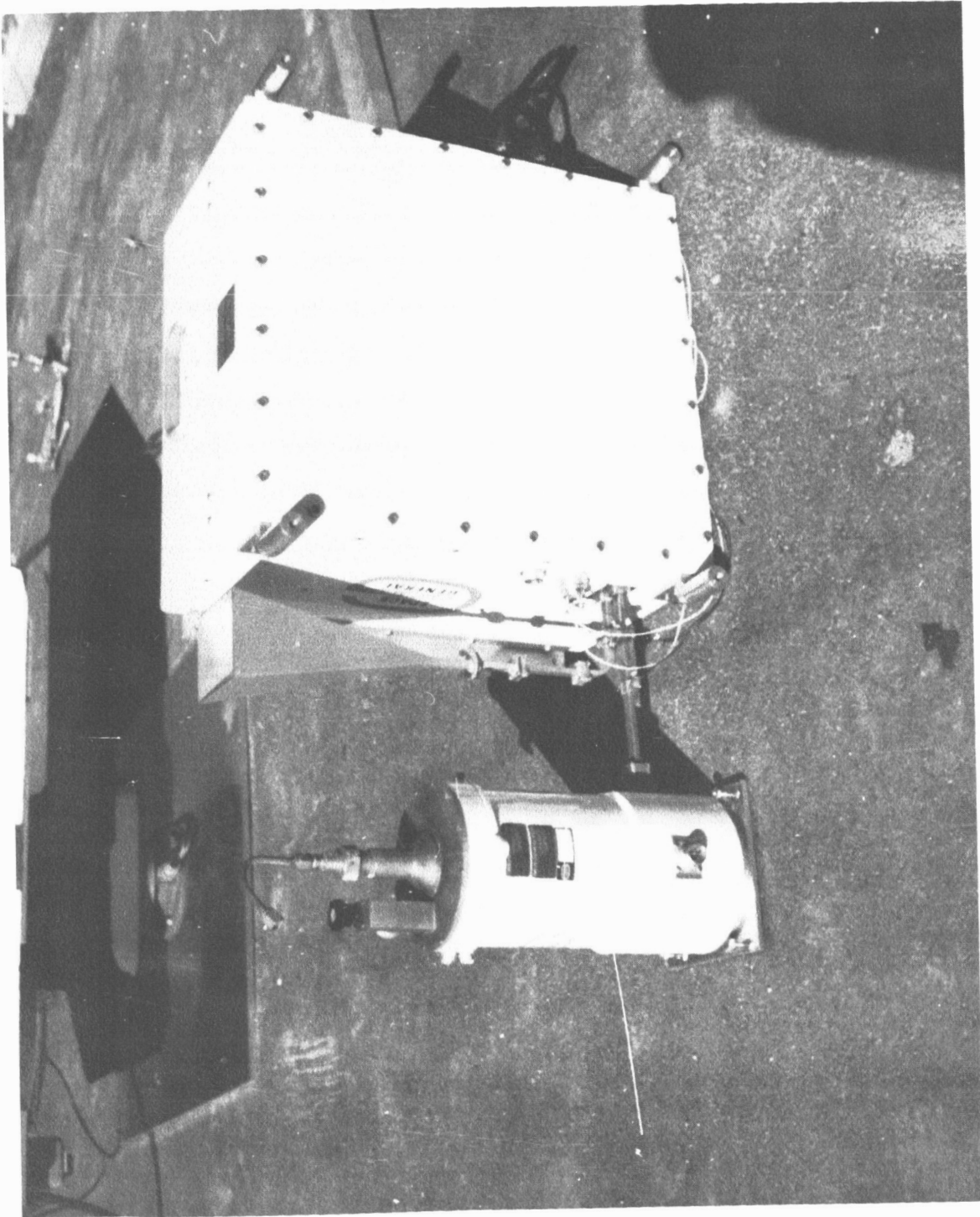


Figure 2-4. Standard Gain Horn Connected to Calibration Port

939/042

Section 3

TEST PROCEDURE

STEPS FOLLOWED DURING TESTS

1. The radiometer was recalibrated with the cryogenic bench test set on arriving at Table Mountain before proceeding with the tests of the antenna. A calibration curve is shown in Figure 3-1 for liquid nitrogen filling the bench test set cryoflask.
2. The radiometer and antenna were mounted on a pedestal with the cryogenic load attached to the cold reference waveguide port (see Figure 3-2).
3. The antenna coil currents were set to produce the 0° beam position and the antenna was mechanically oriented to point the beam at the zenith. A measurement was made with no reflectors to get an estimate of the energy in the back lobes.
4. The reflectors were placed around the radiometer to shield the antenna from the ground.
5. The radiometer output was recorded for five minutes by means of the digital printer, both with and without a polyfoam enclosure to measure the effect of this enclosure.
6. During the measurement of Step 5, the following parameters were also recorded:
 - a. Ambient air temperature
 - b. Humidity
 - c. Barometric pressure
 - d. Sky cover
 - e. Thermal temperature of antenna at center and two edges of array
 - f. Temperatures within the antenna and radiometer enclosure
 - g. Temperature distribution along cold load feed line
7. From the data of Steps 5 and 6, the antenna loss in dB was calculated.

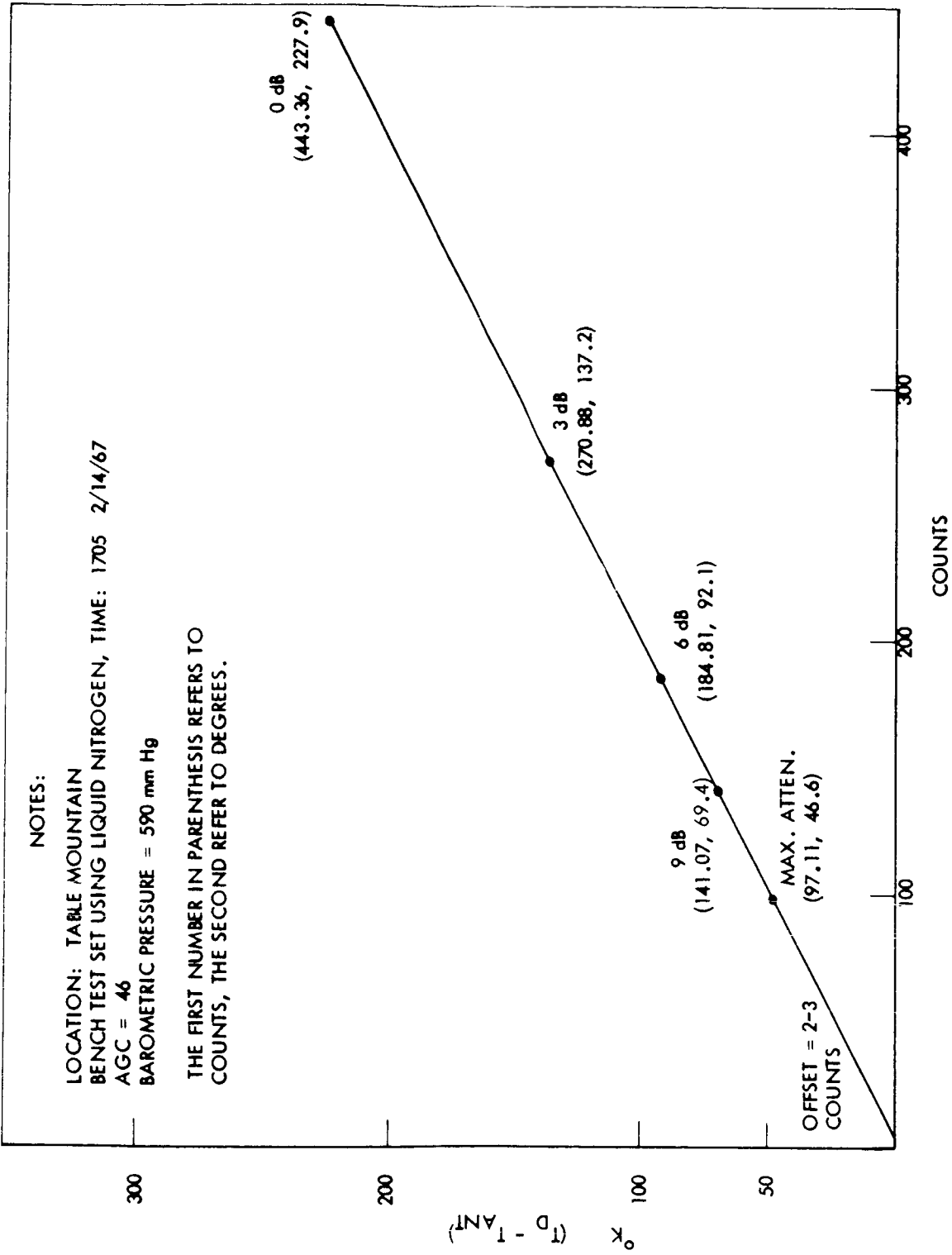


Figure 3-1. Calibration Curve of Radiometer



939/022

Figure 3-2. Cold Reference Load and Radiometer

8. By means of towers a disk of absorbing material was positioned over the antenna so that it filled the main lobe out to the null points. (See Figure 3-3.) The height of the disk above the antenna was approximately thirty-five feet.
9. The radiometer output was then recorded for five minutes by means of the digital printer.
10. During the measurement of Step 9, the following parameters were also recorded:
 - a. Ambient air temperature
 - b. Humidity
 - c. Barometric pressure
 - d. Sky cover
 - e. Thermal temperature of antenna at center and two edges of array
 - f. Temperatures within the antenna and radiometer enclosure
 - g. Thermal temperature of absorbing disk
 - h. Temperature distribution along the cold reference load feed line
 - i. Height of disk above antenna
 - j. Motion of disk (estimated)
11. The disk's position was then moved while observing the radiometer output to maximize the temperature recorded at the output of the radiometer, and data taken, as discussed in Steps 9 and 10.
12. From the measurements in Steps 10 and 11 and the antenna loss calculated in Step 7, the percentage of energy in the main lobe of the antenna was calculated.
13. The antenna coil currents were then set to position the antenna at other beam positions and the measurements described in Steps 2 through 12 repeated. In all cases the antenna was tilted mechanically so that the main beam pointed at the zenith.
14. The above measurements were repeated for the scan angles of approximately -45, -31, -16, +16, +31, and +45, in that order, repeating the procedure in Steps 5 through 12.



939/043

Figure 3-3. Absorbing Disk Over Antenna Array

15. From the above measurements, the antenna loss and percentage of energy in the main lobe of the antenna have been determined for the scan angles of -45° , -31° , -16° , 0° , $+16^{\circ}$, $+31^{\circ}$, $+15^{\circ}$, and this data was compared to the antenna loss and beam efficiency obtained from the antenna pattern measurements and the antenna loss obtained from the measurements of the loss of individual components.
16. The standard gain horn was then connected to the cold reference load port through a precision variable attenuator and some additional waveguide. The attenuator was set on 0 dB setting and the radiometer output was then recorded.
17. Comparison of the calibration output and antenna output readings were made. Additional attenuation was inserted via the variable attenuator until the calibration output and antenna output readings were nearly equal.
18. The connecting line from the standard gain horn, including the precision attenuator, was then estimated to have 2.5 dB loss.

Section 4

TEST RESULTS

The two measured antenna parameters of major importance are the antenna insertion loss and beam efficiency. Secondary quantities measured while at Table Mountain were the sky zenith temperature and the temperature of the sun. These measurements also provide some degree of correlation on the antenna loss. Sample calculations of the insertion loss and beam efficiency are included below. Table 4-1 lists these quantities as well as those values obtained from the integration of antenna patterns as measured at the SGC antenna range.

4.1 INSERTION LOSS AND BEAM EFFICIENCY

The equation for the insertion loss was presented in Section 2. This equation was derived assuming that all the incident energy from the main antenna beam as well as from the side lobes and back lobes of the antenna is from the sky. This condition is presumably established by placing a reflecting surface at the back and flaring out along the sides of the antenna as shown in Figure 2-1. To determine the reflector effectiveness and/or the back lobe level, a measurement of the sky temperature was performed at 0° beam position, both with and without the reflectors. A comparison of the resulting antenna temperatures shows that the total energy in the back lobes is less than 0.5 percent and that the reflectors do some good, although if they were not used only small errors would result.

Next, several measurements were performed, both with and without the polyfoam enclosure which housed the receiver and antenna. This measurement resulted in the somewhat intriguing fact that the antenna loss was slightly less with the enclosure on than with it removed. This may be attributed to the fact that antenna reflection losses, although thought to be small enough to be ignored, were measurable with such a sensitive receiver. The effect of the polyfoam is to improve the impedance match from a VSWR value

Table 4-1
TEST RESULTS

Beam Position	Insertion Loss (dB)	Beam Efficiency Measurements (%)	Antenna Thermal Temperature °C	T _z ' Calculation °K	Reference Load	Beam Efficiency Calculation (%)
0°	2.66	-	+ 4	7	Cold Load, N ₂	88.9**
0°	2.60	86.3	+14	8	Cold Load, N ₂	
0°	2.52	87.3	+17.1	7	Cold Load, N ₂	
0°	2.66	-	+18.4	7	Ref. Horn	
0°	2.49	-	+19.1	7	Cold Load, N ₂	
0°	2.57	89	+28.9	6	Cold Load, N ₂	
0°	2.54	72*	+35.7	8	Cold Load, N ₂	
0° Avg	2.57 ^{+0.09} _{-.08}					
+16°	2.50	90	+37.2	6.5	Cold Load, N ₂	
+31°	2.54	80.8*	+12.4	9	Cold Load, N ₂	93
+31°	2.60	90.5	+18.1	7	Ref. Horn	
+31°	2.69	-	+19.4	7	Ref. Horn	
+31° Avg.	2.61 ^{+0.08} _{-.07}					
+45°	2.76	86	+18.5	8.5	Ref. Horn	
+45°	2.64	82	+16.3	8.5	Cold Load, N ₂	
+45° Avg.	2.70 ± .06					
Fail Safe	2.46	89.5	23.1	6.5	Cold Load, N ₂	
Fail Safe	2.58		18.5	7	Ref. Horn	
Fail Safe, Avg	2.52 ± .06					
-16°	2.52	90.5	+35	6	Cold Load, N ₂	88.6
-31°	2.57	81	+ 4.7	8	Cold Load, N ₂	
-45°	2.79	80	- 1	7	Cold Load, N ₂	
-45°	2.74	78.6	+35.7	7	Cold Load, N ₂	
-45° Avg.	2.765 ± .025					

NOTES:

* The disk did not fill the main beam of the antenna during these measurements.

**Beam efficiencies were not calculated for all scan angles.

of, say, 1.2 to a value of 1.1. These numbers are not quoted measured values but are only mentioned here to show the relative values of impedance match under discussion. The resulting antenna insertion loss difference, with and without the enclosure, is on the order of .046 dB and will be neglected since the antenna temperature difference for the two cases was on the order of 1°K.

Table 4-1 lists the measured antenna insertion losses and measured beam efficiencies when using the radiometer receiver. Also included is the thermal temperature of the antenna and the assumed value of T_z for each individual measurement. A column is also provided which lists the beam efficiency calculated when using individual antenna patterns taken at the center operating frequency of the antenna. Several of the measurements were performed using a standard gain horn as the calibration load, while the majority were performed using a cryogenic load cooled to the boiling point of liquid nitrogen. Reasonably good correlation was obtained between the two conditions. A sample calculation of the insertion loss and beam efficiency are shown below for a beam position of +16.2°. The loss is given by the equation

$$L_a = \frac{t - T_z}{t - T_R}$$

where all quantities were defined previously. Values of t , T_z , and T_R used are

$$t = 311.2^\circ\text{K (a measured thermal antenna temperature)}$$

$$T_z = 6.5^\circ\text{K (a calculated zenith sky temperature)}$$

$$T_R = 150^\circ\text{K (a measured radiometric antenna temperature)}$$

Thus,

$$L_a = \frac{311.2 - 6.5}{311.2 - 150} = 1.890 = 2.765 \text{ dB}$$

Included in this loss is a waveguide connection from the antenna port to the radiometer input. This waveguide has a measured loss of .266 dB and must be subtracted from the L_a value obtained above, thus yielding a value of $L_a' = 2.50$ dB. Beam efficiency is given by the equation

$$E = \frac{L_a T_R - T_z - t (L_a - 1)}{t_d - T_z}$$

For the above insertion loss, the following values of temperature were used:

$$t = 310.3^\circ\text{K} \text{ (a measured thermal antenna temperature)}$$

$$t_d = 290.3^\circ\text{K} \text{ (a measured absorbing disk temperature)}$$

$$T_z = 6.5^\circ\text{K} \text{ (a calculated zenith sky temperature)}$$

$$T_R = 283.5^\circ\text{K} \text{ (measured radiometric antenna temperature)}$$

$$E = \frac{1.890 (283.5) - 6.5 - 310.3 (.890)}{290.3 - 6.5} = 90\%$$

Notice that the insertion loss of the waveguide connection from the antenna port to the radiometer input is included in this calculation. This is necessary because the radiometric antenna temperature is measured at the radiometer input port. This input port is the reference plane for all measured radiometric data.

4.2 ERRORS IN INSERTION LOSS DUE TO UNCERTAINTIES IN TEMPERATURE MEASUREMENTS

The expression for antenna insertion loss contains three temperature terms, two of which are radiometric temperatures while the other is a thermal temperature. Uncertainties in the measurement or assumed values of these quantities result in an overall uncertainty or error in values of insertion loss. The maximum uncertainty in L is given by

$$\Delta L = \frac{|\Delta T_z|}{t - T_R} + \frac{|T_z - T_R| |\Delta t|}{(t - T_R)^2} + \frac{|t - T_z| |\Delta T_R|}{(t - T_R)^2}$$

Typical values of these quantities are:

$$t \approx 270 - 300^\circ\text{K} \pm .5^\circ\text{K}$$

$$T_R \approx 140 - 150^\circ\text{K} \pm 1^\circ\text{K}$$

$$T_z \approx 6 - 8^\circ\text{K} \pm 2^\circ\text{K}$$

Under the worst combination of these values of temperature the maximum uncertainty is:

$$\begin{aligned}\Delta L &= \frac{2}{130} + \frac{144(.5)}{(130)^2} + \frac{264(1)}{(130)^2} \\ &= .0154 + .00435 + .0161 = .036\end{aligned}$$

For $L = 1.9$

$$\frac{\Delta L}{L} = \frac{.036}{1.9} = 1.9\% = .18 \text{ dB error, maximum}$$

This is the maximum possible error. The rms error is probably on the order of $\pm .06$ dB.

4.3 BEAM EFFICIENCY ERRORS

The equation for beam efficiency was derived in Section 2. In a different form it is:

$$E = \frac{L_a T_R - T_z - t(L_a - 1)}{t_d - T_z}$$

Errors in the temperature measurements, both thermal and radiometric, and in the antenna insertion loss, result in uncertainties in the antenna efficiency measurement. It will be assumed here that errors in filling the main beam with the disk are negligible compared to other errors.

The total maximum error in measuring E is the sum of the errors in measuring each of the quantities in the above expression for E . These will be discussed separately below.

The uncertainty in E due to uncertainties in L_a are:

$$\Delta E_L = \frac{|T_R - t| \Delta L}{t_d - T_z}$$

This term will add the most uncertainty to the total, since the uncertainty in L is somewhat large for this measurement. For the typical values

which occur, i.e., $T_R = 260^\circ\text{K}$, $t = 290^\circ\text{K}$, $t_d = 290^\circ\text{K}$, $T_z = 9^\circ\text{K}$
and for the value of $\Delta L = .028$ calculated previously ΔE_L equals $\approx 3\%$.

The following typical values for the other variables in the equation are:

$$L_a = 1.9, T_R = 260^\circ\text{K}, T_z = 9^\circ\text{K}, t = 290^\circ\text{K}, t_d = 290$$

$$\Delta L_a = .028 \quad \Delta T_R = 1^\circ\text{K} \quad \Delta T_z = 1^\circ\text{K} \quad \Delta t = .5^\circ\text{K} \quad \Delta t_d = 2^\circ\text{K}$$

The uncertainty in E due to uncertainty in T_R is given by

$$\Delta E_{TR} = \frac{L_a |\Delta T_R|}{t_d - T_z} = .675\%$$

The uncertainty in E due to uncertainty in T_z is:

$$\Delta E_{Tz} = \frac{|t_d - T_z| |\Delta T_z| - |L_a T_R - T_z - t(L_a - 1)| |\Delta T_z|}{(t_d - T_z)^2} = .07\%$$

The uncertainty in E due to the uncertainty in t is

$$\Delta E_t = \frac{(L_a - 1) (\Delta t)}{t_d - T_z} = .16\%$$

and the uncertainty in E due to the uncertainty in t_d

$$\Delta E_{td} = \frac{|L_a T_R - T_z - t(L_a - 1)| |t_d|}{(t_d - T_z)^2} = .56\%$$

It is interesting to note that the uncertainty in the disk temperature, although somewhat large, does not contribute appreciably to the overall uncertainty.

The total maximum uncertainty is the sum of these, or

$$\Delta E_\Sigma = 4.465\%$$

The rms error is on the order of $\pm 1.5\%$.

4.3.1 SKY HORN MEASUREMENT RESULTS

When the standard gain horn and attenuator were connected as the calibration load, the attenuator was positioned to obtain equal output readings on the antenna output and calibration output. Fairly good correlation was obtained between this rough insertion loss measurement and the method described in Section 2. For the two beam positions used the results are as follows:

<u>Insertion Loss of Cold Horn Waveguide Run</u>	<u>Beam Position</u>	
	<u>+16.2°</u>	<u>0°</u>
Precision Attenuation Reading (meas.)	1.55 dB	1.60
Residual Loss at 0 dB (meas.)	.46 dB	.46
Loss of w/g (meas.)	.21 dB	.21
Loss of Standard Gain Horn (est.)	.20 dB	.20
	<u>2.42 dB</u>	<u>2.47 dB</u>
Less the Loss of Antenna Feed	<u>-.27</u>	<u>-.27</u>
Total Loss, Approx.	2.15	2.20

These values are approximately .35 dB lower than obtained by the more exact method although they indicate that the antenna loss is indeed greater than 2 dB. This measurement is interesting in that no value of the zenith temperature and no value of the calibration port (cold reference load) temperature are required.

4.4 SKY TEMPERATURE MEASUREMENT

A measurement of the sky temperature was performed at an electrical beam position of + 31.2°. The antenna was tilted mechanically to observe five different angles from the zenith. The sky temperature is given by:

$$T_z = t - L_a (t - T_R)$$

where all terms have previously been defined. A table of these measurements is given below:

<u>Angle from Zenith</u>	<u>T_z</u>
+ 11°	8.08°K
+ 31°	9.92°K
+ 45°	10.89°K
+ 60°	16.43°K
+ 76°	27.58°K

The error in this measurement can be quite pronounced for such a large antenna loss, although the calculated value for this measurement was 7.9°K at zenith position (0°). Due to the error in antenna loss alone the uncertainty in T_z is typically 3°K, not a small number in comparison.

Calculated values of the sky temperature have been made for this altitude (pressure), humidity and ambient temperature utilizing several well-known references. The calculated values of from 6 - 9°K agrees quite well with the value measured with this antenna. (See Section 8.)

4.5 SUN-DRIFT CURVES

For antenna beam positions of +16° and +31.2° the antenna was pointed with the main beam looking directly at the sun by maximizing the output signal. Then, the output of the radiometer was recorded while the sun drifted through the antenna response curve, i. e., the antenna pattern. From this data the antenna half-power beamwidth was measured and the sun's brightness temperature calculated. It is possible to obtain the antenna pattern as well from the measurement.

Two sun-drift curves were made at +31.2°, one using the standard gain horn as a reference load, the other using the cold reference load filled with liquid nitrogen. One drift curve was made at +16° using the cold reference load, this being done on a different day than the two measurements at +31.2°. Plots of these responses are shown in the figures of Section 9.

Table 4-2 shows the half-power beamwidths and sun temperatures obtained from these measurements, as well as the half-power beamwidths obtained from antenna patterns measured at the SGC antenna range at a single frequency. The accuracy of the measurements in either case is on the order of 0.1° thus reasonable correlation was established. The patterns measured on the antenna range were for the two principal planes of the antenna, while the sun-drift path was slightly skewed from the ϕ reference plane. This is discussed further in Section 9, along with the sun temperature calculations. This measurement assumes that the antenna pattern is symmetrical, a condition which is closely approximated.

A further discussion of the sun-drift measurements can be found in Section 9.

Table 4-2
MEASUREMENTS

Date	Time	Elevation Angle, Sun	Electrical Beam Position	Beamwidth from Sun-Drift Curve	Principal Plane Beamwidth from Antenna Range		Measured Sun Temp.
					θ	ϕ	
2-21-67	1222	44°	$+16^\circ$	2.91°	2.44°	2.98°	7080°K
2-17-67	1445	34°	$+31.2^\circ$	3.02°	2.71°	2.98°	7100°K
2-17-67	1533	23°	$+31.2^\circ$	3.04°	2.71°	2.98°	7200°K

Section 5

CONCLUSIONS

Absolute measurements of the major characteristics of any antenna which is intended for radiometric applications rely upon the use of resistive sources at known temperatures; sources heated and regulated by resistive networks and control amplifiers, as well as sources maintained at cryogenic temperatures have been very useful and practical. These sources are necessary not only in providing comparison standards for the antenna brightness temperatures but also to accurately calibrate the radiometer receiver used in performing the measurements. The accuracy of these radiometric sources determines to a large degree the accuracy of the antenna parameter measurements. In addition, other factors contribute to the overall accuracy to be sure, among the most important being the antenna thermal temperature.

The results of these measurements on this particular antenna show that the calculated values of errors expected are in close agreement with those actually observed. For example, the average insertion loss at 0° beam position was found to be $2.57 \pm .09$ dB which includes variations with temperature. At all other beam positions, the loss averages fell below this range of errors.

Some refinements in the beam efficiency measurement are evidently necessary; however, the measurements where the disk did not fill the main beam were performed on days when the winds were very gusty, not the best condition under which to perform this particular measurement. The average value of three beam efficiency measurements at 0° beam position when performed under more ideal conditions was $87.5\% \pm 1.5\%$, which agrees quite favorably to a value of 88.9 percent obtained from a single frequency pattern integration. It is expected that the beam efficiencies measured radiometrically, i. e., broadband integration using the radiometer receiver as a measuring device, would be somewhat different than values obtained at a

single frequency. In most cases the radiometric measurement will give lower efficiency since the antenna is optimized at the center frequency but this was not true for a beam position of -16° .

The antenna loss is appreciably higher than the design goal of 1.3 dB but the beam efficiency is quite close to the design goal of 92 percent. The antenna has proved to be electronically steerable and the radiometer was proved to have a sensitivity of less than 0.7°K and capable of performing absolute measurements of better than $\pm 1^\circ\text{K}$. It must be further pointed out that this breadboard unit, including the radiometer receiver and electronically steerable array, operated over a range of temperature approximately equal to the specified values of 0°C to $+50^\circ\text{C}$.

The sun temperature measurement proved to be quite interesting. Generally accepted values of the sun temperature at radio frequencies are approximately 6000°K from the submillimeter band down to approximately 1 cm (30 GHz). At this point the temperature of the quiet sun varies up to a maximum value of 1 million $^\circ\text{K}$ at a wavelength of 5 meters. In the 1 to 2 cm band the temperature is generally believed to be from 6,000 to 10,000 $^\circ\text{K}$ and according to this measurement is around 7,100 $^\circ\text{K}$ at 1.5 cm.

Section 6

BENCH CALIBRATION OF MICROWAVE RADIOMETER

6.1 INTRODUCTION

This radiometer is of the Dicke-type with an additional RF switch inserted between the Dicke switch and antenna (see Figure 6-1). The purpose of the additional switch is to allow switching from the antenna port to a calibration port where a fixed known temperature load is placed. This allows measurement of the system gain in terms of radiometric temperature at regular intervals.

Calibrating this type of radiometer is relatively straightforward. The two external microwave inputs are labeled the antenna port and the calibration load port, respectively. These two ports, together with a third port terminated in a hot radiometric reference load, constitute the three inputs to the microwave switching network located between the signal antenna and the receiver. These ports are as labeled in Figure 6-1.

In the discussions devoted to the radiometer calibration procedures the following assumptions are made:

- a. The voltage reflection coefficients associated with the microwave switches (cal switch, S_1 , and Dicke switch, S_2) are sufficiently small so that the mismatch insertion losses are negligible compared to the dissipative components of the forward direction insertion losses.
- b. The impedance mismatches of the terminations on Ports 1, 2, 3, 4 and 5 are sufficiently low so that all power reflection coefficients are less than 10^{-3} (i. e., $VSWR < 1.06$).
- c. The intrinsic isolation between two adjacent ports of the circulator switches is sufficiently high so that the observed isolation is determined solely by the power reflection coefficient of the third port.
- d. The input circulator of the receiver has sufficiently high isolation so that the excess temperature of the receiver as seen at Port 5 is within 1°K of the thermal ambient temperature of the receiver.

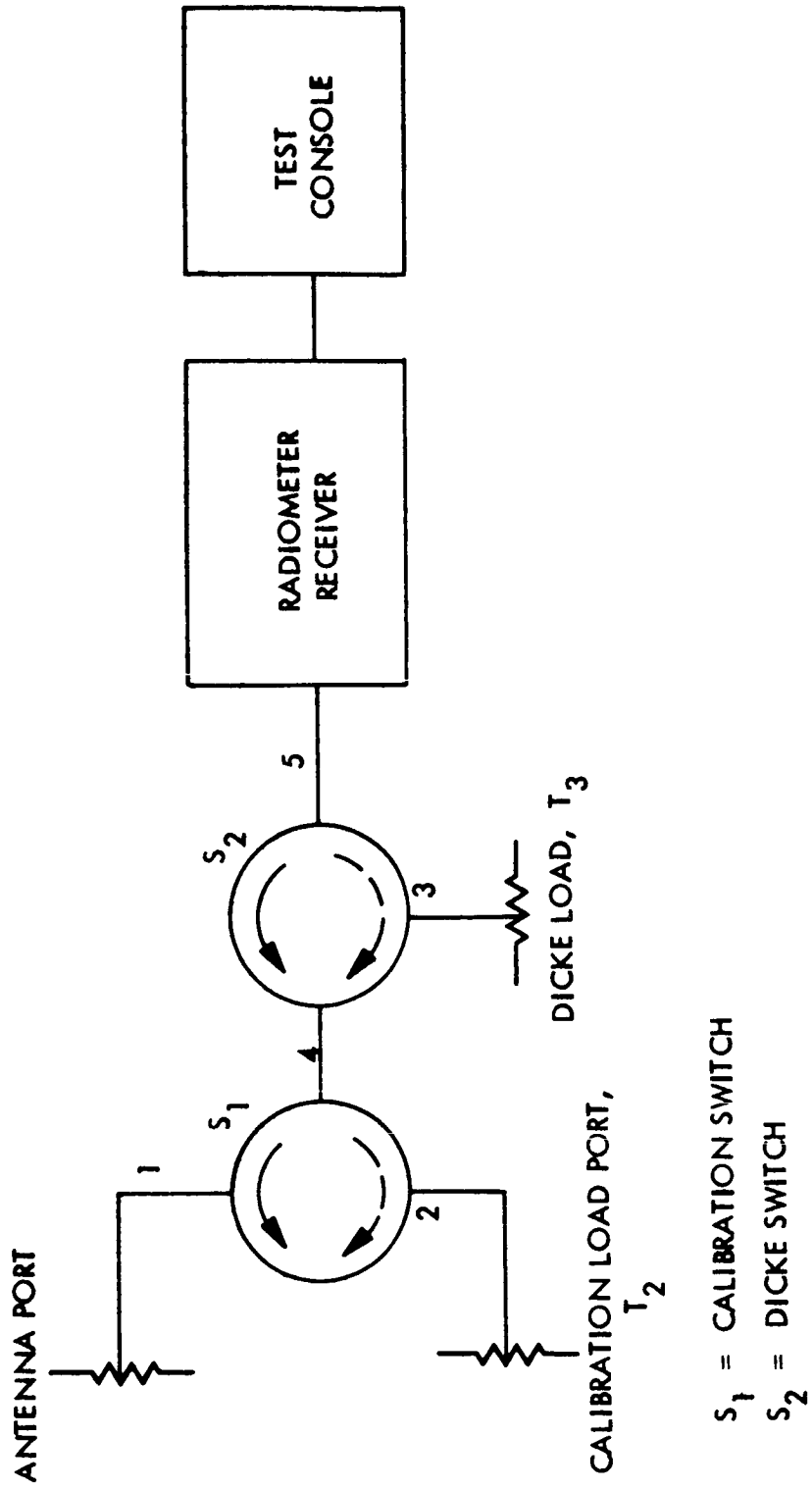


Figure 6-1. Radiometer Switching Network

- e. The isolation of the input circulator of the receiver is sufficiently high so that the receiver gain is totally independent of any impedance variations introduced by the switching network to the left of Port 5.

With these conditions satisfied (or nearly so) it is possible to relate the radiometric temperature of the switching network outputs at Port 5 to the radiometric temperatures of the terminations at Ports 1, 2 and 3, the insertion losses of the transmission paths, and the thermal temperatures of these losses.

The radiometric temperature outputs corresponding to the various combinations of the settings of the switches are (see list of definitions):

S_1	S_2	T_{in}
1 or 2	3	$T_{in} = \frac{T_3}{L_{35}} + \left(\frac{L_{35} - 1}{L_{35}} \right) T_{amb}$
1	4	$T_{in} = \frac{T_1}{L_{15}} + \left(\frac{L_{15} - 1}{L_{15}} \right) T_{amb}$
2	4	$T_{in} = \frac{T_2}{L_{25}} + \left(\frac{L_{25} - 1}{L_{25}} \right) T_{amb}$

List of definitions for terms in equations are as follows:

- T_n radiometric temperature of the terminations at Ports
n = 1, 2 and 3.
- L_{n5} insertion loss from Ports n = 1, 2 and 3 and Port 5.
- T_{amb} thermal ambient temperature of the transmission paths in
the switching network
- G_r radiometer gain coefficient, volts per degree Kelvin.

Since the Dicke switch is switching between Positions 3 and 4 at a periodic rate and the calibration switch is switched only at non-periodic intervals, the radiometer output voltages are

Position of S_1	Output Voltage
1	$V_{o1} = G_r \left[\frac{T_3}{L_{35}} + \left(\frac{L_{35} - 1}{L_{35}} \right) T_{amb} - \frac{T_1}{L_{15}} - \left(\frac{L_{15} - 1}{L_{15}} \right) T_{amb} \right]$
2	$V_{o2} = G_r \left[\frac{T_3}{L_{35}} + \left(\frac{L_{35} - 1}{L_{35}} \right) T_{amb} - \frac{T_2}{L_{25}} - \left(\frac{L_{25} - 1}{L_{25}} \right) T_{amb} \right]$

Terminations 2 and 3 are used as radiometric references to establish the overall system gain and, thus, provide an absolute scale which relates the radiometric temperature at Port 1.

Absolute measurements of gain and antenna temperatures may be accomplished in two ways. The first method requires that L_{15} , L_{25} and L_{35} be accurately known as well as their thermal temperature, T_{amb} . Then, by measuring the output voltage under the two switch positions of S_1 , one can solve for T_1 .

A somewhat simpler way to achieve the absolute gain is to make all the losses equal (i. e., $L_{15} = L_{25} = L_{35}$), which results in the following equations:

Position of S_1	Equation
1	$V_{o1} = G_r' (T_3 - T_1)$
2	$V_{o2} = G_r' (T_3 - T_2)$

The losses may be equalized by adding some dissipative loss to whichever transmission paths require it, taking the value of the path with the greatest loss as the final value of L . Over a 330°K antenna brightness temperature range the three losses must be equal to within 0.03 dB to cause an error of less than 1°K .

When the conditions of equal loss are established the gain constant is measured whenever the calibration switch is switched to the termination,

$$G_r' = \frac{V_{o2}}{T_3 - T_2}$$

and, thus,

$$T_1 = T_3 - \frac{V_{o1}}{V_{o2}} (T_3 - T_2)$$

It is apparent from the above equations that, if the insertion losses in all three transmissions paths in the switching network are equalized and Ports 1, 2 and 3 are terminated in equal temperature loads, the radiometer zero is established. Also, the output is independent of the three termination temperatures; thus, a zero check can be performed for any termination temperatures.

The first stage of the radiometer calibration consists of establishing the radiometer zero setting and equalizing the switching network insertion losses. This equalization eliminates the dependence of the radiometer calibration on the ambient temperature of the switching network, provided the insertion losses are sufficiently constant within the required 0° to 50°C ambient temperature range. Even if the insertion losses vary slightly the temperature dependence is greatly reduced to a point where any corrections required using the switch (module) temperature monitor output should amount to less than 3°K over the full range of 0° to 50°C ambient.

6.2 STEPS IN BENCH CALIBRATION

6.2.1 RADIOMETRIC ZERO SETTING AND EQUALIZATION OF MICROWAVE SWITCHING NETWORK INSERTION LOSSES

6.2.1.1 RADIOMETRIC ZERO SET

The RF portion of the radiometer is brought to an ambient temperature of 35°C together with all three of the matched terminations. For this condition the radiometric temperature presented by the switch output

Port 5 to the receiver input is independent of the insertion loss associated with a particular selection of Ports 1, 2 and 3. Consequently, the radiometer output voltages corresponding to S_1 positions 1 and 2 should both be equal to zero. This procedure provides an output voltage reference corresponding to the radiometric zero point calibration. The individual steps of this measurement are described in the paragraphs following.

Place the radiometer in an oven stabilized to within $\pm 0.5^\circ\text{C}$ at 35°C . The hot reference load heater is disconnected and matched waveguide loads are placed on the two external waveguide ports normally occupied by the signal antenna and the cold reference.

Calibrated thermistors are placed on each of the two external loads and also on the aluminum block housing the two ferrite switches. These three thermistors, together with the monitor thermistor in the internal reference load, are continuously monitored to provide a record of the termination temperatures and the temperature of the ferrite switches.

Sufficient time must be allowed with the radiometer operating in the temperature controlled oven to insure that the switches and loads on temperatures become equalized and stabilized to within $\pm 0.2^\circ\text{C}$. In this condition the radiometer output voltage is measured at the output of the synchronous detector by means of an operational amplifier integrator housing a 10-second (6 dB per octave) integration time.

This will result in the peak-to-peak fluctuations of the radiometric output voltage originating from receiver thermal noise to correspond to approximately 0.4° peak-to-peak fluctuations in the radiometer input temperature. It is, thus, apparent that if the measurement is to be limited only to receiver thermal noise, then fluctuations in the thermometric temperature of the receiver source must be smaller, e. g., $\pm 0.2^\circ\text{K}$ occurring at a periodically large time compared to the integration time.

The output voltage is then recorded simultaneously with the four thermistor bridge output voltages and a timing marks with a calibrated six-channel chart recorder.

The radiometer output voltage is then observed under the following conditions:

- a. With RF Switch S_1 set at the signal antenna Port 1
- b. With the Switch S_2 set at the cold reference Port 2
- c. With the 600 cps drive removed from the modulator RF Switch S_2 .

NOTE: The radiometer output voltage (previously measured in the pick-up and ground-loop tests) with modulator Switch S_2 operating but with the receiver input disconnected from the switch output by means of a metal window across the guide connecting the Switch S_2 output to the receiver input isolator, gives the component of radiometer output voltage due to electromagnetic coupling between the Switch S_2 drive coil and the video amplifier.

The difference between the average of the voltages measured in Step a and Step b, and the output voltage measured in Step c, (above paragraph) gives the magnitude and sign of the radiometer output which is the summation of the voltages resulting from any slight thermal differences in the switches and terminations, synchronous variation of the reflection coefficients looking into Switch S_2 from the receiver direction, and electromagnetic pickup of the 600 cps by the video amplifier due to ground loops and electromagnetic coupling from the drive coil of the modulator Switch S_2 . Since this ground loop and pickup voltage has been previously measured, the difference is the radiometer output component resulting from small temperature differences and synchronous modulation of the reflection coefficient presented to the receiver.

Although it is anticipated that this quantity will correspond to a temperature difference of less than 1°K it is important to obtain quantitative verification.

The difference of the output voltage magnitudes obtained in Steps a and b is indicative of the degree to which the temperatures of the external port terminations differ from each other and any differences in their impedance match.

From a previous approximate calibration of the radiometer it is possible to relate these voltages to relative temperature differences. The voltages obtained in Steps a, b and c should each correspond to less than 1°K temperature difference.

The average of Voltages a and b then correspond to zero radiometric temperature difference within the limits of the experimental ability to measure temperatures of the three sources and the switches.

With the radiometer zero point established the insertion loss equalization of the switching network can be initiated.

6.2.1.1.1 EQUALIZATION OF INSERTION LOSS FROM PORTS 1 AND 2 TO PORT 5

Place two 65°C hot loads on Ports 1 and 2 with the reference hot load remaining at the 35°C ambient temperature of the Switches S₁ and S₂. Then, observe the radiometer output voltage and observe with Switch S₁ set at Port 1 and then at Port 2. Then, interchange the loads on Ports 1 and 2, and again observe the output voltages with S₁ set at 1 and at 2. Designating the two sets of voltages as v_{a1}, v_{b1}, and v_{a2}, v_{b2}, respectively, the radiometer voltage output due to any radiometric temperature difference in the two sources is given by

$$ST = \frac{(v_a - v_b)_1 - (v_a - v_b)_2}{2g}$$

while the radiometer output voltage due to difference in the insertion losses L₁₅ and L₂₅ is proportional to

$$\Delta T = \frac{(v_a - v_b)_1 + (v_a - v_b)_2}{2g}$$

where g, the approximate radiometer gain coefficient, is expressed in terms of the average voltage output increase 'V' over the previously established radiometer zero output by the relation

$$g = \frac{V}{T_H - T_o} = \frac{V}{(65 - 35)^{\circ}\text{K}}$$

the difference between the two attenuations L_{15} and L_{25} is determined from the indicated radiometric temperature difference ΔT .

$$\Delta T = \left[\frac{T_H}{L_{15}} + \left(\frac{L_{15} - 1}{L_{15}} \right) T_o \right] - \left[\frac{T_H}{L_{be}} + \left(\frac{L_{25} - 1}{L_{25}} \right) T_o \right]$$

assuming

$$L_{15} = L_{25} (1 + \delta), \text{ and } (L_{15} - 1) \ll 1$$

$$T_o < T_h$$

The differential attenuation δ equals

$$\delta = \frac{\Delta T}{T_H - T_o}$$

attenuation is added to the lower attenuation input port until ΔT in the above equation is reduced to 0.2°K . Previous insertion loss measurements indicate approximately 0.08 dB corresponding to an initial value of $ST = .02$ and $\Delta T \approx 6^{\circ}\text{K}$.

6.2.1.1.2 EQUALIZATION OF INSERTION LOSS FROM PORT 3 to PORT 5

With Ports 1 and 2 giving the same radiometric indication, the heating element in the reference hot load on Port 3 is then activated, allowing at least one hour for the temperature to stabilize to the value $T_H = 65^{\circ}\text{C}$. The radiometer output is then observed with the Switch S_1 in either position 1 or 2. Now, all three ports are terminated in the same temperature to within the accuracy of the monitor thermistors in the three hot loads. If the insertion loss L_{35} equalled L_{15} and L_{25} , the radiometer output voltage would be equal to the previously determined radiometric zero value. The same procedure of interchanging hot loads is used to eliminate the effects of load temperature differences and attenuation is added to transmission path 35 until the output voltage equals the radiometric zero value with $\pm 0.2^{\circ}\text{K}$.

6.2.1.1.3 CHECK OF TEMPERATURE SENSITIVITY OF INSERTION LOSS EQUILIZATION

Maintaining the hot loads on the three ports at 65°C , the ambient temperature of the radiometer is then very slowly (over a period of four hours) reduced to 0°C and the output voltage change observed. If the load monitor thermistors readings remain unchanged then any change in the output voltage is a radiometric zero shift resulting either from a gain change in the receiver electronics or more likely from attenuation unbalance resulting from attenuation change with temperature in the ferrite Switches S_1 and S_2 . The same observation should be made with a 50°C ambient temperature for the radiometer. Repeating these measurements should permit correlation of radiometric zero drift with ambient temperature and, thus, allow the derivation of a radiometric data correction factor for use with the switch monitor thermistor data output record; e. g. , in the above measurements as the ambient is changing it should be possible to obtain a repeatable curve of radiometric zero shift as a function of the switch temperature monitoring thermistor.

6.3 RADIOMETER CALIBRATION WITH EXTERNAL RADIOMETRIC TEMPERATURE REFERENCES

The radiometric zero setting and the insertion loss equalization of the switching network is completed. Calibration of the radiometer output voltage versus varying antenna port temperature for several different values of fixed temperature terminations on Port 1 can be performed. Interchanging the radiometric sources with the various fixed temperature terminations on the antenna Port 1 and varying the cold reference Port 2 termination should produce the same radiometric output. Repeating these procedures for several different ambient temperatures between 0°C and 50°C and employing, if necessary, any ambient temperature dependent correction factors previously determined in Section A. 2. 1. 1. 3, should establish the absolute accuracy to which the radiometric temperature of the antenna port can be ascertained from the radiometric output voltage and knowledge of the hot and cold reference ports radiometric temperatures and the switching network ambient temperature.

When these steps in the basic calibration procedure have been completed, an accurate temperature calibration curve may be obtained using the cold load bench test set described in Section 7. Such a curve was obtained using this bench test set and is shown in Figure 6-2 for both liquid nitrogen and liquid helium. Note that the gain of the system in counts per degree Kelvin is the reciprocal of the slope of the calibration curve. The gain under these two conditions is different due to the nature of the radiometer AGC, which is discussed in the original proposal to NASA Goddard for the entire radiometer (SGC P-6308). The value of the offset is roughly 2 counts or 1°K .

The radiometer sensitivity was measured and found to be consistently better than 0.66°K rms, which is somewhat better than the required specification of 0.70°K .

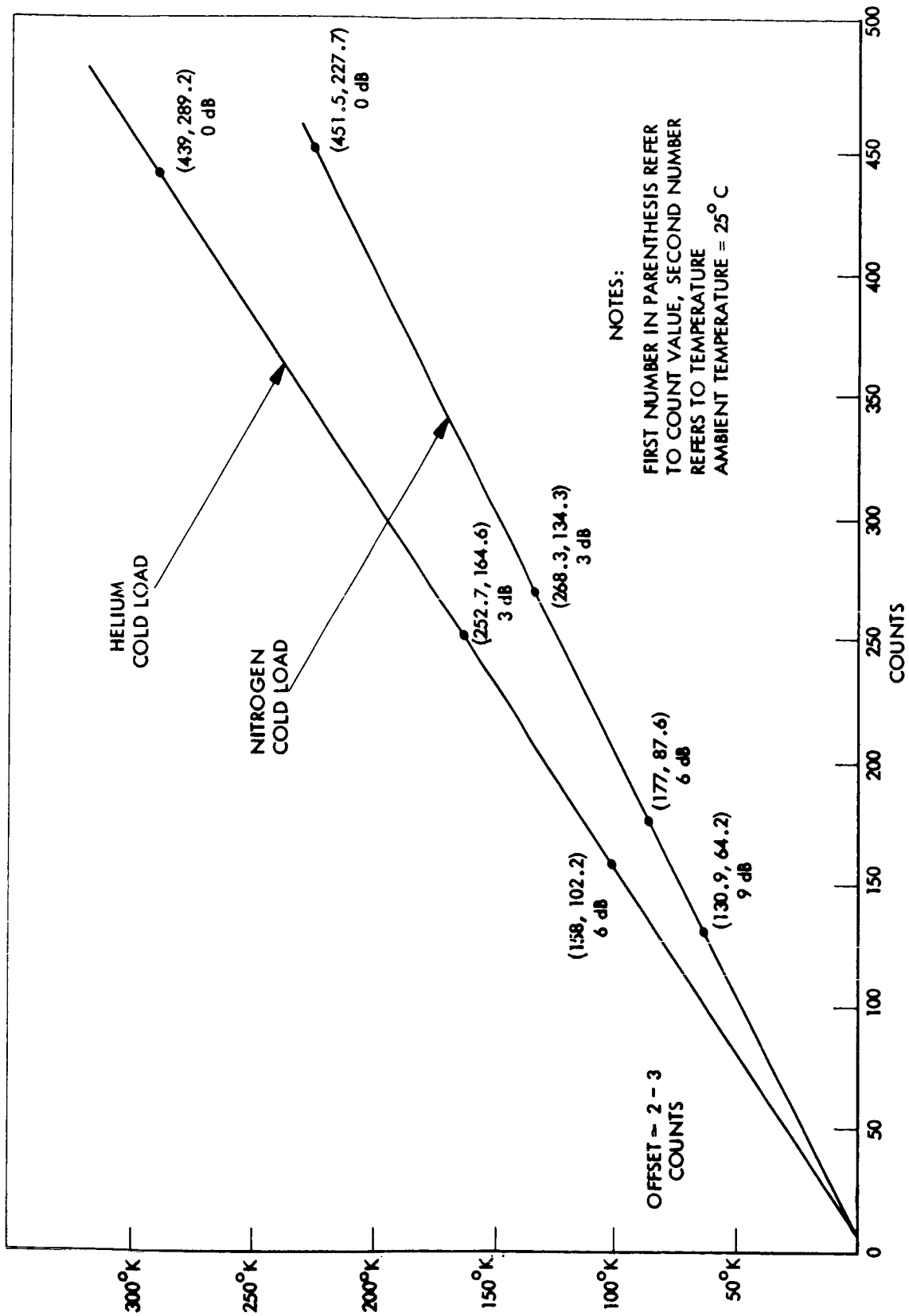


Figure 6-2. Typical Calibration Curves of Radiometers Using Bench Test Set

Section 7

COLD LOAD TEST SET

7.1 INTRODUCTION

The purpose of the cold load bench test set is to provide an accurate temperature calibration of the radiometer response as a function of antenna brightness temperature. Secondary results of such a calibration are to provide a linearity check and to correlate previous measurements of the amount of offset produced when the radiometer antenna temperature is equal to the radiometer Dicke temperature; i. e., the temperature of the hot load located inside the radiometer module. This is done by extrapolation of the calibration curve. The value of offset obtained may then be compared to values obtained in previous bench calibrations. The exact testing procedure used will be described below. Once the radiometer response is established, the radiometer may then be used to measure the antenna parameters and to perform absolute radiometric measurements.

7.2 DESCRIPTION OF THE COLD LOAD TEST SET

Briefly, the cold load test set is constructed as follows: two matched terminations are heat-sunk to a Texas Instruments' cryoflask. The vacuum seal of this flask is maintained by the insertion of two matched mica windows into the flange which is sealed to the side of the cryoflask. Two lengths of waveguide join this flange to another flange which is the output port of the bench test set. One waveguide arm contains a calibrated precision attenuator, the other contains only various sections of waveguide. The attenuator arm connects to the radiometer antenna port, the other goes to the radiometer calibrate port. The cryoflask may be filled with cryogenic liquids such as nitrogen or helium to bring the loads down to the liquid temperatures. A block diagram of the test set is shown in Figure 7-1.

Since the resultant radiometric temperature of a load at a designated temperature is a function of various power transmission parameters

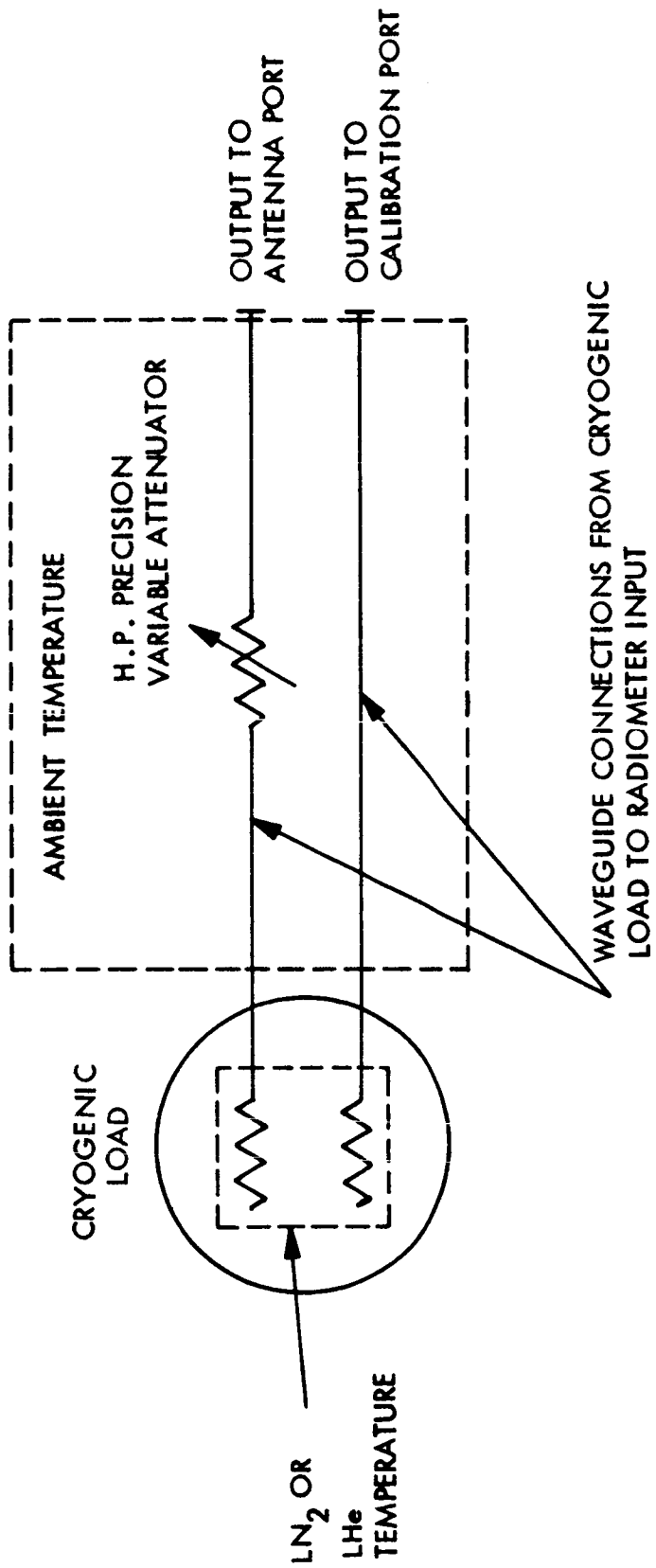


Figure 7-1. Block Diagram of The Cold Load Bench Test Set

existing between the observation port and the load, the numerous losses present (both dissipative and reflective) must be known to a considerable degree of accuracy. With this end in view, the total insertion losses and standing wave ratios of both arms were measured. The same measurements were made with the individual arm components as well as with the mica window and the plated waveguide inside the cryoflask itself.

The Hewlett-Packard precision attenuator used in the antenna arm was measured for residual insertion loss at four different settings: 0, 3, 6, and 9 decibels. Since this residual loss is either constant or increases slightly (and in a linear fashion with attenuation), interpolation of the measured losses to obtain losses for other attenuator settings poses no problem. The drift of the attenuator with a 50°C temperature range was also measured and found to be negligible (approximately 0.005 dB). Incidentally, the 0-decibel residual loss of 0.46 decibels causes the apparent temperature of the attenuator arm to be always greater than that of the calibration arm.

To know the radiometric brightness temperature of the bench test set to within 1/2°K or less, it was necessary to make all insertion loss measurements on the SGC insertion loss test set, which is modeled after the test set proposed by C. T. Stelzried and S. M. Petty of JPL in the IEEE Transactions on Microwave Theory and Techniques. The following is a quotation of the article's summary:

"A simple, accurate test set has been devised for measuring insertion losses at microwave frequencies. It is composed almost entirely of commercially available equipment and components. The short-term jitter is about 0.0004 dB peak-to-peak, and long-term drift is typically 0.0015 dB per hour. Accuracy of the measurements depends upon the value of the insertion loss to be measured and is better than +0.001 to +3 percent for insertion losses in the 0 to 25 dB range. These accuracies include the non-repeatability of connecting and disconnecting the waveguide flanges used in the system."

The accuracy of the SGC test set is believed to be better than 0.003 dB for small losses.

VSWR measurements of the waveguide sections, attenuator, and window were made on a Hewlett-Packard slotted line. Both the VSWR and the phase of the reflection coefficient were measured for each item. Attenuation

measurements for each piece of waveguide and the attenuator were made a number of times on the insertion loss test set to minimize errors due to drifts in the test set. Averages were taken to determine the various values for loss.

7.2 OUTPUT TEMPERATURES OF THE COLD LOAD TEST SET

Computations of apparent brightness temperature were carried out using the model in Figure 7-2 for the test set.

- a. The load is assumed to be at the boiling point of the cryogenic liquid in the flask. This is thermometric temperature, t_L , and it gives the matched termination a radiometric brightness temperature, T_L .
- b. Between the termination and the mica window is a length of stainless steel waveguide with a constant loss per unit length and a linear temperature distribution between the boiling point temperature of the cryogenic liquid and the prevailing ambient temperature. These temperatures are t_L and t_A , respectively.
- c. The equivalent radiometric temperature seen at the output of the guide is given by $T_{eq} = T_L + (t_A - t_L)(1 - 1/L_1)/\mathcal{L}$ where $\mathcal{L} = 0.23026 L_1$ (dB). Note that T_L is numerically equal to t_L .
- d. The temperature seen just past the mica window due to reflective losses only is given by:

$$T' = \frac{(1 - |\Gamma_1|^2)(1 - |\Gamma_2|^2)}{(|1 - \Gamma_2 \Gamma_3|)^2} T_{eq}$$

This is the equation representing power delivered to a mismatch load by a mismatch generator. Note that the phases of Γ_1 and Γ_2 are required in the denominator.

- e. When the dissipative loss of the window is taken into account, the resulting radiometric temperature is given by: $T_1 = T'/L_2 + t_A(1 - 1/L_2)$.

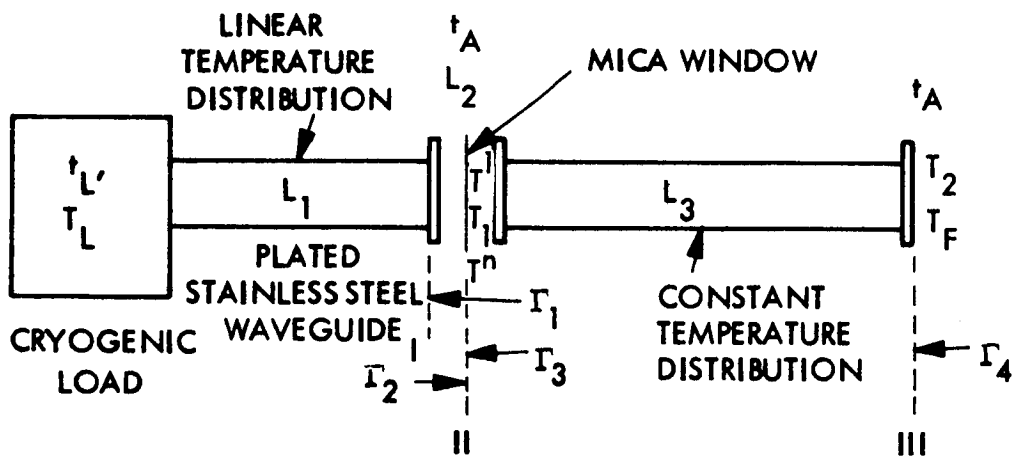


Figure 7-2. Model for Cold Load Test Set Calibration

- f. Reflections between the mica window and the external waveguide cause more loss. The equation for this reflective loss is:

$$T'' = \frac{(1 - |\Gamma_2|^2)(1 - |\Gamma_3|^2)}{(|1 - \Gamma_2 \Gamma_3|)^2} T_1$$

- g. The dissipative loss of the external waveguide arms is taken into account in the same manner as the window loss, since the waveguide is at the constant temperature t_A .

This gives the output temperature of the bench test set as:
 $T_F = T''/L_3 + t_A (1 - 1/L_3)$.

- h. The output temperature, T_F , of the test set is not the same as that seen by the radiometer because the set presents a certain VSWR to the radiometer and, hence, reflects a certain portion of the radiometer's own brightness temperature back into the radiometer itself. This can be corrected for by adding the term $|\Gamma_4|^2 t_A$ to the output temperature, T_F . This is the apparent brightness temperature seen by the radiometer.

7.3 ERROR ANALYSIS

For losses less than 0.5 dB, the equivalent temperature at the output of the stainless steel waveguide may be expressed accurately as:

$$T_{eq} = T_L + .115 (t_A - t_L) L$$

The maximum uncertainty in T_{eq} is then given by:

$$\Delta T_{eq} = |\Delta T_L| + .115 (t_A - t_L) |\Delta L| + .115 L |\Delta(t_A - t_L)|$$

The loss of this section of waveguide is approximately 0.06 dB and is known to well within ± 0.003 dB. For $t_A - t_L \approx \pm 210^\circ\text{K}$ and $\Delta(t_A - t_L) \approx \pm 0.2^\circ\text{K}$ the uncertainty in ΔT_{eq} is

$$\Delta T_{eq} = |\Delta T_L| + .072 + .0014 = (|\Delta T_L| + .0734)$$

The boiling point of the cryogenic used is known very well (see Table 7-1) for various pressures. The uncertainty in the actual temperature of the resistive portion of the load is felt to be less than 0.1°K resulting in an uncertainty in ΔT_{eq} of less than $.175^{\circ}\text{K}$.

For the reflection loss equations, we have:

$$\Delta T' = \Delta T_{\text{eq}} [\text{mismatch factor}] + \Delta(\text{mismatch factor terms}) T_{\text{eq}}$$

"Since Γ 's are $\gg 1$, the mismatch factor is close to unity and the Δ (mismatch factor terms) are $\geq 10^{-3}$ and the term of significance is still ΔT_{eq} ."

Further analysis indicates that the significant error still lies in the uncertainty in the load temperature, T_{L} , which determines to a great degree the uncertainty in T_{eq} . All other terms combined add a negligible amount to the uncertainty in T_{F} , because of the accuracy of the insertion loss measurements and the negligible effect of the small reflections. The accuracy of T_{F} is then equal to the accuracy in knowing T_{eq} . Since $\Delta T_{\text{eq}} = .175^{\circ}\text{K}$, one can perform an absolute calibration of this radiometer to within $\pm 1^{\circ}\text{K}$ with a high degree of probability.

Table 7-1
CRYOGENIC BOILING POINTS

Pressure Mm. Hg.	Temperature	
	Helium	Nitrogen
1	1.3°K	47.0°K
10	1.8°K	54.0°K
40	2.2°K	59.1°K
100	2.6°K	63.4°K
400	3.9°K	72.2°K
760	4.2°K	77.3°K

Boiling Points of Liquid Helium and Nitrogen

The expression in the denominator of the third equation indicates the necessity of making phase measurements. However, a sample calculation shows that errors made by assuming the denominator is equal to 1.0000 are negligible; that is, they are about equal to one part in 10^4 .

The relevant equations were solved for sixty discrete values of ambient temperature and for four attenuator settings, using an IBM System-360 computer. The resulting printouts (see Tables 7-2 and 7-3) give the apparent radiometric temperatures at the antenna and calibration ports as a function of both ambient temperature and attenuator setting for both liquid nitrogen and liquid helium.

To use the test set as a calibration device, one must first note the ambient temperature and pressure. The pressure determines the boiling point of the cryogenic liquid used in the flask, and the temperature determines the apparent output temperature as read from the computer tables. Differences in boiling points may be added directly to the computed results with negligible error.

After connecting the test set to the radiometer through waveguide sections whose loss is precisely known, one actuates the radiometer and gathers several frames of digital output. The average of 100 antenna temperature counts is computed, as is the average of all the calibration port counts. This is done for a number of attenuator settings on the test set. If the calibration count is found to drift, the antenna average for a given run may be corrected by multiplying it by the ratio of the first calibration count to the calibration count for the run of interest.

It is now possible to plot antenna counts versus radiometric temperature. The resulting graph should be a straight line, but only if the apparent cold load temperatures are first subtracted from 339.0 degrees Kelvin, the temperature of the Dicke load inside the radiometer. It thus becomes apparent that as the radiometric temperature increases, the difference between it and the Dicke temperature becomes smaller and the output count diminishes. The intercept on the graph where this temperature equals zero gives a residual count which ideally should also equal zero but which, in fact, is on the order of this counts, or about 1 degree Kelvin, a value which agrees with the offset obtained in the measurements described in Section 6.

Table 7-2

COLD LOAD BENCH TEST SET OUTPUTS FOR
 VARIOUS ATTENUATOR SETTINGS,
 LIQUID NITROGEN

TLOAD OF NITROGEN = 77.3

TR	0	3	6	9	CAL
261	108.07	184.65	222.85	242.06	95.07
262	108.24	185.23	223.64	242.96	95.17
263	108.41	185.82	224.44	243.86	95.26
264	108.58	186.40	225.23	244.76	95.36
265	108.74	186.99	226.02	245.65	95.46
266	108.91	187.57	226.81	246.55	95.56
267	109.08	188.16	227.61	247.45	95.65
268	109.25	188.74	228.40	248.34	95.75
269	109.42	189.33	229.19	249.24	95.85
270	109.58	189.91	229.98	250.14	95.95
271	109.75	190.50	230.78	251.03	96.04
272	109.92	191.08	231.57	251.93	96.14
273	110.09	191.66	232.36	252.83	96.24
274	110.26	192.25	233.15	253.72	96.33
275	110.42	192.83	233.95	254.62	96.43
276	110.59	193.42	234.74	255.52	96.53
277	110.76	194.00	235.53	256.41	96.63
278	110.93	194.59	236.32	257.31	96.72
279	111.10	195.17	237.12	258.21	96.82
280	111.26	195.76	237.91	259.11	96.92
281	111.43	196.34	238.70	260.00	97.02
282	111.60	196.93	239.49	260.90	97.11
283	111.77	197.51	240.29	261.80	97.21
284	111.94	198.10	241.08	262.69	97.31
285	112.10	198.68	241.87	263.59	97.41
286	112.27	199.26	242.66	264.49	97.50
287	112.44	199.85	243.45	265.38	97.60
288	112.61	200.43	244.25	266.28	97.70
289	112.78	201.02	245.04	267.18	97.79
290	112.94	201.60	245.83	268.07	97.89

Table 7-2 (Continued)

COLD LOAD BENCH TEST SET OUTPUTS FOR
VARIOUS ATTENUATOR SETTINGS,
LIQUID NITROGEN

TLOAD OF NITROGEN = 77.3

TR	0	3	6	9	CAL
291	113.11	202.19	246.62	268.97	97.99
292	113.28	202.77	247.42	269.87	98.09
293	113.45	203.36	248.21	270.77	98.18
294	113.62	203.94	249.00	271.66	98.28
295	113.78	204.53	249.79	272.56	98.38
296	113.95	205.11	250.59	273.46	98.48
297	114.12	205.69	251.38	274.35	98.57
298	114.29	206.28	252.17	275.25	98.67
299	114.46	206.86	252.96	276.15	98.77
300	114.62	207.45	253.76	277.04	98.87
301	114.79	208.03	254.55	277.94	98.96
302	114.96	208.62	255.34	278.84	99.06
303	115.13	209.20	256.13	279.73	99.16
304	115.30	209.79	256.93	280.63	99.25
305	115.46	210.37	257.72	281.53	99.35
306	115.63	210.96	258.51	282.43	99.45
307	115.80	211.54	259.30	283.32	99.55
308	115.97	212.13	260.09	284.22	99.64
309	116.14	212.71	260.89	285.12	99.74
310	116.30	213.29	261.68	286.01	99.84
311	116.47	213.88	262.47	286.91	99.94
312	116.64	214.46	263.26	287.81	100.03
313	116.81	215.05	264.06	288.70	100.13
314	116.98	215.63	264.85	289.60	100.23
315	117.15	216.22	265.64	290.50	100.33
316	117.31	216.80	266.43	291.39	100.42
317	117.48	217.39	267.23	292.29	100.52
318	117.65	217.97	268.02	293.19	100.62
319	117.82	218.56	268.81	294.08	100.71
320	117.99	219.14	269.60	294.98	100.81

Table 7-3

COLD LOAD BENCH TEST SET OUTPUTS FOR
VARIOUS ATTENUATOR SETTINGS,
LIQUID HELIUM

TLOAD OF HELIUM = 4.2

TR	0	3	6	9	CAL
261	47.34	154.32	207.69	234.53	29.19
262	47.51	154.90	208.48	235.42	29.29
263	47.68	155.49	209.27	236.32	29.38
264	47.85	156.07	210.06	237.22	29.48
265	48.02	156.66	210.86	238.11	29.58
266	48.18	157.24	211.65	239.01	29.68
267	48.35	157.83	212.44	239.91	29.77
268	48.52	158.41	213.23	240.80	29.87
269	48.69	159.00	214.03	241.70	29.97
270	48.86	159.58	214.82	242.60	30.07
271	49.02	160.17	215.61	243.49	30.16
272	49.19	160.75	216.40	244.39	30.26
273	49.36	161.33	217.20	245.29	30.36
274	49.53	161.92	217.99	246.19	30.46
275	49.70	162.50	218.78	247.08	30.55
276	49.86	163.09	219.57	247.98	30.65
277	50.03	163.67	220.37	248.88	30.75
278	50.20	164.26	221.16	249.77	30.84
279	50.37	164.84	221.95	250.67	30.94
280	50.54	165.43	222.74	251.57	31.04
281	50.70	166.01	223.54	252.46	31.14
282	50.87	166.60	224.33	253.36	31.23
283	51.04	167.18	225.12	254.26	31.33
284	51.21	167.76	225.91	255.15	31.43
285	51.38	168.35	226.70	256.05	31.53
286	51.54	168.93	227.50	256.95	31.62
287	51.71	169.52	228.29	257.84	31.72
288	51.88	170.10	229.08	258.74	31.82
289	52.05	170.69	229.87	259.64	31.92
290	52.22	171.27	230.67	260.54	32.01

Table 7-3 (Continued)

COLD LOAD BENCH TEST SET OUTPUTS FOR
VARIOUS ATTENUATOR SETTINGS,
LIQUID HELIUM

LOAD OF HELIUM = 4.2

TR	TRAD				CAL
	0	3	6	9	
291	52.38	171.86	231.46	261.43	32.11
292	52.55	172.44	232.25	262.33	32.21
293	52.72	173.03	233.04	263.23	32.30
294	52.89	173.61	233.84	264.12	32.40
295	53.06	174.20	234.63	265.02	32.50
296	53.22	174.78	235.42	265.92	32.60
297	53.39	175.36	236.21	266.81	32.69
298	53.56	175.95	237.01	267.71	32.79
299	53.73	176.53	237.80	268.61	32.89
300	53.90	177.12	238.59	269.50	32.99
301	54.06	177.70	239.38	270.40	33.08
302	54.23	178.29	240.18	271.30	33.18
303	54.40	178.87	240.97	272.20	33.28
304	54.57	179.46	241.76	273.09	33.38
305	54.74	180.04	242.55	273.99	33.47
306	54.90	180.62	243.34	274.89	33.57
307	55.07	181.21	244.14	275.78	33.67
308	55.24	181.79	244.93	276.68	33.76
309	55.41	182.38	245.72	277.58	33.86
310	55.58	182.96	246.51	278.47	33.96
311	55.74	183.55	247.31	279.37	34.06
312	55.91	184.13	248.10	280.27	34.15
313	56.08	184.72	248.89	281.16	34.25
314	56.25	185.30	249.68	282.06	34.35
315	56.42	185.89	250.48	282.96	34.45
316	56.59	186.47	251.27	283.85	34.54
317	56.75	187.06	252.06	284.75	34.64
318	56.92	187.64	252.85	285.65	34.74
319	57.09	188.23	253.65	286.55	34.84
320	57.26	188.81	254.44	287.44	34.93

7.4 REFERENCES FOR COLD LOAD TEST SET

1. A. J. Estlin, C. L. Trembath, J. S. Wells, and W. C. Daywitt, "Absolute Measurement of Temperatures of Microwave Noise Sources," IRE Trans. on Inst. and Meas., pp. 209-213, Sept. 1960.
2. J. S. Wells, W. C. Daywitt, and C. K. S. Miller, "Measurement of Effective Temperatures of Microwave Noise Sources," IRE Trans. on Inst. and Meas., pp. 17-28, March 1964.
3. C. T. Stelzreid, "Temperature Calibration of Microwave Thermal Noise Sources," IEEE Trans. on Microwave Theory and Techniques, pp. 128-130, Jan. 1965.
4. C. T. Stelzreid, "A Liquid Helium-Cooled Coaxial Termination," Proc. of IRE, p. 1224, July 1961.
5. R. C. Clauss, W. Higa, C. Stelzreid, and E. Wiebe, "Total System Noise Temperature: 15°K," IEEE Trans. on Microwave Theory and Techniques, pp. 619-620, Nov. 1964.
6. C. T. Stelzreid, "Temperature Calibration of Microwave Terminations," JPL Space Programs Summary No. 37-26, Vol. IV, pp. 189-194.
7. C. T. Stelzreid and S. M. Petty, "Microwave Insertion Loss Test Set," IEEE Trans. on Microwave Theory and Techniques, pp. 475-477, July 1964.
8. R. C. Menon, N. P. Albaugh, and J. W. Dozier, "Cooled Loads as Calibration Noise Standards for the mm-Wavelength Range," Proc. of IEEE, pp. 1501-1503, Oct. 1966.
9. R. W. Beatty, "Mismatch Errors in the Measurement of Ultrahigh-Frequency and Microwave Variable Attenuators," Journal of Research of the National Bureau of Standards, pp. 7-9, Vol. 52, No. 6, June 1964.
10. R. W. Beatty, "Insertion Loss Concepts," Proc. of IEEE, pp. 663-671, Vol. 52, No. 6, June 1964.

11. J. E. Sees, "Fundamentals in Noise Source Calibrations at Microwave Frequencies," Naval Research Lab., Wash., D.C., Rept. No. 5051, 1958.
12. A. E. Siegman, "Thermal Noise in Microwave Systems," Part 1, Microwave Journal, pp. 81-90, March 1961.
13. D. Schuster, C. T. Stelzreid, and G. S. Levy, "The Determination of Noise Temperatures of Large Paraboloidal Antennas," IRE Trans. on Antennas and Propagation, pp. 286-291, May 1962.

Section 8

ZENITH SKY TEMPERATURE

8.1 DISCUSSION

In this section the effective radiometric temperature of the sky in the zenith direction will be calculated for the 19.35 GHz region. Contributions to the zenith temperature, T_z , consist of three sources of radiation; that from the cosmic background, T_b ; that from the radiation due to the oxygen in the atmosphere, T_{O_2} ; and that from radiation due to the water vapor in the atmosphere, T_{H_2O} .

The zenith temperature, T_z , is given by:

$$T_z = \frac{T_b}{L} + T_{O_2} + T_{H_2O}$$

where L is the total zenith loss due to the O_2 and H_2O attenuation.

The cosmic black body radiation has only recently been discovered.⁽¹⁾⁽²⁾⁽³⁾ It appears to be isotropic, unpolarized and constant with regard to seasonal variations. In addition, from the limited number of observations made and from theoretical considerations, it appears to be independent of frequency. A measured value for this radiation at a frequency of 4080 MHz by BTL⁽¹⁾, using a low-noise hog-horn antenna, is $3.5^\circ \pm 1^\circ K$. Other values measured for T_b have ranged from 2-4^oK. Since this measurement is a difficult one to perform, the value for T_b is still not accurately known. However, for the purpose of these measurements a value of $3.5^\circ \pm 1^\circ K$ will be used.

The absorption of oxygen and water vapor gases at microwave frequencies has been studied theoretically by Van Vleck⁽⁴⁾, and the resultant radiant temperatures due to oxygen and water vapor have been calculated by Hogg⁽⁵⁾, based on a standard model of the atmosphere shown in Figure 8-1.

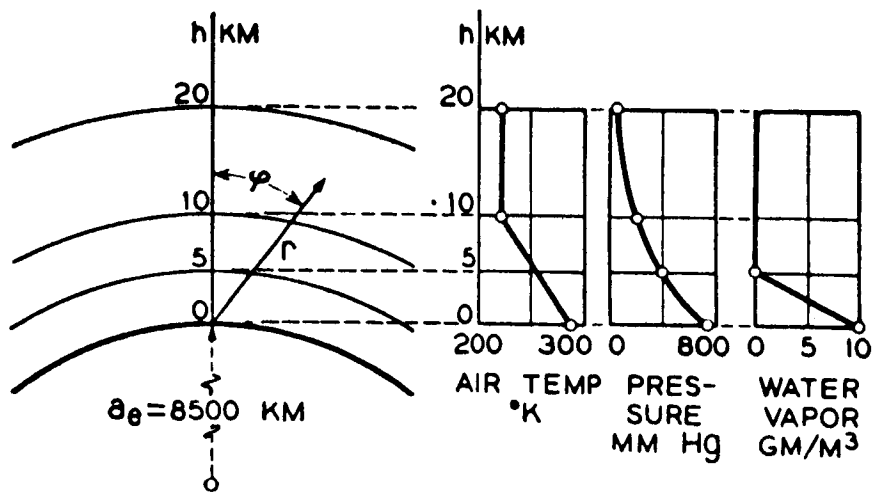


Figure 8-1. Model of The Earth Assumed in Calculations

Attenuation due to oxygen is the result of resonances of the oxygen molecules at 60 GHz. Due to pressure broadening, the lines blend together to give a width of approximately 0.5 to 1 GHz.

A curve of temperature versus frequency for various zenith angles is shown in Figure 8-2. ⁽⁵⁾ This is based on a standard atmosphere with a sea level pressure of 760 mm and a temperature of 290°K. At 19.35 GHz, we are well out on the skirt of the absorption curve and obtain a temperature of 3.4°K. Since the measurements were taken at a 7200-foot elevation, the absolute barometric pressure range was 588 to 5.94 mm/Hg. Thus, the radiated temperature would be reduced by approximately the ratio of the barometric pressures to a value of 2.64°K. The ambient temperature at 7200 feet ranged from 270°K to 288°K. For low values of attenuation the radiometric temperature is approximately a linear function of ambient temperature range and will be 2.46°K to 2.62°K. For the purpose of these measurements, an average value of 2.5°K will be used.

The atmospheric absorption due to the water vapor results from a resonance line at 22.5 GHz. Figure 8-3 shows the radiometric temperature versus frequency for various zenith angles due to the presence of water vapor. ⁽⁵⁾ This is based on a water vapor content of 10 g/m³ at sea level, linearly decreasing to 0 g/m³ at an altitude of 5 Km. At a frequency of 19.35 GHz, the temperature is a rapid function of frequency since it is close to the resonance frequency, 22.5 GHz making it more difficult to obtain an accurate value of T_{H_2O} .

From Figure 8-3, a value of $T_{H_2O} = 11.6^{\circ}K$ is obtained for the zenith at 19.35 GHz. For low attenuation values such as we have here, T_{H_2O} will be approximately a linear function of the absolute humidity. The absolute humidity, ρ , is expressed in grams/m³ and was calculated for each data run from the recorded air temperature and the relative humidity. The relative humidity was frequently low (0 - 15 percent) where it is difficult to measure accurately. Fortunately, however, the radiometric temperature contribution is small for low moisture content. Also, the sky was completely

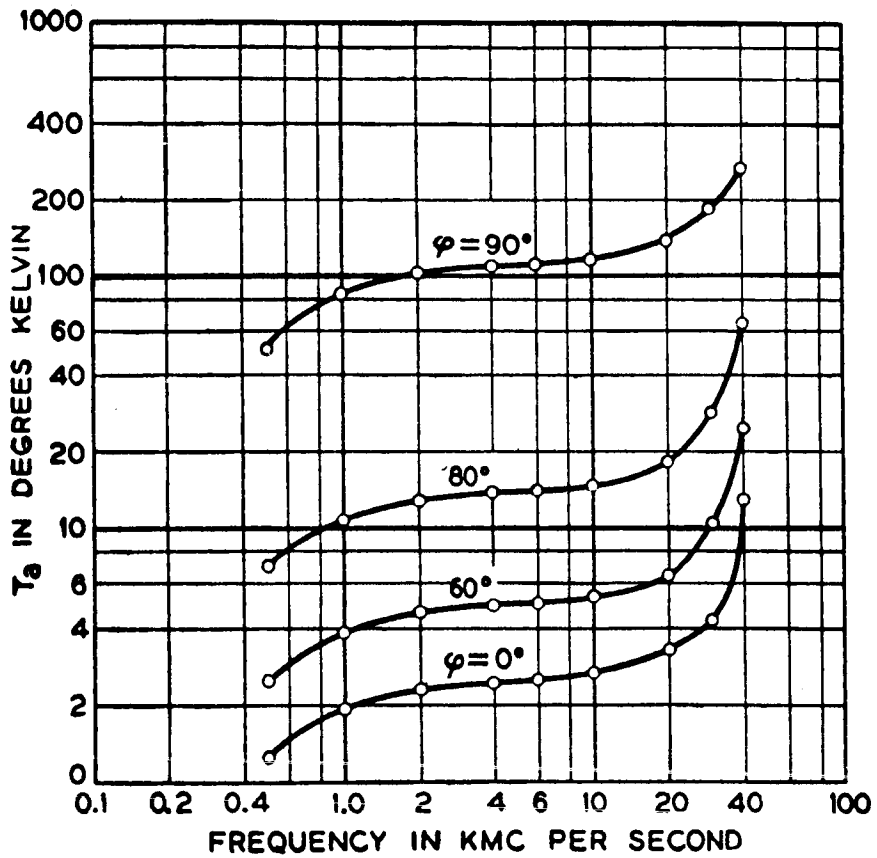


Figure 8-2. Zenith Temperature Contribution from Oxygen

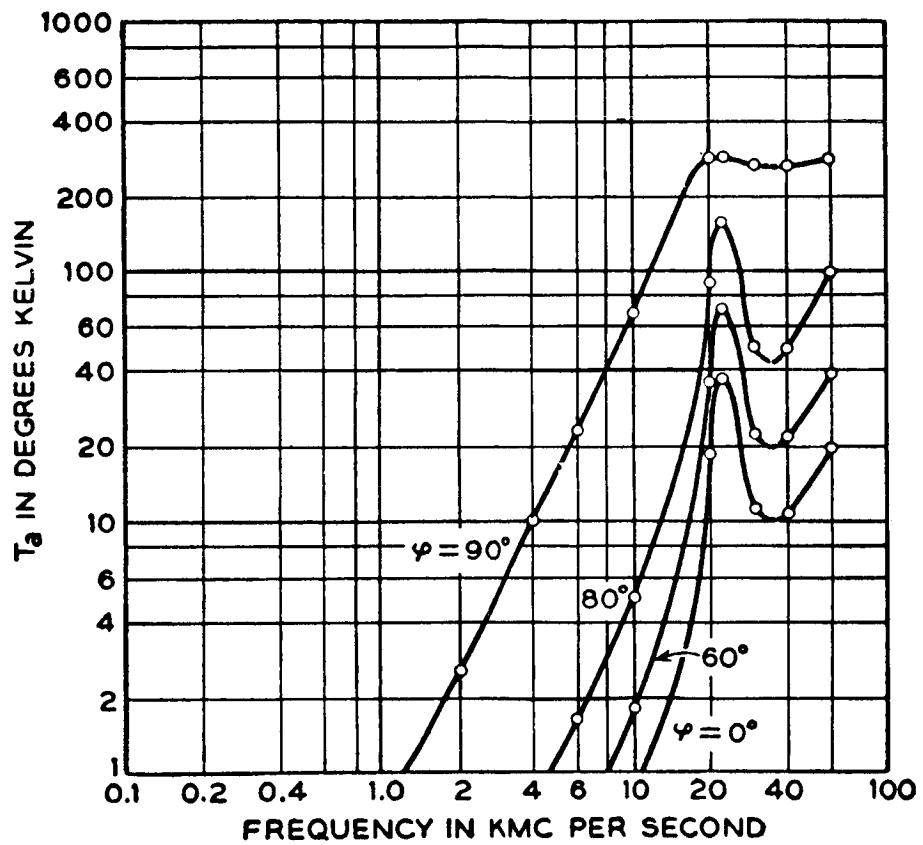


Figure 8-3. Zenith Temperature Contribution from Water Vapor

clear for most runs with the exception of a few runs having high thin cirrus clouds below a 60° zenith angle. Being at 7200 feet, the site was also above the temperature inversion layer which frequently occurs at lower altitudes in the Los Angeles basin, making the standard atmosphere curves of Figure 8-1 applicable.

The following table lists the radiometric temperature received from the zenith as a result of water vapor attenuation alone as a function of absolute humidity for the extremes of ambient temperature, t_A , of -3°C and 17°C .

Table 8-1
ATMOSPHERIC ZENITH TEMPERATURES

(Absolute Humidity)	$T_{\text{H}_2\text{O}}$ (for $t_A = -3^\circ\text{C}$)	$T_{\text{H}_2\text{O}}$ (for $t_A = 17^\circ\text{C}$)
0 gm/m ³	0°K	0°K
0.5	0.6	0.6°K
1	1.1	1.2°K
2	2.2	2.4°K
3	3.3	3.6°K
4	4.5	4.8°K
5	5.6	6°K
10	11.1	12°K

The absolute humidity ranged from 0 to 3 gm/m³ for all runs. Combining T_{O_2} and $T_{\text{H}_2\text{O}}$ for $\rho = 3 \text{ gm/m}^3$, we get a zenith temperature due to the atmosphere of 4.9°K . This is equivalent to a total attenuation of 0.98 which attenuates the galactic background temperature by a small amount from 3.5°K to 3.4°K .

Table 8-1 summarizes the zenith sky temperatures.

Table 8-2

ZENITH TEMPERATURE

Absolute Humidity	Cosmic Background T_b	Oxygen T_{O_2}	Water Vapor T_{H_2O}	Total T_z
0 gm/m ³	3.5°K	2.5°K	0°K	6.0°K
0.5	3.5	2.5	0.6	6.6
1	3.5	2.5	1.1	7.1
2	3.5	2.5	2.3	8.3
3	3.4	2.5	3.4	9.3
4	3.3	2.5	4.6	10.4
5	3.3	2.5	11.6	17.2

Since the absolute humidity was $< 3 \text{ g/m}^3$ during the measurements the zenith temperature range was 6-10°K during the runs. While the error in absolute value of the zenith temperature is probably $\pm 2^\circ\text{K}$ the relative values are probably accurate to $\pm 0.5^\circ\text{K}$ for different runs. Since the zenith temperature is low the effect on the accuracy of the antenna measurement is small, as discussed in the previous sections. Additional references on atmospheric radiation are ⁽⁶⁾ and ⁽⁷⁾ which include the effects of clouds and precipitation.

8.2 REFERENCES

1. Penzias, A. A., and Wilson, R. W., 1965, Ap. J, Vol. 142, (419)
2. Dicke, R. H., Peebles, P. J. E., Roll, P. G., and Wilkinson, D. T., 1965, Ap. J, VI42 (414)
3. Thaddeus, P., Inst. for Space Studies, NASA, Priv. Communications.
4. Van Vleck, J. H., Phys. Rev., (1947) Vol 71, (413)
5. Hogg, D. C., J.A.P., 1959 Vol 30 (1417)
6. Hogg, D. C., and Semplak, R. A., B.S.T.J., Sept. p 961, (1331)
7. Orhaug, T., National Radio Astronomy Observatory, Greenbank, Vol. I, No. 14, Oct. 1962

Section 9

SUN DRIFT CURVE

9.1 DISCUSSION

Since the sun is a strong source of thermal radiation at microwave frequencies and is relatively small in angular size it can be used as a source for calibrating the antenna and radiometer. The temperature of the sun is uniform across the disk and is equal to 6000°K or greater at 19 GHz. Its optical angular diameter is 32.4 minutes of arc. At 19 GHz the radio diameter and the optical diameter are almost equal.

By taking a cut of the sun with the antenna, the antenna pattern can be obtained. This is accomplished by positioning the beam to maximize the signal received from the sun. Then the mount is left stationary and the sun is allowed to drift through the antenna pattern. Because the sun moves through the sky at a constant 15° of arc per hour in right ascension or hour angle with a small change in declination ($\sim 0.1^{\circ}/\text{day}$), time can be converted into angular movement in degrees. Since the sun travels in a curved path the direction of the cut through the antenna pattern will be determined by the sun's path for that time of day. At noon the sun is moving in azimuth only.

If the sun were a point source the drift curve would be the same as the antenna pattern. Since the sun has a finite diameter the antenna pattern will appear to be broader. The observed pattern broadening as a function of the source width can be calculated for a uniform source⁽¹⁾. For example, if the source diameter, in degrees, equaled the half-power beam width, the broadening would be 20 percent. For the case of the Nimbus antenna with a beamwidth of 3° and a sun diameter of $.54^{\circ}$ the broadening would be 5 percent.

The absolute temperature of a uniform radio source is related to the antenna temperature by⁽²⁾:

$$T_a = T_s \left(\frac{\Omega_s}{\Omega_A} \right)$$

for $\Omega_s \ll \Omega_A$

where

T_A = antenna input temperature

T_s = source temperature

Ω_A = antenna beam area, rad^2

Ω_s = source solid angle, rad^2

The antenna solid angle Ω_A is related to the half-power beamwidth by⁽²⁾:

$$\Omega_A = \frac{\theta \phi}{\epsilon_M}$$

where

θ = half-power beamwidth in θ plane, rad.

ϕ = half-power beamwidth in ϕ plane, rad.

ϵ_M = main beam efficiency

From the above equations we have for a circular source:

$$T_A = T_s \frac{\theta_s^2}{(\phi \theta) \epsilon_M}, \text{ for } \theta_s^2 \ll \phi \theta$$

where

θ_s = angular width of source

Since the dimensions of the angles cancel they may be expressed in degrees or radians.

Correcting for the atmospheric attenuation we have:

$$T_A = \frac{T_s \theta_s^2}{L (\phi \theta) \epsilon_M} + T_{O_2, H_2O} + T_{sky}$$

where

L = attenuation due to water vapor and oxygen

T_{sky} = total sky temperature received outside source solid angle

$T_{\text{O}_2, \text{H}_2\text{O}}$ = temperature received due to oxygen and water vapor inside source solid angle

Figures 9-1, 9-2, and 9-3 are sun-drift curves taken with the Nimbus antenna for Run Nos. 9, 10, and 35.

The calculated sun disk temperature and one-half power beam widths of the antenna are summarized in Table 9-1.

The measured beamwidth was neither of the principal phase beamwidths because the sun drifted through a plane slightly skewed from either of these planes.

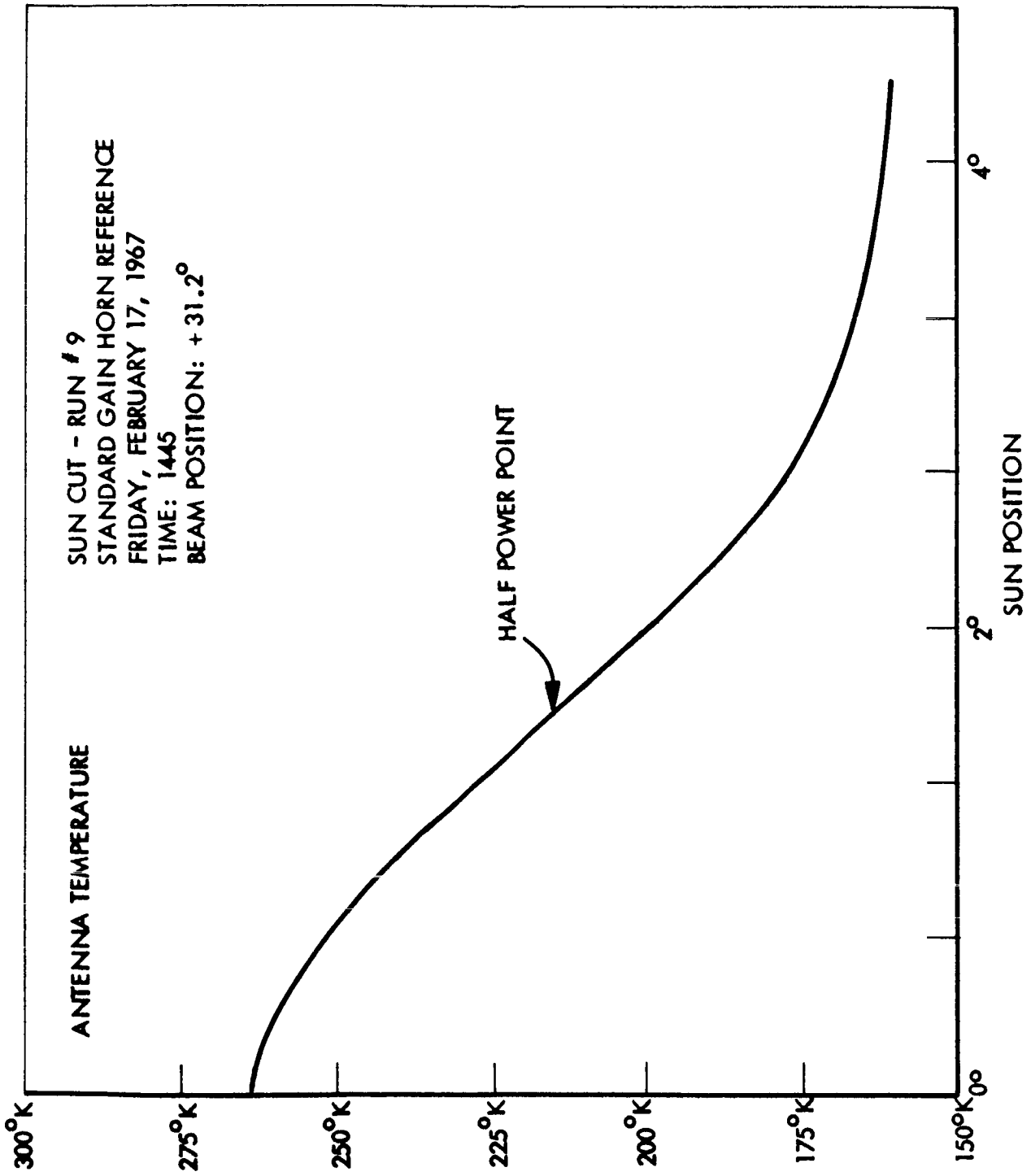


Figure 9-1. Sun-Drift Curve Run No. 9

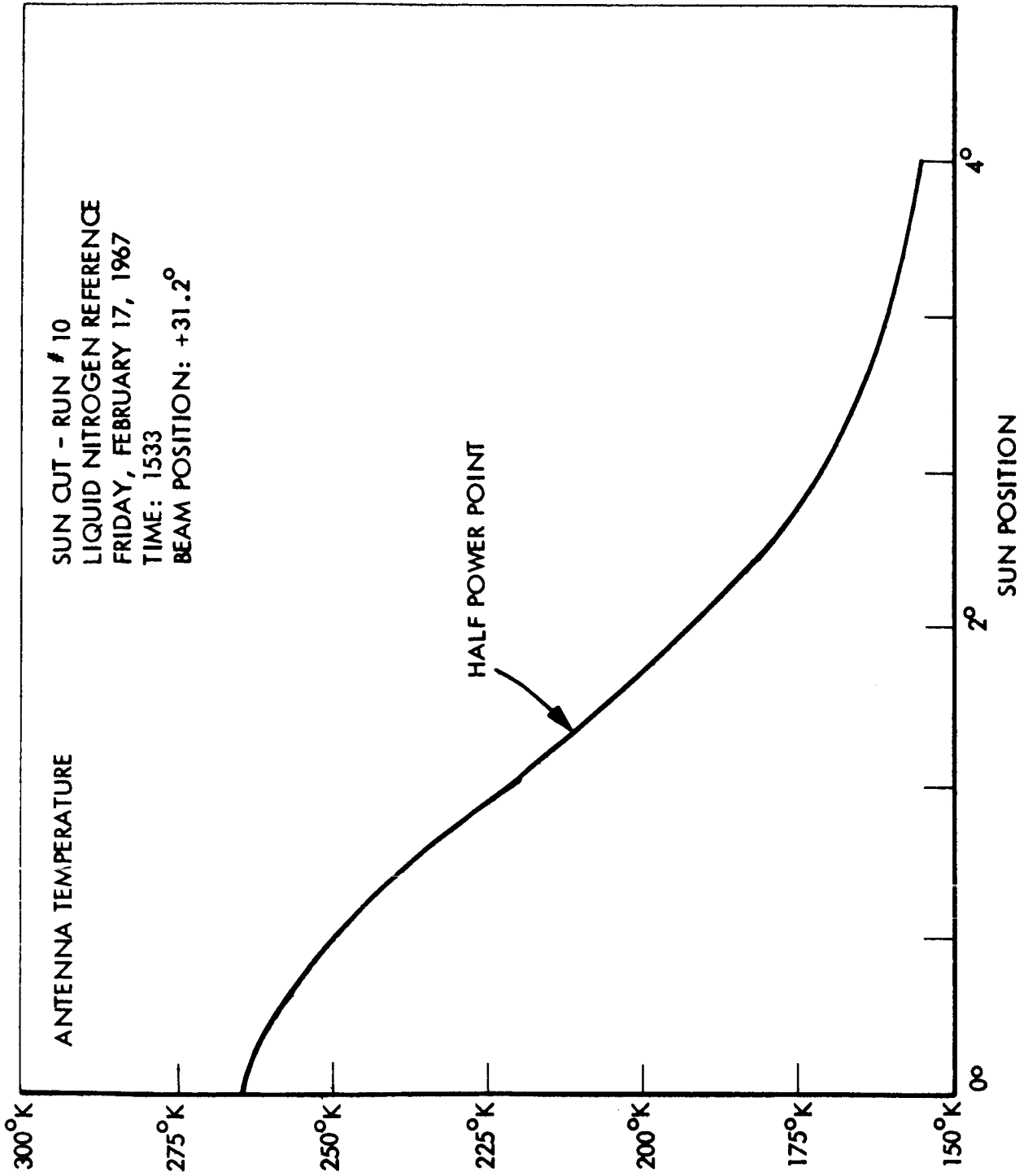


Figure 9-2. Sun-Drift Curve Run No. 10

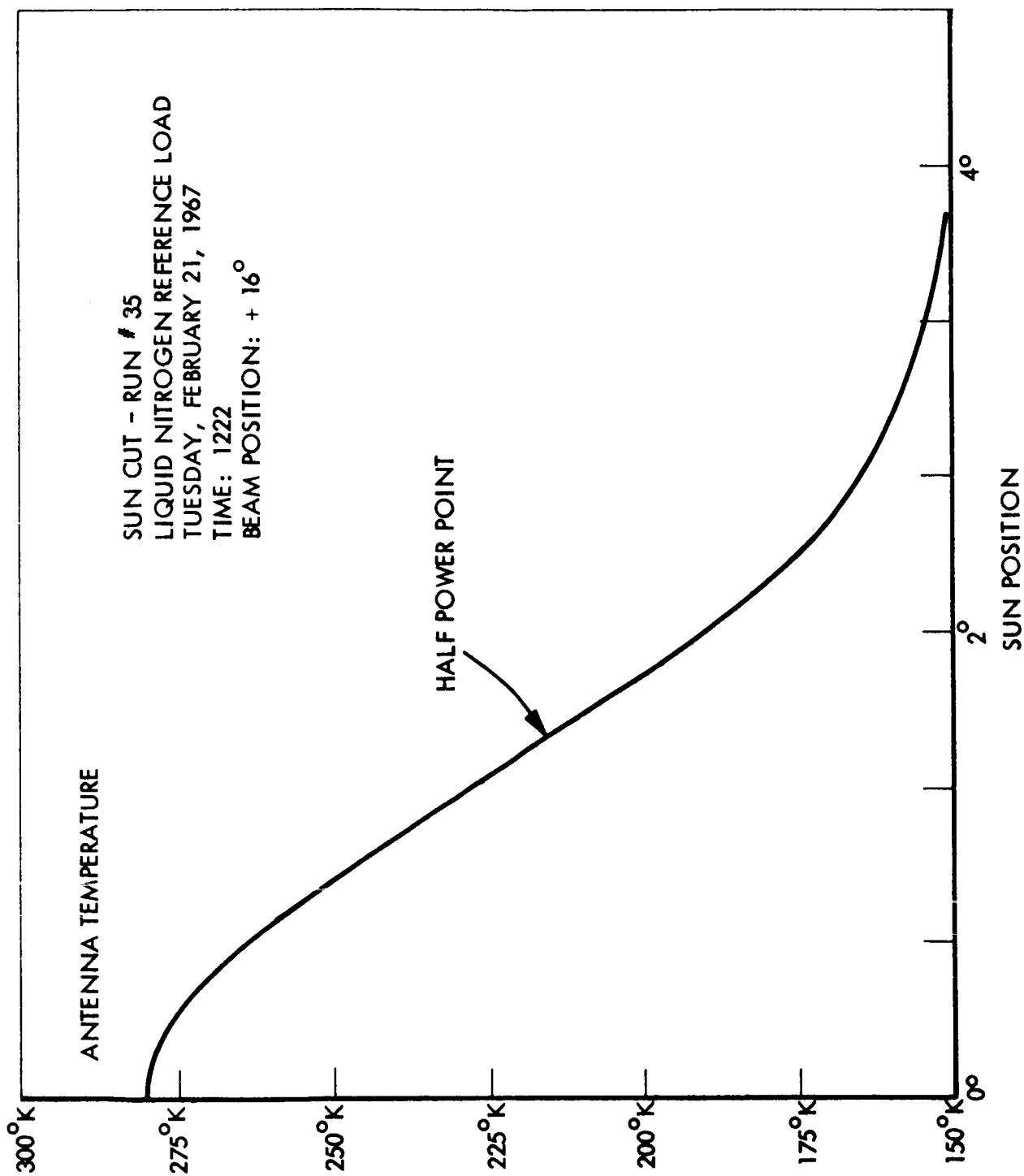


Figure 9-3. Sun-Drift Curve Run No. 35

Table 9-1

SUN MEASUREMENTS

Date	Time	Elevation Angle, Sun	Electrical Beam Position	Beamwidth From Sun Curve	Principal Plane Beamwidths From Antenna Range	Measured Sun Temperature
					θ ϕ	
2-21-67	1222	44°	+16°	2.91°	2.44° 2.98°	7080°K
2-17-67	1445	34°	+31.2°	3.02°	2.71° 2.98°	7160°K
2-17-67	1533	23°	+31.2°	3.04°	2.71° 2.98°	7200°K

9.2 REFERENCES

1. Kraus, J. D., Radio Astronomy, 1966, McGraw Hill, p. 171
2. Ibid, p. 72 and p. 158

Appendix XXV

FREQUENCY STABILITY OF SOLID STATE SOURCE

The prototype solid state source was designed and tested in a relatively short period of time. One of the pitfalls in doing this is the possibility that power or frequency instabilities can and do appear. This was the case with this source when demonstrated at Table Mountain. The source was very erratic at high temperatures, and until now the problem was not isolated.

It was shown that the flight model source (Figure 1) varied in frequency 110 MHz in a 60°C temperature change. A thermistor network was inserted into this unit. The resultant was a 25 MHz variation of frequency. This completely stabilized the source and the prototype unit was immediately tested. Its variation was far worse than the flight model (170 MHz). A correction network is being designed for this unit, and it is felt that this will completely cure any instabilities of the source.

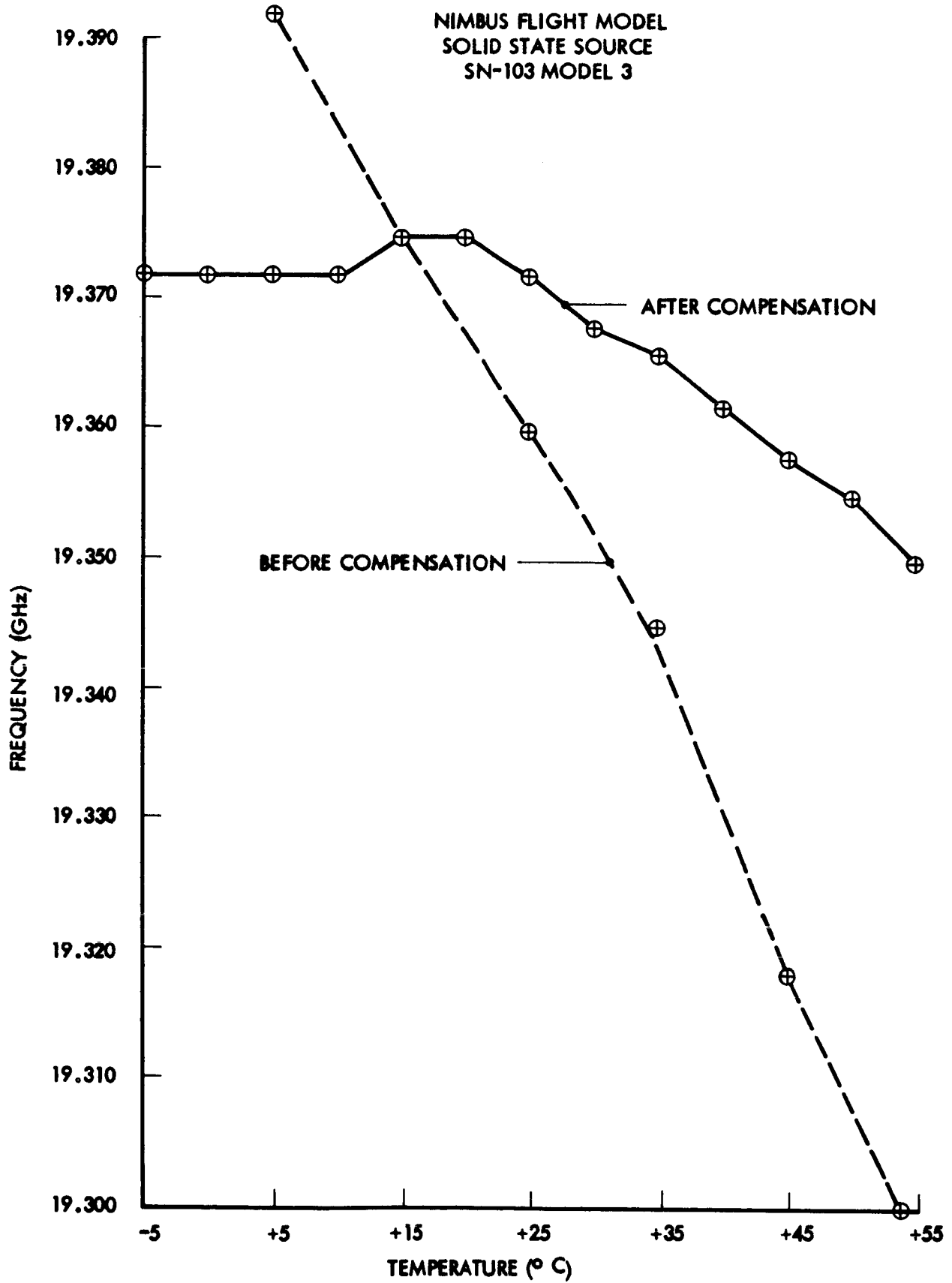


Figure 1. Frequency Variation with Temperature Change

Appendix XXVI

TEST RESULTS OF SOLID STATE SOURCE

A 19.35 GHz solid state source has been developed for use as a local oscillator in the receiver of the Nimbus meteorological measurement system. The prototype unit, because of scheduling, lacked sufficient time to fully test its performance. The flight model solid state source, however, has been extensively tested and graphs are presented. The final tests of the solid state source involve the integration of the mixer-IF strip and measuring noise figure, relative power output and frequency versus operating temperature.

The block diagram of this measurement is shown in Figure 1. The procedure is to set the oven temperature at discrete intervals, recording the following: (1) Frequency, by tuning the wave meter and observing a dip in the crystal currents; (2) Power output (relative), by recording the crystal currents; (3) Noise figure, by recording the precision attenuator setting required to produce twice the noise voltage on the VTVM when the noise tube is turned from the "off" to "on" state. This attenuator reading is then subtracted from the noise tube's excess noise power (15.6 dB).

The results of the measurements are shown in Figures 2 through 4.

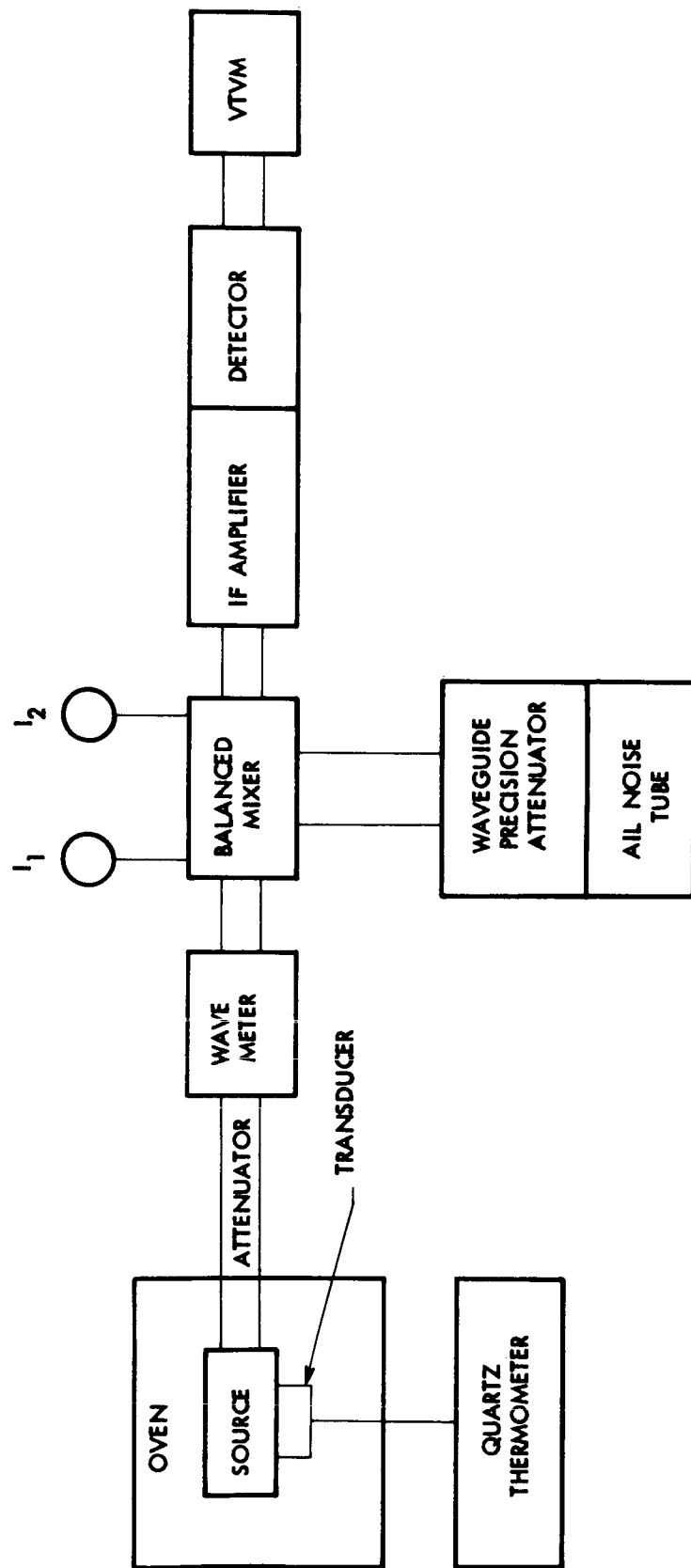


Figure 1. Block Diagram of Noise Figure Test

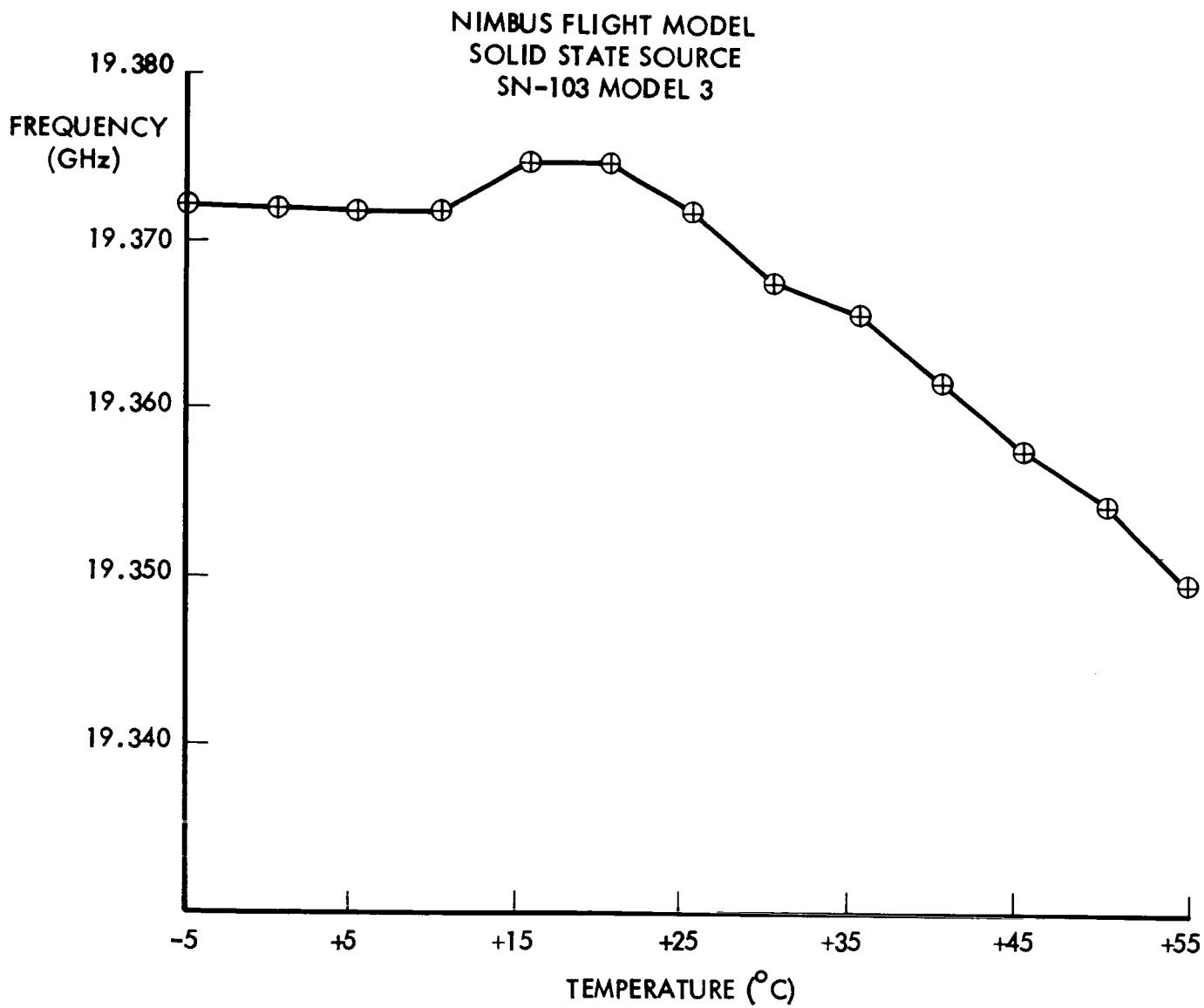


Figure 2. Frequency versus Temperature

NIMBUS FLIGHT MODEL
SOLID STATE SOURCE
SN-103 MODEL 3

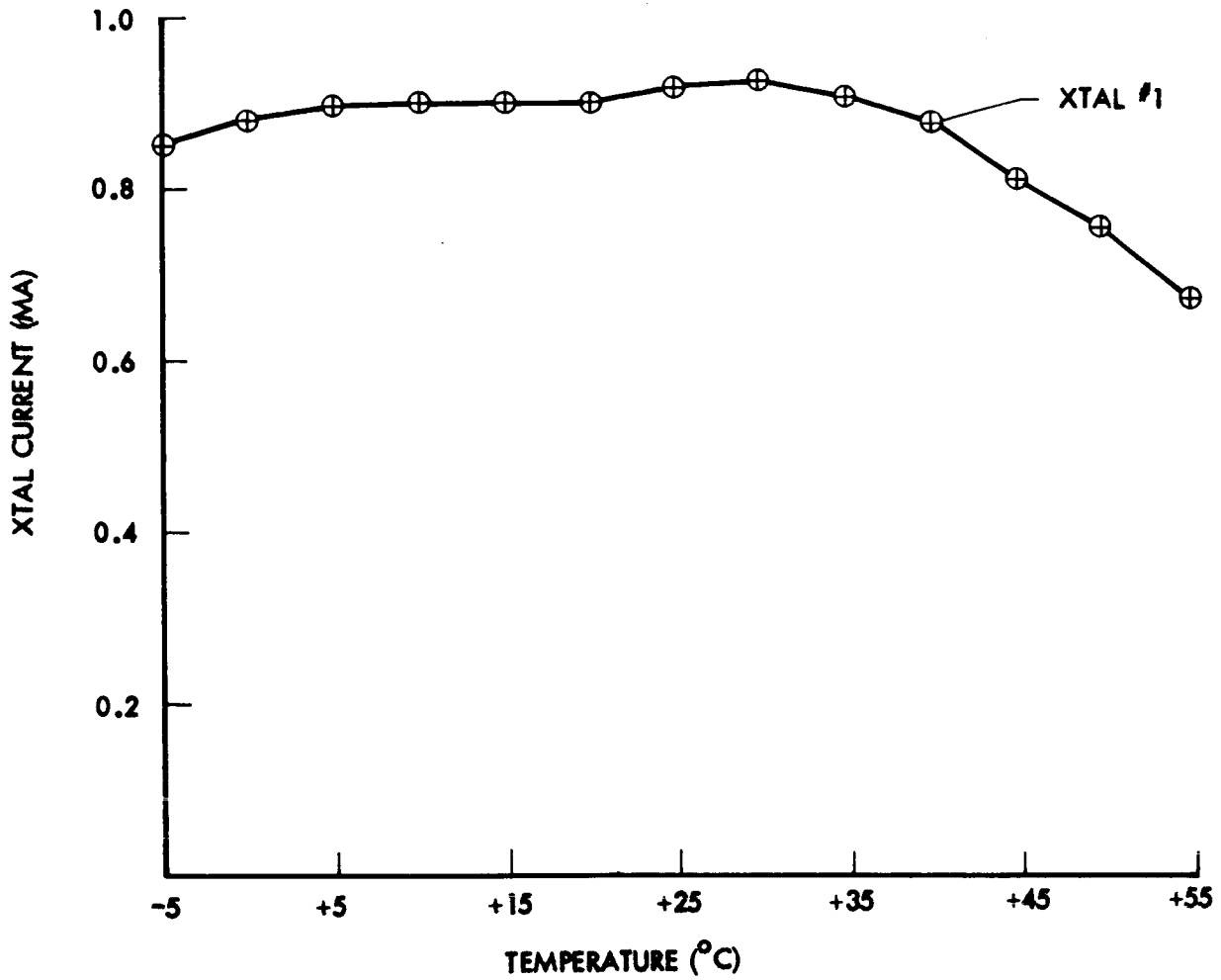


Figure 3. Relative Power Output versus Temperature

NIMBUS FLIGHT MODEL
SOLID STATE SOURCE
SN-103 MODEL 3

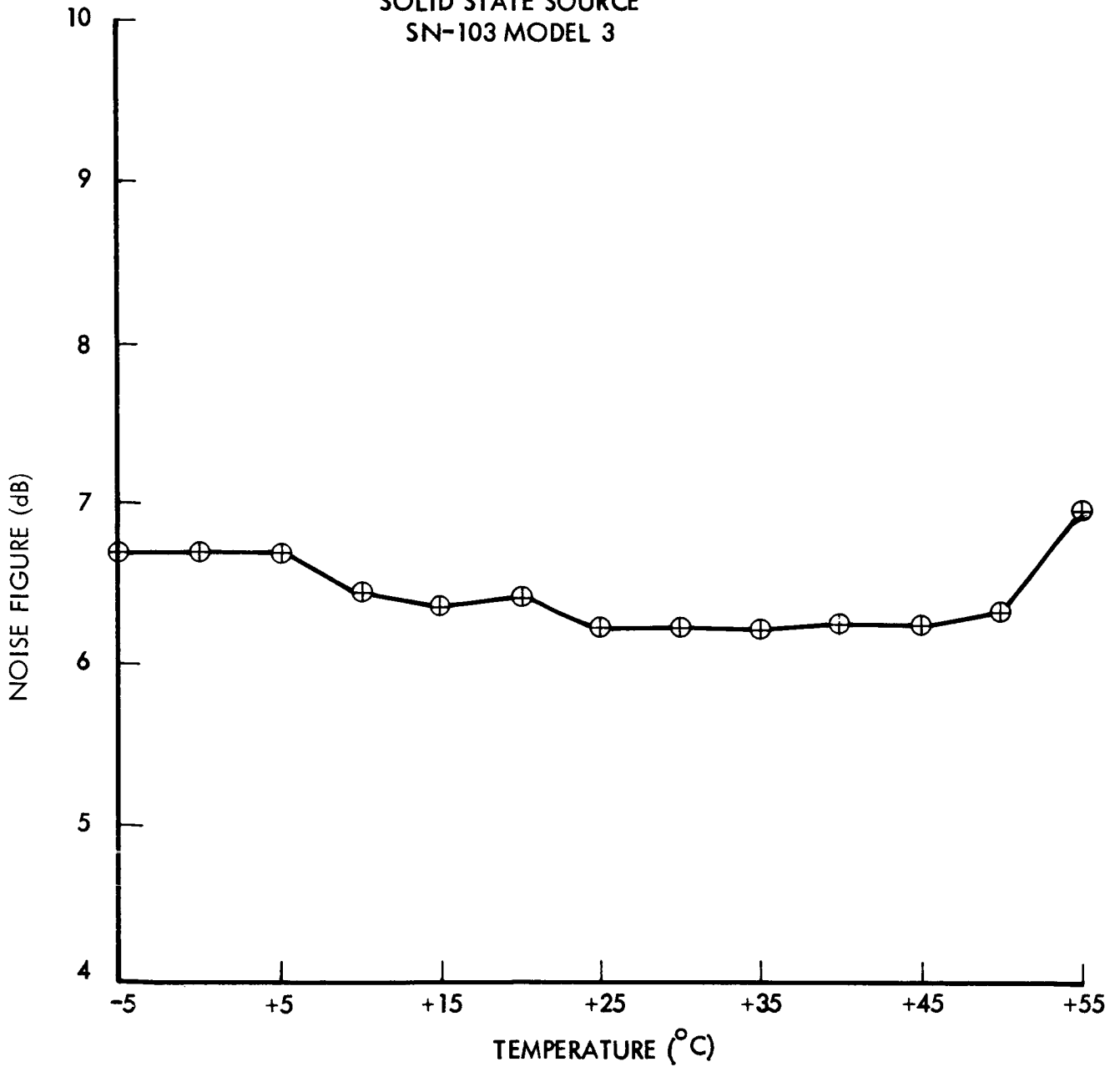


Figure 4. Receiver Noise Figure versus Temperature

Appendix XXVII

NIMBUS PHASE SHIFTER DESIGN

INTRODUCTION

The phase shifter used for the Nimbus Program is of the Reggia Spencer¹ Type. It consists of a rectangular waveguide with a cylindrical ferrite rod held in place in its geometric center by teflon support structures. A coil is wound around the outside of the waveguide to provide a longitudinal magnetic field. Changing the magnetic field (H) changes the phase velocity (V_p) which in turn changes the amount of phase shift (ϕ). In the design of the phase shifter, there were several areas to be considered, i. e., 1) selection of ferrite material; 2) geometry of ferrite rod; 3) applied magnetic field; 4) temperature; and 5) ferrite support structure. Each of these areas will be discussed in detail in this memorandum.

FERRITE CHARACTERISTICS

Since the shift in phase is a function of the magnetization of the ferrite, a prime objective is to select the ferrite material that has the highest magnetization and lowest absorption loss, i. e., highest figure of merit. A comparison of the electrical characteristics of three ferrite materials which were considered is shown in Table 1.

Table 1

COMPARISON OF FERRITE CHARACTERISTICS

Material	Composition	Saturation Magnetization	Relative Dielectric Constant	Loss Tangent
TT1-390	Mg, Mn	2150	13.0	.0005
TT2-101	Ni, Co	3000	13.0	.0025
TT2-111	Ni, Zn	5000	12.5	.0015

¹Reggia, F. and E. G. Spencer, "A New Technique in Ferrite Phase Shifting for Beam Scanning of Microwave Antennas," Proc. IRE, Vol. 45, pp. 1510-1517; November 1957.

The above materials are manufactured by Trans-Tech, Inc., Gaithersburg, Md. As can be seen, the nickel ferrites, i. e., TT2-101 and TT2-111, have a substantially higher saturation magnetization ($4\pi M_s$) than does the magnesium-manganese ferrite. The losses, however, are also higher.

The TT2-111 ferrite material was chosen because of its high figure of merit per unit length. A figure of merit comparison between the two nickel ferrites is illustrated in the next section.

ROD GEOMETRY

The geometry of the ferrite rod should now be considered since it will affect both the amount of phase shift and mismatch or reflective losses. In order to attain the highest phase shift it is necessary to use the largest diameter ferrite rod possible; however, there is a critical diameter at which higher order modes begin to propagate. Propagation of higher order modes causes periodic losses and high VSWR peaks, or resonances, as the phase is varied by means of changing the coil current. The critical diameter relationship is shown below:

$$d (\text{max}) = \frac{\lambda}{1.309 \sqrt{K_e}} \quad (1)$$

where

λ = free space wavelength

K_e = dielectric constant of ferrite

Rods having diameters of 0.125 inch and 0.130 inch were made from each of the nickel ferrite materials. Each ferrite rod was approximately 2.0 inches long and stepped at each end for impedance matching purposes. The geometry of the step will be discussed in a later section.

Phase measurements as a function of applied magnetic field were performed on both of the ferrite materials. For these measurements, the ferrite rods were supported throughout their length by a teflon support structure. However, support structures of a different geometry were tested and will also be discussed in a later section. Data obtained from the above measurements were plotted in the form of phase shift versus magnetic field intensity curves as seen in Figures 1 and 2. In Figure 1, a rod made from TT2-111, having a diameter of 0.130 inch was

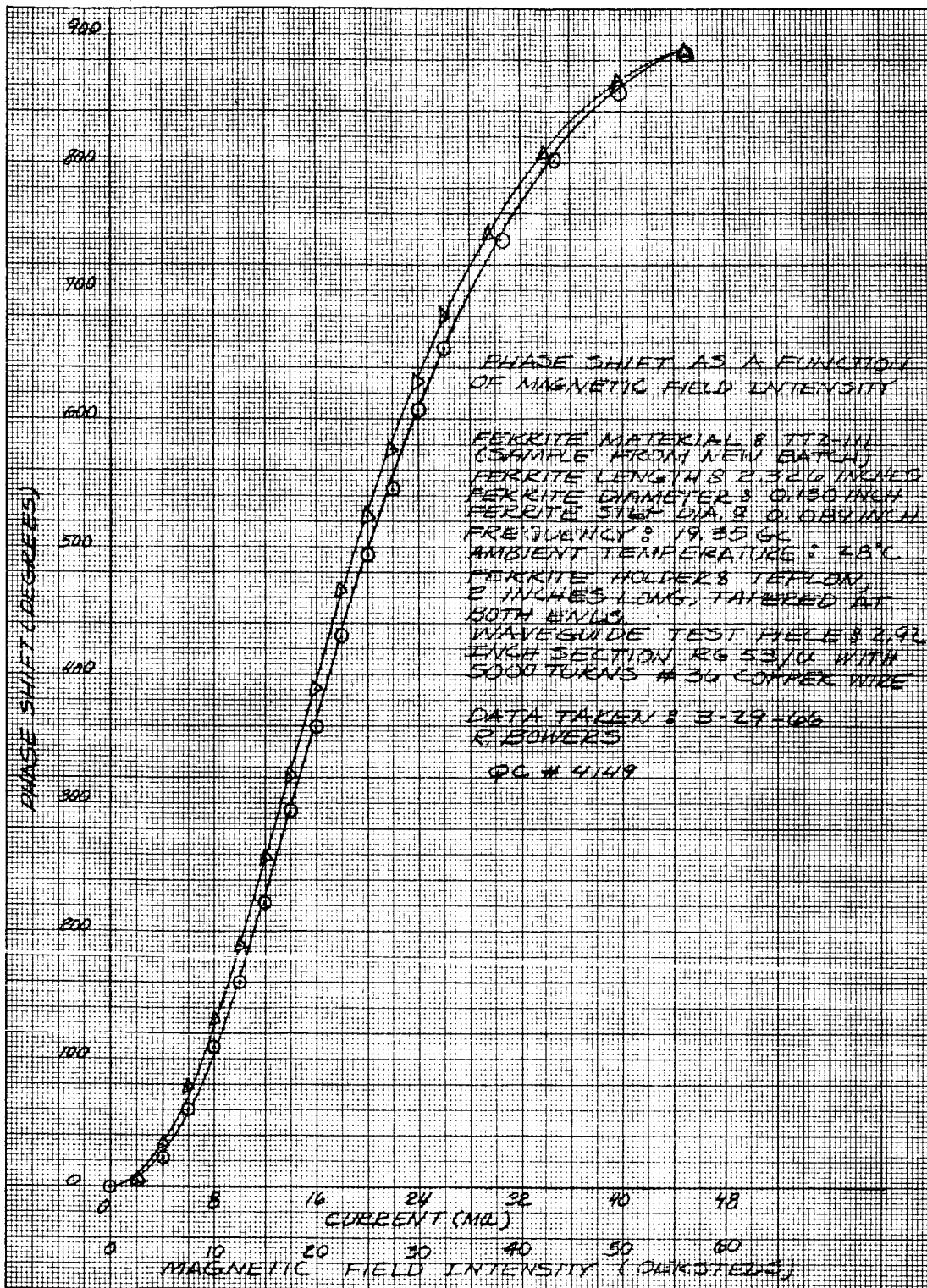


Figure 1

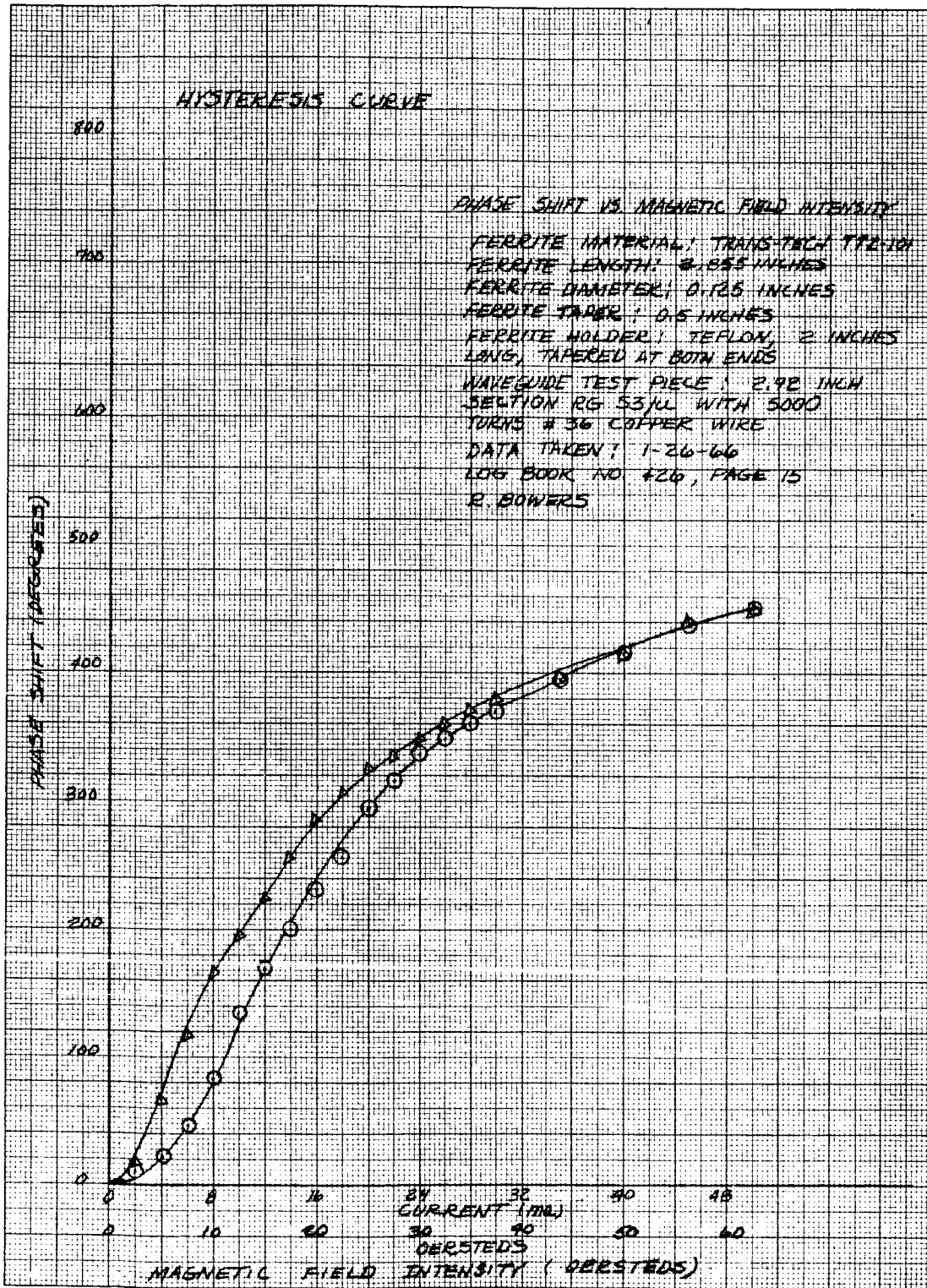


Figure 2

used and in Figure 2 the rod was made from TT2-101 and had a diameter of 0.125 inch. The critical diameter relationship dictated the smaller diameter for the TT2-101 ferrite. As can be seen from the two curves, TT2-111 ferrite gives substantially more phase shift than does the TT2-101 ferrite, for the same applied field. The ferrite rod diameter to be used for the phase shifters was selected to be 0.130 inch.

IMPEDANCE MATCHING

For impedance matching purposes, the ferrite rod was stepped at both ends. In using a step taper for matching, the step length should be on the order of $\lambda_g/4$. The diameter of the step can be found from the following relationship between the rod and step cross-sectional areas:

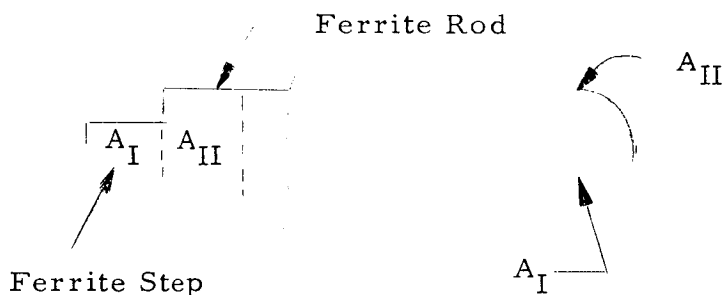
$$A_{II} = 2A_I$$

$$\pi r_{II}^2 = 2\pi r_I^2$$

$$r_I^2 = \frac{r_{II}^2}{2}$$

or

$$r_I = \frac{r_{II}}{\sqrt{2}}$$



The values calculated for the step length and diameter by the above methods give only approximate values. To achieve optimum impedance matching the ferrite rod was placed in a waveguide test fixture that contained tuning screws in front of and along the ferrite step. The screws introduce capacitive or inductive susceptance. By measuring the input VSWR as a function of the screw location and depth it was possible to determine whether a change in the step length or diameter was required. The above method for matching resulted in a final step diameter and length of 0.096 inch and 0.143 inch, respectively.

The ferrite rod support structure also plays a major role in the electrical characteristics of the phase shifter. Due to the diameter of the ferrite rod,

magnetic resonance points (high VSWR peaks) may appear at or near the frequencies of interest. By varying the geometry of the support structure, these resonance points can be moved away from the operating frequency ranges. The first support structure that was investigated supported the ferrite rod throughout its entire length and was tapered at both ends; however, resonant points appeared in the operating frequency range and did not move sufficiently when the geometry of the structure was changed. The second structure investigated was made in two parts, one located at each end of the ferrite rod. The ends of the structures were tapered for matching purposes. The geometry, i. e., the length and width of the structures was varied until all resonance points were removed from the operating frequency range. The final dimensions are indicated in Figure 1.

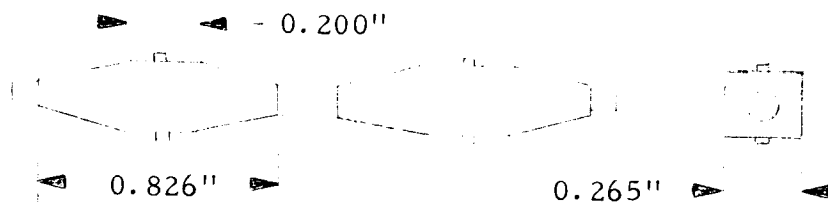


Figure 4

The support structures are made out of teflon due to its low loss tangent. Each structure has a nipple on its top and bottom sides which fit into holes in the waveguide walls. This arrangement thus prevents the structure from moving in either the longitudinal or transverse directions. An interference fit holds the ferrite rod in place in the support structure.

TEMPERATURE EFFECTS

Having established the type ferrite material and rod diameter, measurements of phase variation as a function of applied field for various temperatures were performed to determine the effects of temperature variations on the performance of the phase shifter. A total of six different temperature values was used, these being -25°C , 0°C , 28°C (ambient temperature), 50°C , 75°C , and 100°C .

The data obtained during the above measurements have been plotted in three different manners as seen in Figures 5, 6, and 7. In Figure 5, the phase

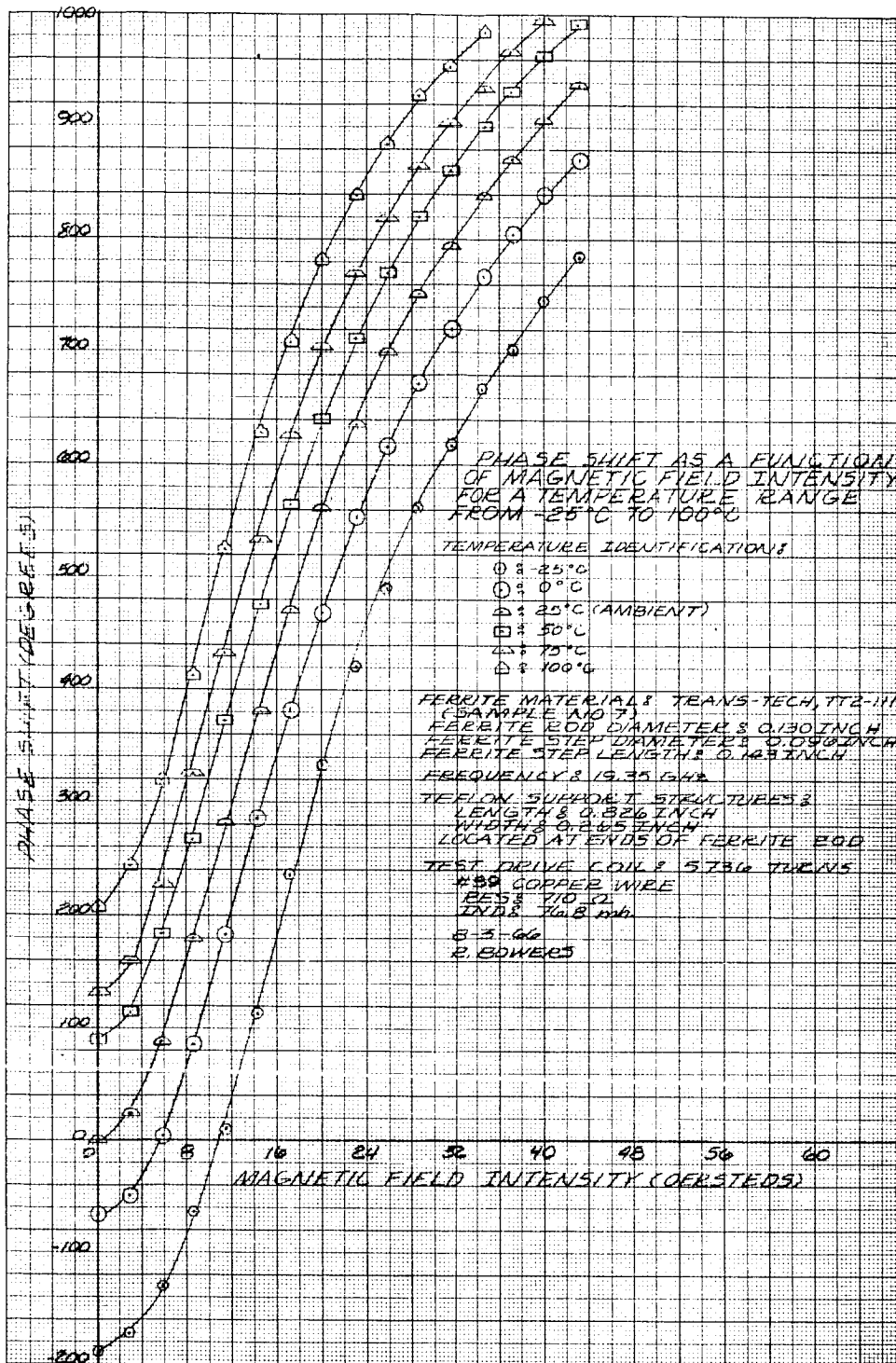


Figure 5

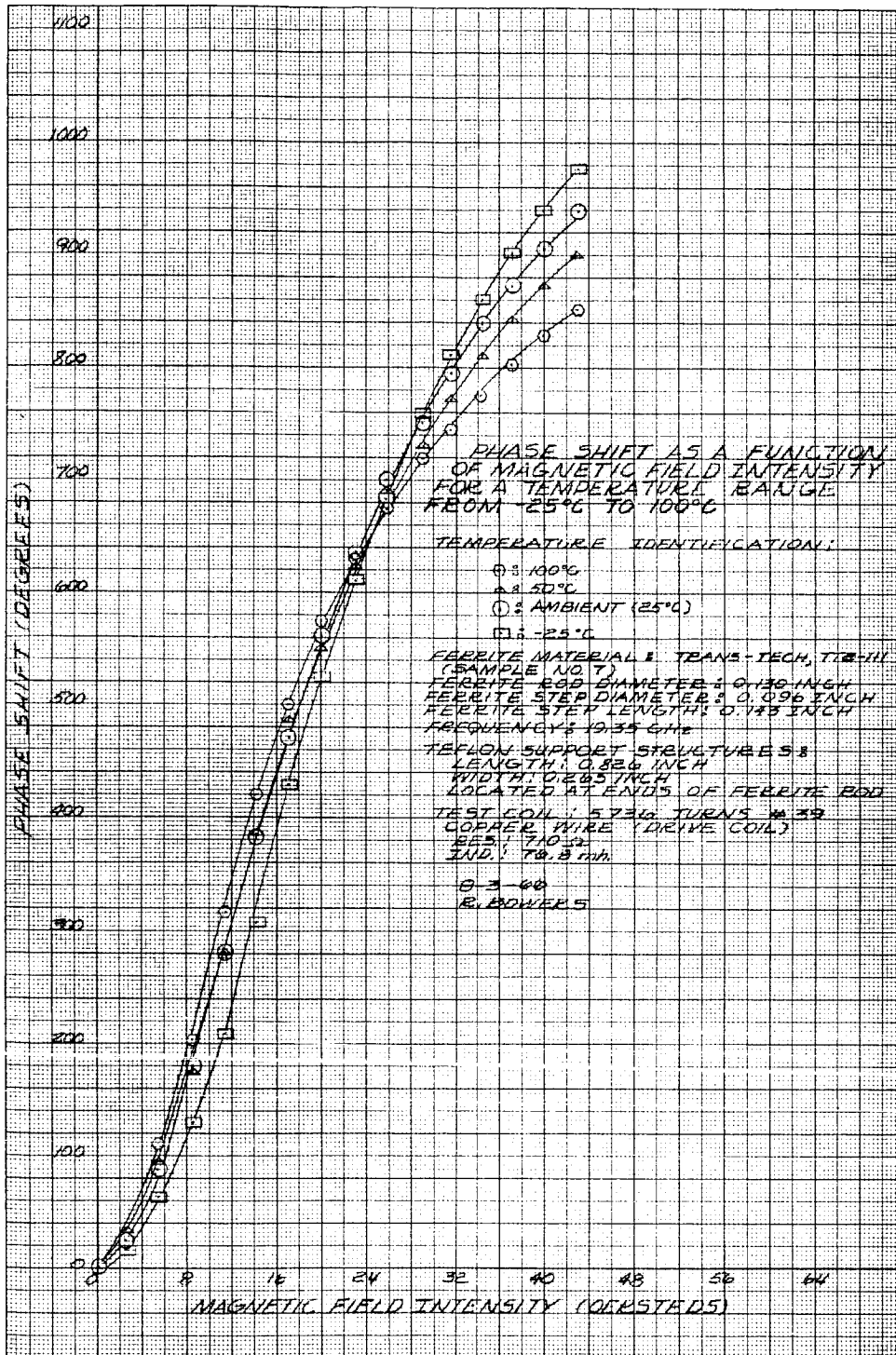


Figure 6

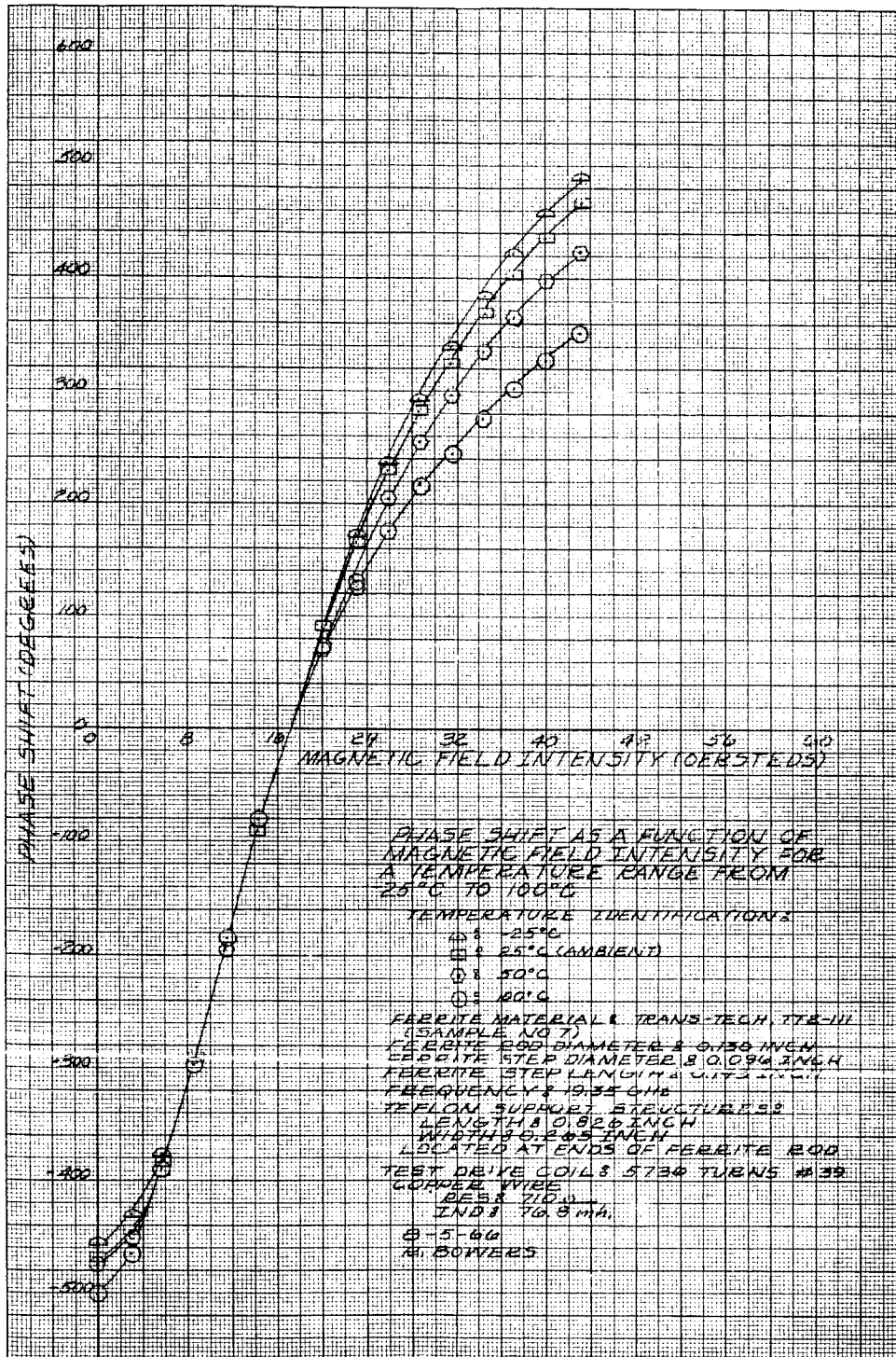


Figure 7

reference was taken for the condition of zero applied field and ambient temperature (28°C). All phases were then referenced to this set of conditions. The result is a plot of absolute phase variations as a function of applied magnetic field and temperature. The plot, however, does not illustrate an accurate picture of the effects of temperature. This same raw data was therefore replotted using the phase for the zero field condition as the reference for all values of temperature. This plot is shown in Figure 6. It is apparent in this figure that the slopes of various curves are quite different over an appreciable portion of the curves, particularly in the low and high field regions. However, in the central portion, the slopes are almost identical. In Figure 7, the reference phase point for all temperatures was taken at an applied field of 17.5 oersteds and the data was again plotted. The identicalness of the slopes is quite apparent in this figure.

COIL DESIGN

In order that the Nimbus planar array be least affected by temperature variations, it is most essential that the slope of the curve of phase shift versus applied magnetic field be constant over a specific range of fields for all temperatures. With this in mind, it is necessary to generate a bias field in order that the drive field will operate in the linear portion of the phase shift vs. magnetic field curve. The use of a single coil, or two separate coils, or possibly a coil and a permanent magnet were considered.

Due to the drive control network and volumetric limitations, the two separate coils (bias and drive) were pursued. The principal limitations on the drive control network dictated the following limitations on the phase shift coils.

- (1) The average current in all coils cannot exceed 5 ma.
- (2) In order to achieve the accuracy that is required in the setting of the various drive currents, the maximum voltage across the drive coil should be on the order of 5 volts.

A trade-off on the coil design, i. e., number of turns, wire size, resistance, etc. had to be considered due to the limitations mentioned above. After considering the trade-offs, the final coil parameters were established as follows:

	<u>Drive Coil</u>	<u>Bias Coil</u>
Wire size	No. 39	No. 35
No. of Layers	12	5
No. of Turns	5736	1480
Resistance (ohms)	711	66
Inductance (mh)	76.8	3.7
L/R (microseconds)	107.9	56.1

These coils give rise to the following drive/bias circuit parameters:

Average Current in Drive Coil	3.90 ma
Total Array Avg. Drive Current	191 ma
Max. Voltage Across Drive Coil	7.11 volts
Bias Coil Current	20 ma
Voltage Drop Across Bias Coil	1.32 volts
Bias Coil Configuration	1 row of 17 coils in series
	2 rows of 16 coils in series
Total Bias Power	1.47 watts
Total Drive Power	4.68 watts
Total Array Power	6.15 watts

PHASE SHIFTER PERFORMANCE

A total of 55 drive/bias coils were procured from Turbo-jet located in Rosemead, California. The ferrite rods were ground by Expert Grinding, Inc., Burbank, California. The ferrite rod support structures were made by W.S. Shamban & Co., Newbury Park, California.

After the complete phase shifter had been assembled, phase shift, re-
turn loss and insertion loss measurements were performed. The data from the
above measurements were tabulated and plotted in three different histograms as
indicated in Figures 8, 9, and 10. At 20 ma bias current, 0 ma drive current and
at a temperature of 35°C the phase shifters exhibited a wide spread of phase shift.
These results are tabulated and shown as a histogram in Figure 8. Possible rea-
sons for this wide-spread in phase shift are mechanical tolerances of the ferrite

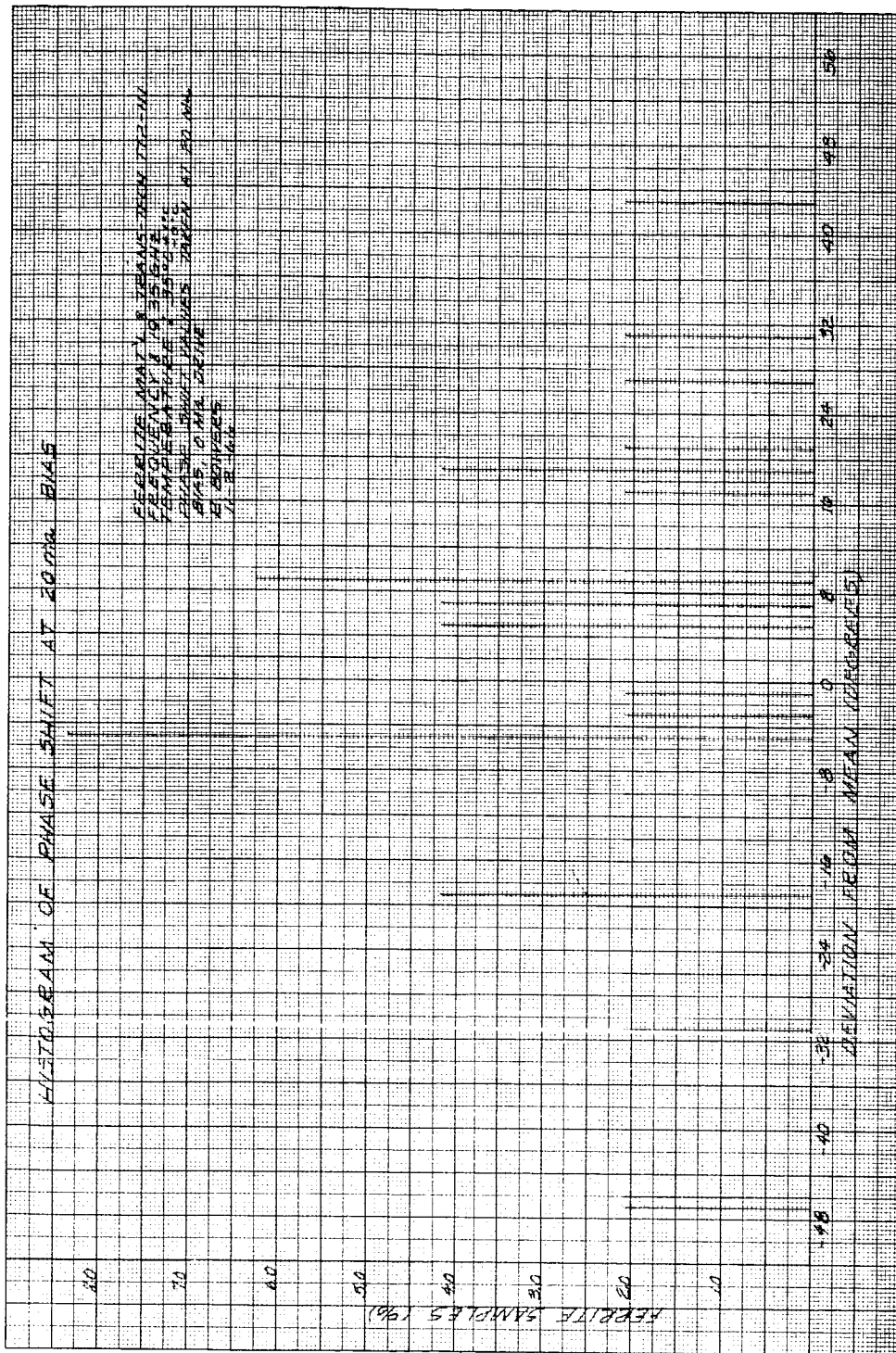


Figure 8

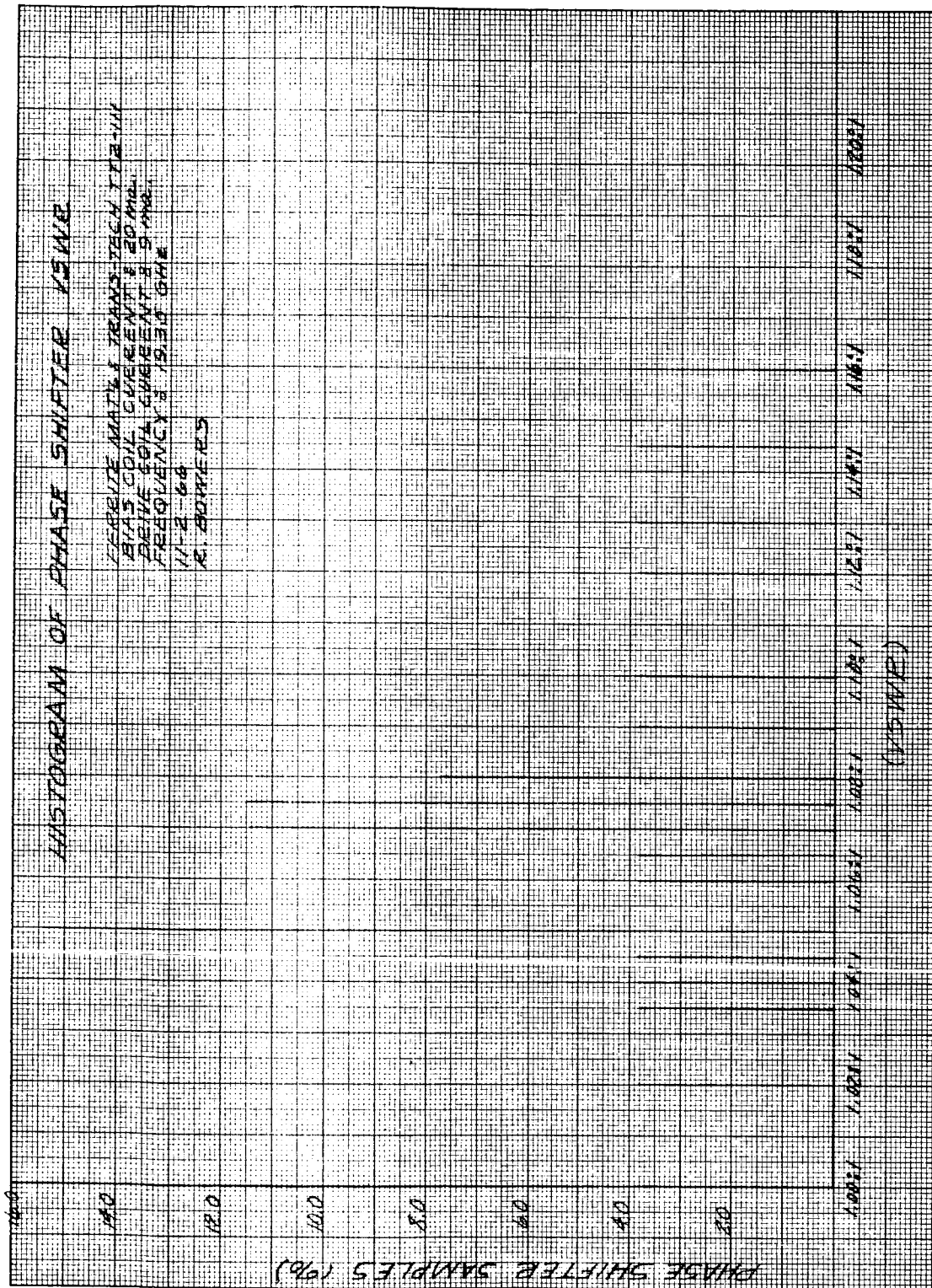


Figure 9

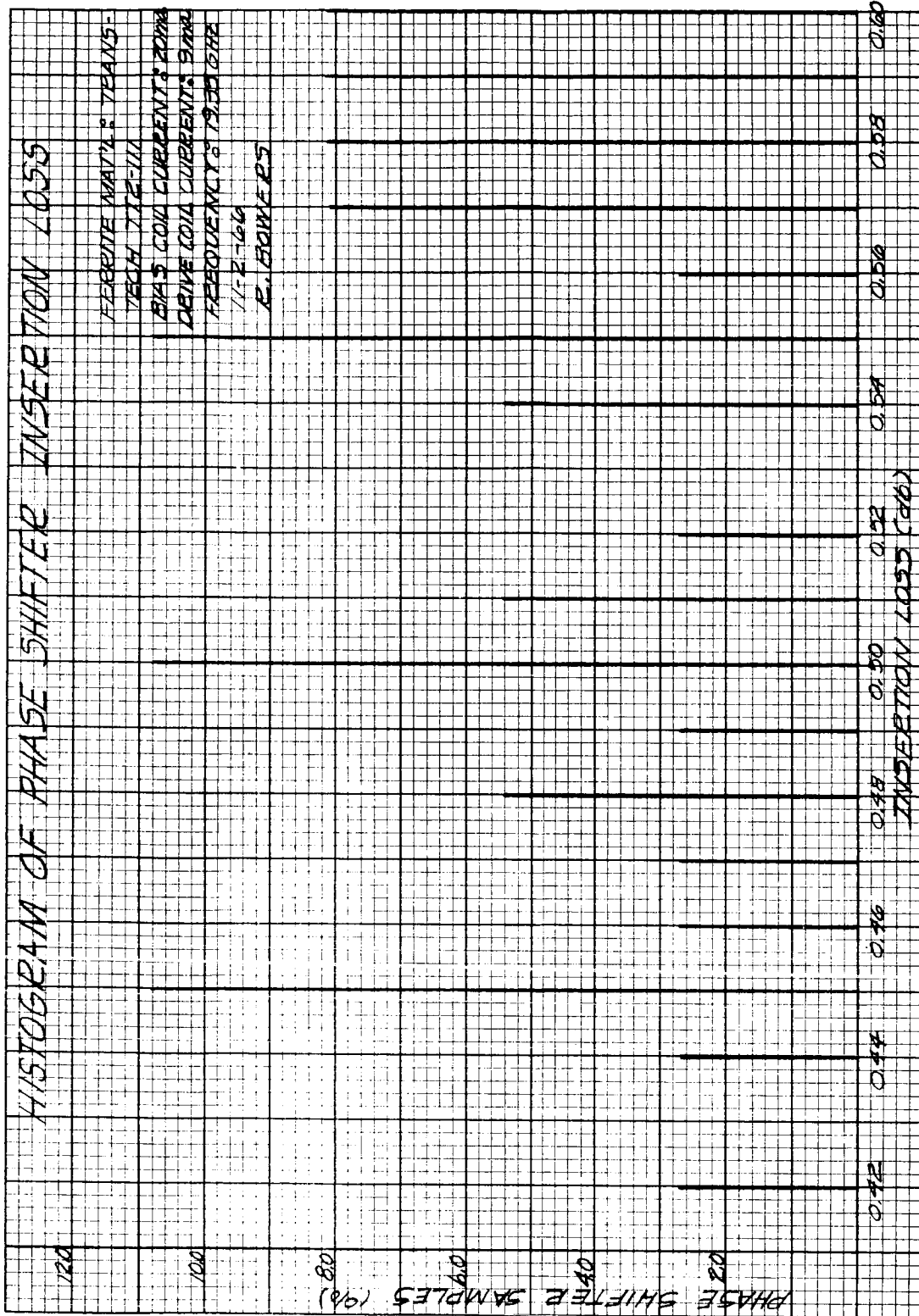


Figure 10

rod, chemical inconsistencies in the ferrite and variations in the number of turns of each coil. These variations in phase shift cause phase perturbations, which in turn increase side lobe levels of the antenna radiation pattern. There are two methods by which these variations in phase shift can be corrected:

- 1) Adjust bias coil current of each phase shifter independently.
- 2) Adjust drive coil current of each phase shifter with constant bias coil current.

The latter approach was pursued since the former method would increase the total bias power requirement.

The data gathered for the histograms of VSWR and insertion loss were taken at a frequency of 19.35 GHz with bias and drive current of 20 ma and 9 ma, respectively. The histograms are representative of data obtained at frequencies of 19.25 GHz and 19.45 GHz at drive current of 0 ma, 3 ma, and 6 ma in that the VSWR and insertion loss remained within the limits of 1.10 ± 0.10 and $0.5 \pm .1$ dB respectively.

At the present time, measurements are being performed to determine the effects on the phase shifter performance of mutual D.C. magnetic fields. The results will be presented in a future memo.

Appendix XXVIII

A SOLID STATE LOCAL OSCILLATOR SOURCE AT 19.35 GHz

ABSTRACT

An efficient solid state source of coherent energy has been developed to be used as a local oscillator for a superheterodyne receiver at 19.35 GHz. Developed under a NASA contract, it has many unique features to be specifically used for space instrumentation.

A high fundamental oscillating frequency was selected to allow a maximum rejection of that frequency in the IF amplifier passband. The oscillator also has been temperature stabilized such that its frequency remained within 20 ppm/ $^{\circ}$ C in the temperature range of -5 to +55 $^{\circ}$ C. A lightweight construction and a compact mechanical design easily lends itself to space environment, allowing system integration in a limited area.

INTRODUCTION

In the past, radiometers were restricted to ground based installation where the incentive to eliminate the klystron tube with its associated cabling, water cooling and bulky power supplies was lacking. Presently, the source is used in an extremely sensitive radiometer system designed for flight environment. Present advances in system technology have evolved many applications of radiometers for air-borne uses. Paralleling these applications was a conscientious effort at Space-General to develop new and improve existing microwave circuits so that they might satisfactorily perform in a flight environment.

The circuit design and performance of a solid state source is presented here. Its reliability and acceptability as a local oscillator power source for space-borne radiometric applications has been verified.

DESIGN

Overall Design and Performance

The solid state source is comprised of a transistor oscillator followed by two frequency multiplier stages. The source block diagram is shown in Figure 1 and its photograph is shown in Figure 2.

The basic oscillator, having a frequency of 1.209 GHz and an output power of 200 mw, drives two cascaded frequency quadrupler circuits. The first quadrupler operates at an efficiency of 40 percent, delivering approximately 80 mw at 4.87 GHz to the second quadrupler. The second quadrupler operates at an efficiency of 10 percent, delivering 8 mw of available power at 19.35 GHz to an attenuator preceding a low drive level balanced mixer.

The source has been temperature compensated so that its output frequency remains within 20 ppm/ $^{\circ}$ C over a 60 degree temperature range. A graph of output frequency versus temperature is shown in Figure 3.

System noise figure measurements were conducted to determine the extent of spurious local oscillator energy concentrated within the passband. It was found that by using the solid state source, its noise figure decreased in relation to a value obtained when a klystron tube was used. An improvement of approximately 0.2 dB was gained in overall system noise figure when a 200 MHz wide band IF amplifier was used.

The dc power required to drive the source is 22 volts at 100 ma, resulting in a K_a band power output of 5 to 10 mw.

Transistor Oscillator Design

The transistor oscillator circuit is shown in Figure 4. It is essentially a Colpitts oscillator. A length of coaxial transmission line is shorted at one end (L_3), which together with a series capacitance C_1 and the collector-to-base capacitance forms the major part of the resonant circuit. Feedback is provided by adjusting capacitor C_2 relative to the emitter-to-base capacitance (C_{eb}). L_4 , C_3 , and C_4 form the output coupling network. Resistor R_5 is inserted to allow a bias voltage to develop in varactor of the first multiplier stage.

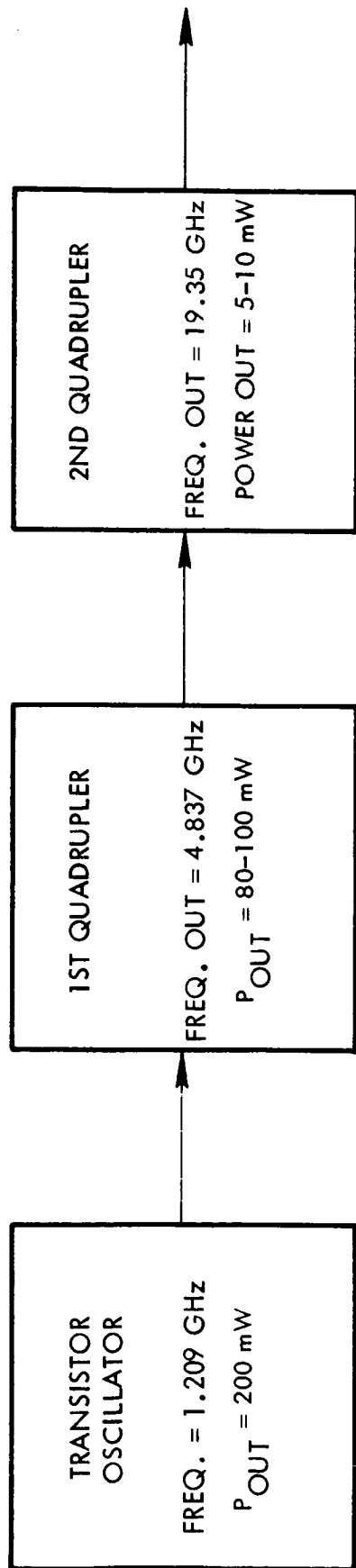


Figure 1. Source Block Diagram

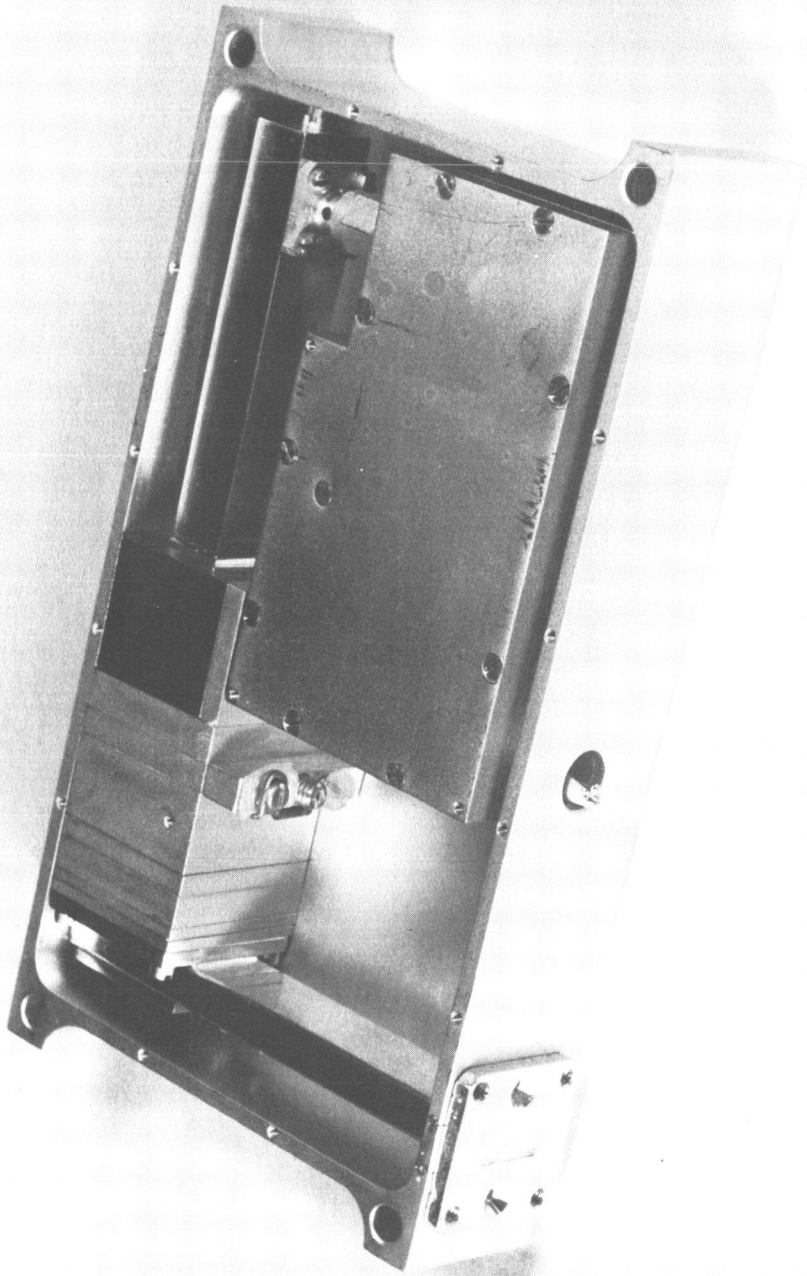


Figure 2. Photograph of Solid State Source

939/037

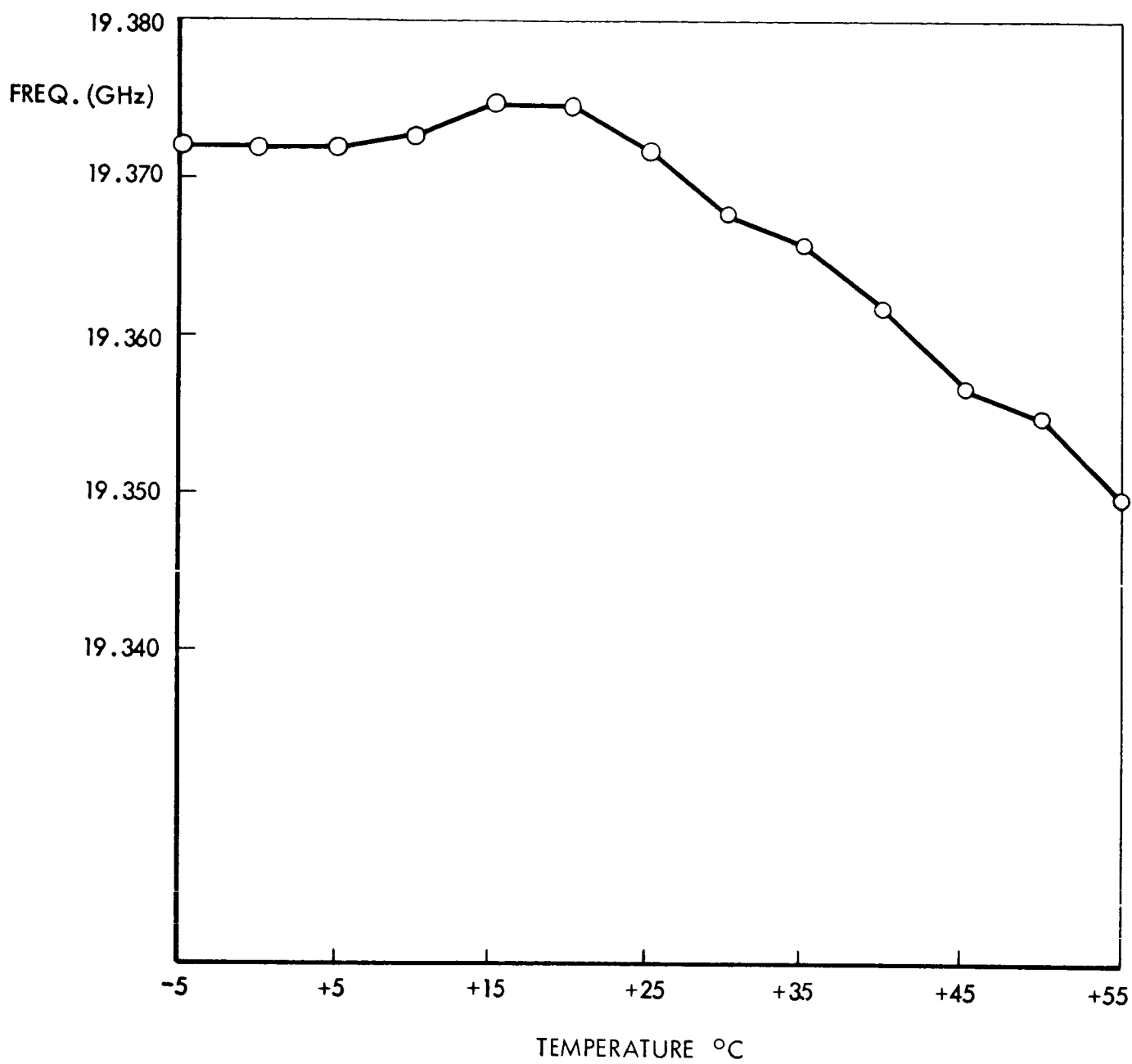
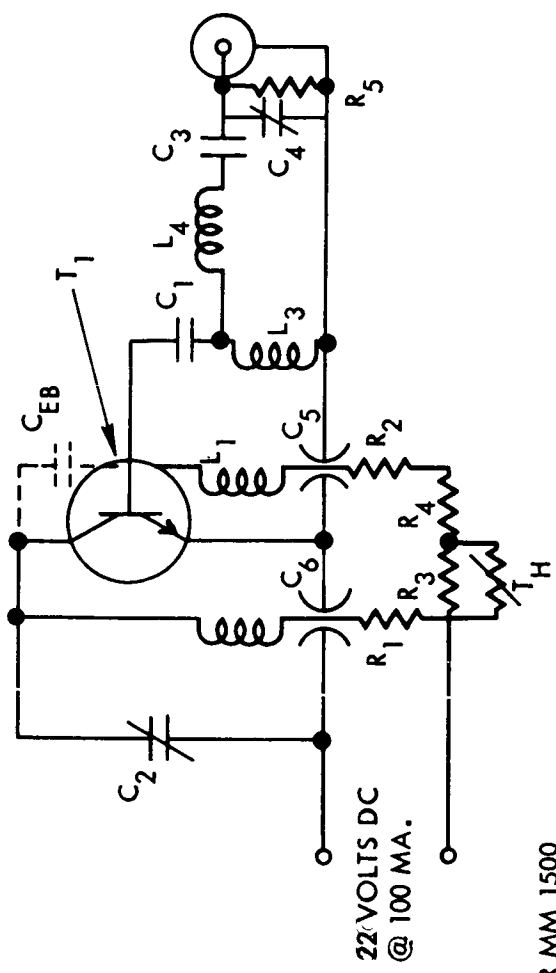


Figure 3. Frequency Versus Temperature Plot



- T₁ = MOTOROLA TRANSISTOR MM 1500
- T_H = FENWAL THERMISTOR GD-25J1
- R₁ = 100 OHM - 2 WATT
- R₂ = 510 OHM - 1/2 WATT
- R₃ = 510 OHM - 1/2 WATT
- R₄ = 240 OHM - 1/2 WATT
- R₅ = SELECTED FOR BIASING
- C₁ = JFD NMC 601
- C₂ = JOHANSON 4640
- C₃ = JFD 3 PF
- C₄ = JOHANSON 4640
- C₅, C₆ = ERIE FEEDTHRU 1000 PF

L₁, L₂ = 3 TURNS #18 WIRE ON 1/8" FORM
 L₃ = COAXIAL TRANSMISSION LINE
 0.900" LONG

Figure 4. Transistor Oscillator Circuit Diagram

This oscillator delivers approximately 200 mW of power at 1.2 GHz into a 50 ohm load. A temperature-compensating thermistor connected from emitter to base is added to stabilize the output frequency to less than 20 ppm/°C in the temperature range of -5°C to +55°C.

Frequency Multiplier Design

The first frequency multiplier stage (Figure 5) utilizes a step recovery diode for efficient higher order idlerless multiplication. The input circuit contains two current restricting chokes having anti-resonances at $2 F_0$ and $4 F_0$ which are positioned to appear as short circuits at the radial cavity wall. A capacitor is used at the input connector for tuning of the input frequency. The output circuit consists of a coaxial radial cavity whose output is probe coupled to satisfy the dc requirements of the preceding stage.

Computations of the diode parameters are as follows: The notations used are taken from Reference 1 using the punch-through overdriven case. $C_{\min} = 0.750$ pf, $\omega_c = 1.1 \times 10^{12}$, $C_c = 0.20$ pf, $L_s = 0.5$ nh, $V_b = 40$ volts, $M = 0.163$, $n=4$, $r = 4.72$, $\omega_0 = 7.58 \times 10^9$.

The equation for determining input power is

$$P_{in} = \sqrt{\frac{r}{n} M^2 + 1} \cdot P_c,$$

where
$$P_c = \frac{n^2}{(n^2 - 1)\pi} \cdot \frac{V_b \omega_0 C_{\min}}{(r + 1)^2 \sin^2 \frac{r\pi}{2(r+1)}} = 0.0517$$

$$P_{in} = 0.062 \text{ watts.}$$

The equation for determining input resistance is

$$R_{in} = \frac{2n}{r(n^2 + 1)\pi} \cdot \frac{S_{\max}}{\omega_0} + R_s$$

The equation for determining the output resistance is

$$R_{out} = \frac{2r}{n(n^2 + 1)\pi} \cdot \frac{S_{\max}}{\omega_0} + R_s$$

$$R_{out} = 5.39 \text{ ohms}$$

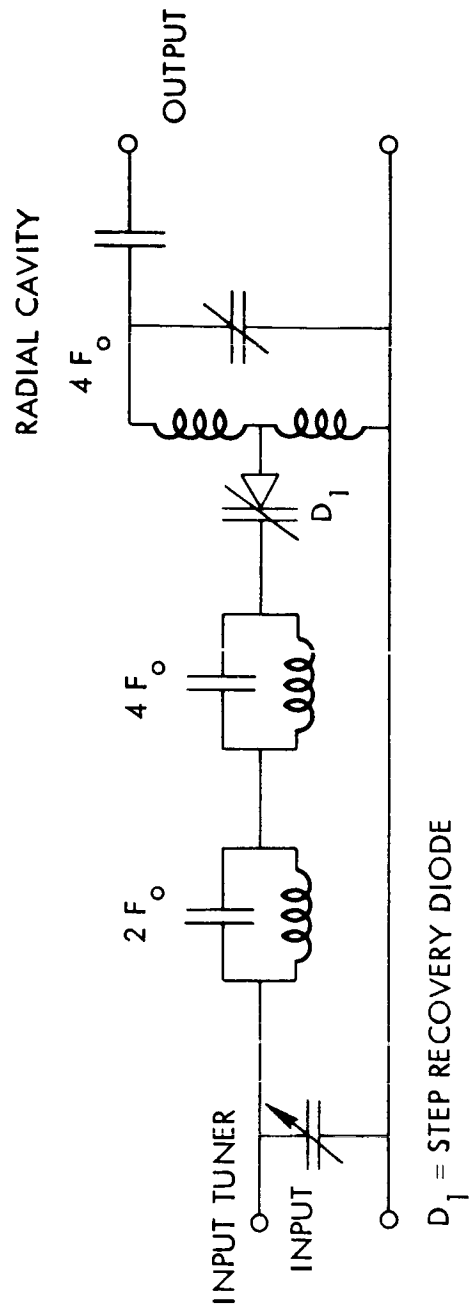


Figure 5. First Quadrupler Circuit Diagram

The equation for the average input and output elastance is

$$S = \frac{S_{\max}}{2} ,$$

Thus $X_{\text{in}} = \frac{S}{\omega_0} = -j88 \text{ ohms},$

and $X_{\text{out}} = \frac{S}{4\omega_0} = -j22 \text{ ohms}.$

These diode parameters are then transformed, using the diode model in Figure 6a, to an effective input and output impedance (Z'_{in} , Z''_{out}) in Figure 6b.

$$Z'_{\text{in}} = 3.5 - j80$$

$$Z''_{\text{out}} = 5.39 - j20$$

At the input connector Z'_{in} was transformed to be $50 + j350$. A capacitor was placed there to resonate out the inductance for a matched input.

The Z''_{out} is transformed through a resonant radial cavity into a probe coupling output having an impedance level of 50 ohms.

The second quadrupler circuit (Figure 7) utilizes a very high quality varactor diode for its active element. The input circuit contains current restricting radial chokes at $2F_0$, $3F_0$ which restrict the harmonic frequencies from entering the input port. The diode is located in series with the input coaxial circuit and in shunt with the output waveguide circuit. Embedded into a reduced height waveguide the diode (at the output frequency) is terminated into a short circuit appropriately placed to cause a real impedance to appear at that plane. The output circuit consists of a tuner and a waveguide bandpass filter. The tuner transforms the power to the waveguide impedance and the bandpass filter assures that the desired energy is concentrated in the correct harmonic number.

The computations for diode parameters are as follows.

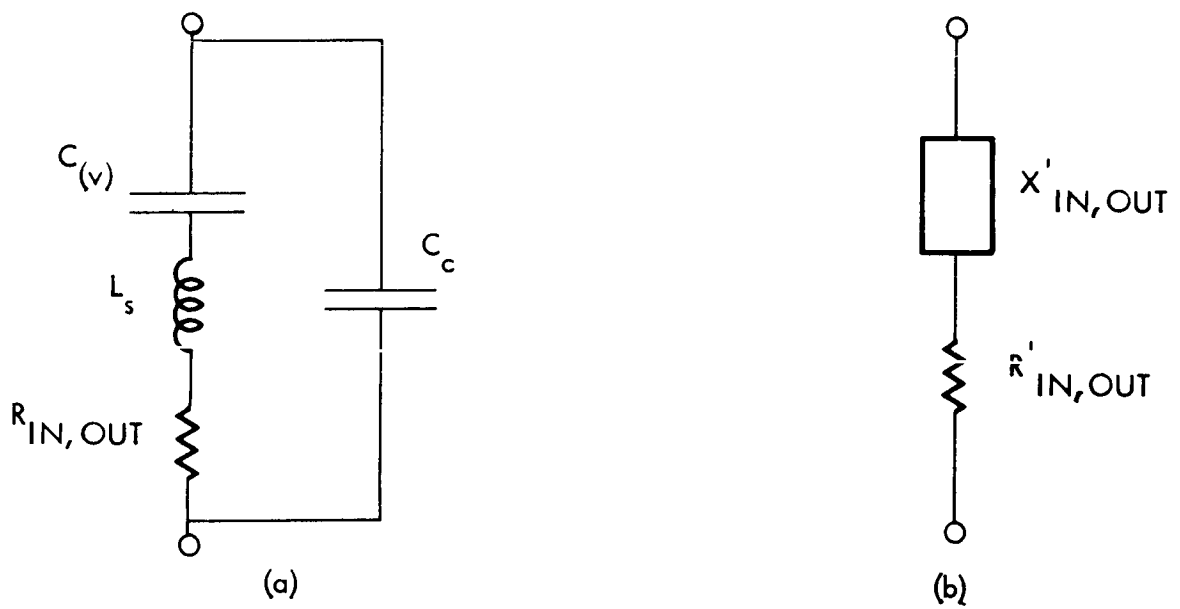
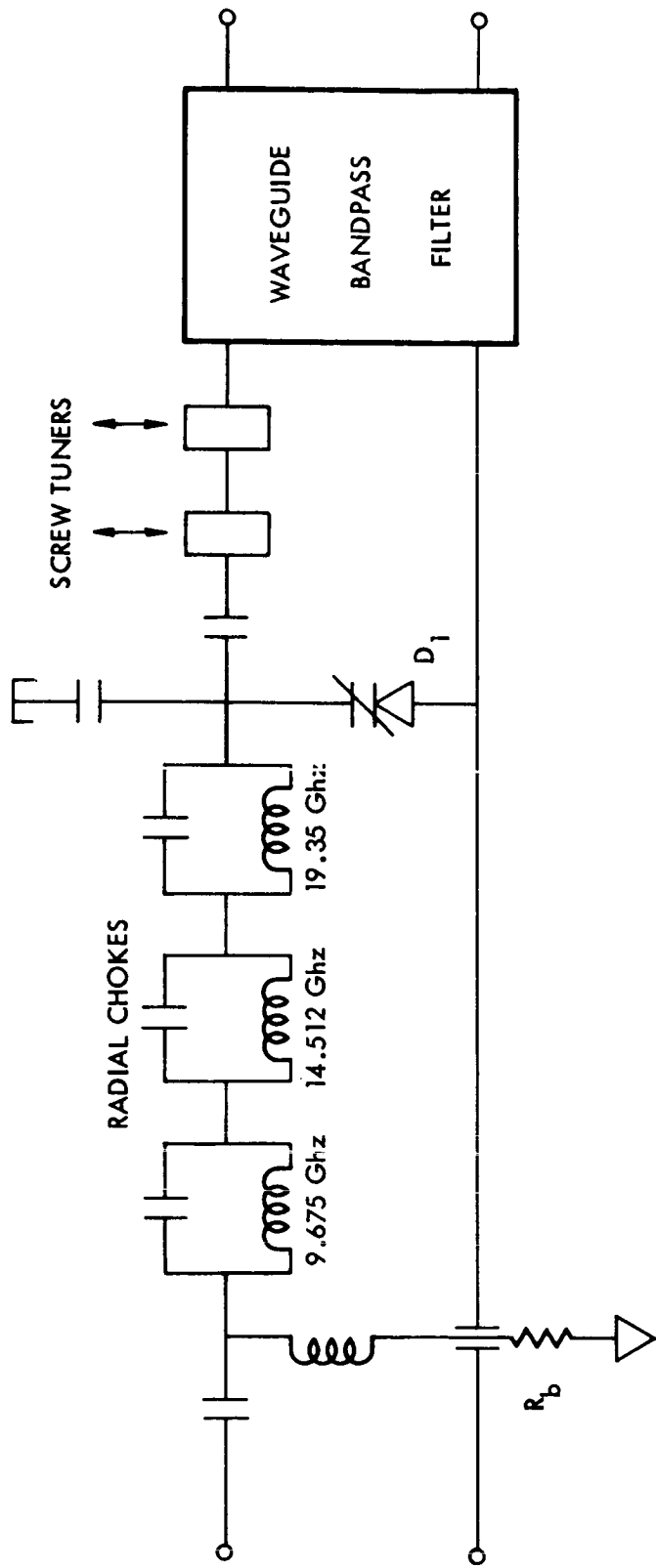


Figure 6. Diode Model Transformation Through Its Case Capacity



D_1 = HIGH QUALITY VARACTOR DIODE

Figure 7. Second Quadrupler Circuit Diagram

Notations are taken from Reference 2 assuming the overdriven abrupt junction quadrupler case.

With $C_{\min} = 0.07$ pf, $C_{j-6} = 0.13$ pf, $F_{c-6} = 350$ GHz, $C_c = 0.16$ pf, $L_s = 0.4$ nh, and $V_b = 35$ volts, $\omega_o = 3.03 \times 10^{11}$

The equation for determining input power is

$$P_{in} = \frac{\beta(V_b)^2 \omega_o}{S_{max}},$$

where $\beta = 0.02$,

$$P_{in} = 100 \text{ mW.}$$

The equation for determining input resistance is

$$R_{in} = A \frac{S_{max}}{\omega_o},$$

where $A = 0.15$,

$$R_{in} = 35.5 \text{ ohms.}$$

The equation for determining output resistance is

$$R_{out} = \frac{\beta S_{max}}{\omega_o},$$

where $\beta = 0.05$

$$R_{out} = 15 \text{ ohms.}$$

The average input and output elastance is

$$S = \frac{S_{max}}{2} = 7.15 \times 10^{12},$$

thus $X_{in} = \frac{S}{\omega_o} = -j 118 \text{ ohms},$

and $X_{out} = \frac{S}{4 \omega_o} = -j 29.7 \text{ ohms.}$

The diode parameters are then transformed using the diode model in Figure 6a to an effective input and output impedance in Figure 6b.

The input impedance at the diode plane is $= 35.5 - j118 + j12.1$, which is then transformed through its case reactance ($-j200$) into an equivalent series impedance (Z') at the diode plane

$$Z' = 130 - j178.$$

This value is transformed into the radial cavity wall by using a fifty ohm matching line having an electrical length of 0.136λ .

The output impedance at the diode plane is $= 15 - j29.7 + j48.6$, which is then transformed through its case reactance ($-j50$) into an equivalent series impedance (Z'') at the diode plane.

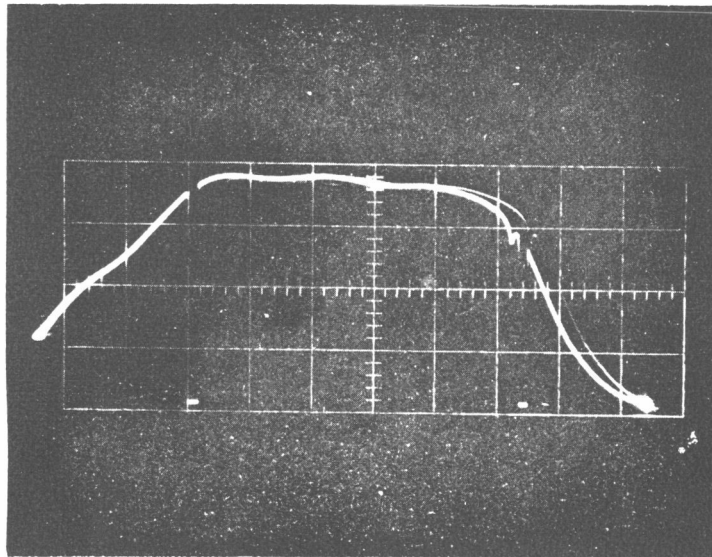
$$Z'' = 41.6 + j83.$$

The waveguide short circuit is positioned to cause a real admittance at that plane. The tuning screws are then adjusted to transform this value to the impedance of the waveguide. The output waveguide contains a three section Tchebycheff bandpass filter which was designed for a ripple component of 0.01 dB and a bandwidth of 2 percent (386 MHz). A photograph of this response is shown in Figure 8. The filter was designed from an existing computer program and was constructed using inductive posts (which were pressed into the waveguide) as the coupling element.

CONCLUSION

A solid state source has been developed for use as a local oscillator in space-borne radiometric systems. Mechanical considerations in the construction of the source were directed at minimizing weight, preserving structural strength and of being compact in nature. Electrical considerations included maximizing circuit efficiencies, minimizing dc input power and maintaining a stable frequency output. The results clearly show that the performance of this solid state source exceeds the requirements of a local oscillator power source for a space-borne radiometer system.

BANDPASS FILTER RESPONSE



MARKERS ARE AT 19.20 AND 19.50 GHz

Figure 8. Waveguide Bandpass Filter Response

REFERENCE

1. Steinbrecher, D. and Rafuse, R., "Harmonic Multiplication with Punch-Through Varactors," Solid State Circuits Conference, 1966.
2. Rafuse, R., "Recent Developments in Parametric Multipliers," Proceedings of the National Electronics Conference, Vol. XIX, pp. 461-470, Chicago (Oct., 1963).

Appendix XXIX

ANTENNA MEASUREMENTS

The information shown in the table below is a comparison of the beam efficiency data of the breadboard and aircraft models of the two-dimensional electronically-scanned K-band phased array antenna. This data has been obtained via radiation pattern integration measurements on the SG antenna pattern range. Complete 360 degree azimuth cuts were made at half degree elevation angle intervals, the entire sphere of radiation being covered in this fashion.

Also shown for informational purposes is the breadboard antenna gain as measured on the pattern range by gain comparison techniques and the breadboard antenna beam efficiency as measured at Table Mountain by radiometric techniques.

Beam Position Angle	Gain ⁽¹⁾ (dbi)	Beam Efficiency (Percent)		
		Range ⁽¹⁾	Table Mtn ⁽¹⁾	Range ⁽²⁾
+49.3	33.06	90.7	-	-
+42.7	33.56	91.2	84.0 (at 45°)	-
+31.2	34.36	93.1	90.5	93.17
+16.2	35.76	92.9	90.0	-
0	35.96	88.9	87.5	89.70
-13.7 (Fail Safe)	36.26	88.9	89.5	-
-16.2	35.06	88.6	90.5	-
-31.2	34.26	90.9	81.0	88.64
-42.7	32.76	83.8	79.3 (at -45°)	-
-49.3	31.96	83.5	-	-

(1) Breadboard Model

(2) Aircraft Model

Appendix XXX

CRYOGENIC BENCH TEST SET

INTRODUCTION

Absolute calibration of microwave radiometers relies upon the use of resistive sources at known temperatures. The accuracy of these resistive sources determines to a large degree the accuracy of the calibration; the outputs of these sources must be completely calculable to qualify as standards. For these reasons, one must properly determine the characteristics of the resistive loads and the connecting transmission lines to the output ports over the frequency range of interest.

The Cryogenic Bench Test Set is designed to exhibit precisely controlled and repeatable radiometric brightness temperatures at its output ports. These temperatures, in turn, are used as the calibration standards for determining the linearity of the radiometer response along with offsets, if any.

TEST SET CONSTRUCTION

The following general rules have been observed in the construction of the Cryogenic Bench Test Set:

- a. The resistive load material is in close thermal contact with the cryogenic liquid which determines the load temperature.
- b. The RF losses between the resistive material and the output flange of the load have been minimized. The losses and temperature distribution along the interconnecting transmission line are accurately known.
- c. The VSWR of the load is less than 1.10 across the band of interest and is independent of temperature.
- d. The output temperature of the load is independent of the cryogenic liquid level.
- e. A vacuum is maintained on the load and the load is sealed to prevent an accumulation of water inside the wave guide.

The test set is constructed as follows: two matched resistive terminations are intimately placed in a transmission line to provide good thermal coupling to a copper block which surrounds the termination. This copper block is heat sunk to the base plate of the cryoflask; the connecting waveguide is brought out the side of the cryoflask. Thermal isolation from ambient is provided by a thin walled gold-plated stainless steel section of transmission line. The vacuum seal is maintained by the insertion of two matched mica windows into a flange which is sealed to the side of the cryoflask. Two lengths of waveguide join this flange to another flange which contains the output ports of the test set. One waveguide arm contains a calibrated precision attenuator; the other contains only various sections of interconnecting waveguide. The attenuator arm connects to the radiometer antenna port, while the other goes to the radiometer calibrate, or cold load, port. Only waveguide whose loss is precisely known should be used to connect the test set to a radiometer. Two such external pieces are supplied with the test set. A block diagram of the set is shown in Figure 1.

OUTPUT TEMPERATURE CALCULATIONS

The following temperature model is used for equivalent brightness temperature calculations: The matched terminations are at the boiling point temperature, T_L , of the cryogenic liquid used. Waveguide sections are designated right, or left, as seen looking toward the output ports from the outside. The gold-plated stainless steel guide sections between the loads and the windows have losses XLR and XLL . A linear temperature distribution exists along these sections-- the temperature rising from T_L or T_{AMB} , the ambient temperature. All other portions of the test set at T_{AMB} , and therefore have constant temperature distributions.

It can be shown (Ref. 3, that the equivalent brightness temperature T_{eq} of a termination at temperature T_L as seen through a loss L -- a power ratio, not in dB -- with a linear temperature distribution T_L to T_{AMB} is given by:

$$T_{eq} = T_L + (T_{AMB} - T_L) \left\{ 1 - \left[\frac{1 - 1/L}{L} \right] \right\} \quad (1)$$

where

$$g = L(\text{in dB}) / (\log_{10} e) \quad 10$$

For a constant temperature distribution at $T = T_{\text{AMB}}$, and all other conditions identical, we have:

$$T_{\text{eq}} = T_L/L + \left[1 - 1/L \right] T_{\text{AMB}} \quad (2)$$

The following terms are used in Equations (1) and (2):

T_L = Cryogenic Boiling Point ($^{\circ}\text{K}$)

T_{AMB} = Ambient Temperature ($^{\circ}\text{K}$)

L = Loss (power ratio)

g = Same as L , but expressed in nepers

T_{eq} = Equivalent Brightness Temperature

For VSWR's less than 1.10, mismatches need not be taken into account, and equations (1) and (2) represent the only calculations necessary for calibrations of the test set.

ADDITIONAL COMMENTS CONCERNING THE COMPUTATIONS

The rationale behind the loss designations to follow is:

- a. The computation is set up for floating-point computer calculations; hence, the "Z" - "L" is fixed-point.
- b. L , obviously, stands for loss.
- c. A, B, C, etc., refer to the order in which the computation employs the loss values.
- d. "R" and "L" denote right and left, respectively.

The computer solves the equation set for sixty values of ambient temperature from 260°K to 320°K . It does this for two cryogenic boiling points 4.2°K (LHe) and 77.3°K (LN_2) and for four attenuator settings - 0, 3, 6, and 9 decibils. In addition, MAX setting may be assumed to represent a temperature

of T_{AMB} , for if $T_{eq} = T_L/L + (1/L) T_{AMB}$, then T_{eq} approaches T_{AMB} for very large values of L, say 70 dB, or $L = 10^7$

Representative losses are as follows:

Gold Plated Stainless Steel Guide

$$XLR = 1.0364 \qquad \epsilon_R = SLR = 0.03571$$

$$XLL = 1.0358 \qquad \epsilon_L = SLL = 0.03521$$

Mica Windows

Waveguide Arm

$$XLAR = 1.0260$$

$$XLBL = 1.0730$$

$$XLAL = 1.0202$$

Attenuator Arm

0 dB Setting

3 dB

6 dB

9 dB

$$XLAR (1) = 1.1883; XLAR (2) = 2.3718; XLAR (3) = 4.7323; XLAR(4) = 9.4422$$

Connecting Arms

Calibrate

Antenna

$$XLCL = 1.0127$$

$$XLCR = 1.0140$$

Using these data, we may calculate a sample brightness temperature.

Assume $T_L = 77.3^\circ\text{K}$, the boiling point of LN_2 , and $T_{AMB} = 24.5^\circ\text{C} = 297.6^\circ\text{K}$.

Also assume the attenuator is set at 3 dB.

$$\text{From (1), } T_{eq} (1) = T_L + (T_{AMB} - T_L) \left\{ 1 - \left[\frac{1 - \frac{1}{XLR}}{SLR} \right] \right\}$$

$$\text{or } T_{eq} (1) = 77.3 + (220.3) \left[1 - \frac{.0364}{1.0364} \right] = 77.3 + 220.3 \left\{ 1 - .9835 \right\}$$

$$\text{or } T_{eq} (1) = 77.3 + 220.3 (.0165) = \underline{80.9^\circ\text{K}}$$

$$\text{From (2), } T_{\text{eq}}(2) = T_{\text{eq}}(1)/L + \left[1 - 1/L\right] T_{\text{AMB}}$$

$$\text{or } T_{\text{eq}}(2) = 80.9/1.026 + \left(\frac{.026}{1.026}\right) 297.6$$

$$= 78.8 + 7.5 = 86.3^{\circ}\text{K} = T_{\text{eq}}(2)$$

$$\text{From (2), } T_{\text{eq}}(3) = 86.3/2.3718 + \left(\frac{1.3718}{2.3718}\right) 297.6$$

$$= 36.4 + 172.1 = \underline{208.5^{\circ}\text{K}} = T_{\text{eq}}(3)$$

$$\text{Finally, from (2), } T_{\text{eq}}(4) = T_{\text{ANT}} = 208.5/1.0140 + \left(\frac{.0140}{1.0140}\right) 297.6$$

$$= 205.6 + 4.1 = \underline{209.7^{\circ}\text{K}} = T_{\text{ANT}}$$

A computer printout of the test set outputs (Figure 2) is included for various ambient temperatures for both liquid nitrogen and liquid helium. These outputs include the effect of the two short pieces of waveguide furnished with the test set. No other pieces of waveguide should be attached if these numbers are to be used as the test set output temperatures.

Using the test set in conjunction with the radiometer, one may obtain digital data at each of the following attenuator settings -- 0, 3, 6, 9 dB and MAX. These data consist of three digit numbers a_i . Computing the mean,

$$\bar{a} = \frac{1}{N} \sum_{i=1}^N a_i \text{ for each setting, one may plot the various values of } \bar{a} \text{ versus}$$

the difference between the radiometer Dicke load temperature and the test set brightness temperature as determined from the computed tables. See Figure 2 for the computer tables and Figures 3 and 4 for representative radiometer calibrations.

Also, one may note from the plotted straight line the system gain for the radiometer, dT/dK --i.e., the slope of the line. One can then calculate the system sensitivity by using:

TLOAD OF NITROGEN = 77.3

TR	0	3	6	9	CAL
261	114.86	187.78	224.30	242.61	98.34
262	115.06	188.38	225.10	243.51	98.45
263	115.26	188.98	225.90	244.41	98.57
264	115.47	189.58	226.70	245.31	98.68
265	115.67	190.19	227.50	246.21	98.80
266	115.88	190.79	228.30	247.11	98.91
267	116.08	191.39	229.10	248.01	99.03
268	116.29	191.99	229.90	248.91	99.14
269	116.49	192.59	230.70	249.81	99.25
270	116.70	193.19	231.50	250.71	99.37
271	116.90	193.79	232.30	251.61	99.48
272	117.10	194.40	233.11	252.51	99.60
273	117.31	195.00	233.91	253.41	99.71
274	117.51	195.60	234.71	254.31	99.83
275	117.72	196.20	235.51	255.21	99.94
276	117.92	196.80	236.31	256.11	100.06
277	118.13	197.40	237.11	257.01	100.17
278	118.33	198.00	237.91	257.91	100.29
279	118.54	198.61	238.71	258.81	100.40
280	118.74	199.21	239.51	259.71	100.51
281	118.94	199.81	240.31	260.61	100.63
282	119.15	200.41	241.11	261.50	100.74
283	119.35	201.01	241.91	262.40	100.86
284	119.56	201.61	242.71	263.30	100.97
285	119.76	202.21	243.51	264.20	101.09
286	119.97	202.82	244.31	265.10	101.20
287	120.17	203.42	245.11	266.00	101.32
288	120.38	204.02	245.91	266.90	101.43
289	120.58	204.62	246.71	267.80	101.55
290	120.78	205.22	247.51	268.70	101.66

Figure 2. Bench Test Set Output Temperatures

LOAD OF NITROGEN = 77.3

TR	TRAD					CAL
	0	3	6	9		
291	120.99	205.82	248.31	269.60	101.77	
292	121.19	206.42	249.11	270.50	101.89	
293	121.40	207.03	249.91	271.40	102.00	
294	121.60	207.63	250.71	272.30	102.12	
295	121.81	208.23	251.51	273.20	102.22	
296	122.01	208.83	252.31	274.10	102.35	
297	122.22	209.43	253.11	275.00	102.46	
298	122.42	210.03	253.91	275.90	102.58	
299	122.62	210.63	254.71	276.80	102.69	
300	122.83	211.24	255.51	277.70	102.80	
301	123.03	211.84	256.31	278.60	102.92	
302	123.24	212.44	257.11	279.50	103.03	
303	123.44	213.04	257.91	280.40	103.15	
304	123.65	213.64	258.71	281.30	103.26	
305	123.85	214.24	259.51	282.20	103.38	
306	124.06	214.84	260.31	283.10	103.49	
307	124.26	215.45	261.11	284.00	103.61	
308	124.46	216.05	261.91	284.90	103.72	
309	124.67	216.65	262.71	285.80	103.84	
310	124.87	217.25	263.51	286.70	103.95	
311	125.03	217.85	264.31	287.60	104.06	
312	125.23	218.45	265.11	288.50	104.18	
313	125.43	219.05	265.91	289.40	104.29	
314	125.63	219.66	266.71	290.30	104.41	
315	125.90	220.26	267.51	291.20	104.52	
316	126.10	220.86	268.31	292.10	104.64	
317	126.30	221.46	269.12	293.00	104.75	
318	126.51	222.06	269.92	293.90	104.87	
319	126.71	222.66	270.72	294.80	104.98	
320	126.92	223.26	271.52	295.70	105.10	

Figure 2. Bench Test Set Output Temperatures (Continued)

LOAD OF HELIUM = 4.2

TR	TRAD				CAL
	0	3	6	9	
261	56.70	158.64	209.70	235.29	33.61
262	56.91	159.25	210.50	236.19	33.72
263	57.11	159.85	211.30	237.09	33.84
264	57.31	160.45	212.10	237.99	33.95
265	57.52	161.05	212.90	238.89	34.07
266	57.72	161.65	213.70	239.79	34.18
267	57.93	162.25	214.50	240.69	34.30
268	58.13	162.85	215.30	241.59	34.41
269	58.34	163.46	216.10	242.49	34.53
270	58.54	164.06	216.90	243.39	34.64
271	58.75	164.66	217.70	244.29	34.76
272	58.95	165.26	218.50	245.19	34.87
273	59.15	165.86	219.30	246.09	34.98
274	59.36	166.46	220.10	246.99	35.10
275	59.56	167.06	220.90	247.89	35.21
276	59.77	167.66	221.70	248.79	35.33
277	59.97	168.27	222.50	249.69	35.44
278	60.18	168.87	223.30	250.59	35.56
279	60.38	169.47	224.10	251.49	35.67
280	60.59	170.07	224.90	252.39	35.79
281	60.79	170.67	225.70	253.29	35.90
282	60.99	171.27	226.50	254.19	36.02
283	61.20	171.87	227.30	255.09	36.13
284	61.40	172.48	228.10	255.99	36.24
285	61.61	173.08	228.91	256.89	36.36
286	61.81	173.68	229.71	257.79	36.47
287	62.02	174.28	230.51	258.69	36.59
288	62.22	174.88	231.31	259.59	36.70
289	62.43	175.48	232.11	260.49	36.82
290	62.63	176.08	232.91	261.39	36.93

Figure 2. Bench Test Set Output Temperatures (Continued)

LOAD OF HELIUM = 4.2

TR	0	3	6	9	CAL
291	62.83	176.69	233.71	262.28	37.05
292	63.04	177.29	234.51	263.19	37.16
293	63.24	177.89	235.31	264.08	37.28
294	63.45	178.49	236.11	264.98	37.39
295	63.65	179.09	236.91	265.88	37.50
296	63.86	179.69	237.71	266.78	37.62
297	64.06	180.29	238.51	267.68	37.73
298	64.27	180.90	239.31	268.58	37.85
299	64.47	181.50	240.11	269.48	37.96
300	64.67	182.10	240.91	270.38	38.08
301	64.88	182.70	241.71	271.28	38.19
302	65.08	183.30	242.51	272.18	38.31
303	65.29	183.90	243.31	273.08	38.42
304	65.49	184.50	244.11	273.98	38.53
305	65.70	185.11	244.91	274.88	38.65
306	65.90	185.71	245.71	275.78	38.76
307	66.11	186.31	246.51	276.68	38.88
308	66.31	186.91	247.31	277.58	38.99
309	66.51	187.51	248.11	278.48	39.11
310	66.72	188.11	248.91	279.38	39.22
311	66.92	188.71	249.71	280.28	39.34
312	67.13	189.32	250.51	281.18	39.45
313	67.33	189.92	251.31	282.08	39.57
314	67.54	190.52	252.11	282.98	39.68
315	67.74	191.12	252.91	283.88	39.79
316	67.95	191.72	253.71	284.78	39.91
317	68.15	192.32	254.51	285.68	40.02
318	68.35	192.92	255.31	286.58	40.14
319	68.55	193.53	256.11	287.48	40.25
320	68.76	194.13	256.91	288.38	40.37

Figure 2. Bench Test Set Output Temperatures (Continued)

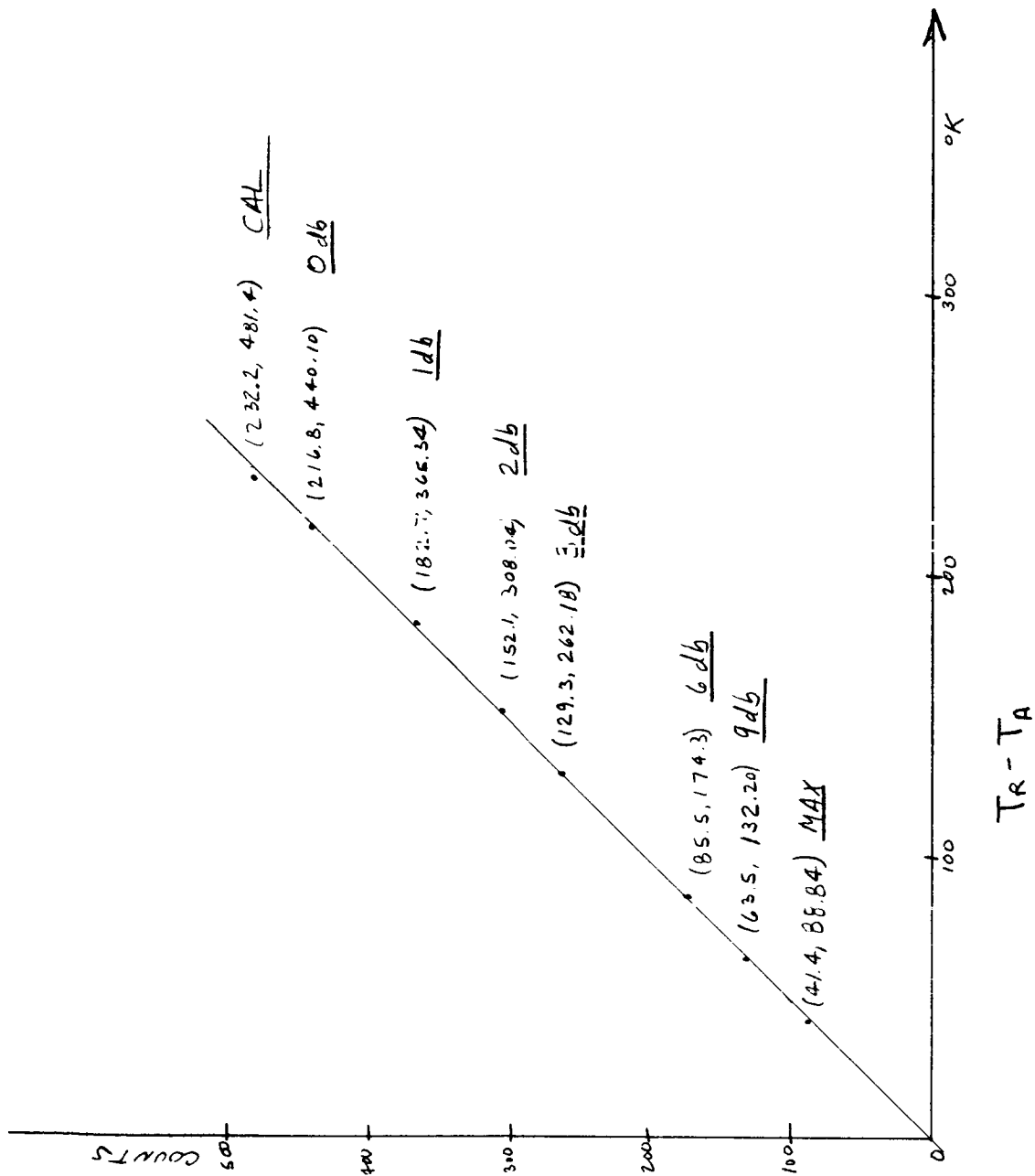


Figure 3. Calibration Curve ($T_{AMB} \approx 24.5^{\circ}C$)

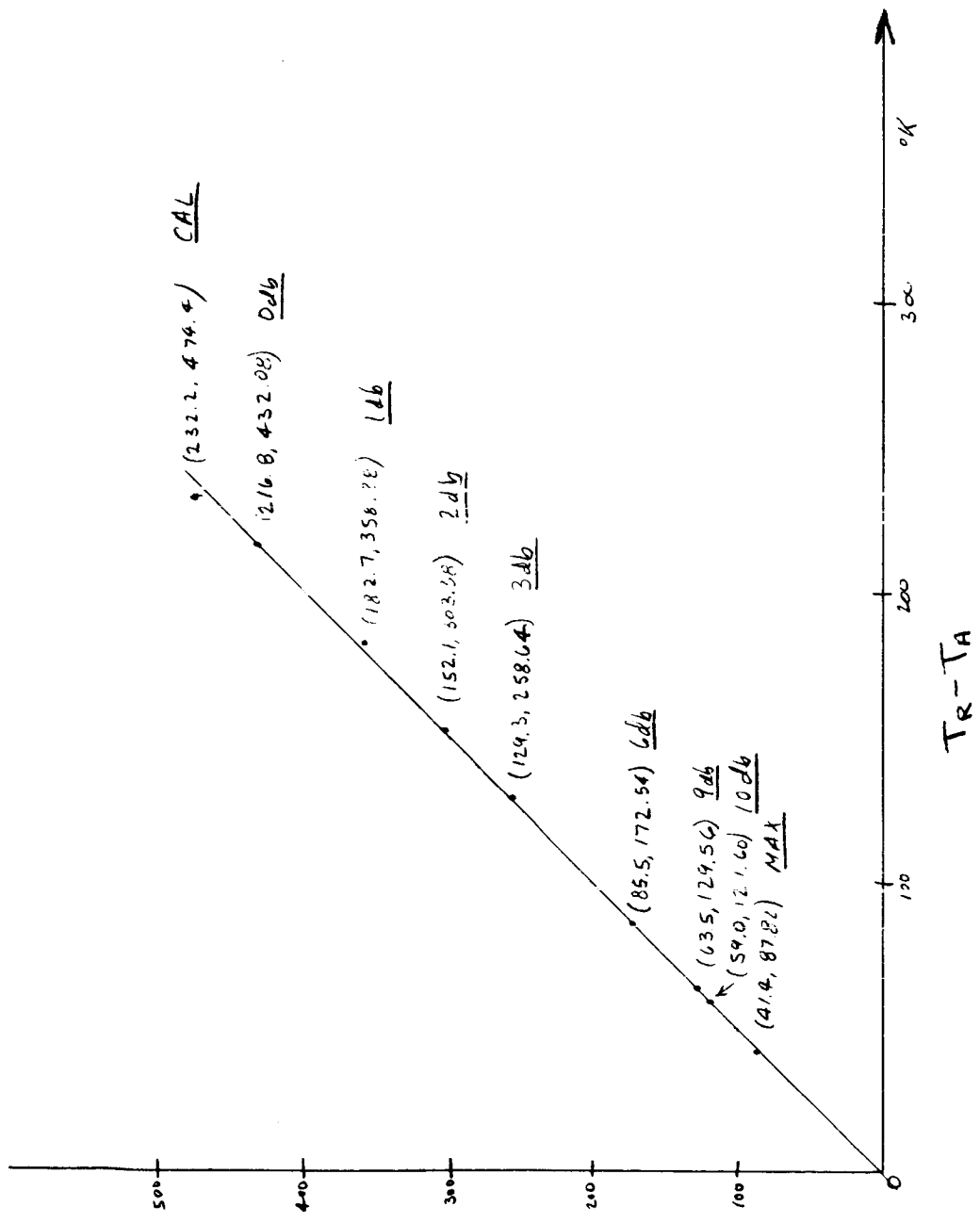


Figure 4. Calibration Curve ($T_{AMB} \approx 24.5^{\circ}C$)

$$\Delta T = \left[\frac{1}{N} \sum_{i=1}^N \left(a_i - \frac{1}{N} \sum_{j=1}^N a_j \right)^2 \right]^{1/2} \frac{dT}{dK}$$

or, using \bar{a} as previously defined,

$$\Delta T = \left[\frac{1}{N} \sum_{i=1}^N (a_i - \bar{a})^2 \right]^{1/2} \frac{dT}{dK}$$

In conclusion and in summary, one may determine the following data from the Cryogenic Bench Test Set:

- a. System linearity
- b. System gain
- c. System offset
- d. System sensitivity

References explaining the calibration of radiometers in greater detail are contained in the bibliography which follows.

CALIBRATION CURVES

Two calibration curves run on the NIMBUS breadboard radiometer using the above described bench test set are shown on Figures 3 and 4. These were run on consecutive days prior to shipment of this radiometer to NASA/GSFC. It is interesting to note the intercept at $(T_R - T_A) = 0$ is approximately 0 counts. This shows that the offset is negligible.

Another point of interest is that the points marked MAX correspond 2°K of the ambient temperature, which is as it should be. The sensitivity of the radiometer has been found to be approximately 0.66°K rms.

REFERENCES FOR COLD LOAD TEST SET

1. A. J. Estin, C. L. Trembath, J. S. Wells, and W. C. Daywitt, "Absolute Measurement of Temperatures of Microwave Noise Sources," IRE Trans. on Inst. and Meas., pp. 209-213, Sept. 1960.
2. J. S. Wells, W. C. Daywitt, and C. K. S. Miller, "Measurement of Effective Temperatures of Microwave Noise Sources," IRE Trans. on Inst. and Meas., pp. 17-28, March 1964.
3. C. T. Stelzreid, "Temperature Calibration of Microwave Thermal Noise Sources," IEEE Trans. on Microwave Theory and Techniques, pp. 128-130, Jan. 1965.
4. C. E. Stelzreid, "A Liquid Helium-Cooled Coaxial Termination," Proc. of IRE, p. 1224, July 1961.
5. R. E. Clauss, W. Higa, C. Stelzreid, and E. Wiebe, "Total System Noise Temperature: 15°K," IEEE Trans. on Microwave Theory and Techniques, pp 619-620, November 1964.
6. C. T. Stelzreid, "Temperature Calibration of Microwave Termination," JPL Space Programs Summary No. 37-26, Vol. IV, pp. 189-194.
7. C. T. Stelzreid and S. M. Petty, "Microwave Insertion Loss Test Set," IEEE Trans. on Microwave Theory and Techniques, pp. 475-477, July 1964.
8. R. C. Menon, N. P. Albaugh, and J. W. Dozier, "Cooled Loads as Calibration Noise Standards for the mm-Wavelength Range," Proc. of IEEE, pp. 1501-1503, October 1966.
9. R. W. Beatty, "Mismatch Errors in the Measurement of Ultrahigh-Frequency and Microwave Variable Attenuators," Journal of Research of the National Bureau of Standards, pp. 7-9, Vol. 52, No. 6, June 1964.
10. R. W. Beatty, "Insertion Loss Concepts," Proc. of IEEE, pp. 663-671, Vol. 52, No. 6, June 1964.
11. J. E. Sees, "Fundamentals in Noise Source Calibrations of Microwave Frequencies," Naval Research Lab., Wash., D.C. Report No. 5051, 1958.
12. A. E. Siegman, "Thermal Noise in Microwave Systems" Part 1, Microwave Journal, pp. 81-90, March 1961.

13. D. Schuster, C. T. Stelzreid, and G. S. Levy, "The Determination of Noise Temperatures of Large Paraboloidal Antennas," IRE Trans. on Antennas and Propagation, pp. 286-291, May 1962.
14. C.K.S. Miller, W. C. Daywitt, and M. G. Arthur, "Noise Standards, Measurements, and Receiver Noise Definitions," IEEE Proceedings, pp. 865-877, June 1967.

Appendix XXXI

RELATIONS FOR THE EXACT CALCULATION OF RADIOMETRIC TEMPERATURES OF CRYOGENIC-COOLED SOURCES

This is to illustrate in some detail the physical and mathematical reasoning behind the equivalent brightness temperature equations presented in Appendix XXX. The differential equation of power flow, including black body radiation effects, is derived. General and specific solutions to the equation are presented.

The following terms are used in the derivation:

- $V(X)$ = voltage along the transmission line - a complex quantity
 - $I(X)$ = current along the transmission line - a complex quantity
 - L - loss of waveguide of length l = Power in/Power out
 - \mathcal{L} = attenuation of transmission line in nepers = $\ln L$
 - l = length of transmission line
 - α = exponential voltage attenuation per unit length
i. e., $|V(X + \Delta X)| = |V(X)| e^{-\alpha \Delta X}$
 - T_c = thermal temperature of load - a constant
 - $T_D(X)$ = thermal temperature along transmission line
 - T_o = thermal ambient temperature - a constant
 - $T_{eq}(X)$ = equivalent brightness temperature along the transmission line
 - T^l = $T_{eq}(l)$ = equivalent brightness temperature of a line of length l
- X is measured from the load to the output port
- k = Boltzmann's constant
 - B = Bandwidth

By definition, $|V(X + \Delta X)| = |V(X)| e^{-\alpha \Delta X}$. Since the wave equations for voltage and current are identical, it follows that $|I(X + \Delta X)| = |I(X)| e^{-\alpha \Delta X}$. If we assume no mismatches, the voltage and current are in phase and hence $P(X) = |V(X)| |I(X)|$. But we also have $P(X + \Delta X) = |V(X + \Delta X)| |I(X + \Delta X)| = |V(X)| |I(X)| (e^{-\alpha \Delta X})^2 = P(X) e^{-2\alpha \Delta X}$.

From the black body radiation theory, we have the approximation that the brightness temperature of a body a thermal temperature T is equal to (emissivity) · kTB. By reciprocity, emissivity equals absorption, where absorption is defined by:

$$\text{Power absorbed} = (\text{Power incident}) (\text{Absorption})$$

However, power absorbed = $P(X) - P(X + \Delta X) = P(X) - e^{-2\alpha \Delta X} P(X) = (1 - e^{-2\alpha \Delta X}) P(X)$. Since $P(X)$ equals power incident, the absorption and hence the emissivity, equal $(1 - e^{-2\alpha \Delta X})$.

By conservation of energy, we know that the power at $(X + \Delta X)$ equals the power left after attenuation plus the brightness temperature contribution. Therefore, $P(X + \Delta X) = e^{-2\alpha \Delta X} P(X) + (1 - e^{-2\alpha \Delta X}) k T_D(X) B$.

Rearranging terms and dividing by ΔX yields:

$$\frac{P(X + \Delta X) - P(X)}{\Delta X} = \left(\frac{e^{-2\alpha \Delta X} - 1}{\Delta X} \right) P(X) + \left(\frac{1 - e^{-2\alpha \Delta X}}{\Delta X} \right) k T_D(X) B$$

Substituting $e^{-2\alpha \Delta X} = \sum_{n=0}^{\infty} \frac{(-2\alpha \Delta X)^n}{n!}$ and taking the limit yields

$$\frac{dP}{dX} = \lim_{\Delta X \rightarrow 0} \frac{P(X + \Delta X) - P(X)}{\Delta X} = -2\alpha P(X) + 2\alpha k T_D(X) B$$

Using the approximation given above, we can say $P(X) = k T_{eq}(X) B$

This gives $\frac{dT_{eq}(X)}{dX} + 2\alpha T_{eq}(X) = 2\alpha T_D(X)$

This is an equation of form $\frac{dy}{dX} + P(X)y = Q(X)$, where $P(X) = 2\alpha$ and $Q(X) = 2\alpha T_D(X)$. Using an integrating factor $e^{\int P dX}$, the solution

$$y = e^{-\int PdX} \left\{ \int Q(X) e^{\int PdX} dX + C \right\} \quad \text{may be derived.}$$

By analogy, using a line of length l and loss $L = e^{2al} = e^{\mathcal{L}}$, we have

$$T_{\text{eq}}(l) = T^1 = e^{-\int_0^l 2adX} \left\{ \int_1^l 2aT_d(X) e^{\int_0^X 2adX} dX + C \right\}$$

where $C = T_{\text{eq}}(0) = T_c$, the load temperature.

$$\text{This reduces to } T^1 = \frac{1}{L} \left\{ \frac{\mathcal{L}}{l} \int_0^l e^{(\mathcal{L}/l)X} T_D(X) dX + T_c \right\}$$

where $\mathcal{L}/l = 2a$ by definition

For a constant temperature distribution, $T_L(X) = T_o$, which, upon substitution and integration, yields:

$$T^1 = T_c/L + T_o (1 - 1/L)$$

For a linear temperature distribution, $T_D(X) = T_c + (T_o - T_c) X/l$

$$\text{and } T^1 = T_c + (T_o - T_c) \left\{ 1 - \frac{1 - 1/L}{\mathcal{L}} \right\}$$

These, then, are the equations used in deriving equivalent temperatures for radiometer calibration sets.